ARCHIVES
OF CIVIL AND MECHANICAL
ENGINEERING

Contents

Spis treści

Assessment of RC structures influenced by crude oil products

T. BŁASZCZYŃSKI

Poznań University of Technology, ul. Piotrowo 5, 60-965 Poznań, Poland.

Thinking about structures far beyond 2000, it has to be remember about those, who are exist. From that point the durability of RC systems in crude oil product environments is now recognised as a very important part of the design process. Durability analysis of RC structures by field and laboratory tests based on data collected over many years are described. The question of crude oil and its products influence on concrete and reinforced concrete is closely connected with this material mining, processing and further exploitation in various industry branches. The oil products affect tanks walls, foundations and other constructions supporting machines and storage floors. Therefore, the range and technical importance of the problem are wide and especially connected with industrial construction. The assessment methods of concrete and RC damage by crude oil products based on their feature tests is presented.

Keywords: *RC structures, crude oil products influence, concrete destruction mechanisms, assessment methods*

1. Introduction

The research of frame foundations used for large power turbines (Figure 1a) showed that along lapse of time considerable damage can be observed. The damage, mainly cracks and fissures and the dynamic stiffness of the structure decrease often causes serious damages to the turbines. It was also stated, that strong oiling of the foundations is one of the main factors causing these damages [1].

Oil drill platforms are another example of concrete constructions undergoing strong crude oil influence (Figure 1b), nevertheless the research of crude oil influence on high-durability concretes used for these structures showed, that they are resistant to this material influence [2–3].

The problem of structural elements oiling is dealt with in industrial buildings as well. Strongly oiled reinforced concrete floors show considerable damage, which often obstructs the buildings exploitation. Due to oil influence after a few years significant cracks enlargement was observed [4–5].

Biczok [6] presented an example of an oiled reinforced concrete floor, in which a significant cracking and deflection appeared, and during repair work concrete was easily separated from the reinforcement bars.

The oil storage floor in Jedlicze Kerosene Refinery, on which mineral oil tanks were placed, represented a similar state (Figure 2a, [7]), as well as the industrial buildings floors, adapted to Social Psychology University in Warsaw, recently analysed by the author (Figure 2b).

a)   b)
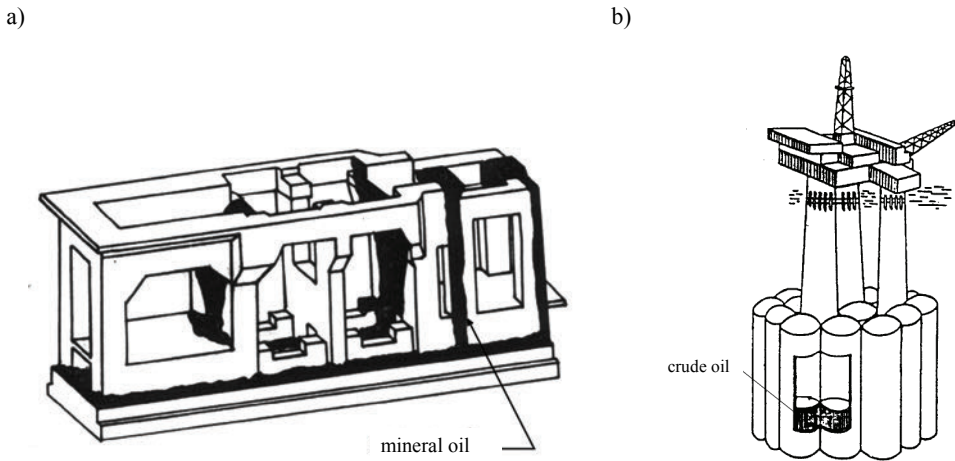
Fig. 1. Example of RC structures influence by crude oil and its products:
a) frame turbine foundation [1], b) oil drill platform [3]

a)   b)
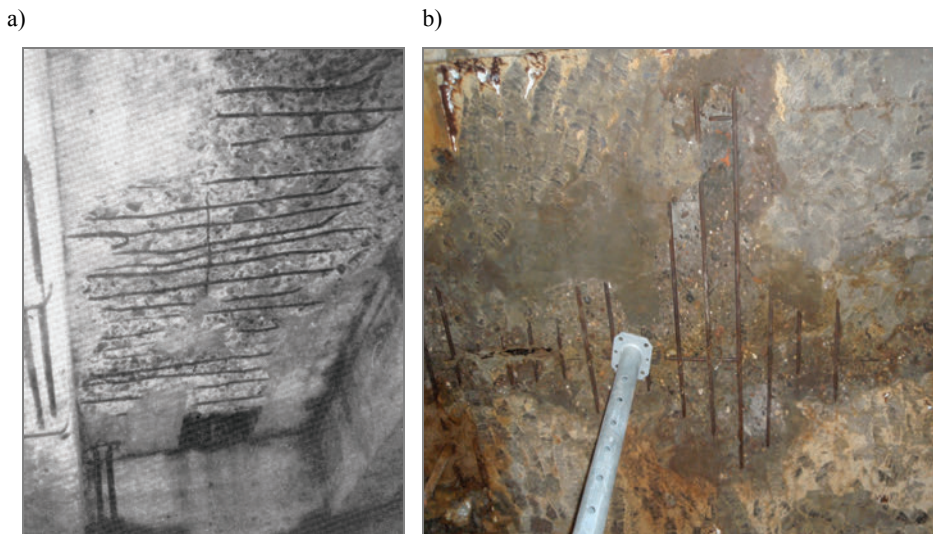
Fig. 2. Destruction of structural floors infected by mineral oils and emulsions: a) floor in Jedlicze
Kerosene Refinery [7], b) floor in Social Psychology University in Warsaw

2. Crude oil products influence on concrete

The hydrocarbon-products (crude oil products) influence over a long period of time
in comparison to water is presented by in [8]. This influence is various: beginning
with lack of it in the case of kerosene, petrol or vaseline oil to significant changes in
case of some mineral oils, Figure 3.

$$\frac{f_b^c}{f_b^{c1}} \ [\%]$$

1 Not oiled	**2** Crude oil	**3** Fuel oil	**4** Vaselene oil
5 H-70 oil	**6** M-40 oil	**7** TU-20 oil	**8** Lux10 oil
9 Wrzecion 2 oil	**10** Petrol	**11** Kerosene	**12** Benzene
13 Water (after 2 years)	**14** Water (after 7 days)		
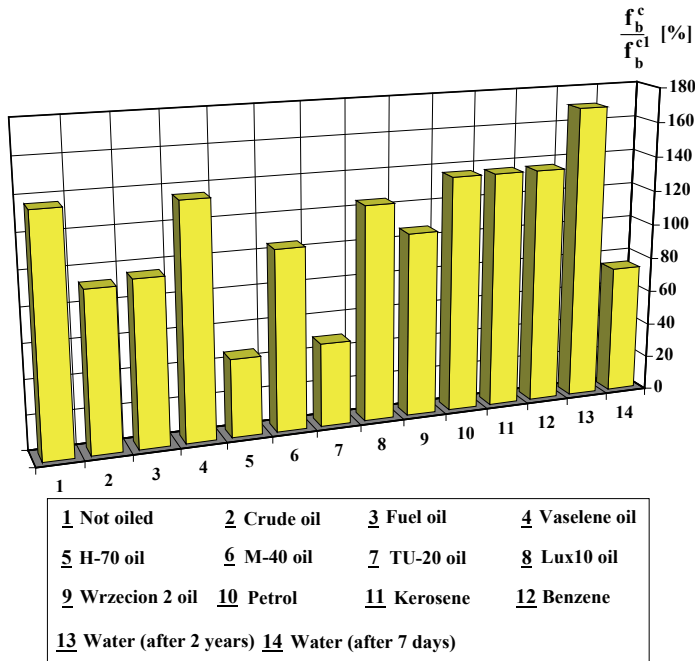
Fig. 3. Effects of different crude oil products influence on concrete
(in comparison to water); f_b^{c1} – initial concrete compressive strength, [8]

Short time changes in properties of concrete saturated with water is due to lowering of cement matrix strength and they are reversible (see 14 in Figure 3). In long term water acts positively on concrete and strengthening occurs (13 in Figure 3).

The author's longstanding research on mineral oils influence on mortars and cement-based concretes led to rebutting the thesis concerning the considerable influence of the crude oil products viscosity, and especially mineral oils on the concrete destruction degree and allowed to allocate more and less destructive substances from the mineral oils group, which denies the common thesis concerning equality affecting of all mineral oils [9–10]. The concrete compression strength f_b^c changes in case of different concrete grade (for mineral oil TU-20) are presented in Figure 4. It clearly shows that if concrete grade is lower, the concrete compressive strength decrease is bigger.

Mineral oils also affect the bond between reinforcing steel and surrounding concrete [11]. For the plain bars the highest rate of the bond decrease occurs during the first 12 months of mineral oils influencing, then it tends to stabilisation. Comparing the influence of the all used oils on adhesion one has to conclude that the oil TU-20 (turbine oil) decreases it the most significantly. This is certainly due to its lowest viscosity, which determines the better penetration of the bond area. However, the relation of this bond decrease and the oil viscosity is observed only in the early stage of oiling.

After 6 month of the influence of the used oils, the bond for the oil H-70 (hydraulic oil) constantly decreased. For this type of oil the decreasing of natural bond is grater then for the oil M-40 (mechanical oil). This means that the kinematic viscosity of mineral oil is not only one determinant of the degree of adhesion damage. The percentage of the adhesion decrease is significant. After a year and a half of influencing of the oil TU-20 in case of concrete grade C28/35 is 33% and in case of concrete grade C16/20 is as large as almost 59%.
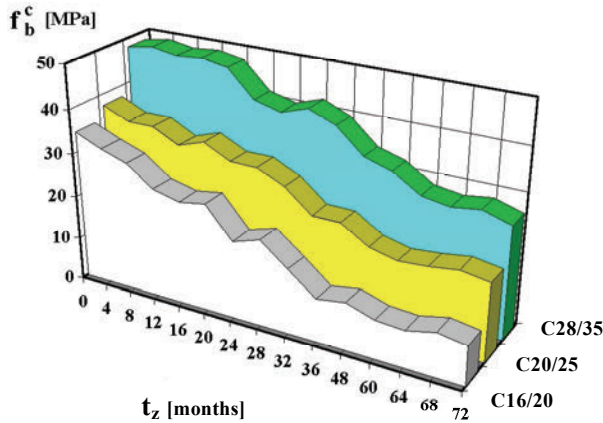
Fig. 4. Variation of different concrete grade compressive strength
during the period of exposure to TU-20 mineral oil

In case of ribbed steel bars initially decrease of bond is negligible, but after 12 months the decrease becomes significant and is stabilised after about 6 years. In that case the direct reason for the decrease of bond is the progressive degradation of oiled concrete and its adhesion to reinforcement. The increase of mineral oil viscosity significantly influences the friction between steel bar and cement matrix. The effect of the various crude oil products on ribbed bars bond is similar to that on concrete compressive strength.

Latest researches of crude oil products (machine oil L-AN 22 and cooling emulsion EMULGOL ES12) on bond of plain bars to oiled concrete introduced Runkiewicz [12]. After about 4 years of applied substance influence, the fall of maximum bond was from 17% to 33%.

The reasons of concrete structure destruction are usually complex and one of them is usually the dominative one [13]. Comparison of physico-chemical influences between water and mineral oils leads to a conclusion, that surface active polar molecules within the hydrocarbon chain are harmful. Water molecules are small dipoles geometrically and when acted positively on concrete strengthening occurs. The hydrocarbon chain is non-polar and non-harmful, but in connection with hydrophilic part gives the problem. This explains why petrol, kerosene, benzene and vaseline oil are not corro-

sive to concrete since they contain non-harmful short hydrocarbon chains. First of all in fuels water is the polar element or there is a very small part of other polar active molecules, but with very short chain, which are not long enough for hydrophobing of the concrete inner structure.

The existence of organic active molecules in liquid may be detected by IR spectroscopy. The degree of polarisation of crude oil products can be measured also indirectly by its lubricity or demulgation method.

3. The method of concrete corrosion rate assessment under crude oil products influence

3.1. IR spectrophotometry method

Using the infra-red spectroscopy with the small amount of oil one can get the whole plot of the examined fluid. Comparing the basic oil and oil with improvers it can be seen the significant peaks in the case of all the most active polar molecules.
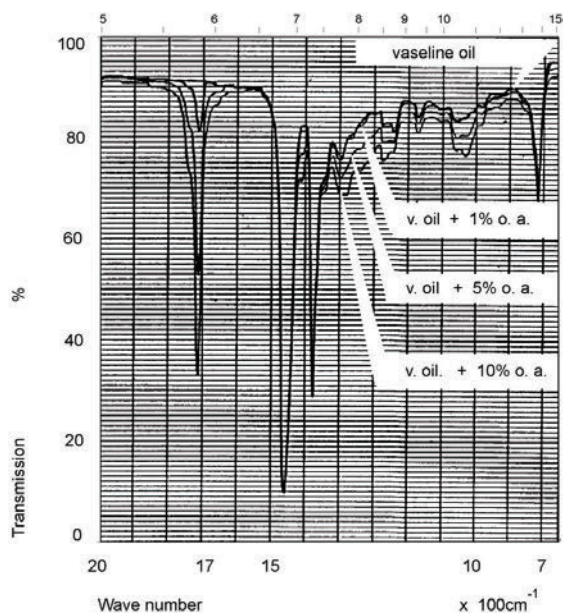
Fig. 5. Comparison of vaseline oil IR spectra with the spectra of other mixtures

Figure 5 shows a comparison of vaseline oil (creating basic non active oil) IR spectra with the spectra of mixtures based on it and added the polar surface active improves in the form of 1%, 5% or 10% of oleinic acid (o. a.). The significant differences in peaks in the case of all the most active polar molecules (wave number 1030, 1070, 1200, 1280, 1340 and 1710 cm^{-1}) are seen.

The content analysis of polar active molecules on the basis of above-spectrograms can be only approximate, because the unique estimation can be received only through the comparison with the base oil, which in the case of industrial mineral oils (like remaining components) is a secret of the producer.

3.2. Lubricity method

Mineral oil lubricity is the feature defining its polarity rate, because the larger value lubricity has, the larger its polarity is. The lubricity measure is mainly considered by means of its friction coefficient value, time, after which two rubbing elements seize up or the value of load needed to break the lubricant layer, so called over welding loading P_z.

For this work purposes lubricity was assessed according to [14] standard by using four-ball instrument constructed by Working Machines Institute in Poznan University of Technology. In the research Japanese steel bearing balls (½" diameter), according to DIN 5401, class III, produced by Amatsuji Steel Ball MEG Company were used. The experiments were carried out at 1 minute time at 1400 rpm. The result of one experiment was over welding loading P_z [kN] of the balls.

In case of various substances influence lubricity also depends on their viscosity. To obtain the dependence connecting the concrete physico-mechanical features changes it is necessary to correlate both lubricity P_z and viscosity η_k with the obtained experimental results. For a more complete picture of this issue lubricity and kinematical viscosity of the most often mineral oils was specified. All oils were examined chemically, and their neutralization number values were in between from 0.05 to 0.13 mg KOH/g. The sulphur compounds vestigial amounts discovered during the analysis could not have influenced the examined concretes corrosion mechanism. The results of this research are presented in Table 1.

Table 1. Kinematic viscosity and lubricity findings for selected substances

Testing substances	Kinematic viscosity in temperature 20 °C [mm²/s]	Lubricity P_z [kN]
TU-20 oil	81.0	1.6
M-40 oil	211.4	1.6
H-70 oil	383.2	2.1
Lux 10 oil	413.3	1.8
Wrzecion 2 oil	25.3	1.3

To assess quantitatively the concrete physico-chemical corrosion rate a trial to subject mathematically its physico-mechanical features to the sort of environment influence. For representativeness aims the dependences the mineral oils TU-20, M-40 and H-70 researches results, presented in Figure 3 were used. The calculations were conducted according to multiply regression method, using the Statgraphics Plus V.5 program. The independent variables were kinematical viscosity η_k of the influencing substance at 20 °C temperature and its lubricity P_z. The dependent variables were

relative compressive strength of the concretes used and their relative adhesion to plain and ribbed reinforcements. Table 2 presents the regression equations obtained for different concretes and Table 3 for its adhesion to plain bars with different roughness ratio R_a and Table 4 to ribbed bars with different ribbed ratio f_R.

Table 2. Regression equations for different grades of concrete

Concrete grade	Regression function
C28/35	$f_b^c / f_b^{c0} = 12.685 \times 10^{-4} \eta_k - 1.007 P_z + 2.258$
	$f_b^c / f_b^{c1} = 44.780 \times 10^{-4} \eta_k - 2.517 P_z + 4.248$
C20/25	$f_b^c / f_b^{c0} = 23.803 \times 10^{-4} \eta_k - 1.658 P_z + 3.061$
	$f_b^c / f_b^{c1} = 36.460 \times 10^{-4} \eta_k - 2.444 P_z + 4.187$
C16/20	$f_b^c / f_b^{c0} = 41.619 \times 10^{-4} \eta_k - 2.735 P_z + 4.390$
	$f_b^c / f_b^{c1} = 39.180 \times 10^{-4} \eta_k - 2.564 P_z + 4.282$

f_b^{c0} – concrete compressive strength in age of 28-days,

f_b^{c1} – initial concrete compressive strength (before oiling),

f_b^c – concrete compressive strength in analysed age.

Table 3. Regression equations for plain bars

R_a [μm]	Regression function
1.38	$\tau_v / f_b^{c0} = 1.572 \times 10^{-4} \eta_k - 0.099 P_z + 0.167$
6.10	$\tau_v / f_b^{c0} = 2.472 \times 10^{-4} \eta_k - 0.145 P_z + 0.259$
6.93	$\tau_v / f_b^{c0} = 2.567 \times 10^{-4} \eta_k - 0.173 P_z + 0.310$

Table 4. Regression equations for ribbed bars

f_R	Regression function
0.065	$\tau_v / f_b^{c0} = 9.426 \times 10^{-4} \eta_k - 0.486 P_z + 0.847$
0.107	$\tau_v / f_b^{c0} = 15.448 \times 10^{-4} \eta_k - 0.538 P_z + 0.987$
0.185	$\tau_v / f_b^{c0} = 16.342 \cdot 10^{-4} \eta_k - 0.634 P_z + 1.150$

The correlation between the relative strength and the influent crude oil product viscosity η_k was very small ($r = 0.04 - 0.42$), which confirms that the influent substance viscosity has little influence on physico-chemical destruction rate. A high correlation was stated between kinematical viscosity η_k and lubricity P_z ($r = 0.87 - 0.92$) as well as between the lubricity and the relative compression strength or adhesion ($r = 0.50–0.81$). Consolidated multiply correlation coefficients for equations in Tables 3 and 4 were between from 0.95 to 0.99. To ease oiled concrete physico-chemical destruction assessment nomographs were prepared to determine concrete compression strength and adhesion decreases directly. Figure 6 presents an example of a diagram for concrete

class C20/25. The methods described above were verified by means of accessible literature data and own research results. The errors of data concerning concrete compression strength decreases, obtained by lubricity method and demulsification method did not exceed 10% in comparison to the data presented in [8, 15–16], which shows, that he methods are useful. The concrete compression strength decreases, calculated according to the proposed methods can be used for crude oil products aggressiveness rate assessment. The issue of hydrocarbon-environments corrosiveness discussed above could constitute the basis for necessary supplements of standard PN-EN 206-1:2003 [17], which classifies environments aggressive towards concrete without hydrocarbon--products.
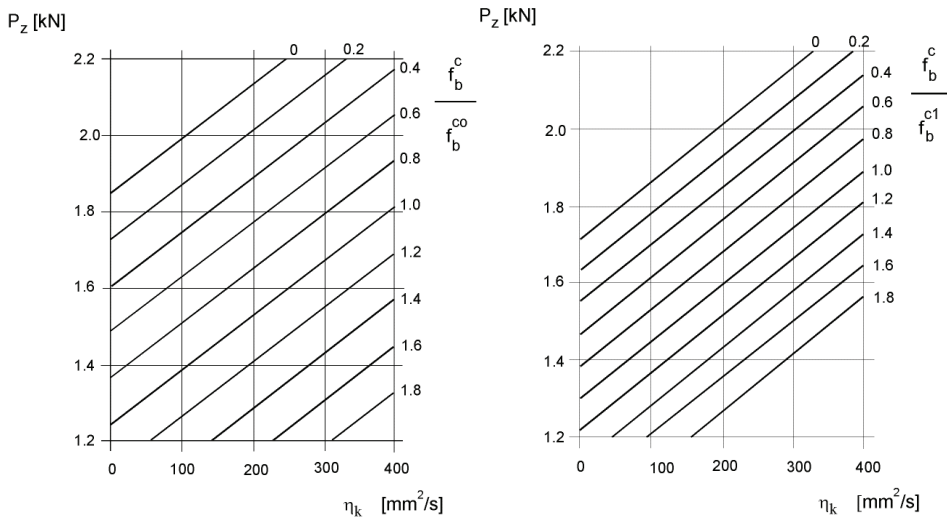
Fig. 6. Charts for determining C20/25 concrete compression strength
under influence of crude oil products

3.3. Deemulgation method

The simplest method worked out by author is the deemulgation method, which is based on assumption, that polar molecules keeping emulsion. This method consists in the mixture of equal volumes of investigated substance and water (14 N, pH ≈ 7), which is heating to the temperature of 50 °C and mixing in the technical mixer (1400 rpm) for one minute. This performed emulsion is pour in to cylinder and after 5, 20, 40 and 60 minutes the deemulgation time t_e (time of phases distribution) and the amount of water phase exuded from oil-water emulsion is defined. Figure 7 shows the dependence between the volumes of exuded water phase W (%) and the deemulgation time t_e for the vaseline oil (creating basic non active oil) and mixtures based on it and added the polar surface active improves in the form of 1%, 5% or 10% of oleinic acid (o.a.).
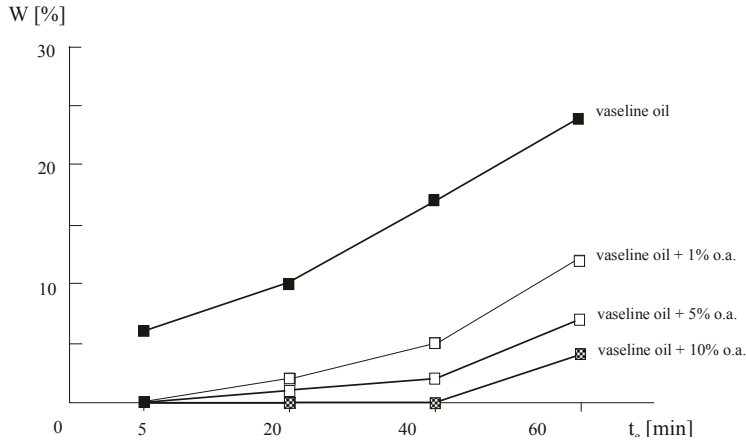
Fig. 7. The dependence of exuded water phase and deemulgation time
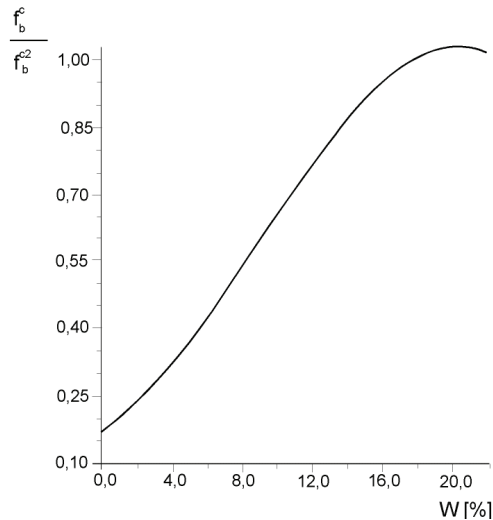
Fig. 8. Relationship between concrete compressive strength and the amount
of exuded water phase from demulgation method after 60 min

For the purpose of the more exact estimation of the degree of concrete physico-chemical destruction the non-linear correlation of volume amount of exuded water phase W for deemulgation time $t_e = 60$ minutes with presented before concrete compression strength f_b^c falls was carried out. Calculations were performed using the Curve software. As the result of this analysis the equation depend exuded water phase W with the fall of oiled concrete compression strength f_b^c was received, with relation to the compression strength of not oiled concrete in the same age f_b^{c2} (Figure 8). This relation became appointed with the correlation coefficient of 0.873.
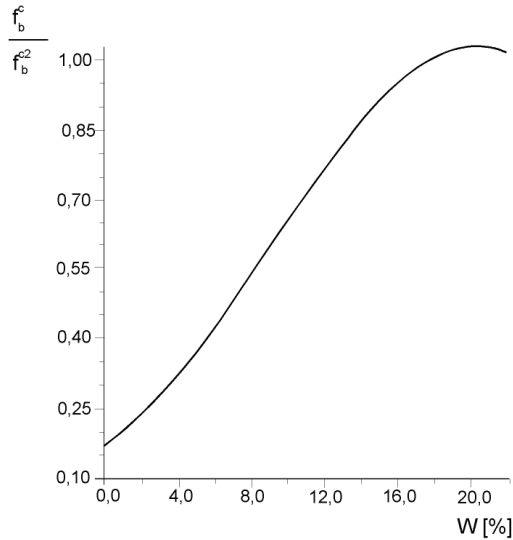
Fig. 8. Relationship between concrete compressive strength and the amount
of exuded water phase from demulgation method after 60 min

4. Conclusions

The durability analysis of RC structures exposed to a crude oil products environment shows that significant reduction of compressive strength and bond to reinforcement can occur. When designing RC structure in contact with crude oil products, apart from checking the value of neutralisation number, it should be taken into consideration the presence of organic surface active molecules using the infra-red spectroscopy, lubricity or demulgation method. Some of the oil products are safe but some are clearly very aggressive.

To systematise the issues discussed, Figure 9 shows a proposal of procedure for crude oil products environment influence corrosiveness analysis. It can be used as a scheme of procedure to be followed in design process of reinforced concrete structures which are to be exposed to crude oil products influence. This procedure allows forecasting the results of environment impact, based on its influence research. Then it is possible to assess the environment aggressiveness and take up preventive measures at design stage. It can be also used for assessment and analysis of already oiled reinforced concrete elements. In the classification aggressiveness terms proposed in PN-EN 206-1:2003 standard [17]: X_0, X_1, X_2 and X_3, were used.

Protection to crude oil products could be done by surface coating of RC elements. Only not cracking coatings are successful in case of crude oil products influence. Interesting modelling of corrosion protection for reinforced concrete structures with surface coatings is presented in [18–19].
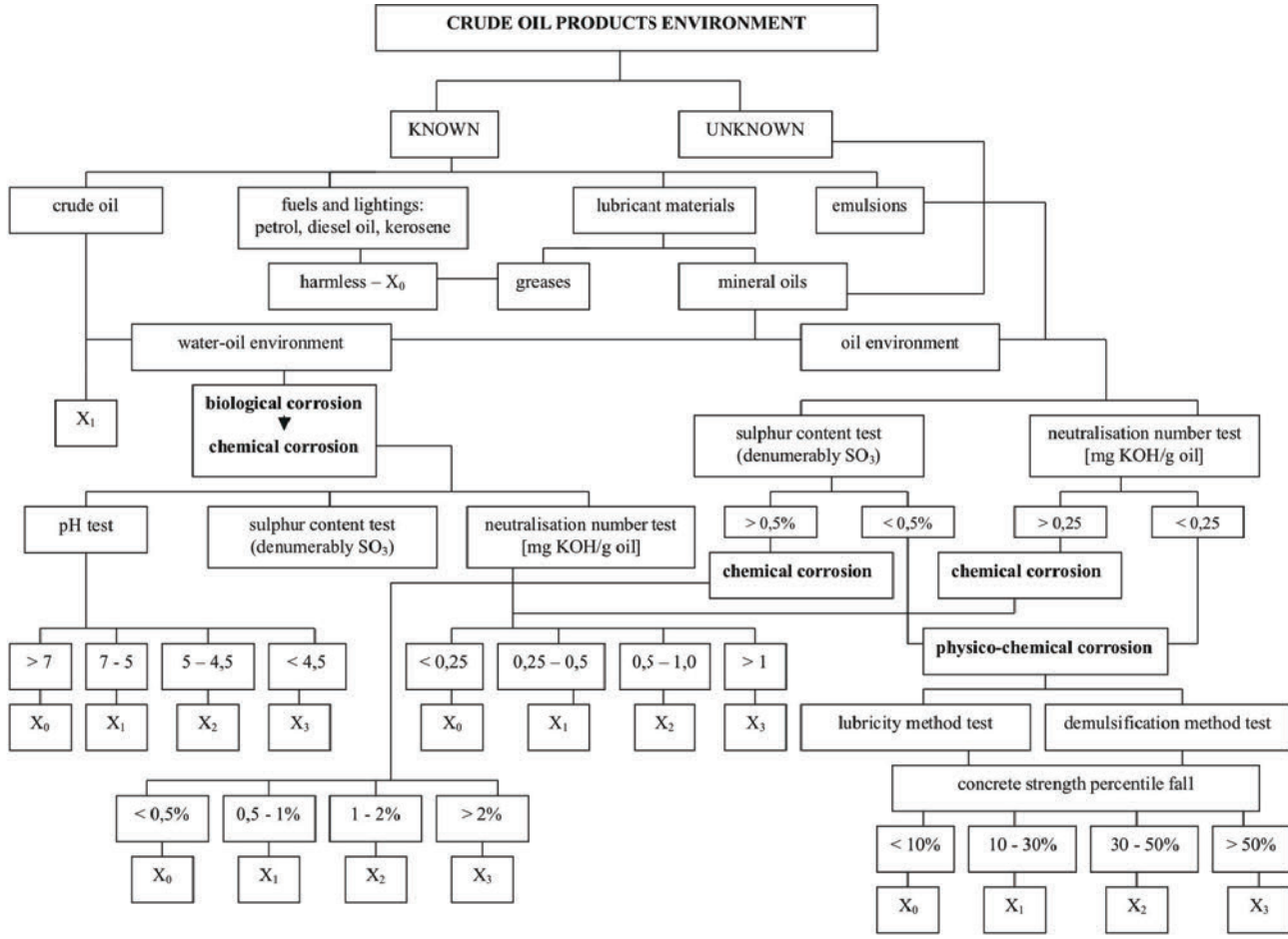
Fig. 9. Scheme of procedure to be followed during analysis of crude oil products environment aggressiveness

References

[1] Błaszczyński T., Kozarzewski J., Nowakowski B.: *Wpływ zaolejenia na beton fundamentów pod maszyny*, Inżynieria i Budownictwo, No. 5−6, 1985, pp. 196–199.
[2] Khoury G.A.: *Effect of hot oil on concrete*, Report, No. 1, London, Imperial College 1981.
[3] Onabolu O.A.: *Effects of hot crude oil on concrete for offshore storage applications*, Ph.D. Thesis, Imperial College of Science and Technology, London, 1986.
[4] Milovidov I.V., Alekseva G.V.: *Sniženie pročnosti betona ot vozdeistviya masel*, Promyšlennoe stroitelstvo, No. 1, 1970, pp. 42−43.
[5] Pluta J., Ciaś A., Skorupski W.: *Korozja olejowa betonu konstrukcji stropów w magazynach produktów naftowych*, w: XXVI Konferencja KILiW PAN i KN PZITB, Krynica, 1980, pp. 197–203.
[6] Biczok J.: *Concrete corrosion – Concrete protection*, 8th edition, Budapest, Academiai Kiado, 1972.
[7] Korzeniowska E., Motak E., Rawicki Z.: *Wpływ zanieczyszczeń olejowych na stan techniczny podłoża gruntowego i budynku*, Przegląd Budowlany, No. 10, 1995, pp. 13–15.
[8] Błaszczyński T.: *Durability analysis of cement based composite system exposed to a physico--chemical environment*, Progress in durability analysis of composite systems, ed. Cardon A.H., Fukuda H., Reifsnider K., Balkema A.A., Rotterdam, 1996, pp. 297–301.
[9] Błaszczyński T.: *Durability analysis of RC structures exposed to a physico-chemical environment*, Proc. of the 3rd Kerensky Conference, Singapore, 1994, pp. 67−70.
[10] Błaszczyński T.: *Some effects of crude oil environment on RC structures*, Foundation of Civil and Environmental Engineering, No. 2, 2002, pp. 7−14.
[11] Błaszczyński T.: *Prediction of bond between steel and concrete under mineral oil exposure*, DABI International Symposium, Reevaluation of concrete structures, Copenhagen – Lyngby, Technical University of Denmark, 1988, pp. 59–68.
[12] Runkiewicz L., Konieczny K., Brzęk R.: *Zmiany wytrzymałości i odkształcalności betonu zaolejonego w konstrukcji*, Przegląd Budowlany, No. 2, 2002, pp. 26–29.
[13] Błaszczyński T.: *Influence of physico-chemical agent on the cement composite materials*, Physico-Chemical Mechanics, Bulgarian Academy of Sciences, No. 20, 1992, pp. 19–23.
[14] PN-76/C-04147. *Badanie własności smarnych olejów i smarów*.
[15] Grabiec K.: *Wpływ olejów mineralnych na wytrzymałość i odkształcalność betonów konstrukcyjnych*, AIL, Vol. XIX, No. 3, 1973, pp. 567–572.
[16] Onabolu O.A.: *Effects of hot crude oil on concrete for offshore storage applications*, Ph.D. Thesis, Imperial College, London, 1986.
[17] PN-EN 206-1:2003. *Beton. Część 1. Wymagania, właściwości, produkcja i zgodność*.
[18] Kamaitis Z.: *Modelling of corrosion protection for reinforced concrete structures with surface coatings*, Journal of Civil Engineering and Management, No. 4, 2008, pp. 241−249.
[19] Kamaitis Z.: *Modelling of corrosion protection as standby system for coated reinforced concrete structures*, Journal of Civil Engineering and Management, No. 4, 2009, pp. 387−394.

Ocena konstrukcji żelbetowych poddanych działaniu produktów ropopochodnych

Praca jest poświęcona oddziaływaniu substancji ropopochodnych na konstrukcje żelbetowe. Na podstawie badań własnych oraz analizy literatury przedmiotu scharakteryzowano efekty wpływu produktów ropopochodnych na cechy fizyczno-mechaniczne dojrzałego betonu. W pracy omówiono także opracowane przez autora metody oceny szkodliwości wpływu produktów węglowodorowych na beton i żelbet, oparte na badaniu cech tych produktów. W celu usystematyzowania poruszonych zagadnień pokazano własny schemat postępowania w procesie projektowania konstrukcji żelbetowych poddanych działaniu substancji ropopochodnych. Ten tok postępowania pozwala prognozować na podstawie badania oddziałującego środowiska skutki jego działania, następnie określać stopień jego agresywności i podejmować niezbędne kroki zapobiegawcze w procesie projektowym. Może także służyć do oceny i analizy już zaolejonych konstrukcyjnych elementów żelbetowych.

The L35GSM cast steel – possibilities of structure and properties shaping at the example of crawler links

D. DUDEK, S. FRYDMAN, W. HUSS, G. PĘKALSKI

Wrocław University of Technology, Wybrzeże Wyspiańskiego 25, 50-370 Wrocław, Poland.

The article presents basic reasons for plastic degradation of track links in working machine undercarriage. Besides the problems related to the loading of links with bending moment caused by passing of a machine (undercarriage) through trajectory curvatures, the important issue is the internal structure of the L35GSM cast steel, which conditions its usefulness as a material for track links. This issue is being discussed in the following publication.

1. Origin of the issue

Contemporary materials engineering pays much attention to the works on new generation materials such as the smart type materials, bionic materials or biomimetic materials. As a result, an interest in materials considered as thoroughly tested and classified seems to drop in somewhat automatic way.

One of such construction materials is the low-alloy manganese-silicon-molybdenum cast steel of the L35GSM grade. Views on its properties and possible applications have been established by the patent specification No 50346 from 1965, as well as the PN-87/H-83156 and PN-88/H-83160 standards. It results from the documents that the material can be applied in the absence of dynamic load conditions. The cited standards foresee two heat treatment processes for the cast steel (normalizing and toughening), but the most frequent practice has been applying the L35GSM cast steel in the after cast state.

In the eighties of the 20th century a concept appeared of applying the L35GSM cast steel as the effective substitute for high-manganese austenitic cast steel of the L120G13 grade for links of brown coal excavators. Later, the applications of that material have been extended to other parts of those machines: bucket teeth, sprocket wheels and driving teeth. All of them operate in the dynamic load conditions, i.e. in conditions contradictory to those presented in the patent specification. In reality, the L35GSM cast steel having a structure *as-cast* could not also keep up to the requirements. For that reason, the attention of the L35GSM steel producers turned away from that product, most frequently to the benefit of the L120G13 cast steel. The tendency was intensified by the fact of bonding the part components by welding, which led to their cracking in the heat influence zones.

In the link itself, the ground contact surfaces and surfaces co-operating with driving teeth should present high wear and high unit pressure resistance, and moreover, the structure of the remaining part of the cast should be prepared for bearing variable loads.

The problems mentioned above were the reason for undertaking extensive tests of the L35GSM cast steel accomplished within the wide team of researchers. Their results have been collected, among others, in works [1–4].

In the article the Authors undertake synthesis and summary of the whole of earlier studies of that material, supplementing them with results of the 2008 and 2009 works. Based at the track links example, the load patterns and most frequently appearing damages and defects (macro and microscopic) in brown coal excavator parts made of the L35GSM cast steel have been discussed.

A reason for particular interest in the crawler chain links is that they are machine structure components subjected to the most frequent wear. It gives the strong incentive for considering improvement of their durability in the face of the actual number of over 21 thousand track segments operating in the Polish brown coal mines [5], and an estimated 50% of them with defects resulting form material reasons [6].

2. Work conditions, loads and damages of track links

The idea of crawler drive operation (Figure 1) is rolling the drive wheels over their „own" road, which is the crawler chain. The segments composing the chain are connected with each other by lugs (ears) and bolts, which enable relative flexibility of the „steel road" (the pivotal joints do not carry the bending moment) and, at the same time, transfer the driving moment. A single segment consists of a link and a plate. Bottom side of a single link is welded to a plate, and its upper part, composed of a steel track and driving teeth, co-operates with support wheels and sprocket correspondingly. The sprocket transmits the driving moment through links' drivers to the crawler chain, and the support wheels bear the machine weight while rolling over the roll-off surface. The links transfer the load from support wheels to the plates, due to which the crawler drives are in general characterised with relatively low unit pressures onto the base and enable the machine moving over the non-hardened base.

Particularly harmful – due to the accelerated degrading – are the dynamic impacts. In the crawler chain they result from changes in velocity of the whole assembly moving. In particular, the links' drivers are exposed to such dynamic loads (along with the sprocket teeth). A stroke into a driver transforms also into a load burst in the bolt joints between links. It leads to additional stresses (besides the static loads), which consequently lead to accelerating the degradation changes (wear, rolling-up). The clearances resulting from those changes increase already existing unfavourable dynamic phenomena – in the area of bolt junction itself (finally leading to ear tearing), and also in relation to the whole chain (a pitch change). A progress in the crawler chain pitch change is an additional reason for dynamic loads at drivers, leading to worsening of the existing problem (Figure 2).
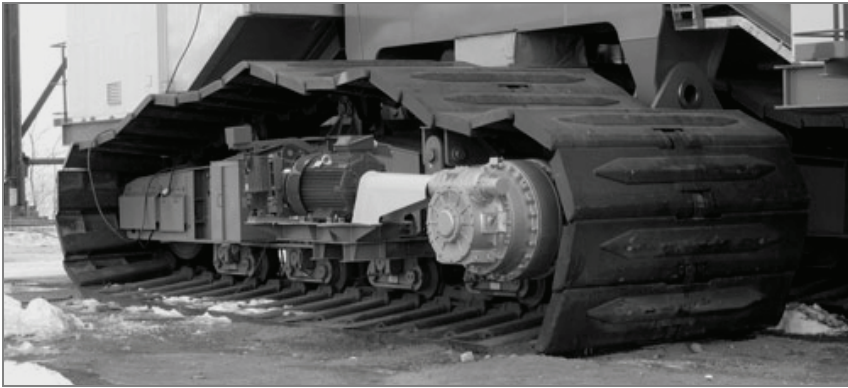
Fig. 1. Crawler mechanism in the KWK-910 [5] excavator
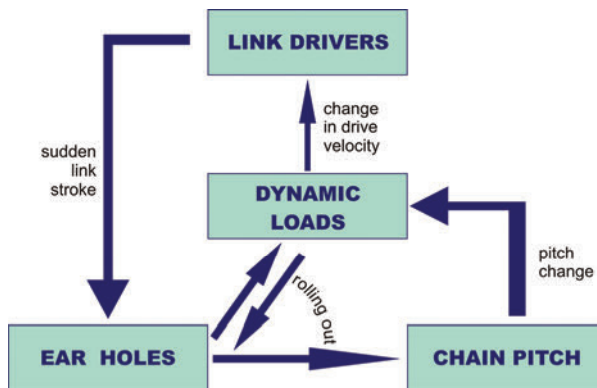
Fig. 2. Diagram of growth and results of dynamic impact between parts of a crawler chain

Four main reasons of loading the crawler chain segments can be distinguished:
- machine weight,
- initial tension in a chain,
- drive moment,
- subsoil reaction.

Eight basic cases of loading the links can be distinguished while additionally considering the segment localisation in the drive chain (position in relation to track rollers, idler and sprocket). The cases collected in Table 1, have been presented in work [7], based at experimental studies of two machines: a dumping conveyor (single support wheel in variants D, E, G) and an excavator (two support wheels).

As a result of interaction cases collected in Table 1, links and plates are subject to various wear and defect types:
- rolling out of the ear hole (Figure 3a),
- cracking and tearing of ears (Figure 3b),

- cracking, breaking and crumbling up of a sleeve from the ear hole (Figure 3a),
- cracking and crumbling up of a sleeve from the ear hole,
- rolling out and wear of a roll-off surface (Figure 4),
- rolling out and wear of driver surfaces (Figure 4),
- abrasive wear of sleeves in ears;
- tearing off plates from links.

Critical damages to the crawler segment components, the repair of which will not lead to the desirable effect are: excessive rolling out of ears and roll-off surface, excessive deformation of plates and excessive wear of bolts. The repair is totally excluded in case of ear tear.
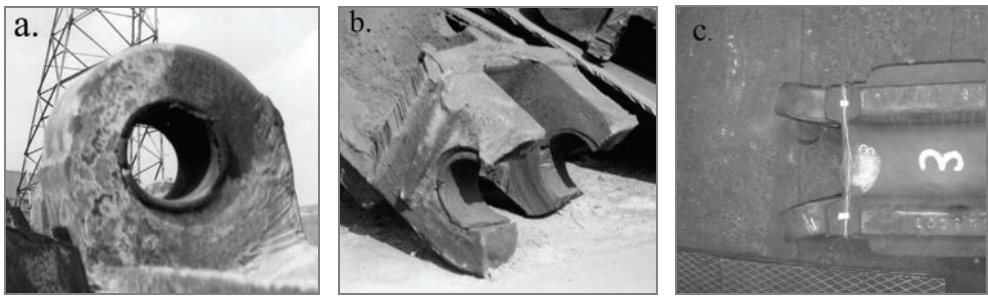
Fig. 3. Damages to the ear holes [7]: a) rolling out of a hole and sleeve damage,
b) ear tearing off, c) plastic strain of ears
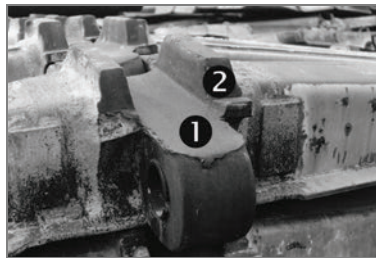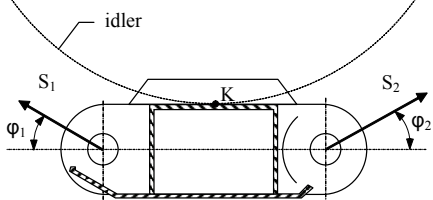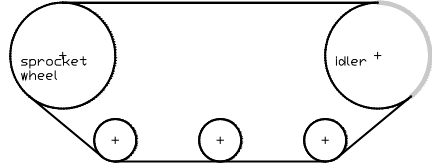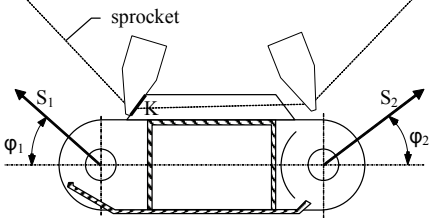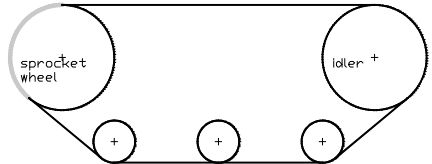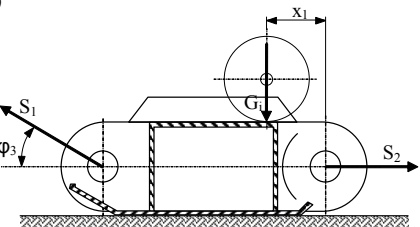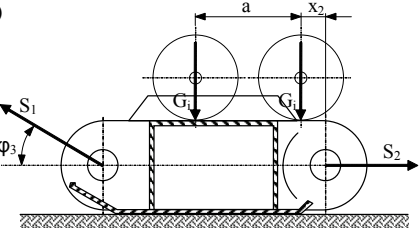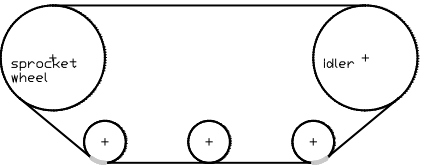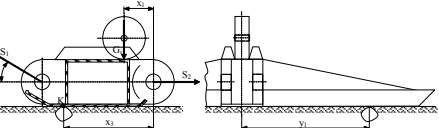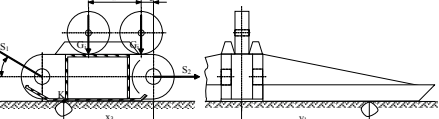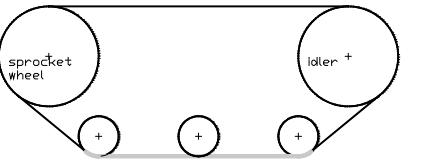
Fig. 4. Macroscopic damages (rolling out) of a roll-off surface (1)
and drivers' surfaces in track links (2) [6]

Table 1. Basic cases of crawler links loading

Load cases	Segment location
A Tensile force resulting from driving force and initial tension.	

B	 A link rests at the idler. It results in a change in direction of ear tensing forces and causes bending of the whole segment.	
C	 A case similar to case B. The difference consists in values of the forces S_1 and S_2, resulting from applying a force through a driver's teeth.	 When the chain pitch is ideally fit to the sprocket teeth, the driving force is distributed evenly. In the extremely unfavourable case only one segment transfers the driving moment.
D		 Change in the force acting direction (a chain enters onto the sprocket) along with the support wheel pressure causes bending.
E		 A case similar to case D, worsened by encountering an obstacle.

F	 Bending caused by running over surface irregularity and pressing down in joints with forces from machine weight.	
G		 For the reason of running over an obstacle with the end part of a plate a bending, indenting and twisting of a link takes place.
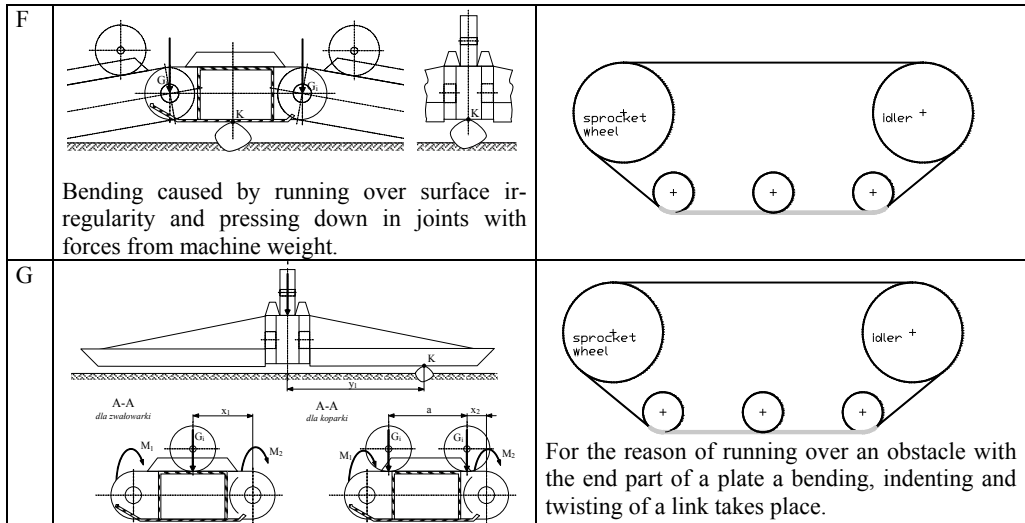
G_i – partial machine weight born by one support wheel,

K – contact place of components co-operating with segments,

M_1, M_2 – torsional moment acting at a segment,

S_1, S_2 – chain tension forces,

a – support wheels pitch,

x_1, x_2 – distance between support wheel axis and axis of the rear link ear hole,

x_3 – distance between obstacle and the rear link ear hole,

y_1 – distance between obstacle and symmetry axis of a segment,

φ_1, φ_2, φ_3 – direction of acting forces S_1 and S_2.

3. Macrostructures, microstructures and selected properties of L35GSM in the as-cast condition

Fractures appearing in cracking zones marked at Figure 5 with lines 1 and 2, usually have similar build. The character of this fracture is brittle and intercrystalline with very complex surface topography (Figure 6). Fractures appearing in the heat influence zone (line 3 at Figure 5), are also brittle in character, except for the fracture surface topography is less developed. It possibly results from structural differences in the link native material (close to the equilibrium one) and that of the heat influence zone (with Wiedmanstatten build or martensitic).

Fracture builds in the as delivered state have also been observed at the impact test samples. Figure 7 presents a magnified view of an impact test sample fracture taken from material of the ear shown in Figure 6.

Microstructures of samples in that state most frequently consisted of areas of non-equilibrated pearlite with ferrite separations at grain borders of the former austenite. However, even at the small intersections of the impact test samples a significant varia-

tion in the material structure has been observed. Ferrite separations appeared also inside the pearlite, and the pearlite itself had a various dispersion build (Figures 8 and 9).
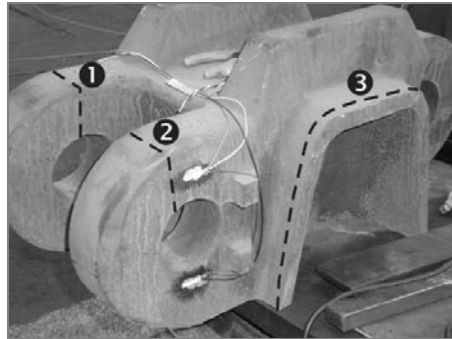
Fig. 5. View of a track link [6]. The broken lines mark the zones of cracking.
Line 3 in the link's material runs in the area of heat influence of a welded joint between link and plate
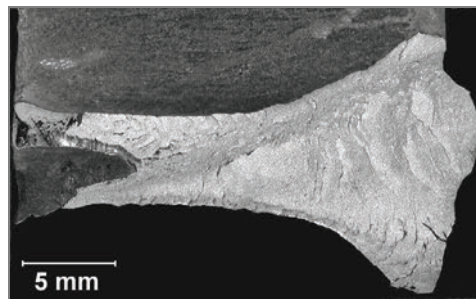
Fig. 6. Macroscopic views of crawler ear fracture made of the L35GSM
cast steel in the as-cast condition – brittle fracture
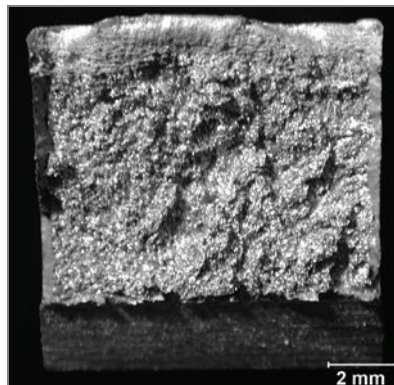
Fig. 7. Macroscopic view of fracture in impact test sample made of the L35GSM
steel after casting – brittle fracture

Such structural variability results in scatter of the hardness measurement results and low impact resistance. Hardness of the steel after casting (in the as delivered state) ranges from 236 to 361 HBW 750/5, i.e. 22–38 HRC. Instead, the average impact resistance in the ambient temperature is 26 J/cm^2. As presented in work [3], based at the impact resistance test at samples taken from link's ears (not from trial bars assembled at the casts), the impact resistance of the L35GSM steel after casting may even be lower, from 6.2 to 12.9 J/cm^2. In the fractures of those samples a share of 10 to 15% of plastic fracture and a ratio of $R_{0.2}/R_m$ equal to about 0.5 have been found.
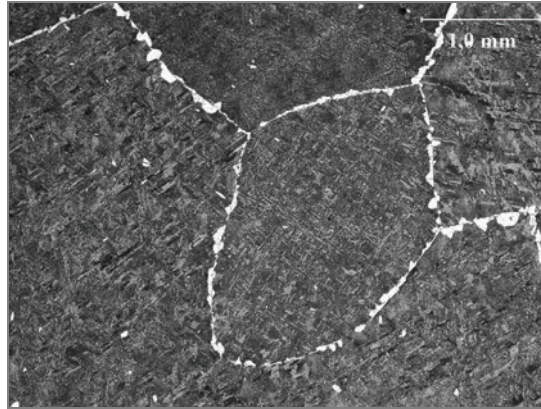
Fig. 8. The L35GSM cast steel in the as delivered (as-cast) condition. Coarse-grained structure of non-equilibrated pearlite with bright ferrite separations at grain borders and inside grains. Etched with Mi1Fe, light microscopy
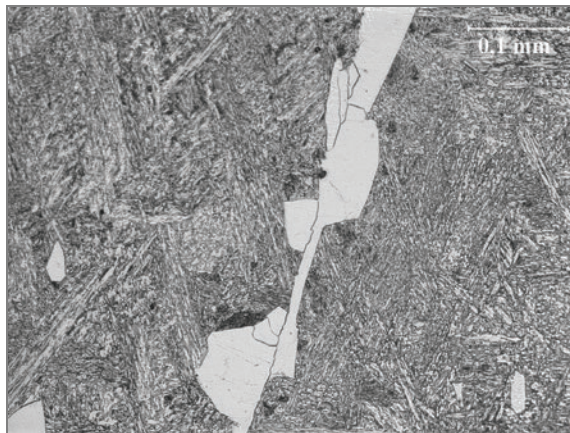
Fig. 9. Magnified view of structure from the grain border area as shown in Figure 8. Bright ferrite separations creating a continuous envelope and singular separations of that phase inside grains. Etched with Mi1Fe, light microscopy

In summary, it can be stated that in the as-cast (as delivered) state the tested cast steel shows diversified structures and low mechanical properties with high scatter. Such state excludes application of that material for crawler chain links.

4. Macrostructures, microstructures and mechanical properties of the L35GSM cast steel in various heat treatment states

In the extensive report [8] the results of testing the L35GSM cast steel in as many as 18 states of heat treatment have been presented. They involved: homogenizing, full annealing, normalising and various hardening and tempering combinations.

Table 2. Versions of heat treatment, structure and properties of the L35GSM cast steel [8, 9]

Pos.	Method and parameters of heat treatment	Structure	Hardness HRC	$R_{m\ śr}$ [MPa]	$R_{0,2\ śr}$ [MPa]	$R_{0,2}/R_m$	$A_{5\ śr}$ [%]	$KCV_{śr2\ °C}$ [J/cm^2]
1	as-cast condition	non-homogenous structure of ferrite, bainite and quasi-eutectoid (pearlite)	22–40	675	346	~0.51	24	26
2	normalising: 930°C/air	irregular fine-grained ferritic-pearlitic with areas of acicular build	23–30 locally 40	996	546	0.55–0.8	22	26
3	annealing + hardening 930 °C/H$_2$O + tempering 600 °C/H$_2$O	temper sorbite	26–30	998	895	~0.9	14	98
4	superficial hardening after:		~50 at external surface					
	normalising	martensite irregular fine-grain ferritic-pearlitic with areas of acicular build						
	toughening	sorbite						

Besides the laboratory sample test results the report contains the results of tests performed at samples taken from the real crawler chain links. At their basis it has been acknowledged that the essential and economically justified processes of heat treatment of that material could be normalising, as well as normalising and subsequent hardening and

high-temperature tempering. For the impact test samples the following parameters of the processes have been established: normalising at temperature 930 °C/60 minutes/air cooling, hardening from temperature 930 °C/60 minutes/water cooling, and tempering at temperature 600 °C/120 minutes/water cooling.

Based at works [8–9], Table 2 collects study results for selected mechanical properties in the two versions of heat treatment and compares them with properties in the as delivered state. The Table also contains data related to structure and properties of the tested cast steel after normalising, toughening and superficial hardening. Such a complex processing has been expected for rolling-off surfaces, links' drivers as well as the hole surfaces in the link ears.

Diversification of mechanical properties shown in Table 2 results from changes in macro and microstructure of the L35GSM cast steel caused by heat treatment (Figures 10–12).
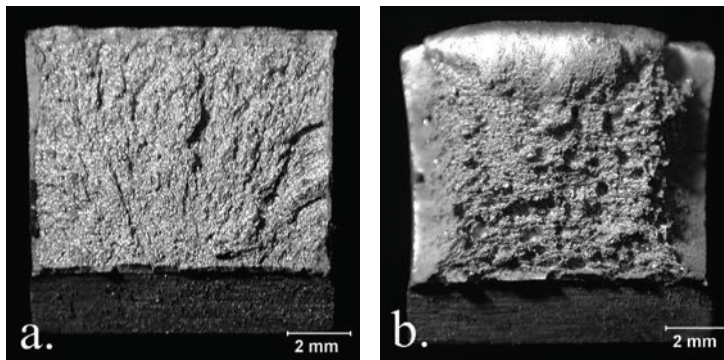
Fig. 10. Macroscopic view of the L35GSM cast steel fracture: a) after normalising; in relation to the after casting state (Figure 7), the fracture is brittle and fine-grained in character, and has less developed surface topography, b) after thermal toughening – the plastic–brittle fracture
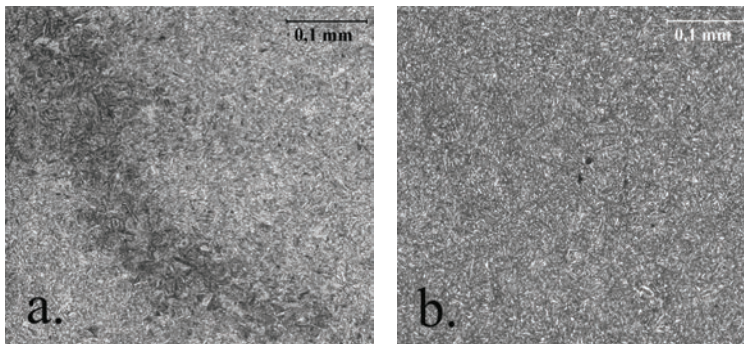
Fig. 11. Microstructure of the L35GSM cast steel samples: a) after normalising; the areas of acicular build appearing besides the irregular ferritic-pearlitic structure, b) after toughening – homogenous tempering sorbite. Etched with Mi1Fe, light microscopy

The most advantageous structure and a set of mechanical properties are presented by the L35GSM cast steel after toughening. At the same time, the tempering sorbite structure being obtained after toughening constitutes the optimal layer under the structures being obtained during superficial hardening. The fact has been used in the course of heat treatment of the track surfaces and crawler link driver surfaces while performing the surface hardening [10]. Effects of the process have been illustrated in Figure 13, in the form of sample hardness changes as a function of a distance from its surface. The pattern of hardness changes is satisfactory, showing mild transition from the zone of tempering martensite to the sorbitic structure of the material beneath the zone of surface hardening.
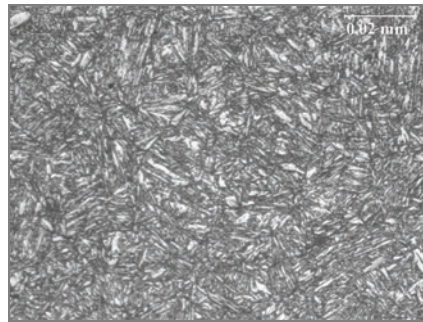
Fig. 12. Magnified view of microstructure after toughening in the sample shown in Figure 11b. The structure of tempering sorbite of after-martensitic orientation with fine coagulated carbides. Etched with Mi1Fe, light microscopy
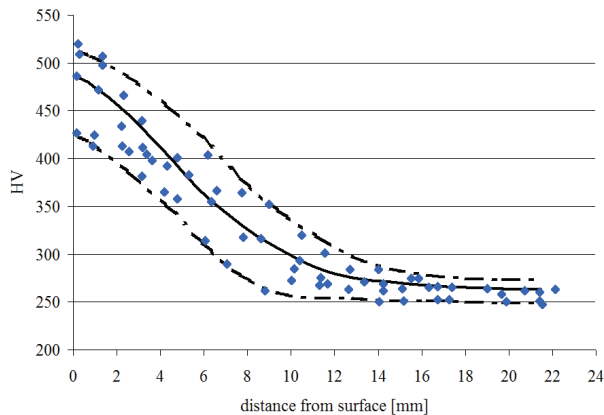
Fig. 13. Distribution of hardness changes in the L35GSM cast steel after toughening and superficial hardening [8]

In relation to the sorbitic structure appearing after hardening and high-temperature tempering, the attention has to be paid to the fact that it will appear in the real link

material only to the depth determined by hardenability of the L35GSM cast steel. In the water cooling conditions the critical diameter for that material is 45–50 mm [8]. Thus, while considering the link structures beginning with drivers surface the following can be observed: tempering martensite, underlying sorbite layer (Figure 11b), and next the pearlite with ferrite structure (Figure 8). It is worth mentioning that after the surface hardening the low-temperature tempering process was not performed. In the experimental treatment of the whole links it proved that the heat cumulated during surface hardening is sufficient for the "self-tempering" process to take place during cooling after surface hardening.

As indicated in Figure 5, the areas of crawler chain links cracking appear also in the zones of heat influence in the link-plate welded joints (from the link material side). The subject has been treated widely in work [11]. In general the problem has been solved by stress relief annealing of the whole crawler chain plates at temperature of 600 °C. It indicates also that the surface hardening procedures described above must be performed after joining the links and plates using welding methods. Heat treatment of the links themselves was scheduled in such a way (considering the tempering times), as to obtain the assumed final structures in a link after completing the heat treatment of the welded joints.

5. Summary

In the first part of the article, eight types of wear and damage to the crawler links have been presented. The tests performed prove that significant part of them could be eliminated and the time of operation prolonged by increasing durability of particular surfaces and intersections. Cracking of the track link's ears is being eliminated by toughening of the whole links preceded with normalising. The normalising process before hardening and high-temperature tempering cause homogenising of the cast structure (in relation to the as-cast condition), grain refinement and, as a consequence, increase in mechanical properties (Table 2). However, this does not convert to an increase in the material impact resistance, and besides, the normalising structures are not the optimal ones for the subsequent superficial hardening of the selected surfaces. Only after toughening, the tempering sorbite structures in the L35GSM cast steel with impact resistance up to three times higher in relation to the as-cast and normalised condition, are being obtained at depths limited by the cast steel hardenability. The issue of rolling out of the tracking surfaces, driver surfaces and bolt holes in ears are being solved by superficial hardening with "self-tempering". Then, the issue of the link-plate welded joints cracking is being eliminated by the stress relieving annealing in the tempering temperatures.

It has to be stressed here, that all settlements resulting from laboratory tests of the L35GSM cast steel have been verified in the real operating conditions. The trials have proved correctness of the proposed solutions and they have been included into the practice of design and materials selecting for basic brown coal

mining machines. It also has to be clearly underlined here, that material problem solution for those machines must not be made selectively in relation to particular parts of any structure assembly. As shown in the article, even applying toughening in relation to a link according to specifications in the PN-88/H-83160 Standard does not result in the required operating properties. In the considerations the link-plate-drivers set has to be taken into account. Looking ahead, it has to be foreseen (and that results from the operating experiments) that the study interest field should be extended by a selection of materials for rolls co-operating with rolling-off surfaces of links, ear bushings and sprockets. All those components influence durability and damageable of the machine driving mechanism by mutually acting at themselves.

Acknowledgements

References

[1] Pękalski G., Pękalska L., Krajczyk A., Wocka N., Milian W.: *Application of voluminal and superficial heat treatment for the parts of mining machines*, New Materials Conference Proceedings – New Technologies in Shipbuilding and Machine Industry, Szczecin–Świnoujście, 2008.

[2] Krajczyk A., Pękalska L., Pękalski G., Stram T.: *Structures of the L35GSM cast steel versus their mechanical properties*, II Conference Proceedings, Experimental Methods in Building and Operating Machines, Szklarska Poręba, 1995.

[3] Krajczyk A., Pękalska L., Pękalski G.: *Heat treatment influence at structure and fracture character in the L35GSM cast steel*, Working Machines Problems, Vol. 3, No. 23, 1994.

[4] Pękalski G.: *Heat-treatment governed design of structures and properties of the Mn-Si-Mo steel casting*, Acta Metallugica Slovaca, No. 3, 2001.

[5] Wocka N., Warcholak A.: *Crawler traversing mechanisms in the basic surface mining machines – solutions increasing durability and reliability of parts*, Brown Coal, No. 3–4, 2008.

[6] Augustynowicz J., Dudek K., Figiel A., Przystupa F., Staszak A.: *Damage analysis and strength tests of the crawler undercarriage in the heavy working machines*, Surface Mining, No. 4–5, 2009.

[7] Alenowicz J., Onichimiuk M., Urbaniak Z., Wygoda M.: *Elaborating the optimisation base for design and recovery of crawler members with consideration of traversing levels in the home brown coal mines*, Wrocław, December, 2001 r., unpublished work.

[8] Krajczyk A., Pękalska L., Pękalski G., Prusak C.: *Elaborating the heat treatment technology for crawler links made of the L35GSM cast steel*, IKiEM Report, Series SPR 053, 1985.

[9] Pękalski G.: *Heat treatment of the L35GSM cast steel, and possibilities of its application for crawler chain links in the brown coal excavators*, Surface Mining, No. 4–5, 2009.

[10] Krajczyk A., Pękalska L., Pękalski G.: *Surface hardening of the L35GSM cast steel*, Proceedings of the National Conference on Surface Treatment, Częstochowa, 1990, pp. 127–131.

[11] Haimann R., Krajczyk A., Pękalska L., Pękalski G.: *Influence of the stress relief annealing at structure and properties of welded joints between cast steel and the 18G2 and 12G2ANb steels*, Welding Technology Overview, No. 8, 1990, pp. 7–13.

**Staliwo L35GSM – możliwości kształtowania struktur i właściwości
na przykładzie ogniw pojazdów gąsienicowych**

W artykule przedstawiono podstawowe przyczyny plastycznej degradacji ogniw gąsienicowych podwozi maszyn roboczych. Oprócz problemów z obciążeniem tych ogniw momentem zginającym wywołanym pokonywaniem przez maszynę (podwozie) krzywizn toru jazdy, bardzo ważnym zagadnieniem są zagadnienia budowy strukturalnej staliwa L35GSM warunkującej jego przydatność jako materiału na ogniwa gąsienicowe.

Forecasting crack resistance of short- and long-term loaded coatings

W. GŁODKOWSKA

Technical University of Koszalin, Śniadeckich 2, 75-453 Koszalin, Poland.

The paper presents crack resistance problem of polymer and polymer-cement coatings used for surface protection of concrete structures. In a result of analysis of operating conditions of the arrangement elements: coating - concrete and loads assisting them in different situations but also anticipated results of their effects, evaluation criteria of crack resistance of protective polymer coatings and polymer-cement ones subject to the activity of short-term and long-term load were work out. On the basis of six coating materials there was made a research verification of crack resistance criteria and effects of mechanical short-term and long-term to crack resistance were defined. Tests carried out showed correctness of worked out criteria for crack resistance and proved their usage in designing protective coatings for concrete structures.

Keywords: *concrete, coating, crack resistance, short- and long-term load*

1. Introduction

Polymer and cement-polymer coatings are used as surface protective means for reinforced concrete structures with uncracked substrate when concrete structural and material protection in given environment becomes insufficient or with cracked substrate to increase structure durability [1–3]. However, despite of good physical and mechanical features of such coatings both successful and unsuccessful implementations have been observed through application of similar material solutions. The principal problem comes down to proper selection of coating properties depending on the concrete substrate characteristic and on the loads applied to the structure [4–5]. On one hand, the coating must provide effective chemical resistance of objects exposed to aggressive environment, on the other hand, it must sustain the strain caused by occurrence of cracks in the concrete and change of their wideness [6–7]. Therefore, selection of coating for reinforced concrete structure protection is a complex problem, particularly due to great variability of the causes of structure damage, conditions of structure operation, loads applied and their combination as well as class and quality of concrete used in the structure [8–11]. The criteria of coating crack resistance proposed in this paper and experimentally checked can considerably facilitate this task.

2. Coating crack resistance criteria

The protective coatings used to protect concrete surface can be divided in three material groups [12]:

- Group 1 – Coatings featuring high tensile strength assuming that no detachment from concrete at crack edge would occur;
- Group 2 – Coatings featuring high tensile strength assuming that detachment from concrete can occur on both crack sides;
- Group 3 – Coatings featuring low tensile strength, low module of elasticity and high deformability.

The coating crack resistance criteria have been developed for three material groups (Table 1).

Table 1. Crack resistance criteria for polymer and polymer-cement coatings [4]

Kind of coating	Kind of load	
	Short-term	Long-term
Group 1	$\alpha\left[(2l_v \cdot \varepsilon_{pt}) + \left(\dfrac{f_{ct} \cdot l_v^2}{2h_p \cdot E_{pt}}\right)\right] = w_d + \Delta w$ where: $l_v = \dfrac{f_{pt} \cdot h_p}{f_{ct}}$	$\alpha\left[(2l_v \cdot \varepsilon_{pt}) + \left(\dfrac{f_{ct} \cdot l_v^2}{2h_p \cdot E_{pt}}\right) \cdot (1 + \varphi_{p_{(t,to)}})\right] = w_d + \Delta w$ where: $l_v = \dfrac{f_{pt} \cdot k_{l,t}^p \cdot h_p}{f_{ct}}$
	$\alpha = \dfrac{h_p}{w_n} \cdot \dfrac{f_{pt}}{E_{pt}}$	
Group 2	$\alpha\left[(2l_v \cdot \varepsilon_{pt}) + \left(\dfrac{f_{ct} \cdot l_v^2}{2h_p \cdot E_{pt}}\right) +\right.$ $\left. + (2c \cdot \varepsilon_{pt})\right] = w_d + \Delta w$	$\alpha\left[(2l_v \cdot \varepsilon_{pt}) + \left(\dfrac{f_{ct} \cdot l_v^2}{2h_p \cdot E_{pt}}\right)\right]$ $\cdot (1 + \varphi_{p_{(t,to)}}) + (2c \cdot \varepsilon_{pt}) = w_d + \Delta w$
	where: $\alpha = \dfrac{h_p}{(w_n + \varepsilon_{pt} \cdot 2c)} \cdot \dfrac{f_{pt}}{E_{pt}}$, l_v – as in the case of Group 1	
Group 3	$\left(\dfrac{h_p}{w_n} \cdot \dfrac{f_{pt}}{E_{pt}}\right) \cdot h_p = w_d + \Delta w$	$\alpha[(2l_v \cdot \varepsilon_{pt}) \cdot (1 + \varphi_{p_{(t,to)}})] = w_d + \Delta w$, where: α, l_v – as in the case of Group 1
f_{ct} – tensile strength of concrete, $f_{pt}(t_o)$ – tensile strength of coating in time t_o, $E_{pt}(t_o)$ – modulus of elasticity under tension for coating in time t_o, $\varepsilon_{pt}(t_o)$ – tensile strain of coating in time t_o, $\varphi_p(t, t_o)$ – creep coefficient for coating material, $k_{l,t}^p$ – coefficient considering influence of long-term load, w_n – crack width damaging coating under short-term load, α – coefficient considering thickness influence and deformation of coating.		

An assumption has been made in theoretical analyses that in the case of reinforced concrete structures where the initial load stage has not developed any cracks yet and a coating has been applied to the concrete surface, the crack that can occur in the concrete substrate is a sum of immediate width opening (w_d) and the increase of width opening (Δw) during object operation. If a coating would be applied to any cracked concrete substrate, the value defining usability of the coating is the increase of the width opening (Δw). It's been further assumed that influence of crack on coating performance would be limited with an interval of width equal to the so-called relaxation zone length (l_v) on both crack sides (Figure 1).
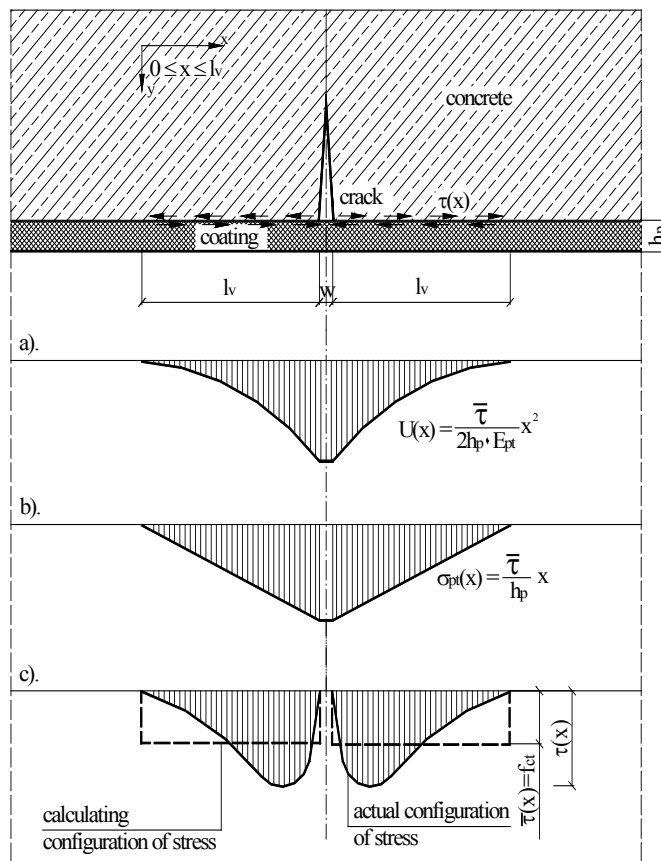
Fig. 1. Graph of the displacement (a), tensile strain (b), sharing strain in the coating-concrete (c) combining plane at relaxation zone length l_v.[4]

The crack does not interact with the coating beyond that interval. Designing Group 2 coatings, one should assume the length of section *c* (Table 1), in which lack of coating adhesion to concrete in the area above the crack is forced. In such case the coating will

operate as a membrane in the above crack area. The tension base of coating is then big enough to sustain even considerable crack width values. The tension base of coating means the length of the deforming coating band over the concrete crack. Allowing for detachment of the coating form concrete within the crack area, one can say that as the coating was not damaged at the moment of crack occurrence and opening, this does not thwart its concrete protection properties. It's been also assumed that selection of material for protection of reinforced concrete structures used in aggressive environment is dependent on the definition of coating thickness and resistance of the coating material to long-term action of such environment. The coating crack resistance criteria presented in Table 1 allow for definition of such coating properties and its thickness at which the coating should not be destroyed during crack in concrete formation and any change of their width values.

3. Experimental study

The objective of this study was definition of the impact of mechanical loads acting statically in short- and long-term periods on protective coating crack resistance. The coating crack resistance shall be meant as maintenance of coating continuity at the moment of occurrence of cracks in the concrete substrate or increase of their width values during object operation. The next objective of the study was verification of the developed crack resistance criteria of coatings used for reinforced concrete structures protection.

3.1. Material selection

The study has a cognitive (coating performance on cracked concrete substrate under short- and long-term load conditions) and practical aspects (verification of theoretical relationships allowing for selection of concrete protecting coatings). Therefore, the study must be based on materials usable in practise both in terms of their technological properties as well as the entire complex of their operational features. Six products differing in properties and application have been selected for the tests (my own material marking system has been applied):

- two-component cement-acrylic materials (PCP-1, PCP-2, PCP-3 and PCP-4) applied as protective coatings for reinforced concrete structures used in the medium aggressive environment (m_a). Those materials are represented by Group 3 coatings;
- single-component acrylic material (PP-1) applied as a protective and decorative coating for reinforced concrete structures used in the low (l_a) and medium aggressive (m_a) environments. This materials is represented by Group 3 coatings;
- two-component polyurethane coating (PP-2) applied as protective coating for reinforced concrete structures used in the strongly aggressive environment (h_a). This material is represented by Group 1 coatings.

In the case of coatings representing Group 2 the tests were commenced with long-term loading.

The materials selected for the experiment feature high deformability. Such material selection has been dictated by the fact that during origination and opening of a crack in the concrete substrate, huge relative deformations must occur in the coating due to zero (or close to zero) coating tension base. The study did not cover, therefore, any brittle coatings such as e.g. in cement or non-modified epoxy coatings.

To make the concrete mixture used for formation of reinforced concrete beams to be tested, Portland cement CEM1 32.5 and natural aggregate with grain size not exceeding 4 mm as well as broken aggregate sized from 4 mm to 16 mm were applied.

3.2. Samples and their seasoning conditions

The crack resistance tests of coatings subjected to short- and long-term loading were performed on reinforced concrete beams $80 \times 150 \times 1700$ mm. The beams were reinforced in the tensioned zone with two ribbed rods dia 12 mm and smooth steel stirrups 4.5 mm spaced at 100 mm. The concrete surround was 20 mm thick. After demoulding of the beams together with control samples (150 mm cubes), in which the crack resistance (f_c) and tensile strength (f_{ct}) were determined as well as concrete chunks $50 \times 250 \times 250$mm intended for testing coating to concrete adhesion in detachment conditions (f_{Ao}) were kept for 28 days at temperature of 19 ±2 °C and air relative humidity 100%. After 30 days of moulding three coating layers were applied to concrete chunks and reinforced concrete beams on the beam tensioned side. The coatings were applied to concrete in accordance with their manufacturer's recommendations. From each batch of coating material control samples intended for definition of properties of the coatings applied such as tensile strength (f_{pt}), ultimate tensile strain (ε_{pt}), tensile elasticity modulus (E_{pt}) and creep coefficient ($\varphi_{p(t,to)}$) were made. The coating material samples were made in accordance with BS 2782: Part 3. "Methods 320A to 320F. Tensile strength, elongation and elastic modulus" standard recommendations. The beam with coating and samples intended for determination of coating and concrete properties were kept, until tested, for the period of 10 days (polymer coatings) and 14 days (cement-polymer coatings) in an air conditioned compartment at temperature of 20 °C and air relative humidity 65%. The adopted test dates were dictated by the maturing period required by the coating materials manufacturer. After coating maturing period the beam, coating and concrete samples were put to test. Before beam loading the coating thickness on beams (h_p) was measured using a microscope with reading accuracy of 0.05 mm and by application of ultrasonic method (UP-E).

The tests comprised only those coating and concrete properties that were used in verification of the developed coating crack resistance criteria.

4. Test methods

4.1. Short-term loading tests

The coated beams were tested as freely supported, loaded with two concentrated forces applied at 1/3 element span. The beams were loaded in stages with measurements being made at each load stage until coating destruction. During element loading, measurements of bottom coating fibres elongation (Δl_p) with application of Huggenberger's extensometer with 100 mm measurement base and reading accuracy of 0.001 mm were performed in the centre section (between the forces applied). Also distances between the cracks (s_r) as well as crack width values ($w_{lim} = w_d + \Delta w$) sustained by the coating were recorded with a microscope featuring the reading accuracy of 0.05 mm.

The coating material properties were defined in accordance with BS 2782: Part 3 [13] standard and RILEM TC 113-CPT 1995 [14] test methodology.

4.2. Long-term loading tests

The coated beams (Figure 2) were loaded with constant load value equal to the cracking moment (M_{cr}).

Before the cracking load was applied, measurements of beam deflection at support points (under own weight) and in mid-span were performed with dial indicators featuring the reading accuracy of 0.01 mm. Also elongations of the bottom coating fibres (Δl_p) with Huggenberger's extensometer with 100 mm measurement base were measured. The crack width values (w_{lim}) sustained by the coating were measured with a microscope featuring a reading accuracy of 0.05 mm. The measurements were being performed until coating cracking or stabilisation of beam deformations.
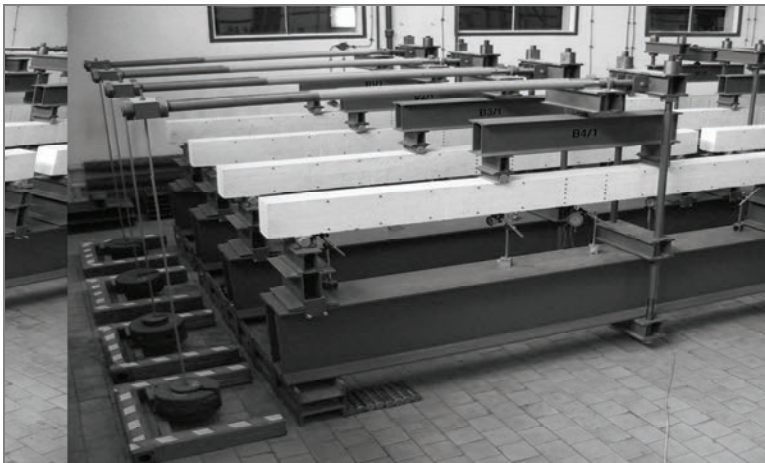
Fig. 2. Test rig for coated beams long-term loading

Verification of the crack resistance criteria defined for the coatings subjected to long-term loadings required definition of the creep coefficient ($\varphi_{p(t,to)}$).

Measurements of PCP-3, PCP-4, PP-1 and PP-2 deformations in coatings subjected to tensile loading equal to $\sigma_{pt} = 0.25 f_{pt}$ were performed at temperature of 22 ± 2 °C and air relative humidity $55 \pm 5\%$ (Figure 3).

Fig. 3. Test stand for coating material creep

The deformation measurements were taken with dial indicators with reading accuracy of 0.01 mm. The tensile stress of $0.25 f_{pt}$ was close to those stress values that were developed in the beam coating loaded with the cracking force. The coating deformations were recorded until their stabilisation but not for less than for 12 months.

5. Test results and discussion

The statistical calculus was applied in processing of test results for coated beams (Table 2), coatings (Table 3) and concrete properties. The number of samples required for definition of the average value of tested coating and concrete features was statistically adequate.

The tests have indicated that the coatings applied to short-term loaded beams maintained their continuity after development of cracks in concrete featuring the average width values from 0.25 mm in the case of PP-1 acrylic coating to 0.95 mm for PP-2 polyurethane coating. The above relationships pertain also to the maximum crack width values (w_{lim}) sustained by those coatings (Table 2). It appears from comparison of PCP-1, PCP-3 and PCP-4 (similar thickness coatings) coating test results and from the results shown in Table 2 that the higher the tensile strength and ultimate tensile strain, the higher is the coating ability to sustain the cracks under short-term loading.

Based on the coating crack resistance criteria (Table 1) and the coating/concrete features defined during the tests, the maximum crack width values at which the coatings should be destroyed under the short- and long-term loading were calculated. An assumption was made for the calculations that width of a crack at which the coating is destroyed (w_n) is equal to the experimental width of the crack (w_{lim}) sustained by the coating under short-term load. The maximum values of width of the cracks sustained by the coatings calculated on the basis of crack resistance criteria defined for the short-term loading are lower than that obtained during the tests (Figure 4). Small differences between the experimentally fixed and calculated crack width values indicate correctness of the developed coating crack resistance criteria.

Table 2. Selected test results of crack resistance of coatings under short-term and long-term load

Tested feature	Coating material marking									
	PCP-3		PP-2		PP-1		PCP-1	PCP-2	PCP-4	
Load	short-term	long-term	short-term	long-term	short-term	long-term	short-term	short-term	short-term	long-term
f_c, MPa	48.3		52.4		47.9		47.9	48.3	51.2	
f_{ct}, MPa	3.9		3.9		4.0		4.0	3.7	4.4	
M_{cr}[3], N·m $\times 10^3$	3.18		3,16		3.24		3.24	3.03	3.58	
M_{cr}[4], N·m$\times 10^3$	2.86	2.75	3.19	3.02	2.95	3.30	2.89	2.80	3.20	3.35
$\varphi_{p(t,to)}$	2.56		1.83		2.68		2.70	–	5.12	
h_p, mm	2.01	2.70	1.24	1.31	0.58	0.55	2.20	2.91	2.05	2.15
Δl_p[4], mm	0.900	0.118	1.861	0.226	0.640	0.187	1.544	1.257	1.421	0.142
s_r[3], mm	45	47	45	47	45	47	45	45	45	47
s_r[4], mm	55	70	48	51	54	56	49	48	41	51
cracks interval w_{lim}[4], mm	0.95–1.15	0.125–0.15	1.75–1.90	0.125–0.175	0.40–0.55	0.10–0.175	1.35–1.50	1.45–1.65	1.60–1.80	0.125–0.18
$\overline{w}$lim[4], mm	1.02	0.13[1]	1.85	0.15[2]	0.51	0.14[2]	1.50	1.52	1.70	0.16[2]
Number of beams, pcs.	10	12	8	6	8	6	8	10	10	6

[1] – values corresponding to coating damage on beams,
[2] – operational crack width,
[3] – values obtained from calculation,
[4] – values obtained from the study,
s_r – distance between of cracks perpendicular.

The coating creep coefficient values $\varphi_{p(t,to)}$ adopted for calculation of the width values of cracks sustained by coatings under a long-term loading have been illustrated in Figure 5.

The $\varphi_{p(t, to)}$ factor for all coatings was determined in 10 samples as a proportion of creep deformation at time t and the deformation recorded after 5 min as of long-term load application.

Table 3. Coating material properties average values specification

Tested feature	Coating material marking					
	PCP-1	PCP-2	PCP-3	PCP-4	PP-1	PP-2
f_{Ao}, [MPa]	1.1[2]	1.9[2]	0.8[2]	1.8[2]	1.3[2]	>2.0[1]
f_{pt}, [MPa]	1.95	1.10	0.39	1.14	0.9	7.1
ε_{pt}, [%]	22	29	22	65	59	65
E_{pt}, [MPa]	5.43	4.56	1.62	1.97	1.59	11.31
Number of samples [pcs.]	6 pieces marked f_{Ao} and from 20 pieces in testing other coating properties PCP-1 to 30 pieces for PCP-3					

[1] – damage to section through the concrete,
[2] – damage to the coating–concrete binding plane.
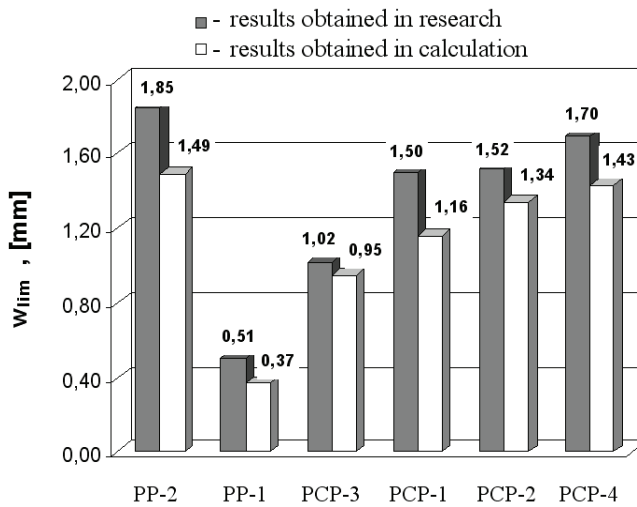
Fig. 4. Comparison of the experimental and calculated crack width values w_{lim} sustained by the short-term loaded coatings
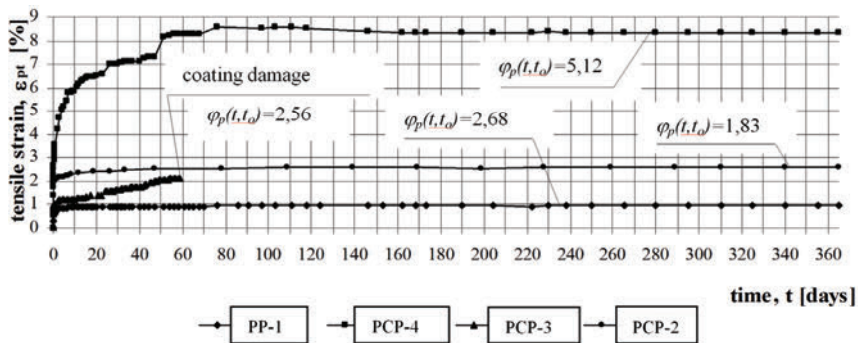
Fig. 5. Coating creep at $\sigma_{pt} = 0.25 f_{pt}$ strain curves

Some samples (5 pcs.) made of PCP-3, subjected to constant value of tensile load, were destroyed within 44 days of load application whereas the remaining 5 samples were destroyed after 51 days. The PP-2 coating deformation stabilisation has been observed after 215 days of load application, PP-1 after 251 and PCP-4 after 364 days of load application.

PCP-4, PP-1 and PP-2 coatings applied to long-term loaded beams did not crack. The average operational crack (the crack after beam deformation stabilisation) width values fell within the interval from 0.08 mm, in the case of PP-1, to 0.10 mm for PCP-4, and the max. w_{lim} values were 0.14 mm and 0.16 mm respectively. It should be pointed out that the calculated crack width values, at which PCP-4, PP-1 and PP-2 coatings would not be destroyed under long-term loading, are much higher than the operational cracks. Based on the crack resistance criteria one can determine the maximum width of a crack that can be sustained by the coating under given circumstances. One can expect that PCP-4, PP-1 and PP-2 will perform their function in the case of such structures in which a possibility of development of cracks in concrete is allowed or increase of structure operational load after coating application has been envisaged.

Impact of long-term loads on coating crack resistance was exposed in PCP-3 material testing. Destruction of PCP-3 coating in 8 beams occurred after 77 days as of load application, whereas in the remaining beams, during the period shorter than 46 days. The average crack width value ($\overline{w}$ = 0.08 mm) sustained by the long-term loaded coating was approx. 80% lower than that obtained in the short-term loading tests ($\overline{w}$ = 0.40 mm). The above observations pertain also to the maximum cracks w_{lim} (Table 2). However, a worrying fact is that PCP-3 coating was destroyed very quickly i.e. after 77 days as of load application. The results obtained from PCP-3 coated beams test give grounds for a statement that this material can be practically applied for protection of such reinforced concrete structures that operate without any cracks therein or the coating has been applied after their cracking.

The above observations induced the author to perform crack resistance tests in PCP-3 coating applied to a cracked concrete substrate. Six reinforced concrete beams without any coating thereon were subjected to a load equal to the cracking moment (M_{cr} = 3.2 kN·m) and cracks with average width of 0.03 mm were developed in them. Then, a coating of average thickness 2.50 mm was applied to the cracked concrete substrate. After 497 days of load application stabilisation of beam deformations, without PCP-3 coating damage, have been observed. The average width of cracks sustained by PCP-3 coating was 0.13 mm and the maximum w_{lim} 0.23 mm. The obtained test results have confirmed author's expectations. The calculations performed with application of the crack resistance criterion for Group 3 coatings have indicated that with a crack of 0.11 mm width the PCP-3 coating will be destroyed under long-term loading. The maximum width of the crack destroying a long-term loaded coating, which has been observed after its destruction, is 15% bigger than the calculated crack value. Good compatibility of the experimental test results with analytical calculations confirms correctness of the developed crack resistance criterion.

6. Conclusions

1. Good compatibility of the experimental test results with calculations confirms correctness of the developed crack resistance criteria for the polymer and cement-polymer coatings.

2. The crack resistance criteria can be useful in designing of protective coatings for reinforced concrete structures for which the initial loading stage has not yet developed cracks as well as at the stage after cracking, during object operation. The criteria can also be used in designing of any new coating materials that could be used in such applications.

3. Long-term loading application causes reduction of polymer and cement-polymer coating crack resistance with relation to crack resistance of coatings subjected to short-term loading.

4. By proper selection of the coating material and its thickness, the reinforced concrete structures can be protected against corrosion in a way preventing translation of the substrate crack to the coating.

References

[1] Ho D.W.S., Ritchie D.: *Surface coatings and their influence on the quality of the concrete substrate*, Polymers in Concrete (ed. Ohama Y., Kawakami M., Fukuzawa K.), Published by E & FN Spon, 1997.

[2] Vipulanandan C., Liu J.: *Performance of polyurethane-coated concrete in sewer environment*, Cement and Concrete Research, Vol. 35, No. 9, 2005, pp. 1754–1763.

[3] Czarnecki L.: *Repairing and protection of reinforced concrete constructions* (in Polish), Polski Cement, Kraków, 2002.

[4] Głodkowska W.: *Rudiments and method of selection of composite properties for concrete repair and protection* (in Polish), Dissertation, Technical University of Koszalin, Koszalin, 2003.

[5] Czarnecki L., Głodkowska W., Piątek Z.: *Compatibility of polymer and cement-polymer composites with ordinary concrete under short-time load conditions*, Archives of Civil Engineering, XLIX, Vol. 1, 2004, pp. 133–150.

[6] Delucchi M., Barbucci A., Cerisola G.: *Crack-bridging ability of organic coatings for concrete: influence concrete cracking, thickness and nature the coating*, Progress in Organic Coatings, Vol. 49, No. 4, 2004, pp. 336–341.

[7] Almusallam A.A., Khan F.M., Dulaijan S.U., Al-Amoudi O.S.: *Effectiveness of surface coatings in improving concrete durability*, Cement and Concrete Composites, Vol. 25, No. 4–5, 2003, pp. 473–481.

[8] Głodkowska W., Staszewski M.: *Weatherability of coating materials for protection of concrete*, Adhesion in Interfaces of Building Materials: a Multi-scale Approach. Advances in Materials Science and Restoration, AMSR No.2. ISBN 978-3-931681-89-0, Aedificatio Publishers, Germany, 2007, pp. 193–206.

[9] Plum D.: *Materials, what to specify*, Construction Maintenance & Repair, No. 37, 2001, pp. 7–8.

[10] Robery P., Shaw J.: *Materials for the repair and protection of concrete*, Construction and Building Materials, Vol. 11, 1997, pp. 275–281.

[11] Maciulaitis R., Vaiciene M., Zurauskiene R.: *The effect of concrete composition and aggregates properties on performance of concrete*, Journal of Civil Engineering and Management, No. 3, 2009, pp. 317–324.

[12] Rische G.: *Rissüberbrückende Kunststoffeschichtungen für Mineralische Baustoffe,* Farbe-Lack, Zentralblatt der Farben und Lackindustrie und des Handels, 85 Jahrgang, Vol. 10, 1979, pp. 824–831.

[13] BS 2782: Part 3. Methods 320A to 320F. Tensile strength, elongation and elastic modulus.

[14] Draft Test recommendations, Technical Committee 113-CPT, RILEM 1995.

Prognozowanie rysoodporności powłok obciążonych krótko- i długotrwale

W artykule omówiono zagadnienia rysoodporności powłok stosowanych do ochrony powierzchniowej konstrukcji żelbetowych. W wyniku przeanalizowania warunków pracy elementów układu powłoka–beton oraz towarzyszącym im w różnych sytuacjach obciążeń, a także przewidywanych skutków ich oddziaływania opracowano kryteria oceny rysoodporności powłok. Na podstawie sześciu materiałów powłokowych dokonano doświadczalnej weryfikacji kryteriów rysoodporności i określono wpływ obciążeń mechanicznych krótko– i długotrwałych na rysoodporność takich powłok. Badania wykazały poprawność opracowanych kryteriów rysoodporności i wskazały na ich przydatność w projektowaniu powłok ochronnych dla konstrukcji żelbetowych, w których początkowe stadium obciążenia nie wywołało jeszcze rozwoju rys, jak i w stadium po zarysowaniu, podczas eksploatacji obiektu. Kryteria te mogą także posłużyć w projektowaniu nowych materiałów przydatnych w takich zastosowaniach.

Moisture influence on the failure of self-compacting concrete under compression

T. GORZELAŃCZYK

Wrocław University of Technology, Wybrzeże Wyspiańskiego 25, Wrocław, Poland.

The paper presents the results of investigations into the failure of four self-compacting concretes under compression. When tested, the concretes were damp to different degrees. The failure processes were investigated by acoustic methods. The levels of cracking initiating stress σ_i and critical stress σ_{cr}, delimiting the stages in the failure process, were determined. Dependence between the moisture content in concrete and the levels of the above stresses has been established. The experimental results were used to calculate the fatigue strength of the tested self-compacting concretes and on this basis the suitability of the latter for erecting structures subject to repeated dynamic loads was assessed.

Keywords: *moisture, acoustic methods, failure, self-compacting concrete, fatigue strength*

1. Introduction

Self-compacting concrete (SCC) is increasingly often used to erect civil engineering structures [14–16, 22–25] subjected to the action of various nonmechanical factors (mainly moisture) in the course of their service life. The question arises: does moisture contribute to the stress failure of SCC, similarly as to that of ordinary concrete [9–12]? Besides advancing our knowledge, the answer to this question could be useful for predicting the behaviour of SCC in service. This particularly applies to self-compacting concrete incorporated into structures subject to repeated dynamic loads, such as bridge deck slabs, industrial floors and concrete carriageways [2–3].

In comparison with ordinary concrete, self-compacting concrete contains not only a higher percentage of dusty fractions and a lower percentage of coarse aggregate, but also new generation superplasticizers endowing the concrete mix with the required flowability [14, 17–18, 21, 23, 25, 28–29]. As a result, self-compacting concrete is characterized by a greater total porosity in comparison with ordinary concrete made using aggregate with a similar maximum particle size and a similar compressive strength, as proved by the tests carried out in [8]. Hence it can be inferred that because of its greater porosity, self-compacting concrete tends to absorb moisture from the environment not less than ordinary concrete does. Therefore one can suppose that the moisture contained in SCC will significantly affect its failure under compressive loading.

In order to confirm this supposition, the failure of four self-compacting concretes, differing in their moisture content, under compression was investigated using acoustic

methods and the levels of cracking initiating stress σ_i and critical stress σ_{cr}, which delimit the stages in this process were determined [6, 10, 19–20, 26]. On the basis of the stress levels, the fatigue strength of the concretes was calculated. It should be mentioned that the dependence between the fatigue strength of concrete and the levels of respectively cracking initiating stress σ_i and critical stress σ_{cr} had already been established [1, 4–6, 10, 13, 27].

2. Effect of moisture content on properties and failure of concrete in light of research to date

Moisture in the structure of hardened concrete is present in both the cement grout and the transitional layer as well as in the pores. Its amount is not without significance for the behaviour of ordinary concrete during its failure under a load [9–10]. The moisture present in mature concrete is in the form of chemically bound water, partially bound water (gel water) and free water. The chemically bound water is an essential component of the crystal lattice of concrete. The partially bound water separates into zeolitic water and adsorption water physicochemically bound with concrete solid phases by surface forces. The partially bound water plays a role in gels. The free water is bound with concrete solid phases through weak physicochemical chemical bonds. It infiltrates into concrete through micropores and capillaries, mainly as a result of the capillary condensation of the water vapour present in the micropores. It is highly significant that the water is relatively easily removed from concrete at a temperature of 105–110 °C.

Depending on the service conditions, the capillary motion of free water in concrete may take place in a wide range of concrete moisture content, i.e. from full saturation, through maximum moisture sorption to dry condition. If pores and capillaries in concrete are filled with water, the compressive strength of this material decreases nonlinearly due to adsorption. This is caused by the dissolution of the bonds between crystals in the structural lattice. The decrease in the strength of water saturated concrete is reversible, in the sense that after it is dried the concrete almost fully recovers its original strength. The decrease in strength is also due to the disintegration of concrete under load by the splitting action of water present in microcracks [9–10]. As explained in the latter papers, the splitting action of water substantially contributes to the stress failure of concrete, especially when it is fully saturated with water.

Research has shown that cracking initiating stress σ_i and critical stress σ_{cr} reach different levels in different concretes [9–10]. They may also reach different levels in concretes with similar compressive strength. This is owing to the fact that the levels are correlated with both the condition of the structure before loading (taking into account the internal stresses and the resulting structural microflaws) and the growing number of microflaws under the load. This means that they are correlated not only with the technological factors and the concrete making conditions, but also with non-mechanical service conditions [10–11]. One should mention here mainly the moisture

contained in the structure, some of it being the remainder of the water introduced into concrete during its making and some infiltrating the concrete as a result of sorption from the environment or capillary rise in the course of the service life of the structure.

The test results reported in [9–12] and elsewhere show that moisture strongly affects the levels of cracking initiating stress σ_i and critical stress σ_{cr} in compressed ordinary concrete. Depending on the moisture content, stress σ_i is in a range of 0.20–0.45 σ_c/f_c while stress σ_{cr} is in a range of 0.71–0.90 σ_c/f_c. A survey of the available literature reveals the lack of similar research on self-compacting concrete, aimed at assessing the effect of moisture content on the failure of such concretes under compressive load.

The marked reduction in the level of stress σ_i in concretes fully saturated with water and the consequent marked reduction in their fatigue strength are critical for the durability and safety of structures which are subject to repeated dynamic loads or overloads and become damp in the course of their service life.

3. Investigations

In order to assess the effect of moisture on the failure of self-compacting concrete under compression, four SCC mixes (denoted by respectively the letters A–D), differing in their superlasticizer and aggregate amount, were designed. The mixes were made from Portland cement CEM I 42.5 R, gravel aggregate, river sand, fly ash, tap water and two different superplasticizers. The maximum aggregate particle size was 16 mm in mixes A and C and 8 mm in mixes B and D. Superplasticizer S_A was used for mixes A and B and superplasticizer S_V for mixed C and D. Superplasticizer S_A was based on polycarboxyl ether while superplasticizer S_V was based on a combination of polycarboxylans and viscosity, setting and hardening regulators. The two superplasticizers are most often used to make SCC mixes. The compositions of the mixes had been experimentally determined according to the recommendations given in [17, 21, 28–29].

Table 1 shows the compositions of the designed concrete mixes and average compressive strengths f_{cm} of the concretes obtained from the mixes, determined for 150 × 150 × 150 mm specimens after 90 days of curing in a climatic chamber at an air temperature of + 18 °C (±1 °C) and a relative air humidity of 95% (±5%).

Table 1. Compositions of designed SCC mixes and average compressive strengths f_{cm} of concretes obtained from mixes [8]

Mix & concrete symbol	Compositions of concrete mixes [kg/m³]						Water/ Cement ratio $\frac{W}{C+F}$	Sand content [%]	Average compressive strength f_{cm} of concrete after 90 days of curing [MPa]
	Course aggregate	Sand	Cement	Fly ash	Water	Super-plasticizer			
A	1064	581	355	143	164	3.15	0.34	35.3	44.52
B	896	747	325	109	195	3.25	0.45	45.5	32.41
C	1064	581	355	143	164	4.18	0.34	35.3	59.22
D	896	747	325	109	195	4.25	0.45	45.5	41.82

The concrete specimens made from mixes A–D were divided into series representing a wider range of moisture content (from full saturation to dry condition). The denotations of the series include information about the way the specimens were stored:

• series A_w–D_w specimens were stored for 86 days in a climatic chamber at an air temperature of + 18 °C (±1°C) and a relative air humidity of 95% (±5%), and subsequently fully saturated with water;

• series A_k–D_k specimens were stored for 90 days in a climatic chamber at an air temperature of + 18 °C (±1 °C) and a relative air humidity of 95% (±5%), (the maximum sorption moisture content);

• series A_s–D_s specimens stored for 86 days in a climatic chamber at an air temperature of + 18 °C (±1 °C) and a relative air humidity 95% (±5%) and subsequently dried at a temperature of 105 °C to a constant weight (dry condition).

The values of moisture content by w_m of the tested self-compacting concrete series are presented in Table 2.

Table 2. Values of moisture content by w_m of tested concrete series [6]

Concrete series symbol	A_w	A_k	A_s	B_w	B_k	B_s	C_w	C_k	C_s	D_w	D_k	D_s
Moisture content by w_m [%]	6.51	4.05	0	7.22	4.69	0	6.71	4.24	0	7.53	4.89	0

The failure process was investigated using an Instron 1126 strength tester and two acoustic methods, the ultrasonic method and the acoustic emission (AE) method.

Ten 100×100×100 mm specimens from each concrete series were investigated using the ultrasonic method. The investigated parameter was longitudinal ultrasonic wave velocity V_L determined in the direction perpendicular to that of the load, as a function of the increase in compressive stress. A UNIPAN 543 tester with digital readout and 100 kHz ultrasonic probes were used.

Six 50×50×100 mm specimens (cut out from larger test pieces) from each concrete series, were investigated using the acoustic emission method. As they were being compressed, AE descriptors, i.e. events rate N_{ev} the *RMS* value of the signal, versus time were registered. Compression was performed without friction at the specimen/strength tester plates' interface. For this purpose the surfaces involved were ground to make them mutually parallel with an accuracy of 0.05 mm and then lubricated with grease. The investigations were carried out using a Vallen-Systeme AMS3 acoustic emission measuring set and two VS 150-M sensors with a 100–450 kHz transmission band.

4. Results of failure investigations and their analysis

In order to show the effect of the moisture content of self-compacting concrete on its failure the specimens of concretes A–D, series A_w, A_k, A_s, B_w, B_k, B_s, C_w, C_k, C_s,

and D_w, D_k, D_s, differing in their moisture content at the time of the tests were subjected to axial compression and investigated using the ultrasonic method and acoustic emission method.

Figure 1 shows diagrams of longitudinal ultrasonic wave velocity versus compressive stress for the investigated concrete series.

The results presented in figure 1 show that as compressive stress increases, velocity V_L of longitudinal ultrasonic waves decreases. For example, in concrete A this decrease is noticeable at 0.24 σ_c/f_c for series A_w, at 0.31 σ_c/f_c for series A_s and at 0.33 σ_c/f_c for series A_k. Once the above stress levels are exceeded, the observed phenomenon intensifies. The velocity of longitudinal ultrasonic waves can be measured only at such a stress level at which they are totally attenuated. The level is different in the particular series. It is the lowest in series A_k concrete, amounting to 0.90 σ_c/f_c and the highest in series A_w concrete, amounting to 0.93 σ_c/f_c.

The above findings can be explained by the fact that the failure of concretes with higher moisture content is less abrupt owing to the presence of a greater amount of water in macro- and microcapillaries. Water filling the microcracks appearing in the structure of the concrete under load, reduces the effect of stress rupture on the attenuation of ultrasonic waves. According to the criteria given in [8, 10], the stress level starting from which a marked decrease in the velocity of longitudinal ultrasonic waves is observed corresponds to the level of cracking initiating stress σ_i while the stress level at which it is no longer possible to measure the velocity of the waves corresponds to the level of critical stress σ_{cr}. The levels are marked in Figure 1.

One should also note that the initial velocity of longitudinal ultrasonic waves in the investigated series is not identical and it clearly depends on the concrete's moisture content. The velocity increases with moisture content. This is so because the attenuation of an ultrasonic wave encountering pores and various microflaws filled with air on its path is greater than in the case of pores and microflaws filled with water.

Similar observations are made with regard to the results shown in Figure 1 for concretes B, C and D.

Figures 2–5 show the registered AE events rate N_{ev} versus time of compression of concretes A_w, A_k, A_s, B_w, B_k, B_s, C_w, C_k, C_s, and D_w, D_k, D_s. The figures include graphs showing the increase in relative compressive stress σ_c/f_c versus failure time t and the levels of cracking initiating stress σ_i and critical stress σ_{cr}, determined in accordance with the criteria given in [7–8].

The test results presented in Figures 2–5 indicate that the pattern of AE events rate during failure is similar in the investigated concretes. The value of this AE descriptor is initially low, then increases moderately and sharply increases in the final stage. It appears from Figures 2–5, however, that the N_{ev} values clearly differ between the investigated series. The lowest acoustic activity, and so the lowest events rate N_{ev}, was found to characterize the concrete series saturated (up to full saturation) with water. The highest acoustic activity was found to characterize the series of dry concrete.
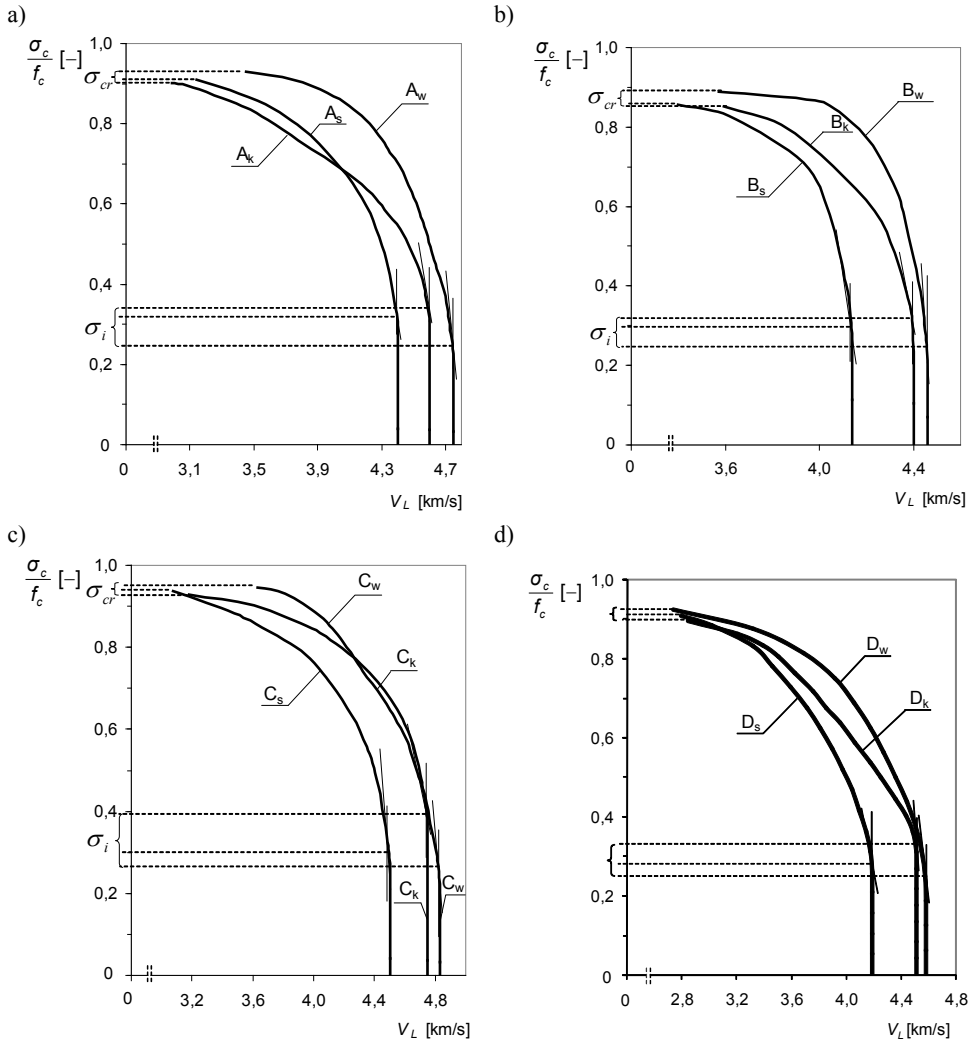
Fig. 1. Longitudinal ultrasonic wave velocity versus increase in relative compressive stress in concretes
of series: a) A_w, A_k and A_s, b) B_w, B_k and B_s, c) C_w, C_k and C_s, d) D_w, D_k and D_s

It can be inferred that moisture content affects AE events rate N_{ev} mainly as a result
the weakening of the bonds between the crystals in the structural lattice, which is due
to the fact that as the moisture content in concrete increases, the bonds partially dis-
solve whereby the concrete's compressive strength decreases slightly. The soaking of
the concrete structure has a direct bearing on the number of potential places where the
structure may undergo damage and on the pattern of its failure, which is reflected in
the number of registered acoustic emission pulses.
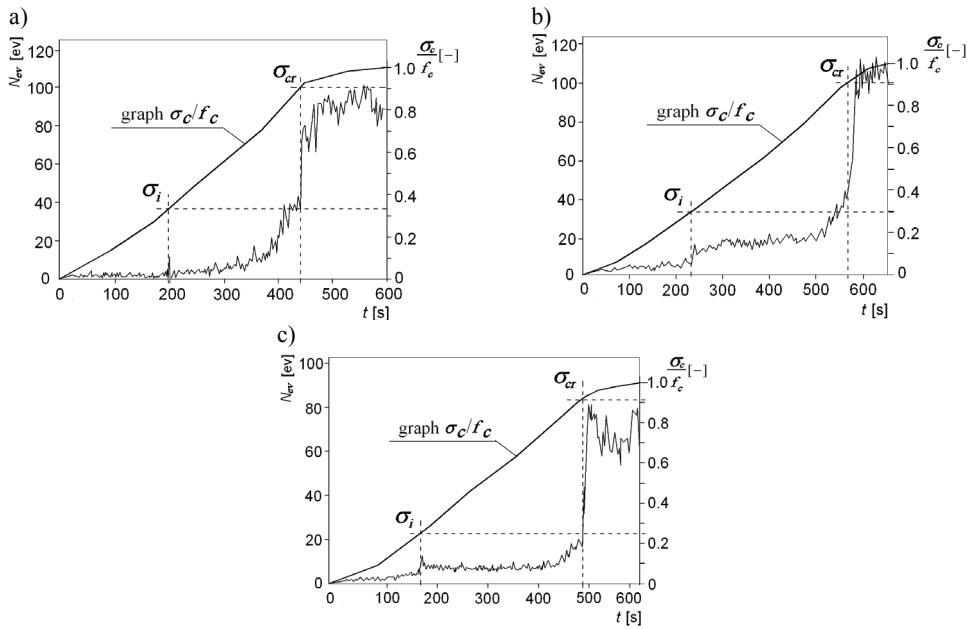
Fig. 2. Registered AE events rate N_{ev} and graph showing increase in relative compressive stress σ_c/f_c versus failure time for self-compacting concretes of series: a) A_k, b) A_s, c) A_w
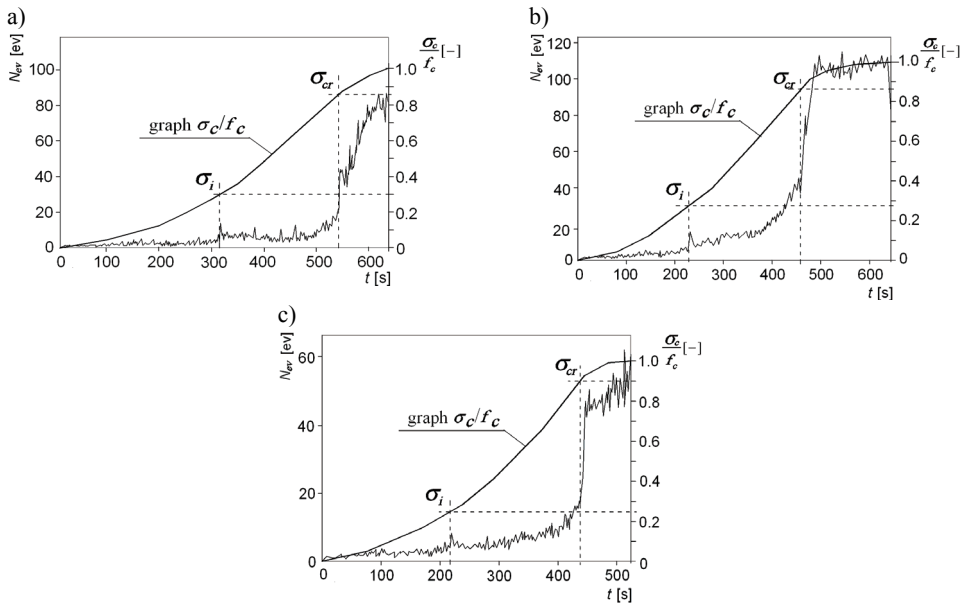
Fig. 3. Registered AE events rate N_{ev} and graph showing increase in relative compressive stress σ_c/f_c versus failure time for self-compacting concretes of series: a) B_k, b) B_s, c) B_w
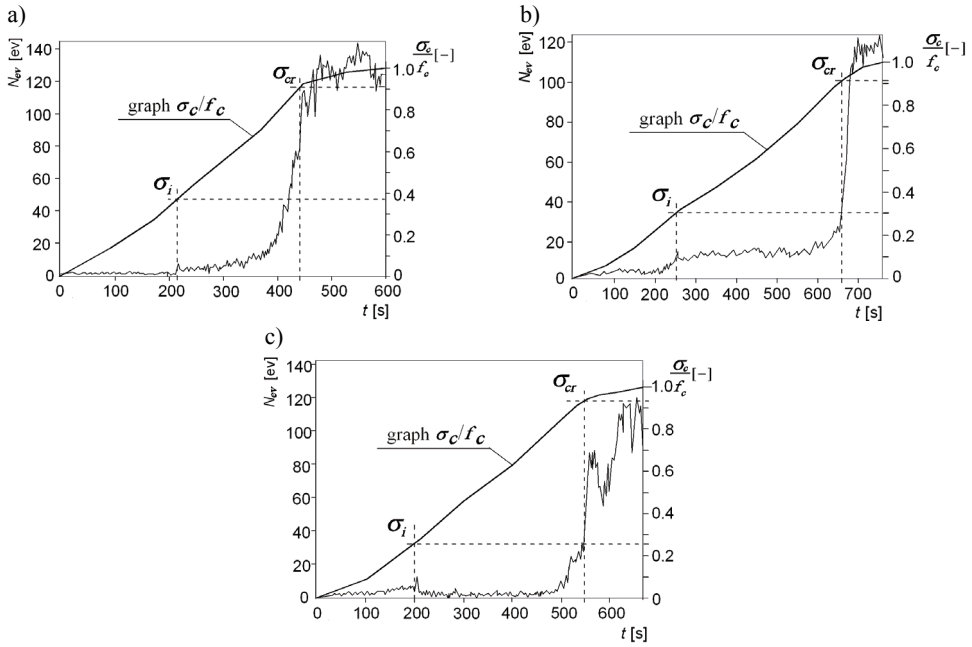
Fig. 4. Registered AE events rate N_{ev} and graph showing increase in relative compressive stress σ_c/f_c versus failure time for self-compacting concretes of series: a) C_k, b) C_s, c) C_w
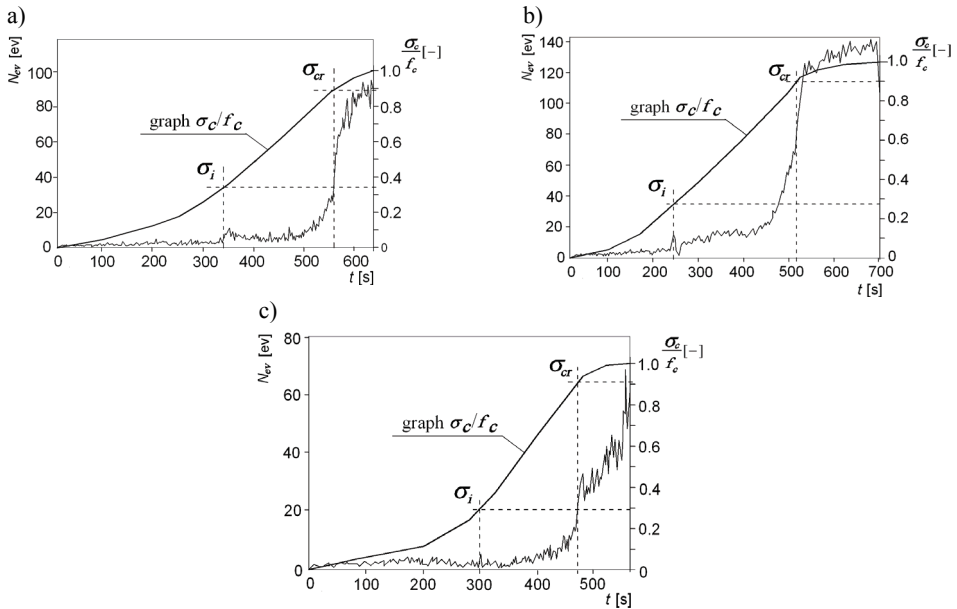
Fig. 5. Registered AE events rate N_{ev} and graph showing increase in relative compressive stress σ_c/f_c versus failure time for self-compacting concretes of series: a) D_k, b) D_s, c) D_w

When the levels of cracking initiating stress σ_i determined for example, for the tested series of concrete A are compared, one finds that series A_k concrete cured in the climatic chamber shows the highest value of this stress while series A_w concrete fully saturated with water shows the lowest value. The same is observed for the concretes of series B_w, B_k, B_s, C_w, C_k, C_s, and D_w, D_k, D_s, i.e. concrete "k" (with the maximum sorption moisture content) shows the highest level of cracking initiating stress σ_i in comparison with the concretes denoted with the index "s" (dry condition) or "w" (fully saturated with water).

The opposite is observed for critical stress: the highest level of this stress was found in the concrete series denoted with the index "w", i.e. in series A_w, B_w, C_w and D_w.

The levels of cracking initiating stress σ_i and critical stress σ_{cr} for the investigated concrete series, marked in Figures 1–5, are presented in Table 3. The latter also includes the average (relative and absolute) values of stress σ_{im} and stress σ_{crm}, calculated from the results obtained by means of the two investigative methods.

Table 3. Levels of stress σ_i and σ_{cr} and average (relative and absolute) values of stress σ_{im} and σ_{crm}, determined for investigated concrete series A_w, A_k, A_s, B_w, B_k, B_s, C_w, C_k, C_s, and D_w, D_k, D_s by means of ultrasonic method and acoustic emission method [8]

Concrete series symbol	Measuring method				Average values			
	Ultrasonic		Acoustic emission		σ_{im}		σ_{crm}	
	σ_i [–]	σ_{cr} [–]	σ_i [–]	σ_{cr} [–]	[–]	MPa	[–]	MPa
A_w	0.24 / 5.4%	0.93 / 1.8%	0.25 / 4.1%	0.92 / 3.2%	0.245	9.61	0.925	37.24
A_k	0.33 / 8.7%*	0.90 / 2.1%	0.33 / 4.3%	0.91 / 3.3%	0.330	15.58	0.905	40.51
A_s	0.31 / 8.6%	0.91 / 2.2%	0.29 / 3.8%	0.91 / 2.4%	0.300	14.56	0.910	42.76
B_w	0.24 / 9.1%	0.89 / 1.2%	0.25 / 3.6%	0.90 / 2.7%	0.245	8.34	0.895	27.42
B_k	0.31 / 7.6%	0.85 / 1.5%	0.30 / 1.8%	0.86 / 2.5%	0.305	10.21	0.855	27.22
B_s	0.29 / 8.3%	0.86 / 2.3%	0.28 / 2.4%	0.87 / 2.1%	0.285	11.69	0.865	34.26
C_w	0.25 / 6.1%	0.95 / 1.0%	0.26 / 3.4%	0.93 / 1.3%	0.255	14.09	0.940	56.36
C_k	0.38 / 6.4%	0.94 / 2.1%	0.38 / 2.7%	0.92 / 1.3%	0.380	22.27	0.930	55.29
C_s	0.29 / 5.4%	0.93 / 2.6%	0.31 / 3.3%	0.91 / 1.1%	0.300	19.03	0.920	58.37
D_w	0.25 / 8.4	0.92 / 1.0%	0.28 / 4.3%	0.91 / 1.4%	0.265	8.94	0.915	30.64
D_k	0.33 / 8.8%	0.90 / 1.3%	0.34 / 3.1%	0.89 / 2.1%	0.335	13.32	0.895	38.97
D_s	0.28 / 7.4%	0.91 / 1.9%	0.30 / 3.3%	0.90 / 1.3%	0.290	11.26	0.905	34.75

 * Note: the values under the line are those of variation coefficients.

a)

b)
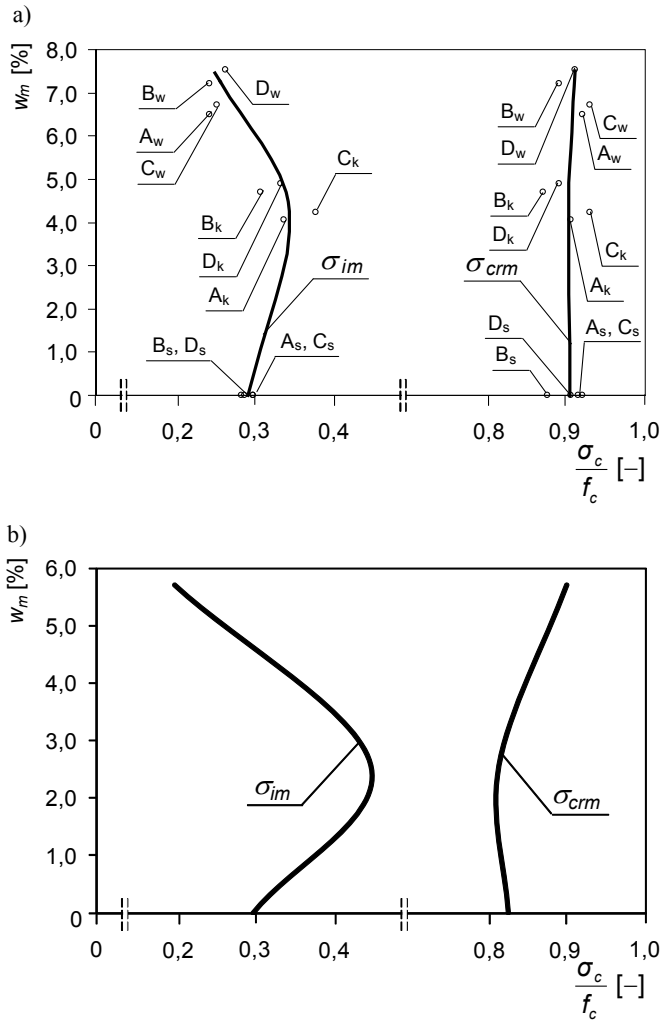
Fig. 6. Generalized diagram of variation in average relative values of initiating cracking stress σ_{im}
and critical stress σ_{crm}, depending on moisture content for investigated series of:
a) self-compacting concretes, b) selected ordinary concrete [8]

In order to better illustrate the effect of moisture content on the levels of cracking
initiating stress and critical stress in the tested self-compacting concretes A–D, a gen-
eralized diagram of the variation in the average relative values of stress σ_{im} and stress
σ_{crm} depending on the moisture content is shown in Figure 6. The latter also includes
a similar diagram for concrete selected from [10], in order to compare the effect of
moisture content on the failure of self-compacting concrete and ordinary concrete. The
particular ordinary concrete was selected since it was characterized by a similar

maximum coarse aggregate particle size and a similar average compressive strength f_{cm} (amounting to 42.35 MPa) after 90 days of curing [10].

It follows from Table 3 and Figure 6a that in the case of the investigated self-compacting concretes, moisture content significantly affects the level of cracking initiating stress σ_i. As the moisture content of the concretes increases (starting from dry condition) so do average values of stress σ_{im}, reaching their maximum at the instant when the sorption moisture content of the concrete is the highest. Then they markedly decrease. However, a comparison of the results with the ones presented in Figure 6b shows that this effect is not as considerable as in the ordinary concrete.

Analyzing the results shown in Figure 6, one can say that it is highly probable that once the moisture content in the concrete reaches approximately the maximum sorption moisture content, the adverse effect of the splitting action of water on the structure manifests itself. The effect can be explained as follows. As the moisture content in concrete increases, free water increasingly fills microcracks, pores and other structural microflaws which arose during concrete making. The increasing compressive stress and the specimen volume decreasing as the compressive stress increases contribute to the migration of water into micropores. This phenomenon intensifies with increasing moisture content in the concrete. To be more precise, this propagation starts earlier, i.e. at a lower relative level of compressive stress.

As regards stress σ_{cr}, it appears from Table 3 and Figure 6 that moisture content has little effect (much smaller than in the reference ordinary concrete) on the level of this stress. This can be ascribed to the fact that in the final stage of failure under compression the existing cracks are so wide that the free water in them no longer causes splitting.

5. Calculation of fatigue strength of investigated self-compacting concretes

The following relation [5], using experimentally determined values of cracking initiating stress σ_i and critical stress σ_{cr}, was adopted for calculating fatigue strength

$$f_c^f / f_c = CN^{-A}\left(1 + B\rho^f \log N\right)C_f, \tag{1}$$

where:

C – a coefficient expressing the ratio of dynamic strength to static strength under single time load,

ρ^f – a stress ratio,

$\sigma_c^{\min}$ – the minimum cycle stress,

$\sigma_c^{\max}$ – the maximum cycle stress,

C_f – a coefficient representing the effect of load change frequency on fatigue strength,

A, B – coefficients representing the state of the concrete structure, owing to the fact that they are interrelated with stresses σ_i and σ_{cr}.

According to [5], stress ratio ρ^f is defined by the relation

$$\rho^f = \sigma_c^{\min} / \sigma_c^{\max} , \tag{2}$$

and coefficient C_f can be expressed by the relation

$$C_f = 1 + 0.07\left(1 - \rho^f\right)\log f, \tag{3}$$

where f is load change frequency (in Hz) and coefficients A and B can be calculated from relations (4) and (5)

$$A = 0.008 - 0.118\log\left(\sigma_i / f_c\right), \tag{4}$$

$$B = 0.118\left(\sigma_{cr} / \sigma_i - 1\right). \tag{5}$$

Figures 7 and 8 show fatigue strength (calculated using the above relation and the average values of stress σ_{im} and σ_{crm} given in Table 3) versus number N of load cycles for the investigated SCC series A_w, A_k, A_s i C_w, C_k, C_s. The calculations were done assuming stress ratio $\rho^f = 0$ and load change frequency $f = 1$ Hz.
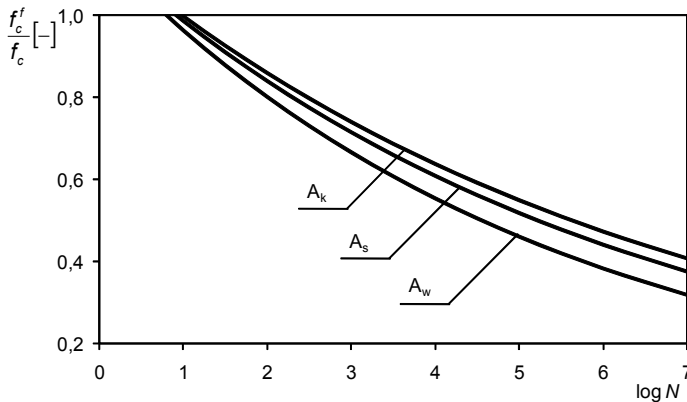
Fig. 7. Calculated fatigue strength versus load cycles at $\rho^f = 0$
and $f = 1$ Hz for series A_w, A_k, A_s concretes

It is clear from Figures 7 and 8 that moisture contained in the investigated self-compacting concretes has a significant effect on their fatigue strength. When concrete becomes fully saturated with moisture, its fatigue strength clearly decreases in comparison with the fatigue strength of concrete whose sorption moisture content is

maximal. This was observed in all the investigated self-compacting concretes. The finding is important for building practice. A situation like this can occur, for example, during the service life of a bridge deck slab when as a result of damage to its deck seal, its concrete becomes fully saturated with moisture.
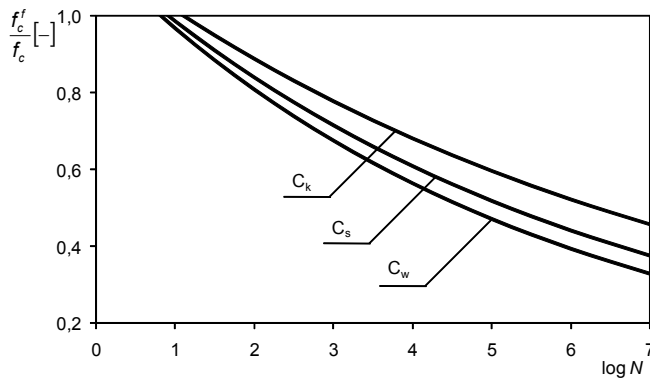
Fig. 8. Calculated fatigue strength versus load cycles at $\rho^f = 0$
and $f = 1$ Hz for series C_w, C_k, C_s concretes

6. Conclusions

It has emerged from the investigations of several self-compacting concretes damp to different degree that moisture significantly affects their failure. This is evidenced by the levels of cracking initiating stress σ_i and critical stress σ_{cr}, delimiting the stages in the failure process. Depending on how damp self-compacting concrete is, the levels of cracking initiating stress and critical stress are in a range of 0.245–0.380 σ_c/f_c and 0.855–0.940 σ_c/f_c, respectively.

Using as the reference, concretes cured in a climatic chamber (for which the level of cracking initiating stress is in a range of 0.305–0.380 σ_c/f_c) one can observe that as the moisture content in concrete increases, the average value of stress σ_{im} decreases and when the concrete is fully saturated with moisture, it is in a range of 0.245–0.265 σ_c/f_c. A similar dependence is observed when moisture content is reduced from the maximum sorption moisture content to dry condition. Concretes being in the latter condition show the level of stress σ_{im} in a range of 0.285–0.300 σ_c/f_c.

As regards the level of critical stress, it was found that moisture content had little effect on it. The effect is much smaller than in the reference ordinary concrete.

It appears from the calculation analyses that the investigated concretes markedly differ in their fatigue strength calculated on the basis of the experimentally determined average values of cracking initiating stress σ_{im} and critical stress σ_{crm}. The fatigue strength of the concretes cured in the climatic chamber is higher than that of the dry concretes and the ones fully saturated with water. This means that very damp struc-

tural elements made from self-compacting concrete when subjected to the repeated dynamic loads may undergo failure after a smaller number of cycles than the same elements whose concrete is less damp or is dry.

References

[1] Beres L.: *Fracture of concrete subjected to cyclic and sustained loading*, ACI Journal, Vol. 69, No. 4, 1971, pp. 304–305.
[2] Bień J., Krzyżanowski J., Rawa P., Zwolski J.: *Dynamic load tests in bridge management*, Archives of Civil and Mechanical Engineering, Vol. 4, No. 2, 2004, pp. 63–78.
[3] Bień J.: *Defects and diagnostics of bridge structures* (in Polish), Wydawnictwa Komunikacji i Łączności, Warszawa, 2010.
[4] Flaga K.: *Effect of internal stresses on the failure and strength parameters of concrete* (in Polish), Inżynieria i Budownictwo, No. 6, 1995, pp. 315–322.
[5] Furtak K.: *Load capacity of normal cross-section of bent reinforced concrete elements subjected to changing loads, as applied particularly to bridges* (in Polish), Scientific Papers of Cracow Polytechnic, No. 4, 1985.
[6] Furtak K.: *Stress failure of concrete* (in Polish), Conference: Days of Concrete – Tradition and Modernity, Szczyrk, 2002, pp. 427–439.
[7] Gorzelańczyk T., Hoła J.: *The use of acoustic emission to assess the influence of dampness on the course of failure of self-compacting concrete*, Defektoskopie, 36th International Conference Exhibition. Proceedings. Tabor, Czech Republic, 2006, pp. 67–73.
[8] Gorzelańczyk T.: *Assessment of the failure of self-compacting concretes by means of acoustic methods* (in Polish), PhD dissertation. Reports of the Institute of Building Engineering at Wrocław University of Technology, Wrocław, Ser. PRE, No. 9, 2007.
[9] Hoła J., Pyszniak J.: *Application of acoustic methods to assessment of concrete humidity influence on the process of concrete destruction*, Archives of Acoustic, Vol. 16, No. 2, 1991, pp. 343–353.
[10] Hoła J.: *Relation of initiating and critical stress to stress failure* (in Polish), Scientific Papers of the Institute of Building Engineering of the Wrocław University of Technology, No. 76, Monographs No. 33, Wrocław University of Technology Publishing House, Wrocław, 2000.
[11] Hoła J.: *Effects of technological and service factors on initiating and critical stress levels and on fatigue strength in compressed concrete in the light of hitherto investigations* (in Polish), Cement-Wapno-Beton, Vol. VI/LXVII, No. 2, 2001, pp. 49–52.
[12] Hoła J.: *Experimentally determined effects of technological and service factors on stress-induced destruction of concrete under compression*, Engineering Transactions, Vol. 50, No. 4, 2002, pp. 251–265.
[13] HSU T.C.T.: *Fatigue of plain concrete*, ACI Journal, Vol. 79, No. 7–8, 1981, pp. 295–305.
[14] Kaszyńska M.: *Self-consolidating concrete for repair of bridges*, 6th International bridge engineering conference: reliability, security, and sustainability in bridge engineering [CD-ROM], Washington: Transportation Research Board, (Journal of the Transportation Research Board CD 11-S), 2005, pp. 429–434.
[15] Klug Y., Holschemacher K.: *Comparison of the hardened properties of self compacting and normal vibrated concrete*, Proceeding PRO33 – 3rd International RILEM Symposium: Self-Compacting Concrete. RILEM Publications S.A.R.L., 2003, pp. 596–605.

[16] Holschemacher K.: *Hardened properties of self-compacting concrete*, Modern building materials, structures and techniques. Proceedings of the 8th International Conference, Vilnius, Selected Papers, 2004, pp. 55–60.

[17] Li L., Hwang C.: *The mixture proportion and property of SCC*, Proceeding PRO33 – 3rd International RILEM Symposium: Self-Compacting Concrete. RILEM Publications S.A.R.L., 2003, pp. 525–529.

[18] Mačiulaitis R., Vaičienė M., Žurauskienė R.: *The effect of concrete composition and aggregates properties on performance of concrete*, Journal of Civil Engineering and Management, Vol. 15, No. 3, 2009, pp. 317–324.

[19] Newman K., Newman I.B.: *Failure theories and design criteria for plain concrete*, Proceedings of the Civil Engineering Materials Conference, Southampton, ed. by M.Te'eni, London, Wiley-Interscience, Part 2, 1969, pp. 963–996.

[20] Ngab A.S., Slate F.O., Nilson A.H.: *Microcracking and time-dependent strain in high-strength concrete*, ACI Journal, Vol. 78, No. 4, 1981, pp. 262–268.

[21] Nagamoto N., Ozawa K.: *Mixture properties of self-compacting, high-performance concrete*, ACI Materials Journal, Vol. 172, 1999, pp. 623–636.

[22] Okamura H., Ouchi M.: SCC. *Development, present use and future*, 1st It. RILEM Symp. on SCC, Stockholm, ed. RILEM Publ. S.A.R.L., pp. 13–14.

[23] Okamura H., Ouchi M.: *Self-compacting concrete*, Journal of Advanced Concrete Technology, Japan Concrete Institute, Vol. 1, No. 1, 2003, pp. 5–15.

[24] Okamura H., Maekawa K., Mishima T.: *Performance based design for self-compacting structural high-strength concrete*, ACI Materials Journal, Vol. 228, 2005, pp. 13–34.

[25] Paczkowski P., Kaszyńska M., Nowak A.S., Lutomirski T.: *Self-consolidating concrete for on-site bridge applications*, Fifth international conference on current and future trends in Bridge design, construction and maintenance: proceedings of the two day international conference ed. Robert Lark London: Thomas Telford Publishing, 2007, pp. 312–320.

[26] Ranachowski Z.: *Application of acoustic emission method to determine the limit of proportionality and static strength in concrete*, Brittle Matrix Composites 3, eds. A.M. Brandt, L.H. Marshall, Elsevier Applied Science Publishers, London, 1991, pp. 234–239.

[27] Raue E., Timmler H.-G., Garke R.: *On the physically non-linear analysis of cyclic loaded reinforced concrete cross-sections with mathematical optimisation*, Journal of Civil Engineering and Management, Vol. 15, No. 2, 2009, pp. 189–195.

[28] Szwabowski J., Łaźniewska-Piekarczyk B.: *Air-entrainment problem in self-compacting concrete*, Journal of Civil Engineering and Management, Vol. 15, No. 2, 2009, pp. 137–147.

[29] The European Guidelines for Self-Compacting Concrete. Specification, Production and Use. EFNARC The European Federation of Specialist Construction Chemicals and Concrete Systems, May 2005, Available from internet: http://www.efnarc.org/pdf/ SCCGuidelinesMay2005.pdf

Wpływ wilgotności na proces niszczenia ściskanego betonu samozagęszczonego

W pracy przedstawiono wyniki badań procesu niszczenia czterech ściskanych betonów samozagęszczonych znajdujących się w chwili badania w różnym stopniu zawilgocenia. Proces

niszczenia betonów zbadano metodami akustycznymi. Określono rozgraniczające ten proces wartości poziomów naprężeń inicjujących pękanie σ_i i krytycznych σ_{cr}. Wykazano istnienie zależności między wilgotnością betonu, a wartościami tych poziomów. Wykorzystując uzyskane rezultaty badań obliczono wytrzymałość zmęczeniową badanych betonów samozagęszczonych i na tej podstawie sformułowano wniosek odnośnie do przydatności tych betonów do wznoszenia konstrukcji poddanych obciążeniom wielokrotnie zmiennym.

On the tolerance modelling of thermoelasticity problems for transversally graded laminates

J. JĘDRYSIAK

Department of Structural Mechanics, Technical University of Łódź,
al. Politechniki 6, 90-924 Łódź, Poland.

The object of considerations is a multilayered composite, made of two components non-periodically distributed as microlaminas along one direction. Macroscopic properties of this composite are assumed to be continuously varied across laminas. The aim of this note is to propose two models of thermoelasticity problems: *the tolerance model*, taking into account the effect of the microstructure size on the overall behaviour of these composites, and *the asymptotic model*, neglecting this effect. The governing equations of both the models are derived by using averaging procedures presented in the book edited by Cz. Woźniak et al. [1], i.e. the tolerance modelling and the consistent asymptotic modelling.

Keywords: *thermoelasticity, functionally graded composites, tolerance modelling, asymptotic modelling*

1. Introduction

In this contribution we consider a multilayered composite. This composite is made of two components, non-periodically distributed in the form of microlaminas along one direction. However, it is assumed that macroscopic properties of this laminate vary continuously along this direction. Hence, this composite can be treated as made of *a functionally graded material*, cf. Suresh and Mortensen [2]. Figure 1 shows a fragment of the composite: in Figure 1a – on a micro-level, in Figure 1b – on a macro-level. Media of this kind can be called *transversally graded laminates* (*TGL* or *TG*-type laminates).

Although representative elements of such laminates cannot be usually defined, various approaches, similar those used for periodic laminates, are applied to analyse the overall behaviour of these media. Some averaged methods used to describe FGM-type composites are discussed in the book [2] and in the paper by Reiter, Dvorak and Tvergaard [3]. Between these modelling techniques it can be mentioned those based on *the asymptotic homogenization*, cf. the monographs by Bensoussan, Lions and Papanicolau [4], Jikov, Kozlov and Oleinik [5]. Various thermoelastic problems of periodic laminates are also investigated using *models with microlocal parameters*, cf. Matysiak [6]. The most of the known approaches leads to model equations without *the effect of the microstructure size*.

Some theoretical and numerical results of thermomechanical problems for functionally graded structures can be found in an extensive list of papers. It can be mentioned

some of them, e.g.: a Green's function approach is used for heat conduction by Kim and Noda [7]; the Laplace transformation is applied to obtain some analytical solutions to thermoelastic problems for a hollow cylinder by Ootao and Tanigawa [8]. *The higher-order theory* is proposed by Aboudi, Pindera and Arnold [9] and reformulated by Bansal and Pindera [10] as an alternative modelling method for functionally graded materials.
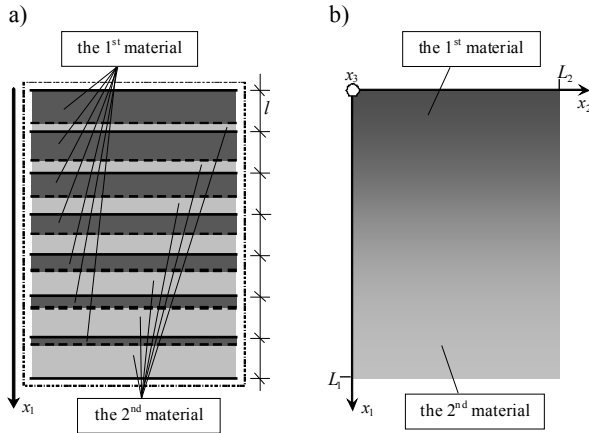
Fig. 1. A cross section of a transversally graded laminate:
a) the microscopic point of view, b) the macroscopic point of view

In order to obtain averaged governing equations, describing the effect of the micro-structure size, the tolerance averaging technique can be applied. This approach was proposed for periodic composites in the book by Cz. Woźniak and Wierzbicki [11]. Then, this modelling procedure was used to derive equations of special problems for various periodic structures in a series of papers. The extensive list of references can be found in the books: [1] and edited by Cz. Woźniak, Michalak and Jędrysiak [12]. In the last decade this technique was also adopted to the modelling of various problems for FGM-type composites and structures. We can mention some of them, e.g. elasto-dynamics problems analysed by Rychlewska and Cz. Woźniak [13] or Szymczyk and Cz. Woźniak [14]; heat conduction for transversally graded laminates investigated by Jędrysiak and Radzikowska [15–16] or for longitudinally graded composites by Michalak and M. Woźniak [17], Michalak, Cz. Woźniak and M. Woźniak [18]. The tolerance averaging technique leads from equations with functional, highly-oscillating, tolerance-periodic and non-continuous coefficients to a system of differential equations with slowly-varying coefficients. The obtained model equations describe the effect of the microstructure size on the overall behaviour of the FGM-type medium. The main idea of the tolerance modelling and various applications of this approach can be found in the books [1, 12].

The main aim of this note is to derive equations of two models of thermoelasticity problems for transversally graded laminates (TGL). One of them is *the tolerance*

model, which describes the effect of the microstructure size. Moreover, as its certain approximation *the asymptotic model* will be proposed which neglects this effect. Both the models are based on concepts of the tolerance modelling or the consistent asymptotic modelling, presented in the book edited by Cz. Woźniak et al. [1].

2. Modelling foundations

Let subscripts $i, j, \ldots$, related to the coordinate system $Ox_1x_2x_3$, run over 1, 2, 3; and subscripts $\alpha, \beta, \ldots$, (related to Ox_2x_3) run over 2, 3. Denote: $\mathbf{x} \equiv (x_2, x_3)$, $x \equiv x_1$; t as the time coordinate. Let derivatives respected to x_i, x_α, x be denoted by $\partial_i, \partial_\alpha, \partial$, respectively. Let H be the laminate length along the x-axis, and L_α be length dimensions along the x_α-axes ($\alpha = 2, 3$). Denoting by $\Omega \equiv (0, H)$, $\Xi \equiv (0, L_2) \times (0, L_3)$, the composite under consideration occupies the region $\Omega \times \Xi$ in the physical space. This laminate is made of two components distributed in m laminas with the same thickness l ($H = ml$). It is assumed that condition $l << H$ is satisfied. Hence, thickness l can be called *the microstructure parameter*. The "basic cell" in the interval Ω can be denoted by $\Omega \equiv (-l/2, l/2)$. Every n-th lamina consists of two homogeneous sub-laminas with thicknesses l'_n, l''_n, which depend on the argument x, cf. Figure 1a. The sub-laminas have properties described by: specific heats c', c'', heat conduction tensors with components k'_{ij}, k''_{ij}, mass densities ρ', ρ'', elasticity tensors with components c'_{ijkl}, c''_{ijkl} and thermoelasticity tensors b'_{ij}, b''_{ij}; where $i, j, k, l = 1, 2, 3$.

Let $v'_n \equiv l'_n / l, v''_n \equiv l''_n / l$ be material volume fractions in the nth lamina. We assume that sequence $\{v'_n\}$, $n = 1, \ldots, m$, is monotone and satisfies condition $|v'_{n+1} - v'_n| << 1$, for $n = 1, \ldots, m$-1. Sequence $\{v''_n\}$ satisfies similar conditions since $v'_n + v''_n = 1$. It can be shown that sequences $\{v'_n\}$, $\{v''_n\}$, $n = 1, \ldots, m$, can be approximated by continuous functions $v'(\cdot), v''(\cdot)$.

These functions describe the gradation of material properties along the x-axis and can be called *the fraction ratios of materials*. Let function $v(\cdot)$, defined by formula $v(\cdot) \equiv [v'(\cdot) v''(\cdot)]^{\frac{1}{2}}$, be *the non-homogeneity ratio*. The above functions of fraction ratios are assumed to be slowly-varying (cf. the book [12]).

Let us denote the unknown displacements along the x_i-axis by u_i ($i = 1, 2, 3$) and the temperature field by Θ. We assume that thermoelasticity problems for the TG-type laminate are described by the known equations:

$$\partial_j (c_{ijkl} \partial_l u_k) - \rho \ddot{u}_i = \partial_j (b_{ij} \Theta),$$
$$\partial_j (k_{ij} \partial_i \Theta) - c\dot{\Theta} = T_0 b_{ij} \partial_j \dot{u}_i, \tag{1}$$

where T_0 is a constant with a temperature dimension.

It has to be emphasised that for these laminates all coefficients of Equations (1), i.e. $k_{ij} = k_{ij}(x)$, $c = c(x)$, $c_{ijkl} = c_{ijkl}(x)$, $b_i = b_{ij}(x)$, $\rho = \rho(x)$ are highly-oscillating, tolerance-periodic, non-continuous functions in x. Hence, Equations (1) cannot be a good tool to analyse thermoelasticity problems. We will replace these equations by differential equations with smooth, slowly-varying functional coefficients by using *the tolerance modelling*, cf. the book edited by Cz. Woźniak et al. [1].

3. Introductory concepts

Following the books [1, 12] some basic concepts of the tolerance modelling, e.g. an averaging operator, a tolerance-periodic function, a slowly-varying function, a highly oscillating function, are reminded below.

The averaging operator for an arbitrary integrable function f in $\overline{\Omega}$ (which can also depend on x_2 and t), is defined by

$$< f > (x) = l^{-1} \int_{x-l/2}^{x+l/2} f(y)dy, \quad x \in [l/2, H - l/2]. \tag{2}$$

Following the above books it can be shown that for tolerance periodic function f of x, its averaged value calculated from (2) is a slowly-varying function in x.

Denote by $\partial^k f$ the k-th gradient of function $f = f(x)$, $x \in \Omega$, $k = 0, 1$, $\partial^0 f \equiv f$; and by $\widetilde{f}^{(k)}(\cdot, \cdot)$ a function defined in $\overline{\Omega} \times R^m$.

Function $f \in H^\alpha(\Omega)$ is *the tolerance-periodic function* (with respect to cell Ω and tolerance parameter δ), $f \in TP_\delta^\alpha(\Omega, \Omega)$, if for $k = 0, 1$ the following conditions hold

    a) $(\forall x \in \Omega)(\exists \widetilde{f}^{(k)}(x, \cdot) \in H^0(\Omega)$ $[\| \partial^k f\big|_{\Omega_x}(\cdot) - \widetilde{f}^{(k)}(x, \cdot)\|_{H^0(\Omega_x)} \leq \delta]$,

    b) $\int_{\Omega(\cdot)} \widetilde{f}^{(k)}(\cdot, y)dy \in C^0(\overline{\Omega})$.

Function $\widetilde{f}^{(k)}(x, \cdot)$ is *the periodic approximation of $\partial^k f$ in $\Omega(x) = x + \Omega$*, $x \in \Omega$, $k = 0, 1$.

Function $F \in H^\alpha(\Omega)$ is *the slowly-varying function* (with respect to the cell Ω and tolerance parameter δ), $F \in SV_\delta^\alpha(\Omega, \Omega)$, if

    a) $F \in TP_\delta^\alpha(\Omega, \Omega)$,

    b) $(\forall x \in \Omega)[\widetilde{F}^{(k)}(x, \cdot)\big|_{\Omega(x)} = \partial^k F(x), k = 0, 1]$.

Thus, periodic approximation $\widetilde{F}^{(k)}$ of $\partial^k F$ in $\Omega(x)$ is a constant function for every $x \in \Omega$.

Function $\phi \in H^\alpha(\Omega)$ is *the highly oscillating function* (with respect to the cell Ω and tolerance parameter δ), $\phi \in HO_\delta^\alpha(\Omega, \Omega)$, if

    a) $\phi \in TP_\delta^\alpha(\Omega, \Omega)$,

    b) $(\forall x \in \Omega)[\widetilde{\phi}^{(k)}(x, \cdot)\big|_{\Omega(x)} = \partial^k \widetilde{\phi}(x), k = 0, 1]$.

Function $f \equiv \phi F \in TP_\delta^\alpha (\Omega, \Omega)$, for every $F \in SV_\delta^\alpha (\Omega, \Omega)$, satisfies the condition

c) $\widetilde{f}^{(1)}(x, \cdot)\big|_{\Omega(x)} = F(x) \partial^1 \widetilde{\phi}(x)\big|_{\Omega(x)}$.

If $\alpha = 0$ then we denote $\widetilde{f} \equiv \widetilde{f}^{(0)}$.

Let us denote by $h(\cdot)$ and $g(\cdot)$ highly oscillating, continuous functions, $h, g \in HO_\delta^1 (\Omega, \Omega)$, defined on $\overline{\Omega}$, which have piecewise continuous and bounded gradients $\partial^1 h, \partial^1 g$. Functions $h(\cdot), g(\cdot)$ are *the fluctuation shape functions* of the 1st kind, if they satisfy conditions:

a) $\partial^k h \in O(l^{\alpha-k}), \partial^k g \in O(l^{\alpha-k})$ for $k = 0, 1, \alpha = 1, \partial^0 h \equiv h, \partial^0 g \equiv g$,

b) $<h>(x) \approx 0, <g>(x) \approx 0$ for every $x \in \Omega$;

and depend on l as a parameter. Set of all fluctuation shape functions of the 1st kind is denoted by $FS_\delta^1 (\Omega, \Omega)$. Condition b) can be replaced by $<\rho h>(x) \approx 0$ and $<cg>(x) \approx 0$ for every $x \in \Omega$, and certain tolerance-periodic functions ρ, c such as $\rho > 0, c > 0$.

4. Tolerance modelling

4.1. Fundamental assumptions

Following the books [1, 12] the modelling assumptions will be introduced.
The micro-macro decomposition is the first assumption, where we assume
a) for the displacements:

$$u_i(x, \mathbf{x}, t) = w_i(x, \mathbf{x}, t) + h(x) v_i(x, \mathbf{x}, t), \tag{3}$$

b) for the temperature:

$$\Theta(x, \mathbf{x}, t) = \vartheta(x, \mathbf{x}, t) + g(x) \psi(x, \mathbf{x}, t), \tag{4}$$

and $w_i(\cdot, \mathbf{x}, t), v_i(\cdot, \mathbf{x}, t), \vartheta(\cdot, \mathbf{x}, t), \psi(\cdot, \mathbf{x}, t) \in SV_\delta^1(\Omega, \Omega)$ for every t; $h(\cdot), g(\cdot) \in FS_\delta^1(\Omega, \Omega)$. Functions $w_i(\cdot, \mathbf{x}, t)$ and $\vartheta(\cdot, \mathbf{x}, t)$ are the basic unknowns, called *the macrodisplacements* and *the macrotemperature*, respectively; $v_i(\cdot, \mathbf{x}, t)$ and $\psi(\cdot, \mathbf{x}, t)$ are additional basic unknowns, called *the fluctuation amplitudes of displacements* and *the fluctuation amplitudes of temperature*, respectively; $h(\cdot)$ and $g(\cdot)$ are the known fluctuation shape functions.

Following the book edited by Cz. Woźniak, Michalak and Jędrysiak [12] *the fluctuation shape functions* $h(x), g(x), x \in \overline{\Omega}$, are assumed to be continuous, linear across every sub-lamina thickness and of an order $O(l)$, and to satisfy the pertinent conditions *a)-b)*, i.e. they can be given in the following form:

$$h(x), g(x) = \begin{cases} -l\sqrt{3}\,\dfrac{v(\overline{x})}{v''(\overline{x})}[2\dfrac{x}{l}+v'(\overline{x})] \text{ for } x \in (-l/2, -l/2 + lv''(\overline{x})), \\ l\sqrt{3}\,\dfrac{v(\overline{x})}{v'(\overline{x})}[2\dfrac{x}{l}-v''(\overline{x})] \text{ for } x \in (l/2 - lv'(\overline{x}), l/2), \end{cases} \tag{5}$$

where $\overline{x}$ is a centre of $\Omega = (-l/2, l/2)$. Because the non-homogeneity ratio $v(\cdot)$ is a slowly-varying function the mean values of h and g in every lamina are equal to zero.

The next modelling assumption is *the tolerance averaging approximation*, in which we assume that in the modelling terms $O(\delta)$ are negligibly small, e.g. in formulas:

$$< f > (x) = < \overline{f} > (x) + O(\delta), \quad < fF > (x) = < f > (x)F(x) + O(\delta)$$
$$< f\partial(hF) > (x) = < f\partial h > (x)F(x) + O(\delta),$$
$$x \in \Omega; \ 0 < \delta << 1; \quad f \in TP_\delta^1(\Omega,,), \ F \in SV_\delta^1(\Omega,,), \ h \in FS_\delta^1(\Omega,,).$$

4.2. Modelling procedure

Following the book edited by Cz. Woźniak et al. [1], the modelling procedure is outlined. The starting point is the formulation of *the extended action functional*:

$$A(u_i(\cdot), \Theta(\cdot), p_i(\cdot), f(\cdot)) =$$
$$= \iint\limits_{\Omega\,\Xi} \int_{t_0}^{t_1} \Lambda(z, \partial_j u_i(z,\xi,t), u_i(z,\xi,t), \partial_i \Theta(z,\xi,t), \Theta(z,\xi,t), p_i(z,\xi,t), f(z,\xi,t))\,dt\,d\xi\,dz, \tag{6}$$

where $\Lambda(\cdot, \partial_j u_i, u_i, \partial_i \Theta, \Theta, p_i, f) \in HO_\delta^0(\Omega, \Omega)$, $p_i(\cdot, \xi, t), f(\cdot, \xi, t) \in HO_\delta^0(\Omega, \Omega)$. The Lagrangian Λ is given by the formula

$$\Lambda = \frac{1}{2}(\rho \dot{u}_i \dot{u}_j \delta_{ij} - c_{ijkl}\partial_j u_i \partial_l u_k + k_{ij}\partial_i \Theta \partial_j \Theta) + p_i u_i + f\Theta, \tag{7}$$

and the constitutive equations determine p_i and f:

$$p_i = \partial_j(b_{ij}\Theta), \quad f = c\dot{\Theta} + T_0 b_{ij}\partial_j \dot{u}_i. \tag{8}$$

For Lagrangian (7) we can write the Euler-Lagrange equations

$$\frac{\partial}{\partial t}\frac{\partial \Lambda}{\partial \dot{u}_i} + \partial_j \frac{\partial \Lambda}{\partial \partial_j u_i} - \frac{\partial \Lambda}{\partial u_i} = 0, \quad \partial_j \frac{\partial \Lambda}{\partial \partial_j \Theta} - \frac{\partial \Lambda}{\partial \Theta} = 0. \tag{9}$$

Using *the extended principle of stationary action* (cf. Part I of the book edited by Cz. Woźniak et al. [1]) from Equations (9) combined with Equations (7) and (8) we obtain the fundamental equations of thermoelasticity problems (1). Then, we apply the

tolerance modelling to action functional (6). Substituting micro-macro decompositions (3) and (4) to formula (6) and using averaging operator (2) to this action functional, we arrive at the tolerance averaging of functional $A(u_i(\cdot), \Theta(\cdot), p_i(\cdot), f(\cdot))$:

$$
\begin{aligned}
A_{hg}(w_i, v_i, \vartheta, \psi, p_i, f) &= \\
&= \iint_{\Omega \Xi} \int_{t_0}^{t_1} < \Lambda_{hg} > (x, \partial_j w_i, w_i, \partial_\alpha v_i, v_i, \partial_i \vartheta, \vartheta, \partial_\alpha \psi, \psi, p_i, f) \, dt \, d\xi \, dx,
\end{aligned}
\tag{10}
$$

where the averaged form $<\Lambda_{hg}>$ of Lagrangian (7) can be written as

$$
\begin{aligned}
< \Lambda_{hg} > =& \frac{1}{2} < k_{ij} > \partial_i \vartheta \partial_j \vartheta + \frac{1}{2} < k_{i1} \partial g > \partial_i \vartheta \psi + \frac{1}{2} < k_{1j} \partial g > \partial_j \vartheta \psi + \\
&+ \frac{1}{2} \underline{< k_{\alpha\beta} g g >} \partial_\alpha \psi \partial_\beta \psi + \frac{1}{2} \underline{< k_{11} \partial g \partial g >} \psi \psi + \\
&+ \frac{1}{2} < \rho > \dot{w}_i \dot{w}_j \delta_{ij} + \frac{1}{2} \underline{< \rho h h >} \dot{v}_i \dot{v}_j \delta_{ij} - \frac{1}{2} < c_{ijkl} > \partial_j w_i \partial_l w_k - \\
&- \frac{1}{2} < c_{ijk1} \partial h > \partial_j w_i v_k - \frac{1}{2} < c_{i1kl} \partial h > v_i \partial_l w_k - \\
&- \frac{1}{2} < c_{i1k1} \partial h \partial h > v_i v_k - \frac{1}{2} \underline{< c_{i\alpha k\beta} h h >} \partial_\alpha v_i \partial_\beta v_k + \\
&+ < p_i > w_i + \underline{< p_i h >} v_i + < f > \vartheta + \underline{< f g >} \psi
\end{aligned}
\tag{11}
$$

and $< p_i >, < p_i h >, < f >, < f g >$ are defined by the constitutive equations:

$$
\begin{aligned}
< f > &= < c > \dot{\vartheta} + < T_0 b_{ij} > \partial_j \dot{w}_i + < T_0 b_{i1} \partial h > \dot{v}_i, \\
< f g > &= \underline{< c g g >} \dot{\psi} + \underline{< T_0 b_{i\beta} h g >} \partial_\beta \dot{v}_i, \\
< p_i > &= \partial < b_{ij} > \vartheta + < b_{ij} > \partial_j \vartheta, \\
< p_i h > &= - < b_{i1} \partial g > \vartheta + \underline{< b_{i\beta} g h >} \partial_\beta \psi.
\end{aligned}
\tag{12}
$$

Underlined terms in formulas (11) and (12) depend on the microstructure parameter l. Using the extended principle of stationary action to A_{hg} the following system of equations is derived:

$$
\begin{aligned}
\frac{\partial}{\partial t} \frac{\partial < \Lambda_{hg} >}{\partial \dot{w}_i} + \partial_j \frac{\partial < \Lambda_{hg} >}{\partial \partial_j w_i} - \frac{\partial < \Lambda_{hg} >}{\partial w_i} &= 0, \\
\frac{\partial}{\partial t} \frac{\partial < \Lambda_{hg} >}{\partial \dot{v}_i} + \partial_\alpha \frac{\partial < \Lambda_{hg} >}{\partial \partial_\alpha v_i} - \frac{\partial < \Lambda_{hg} >}{\partial v_i} &= 0,
\end{aligned}
\tag{13}
$$

$$\partial_j \frac{\partial < \Lambda_{hg} >}{\partial \partial_j \vartheta} - \frac{\partial < \Lambda_{hg} >}{\partial \vartheta} = 0,$$

$$\partial_\alpha \frac{\partial < \Lambda_{hg} >}{\partial \partial_\alpha \psi} - \frac{\partial < \Lambda_{hg} >}{\partial \psi} = 0,$$

(13)

with slowly-varying coefficients.

5. Asymptotic modelling

5.1. Preliminaries

Foundations and the modelling procedure of the asymptotic averaging are presented following the book edited by Cz. Woźniak et al. [1]. Here, as *the asymptotic modelling* it is meant that approach which is called there as *the consistent asymptotic modelling*.

In this technique the concept of highly oscillating function is only used, cf. Section 3. We recall that for the function $f(\cdot) \in HO_\delta^0(\Omega, \Omega)$ there exists its periodic approximation $\widetilde{f}(x, y)$, $y \in \Omega(x)$, $x \in \overline{\Omega}$.

Using an asymptotic approach let us introduce parameter $\varepsilon = 1/n$, $n = 1, 2, ...$ Let us define a scaled cell as $\Omega_\varepsilon \equiv (-\varepsilon l / 2, \varepsilon l / 2)$, and a scaled cell with a centre at $x \in \overline{\Omega}$ as $\Omega_\varepsilon(x) \equiv x + \Omega_\varepsilon$. For function $\widetilde{f}(x, \cdot) \in H^1(\Omega)$ $(\forall x \in \overline{\Omega})$ let $_\varepsilon(x, \cdot) \in H^1(\Omega_\varepsilon)$ $\widetilde{f} \subset H^1(\Omega)$ be a family of functions defined by $\widetilde{f}_\varepsilon(x, y) \equiv \widetilde{f}(x, y/\varepsilon)$, $y \in \Omega_\varepsilon(x)$, $x \in \overline{\Omega}$.

Let us introduce independent highly oscillating functions, $h(\cdot)$ and $g(\cdot)$, $h(\cdot), g(\cdot) \in HO_\delta^1(\Omega, \Omega)$, with their periodic approximations $\widetilde{h}(x, \cdot)$ and $\widetilde{g}(x, \cdot)$, for every $x \in \overline{\Omega}$. Let $\widetilde{h}_\varepsilon(x, \cdot), \widetilde{g}_\varepsilon(x, \cdot)$ be functions given by $\widetilde{h}_\varepsilon(x, y) \equiv \widetilde{h}(x, y/\varepsilon)$ $\widetilde{g}_\varepsilon(x, y) \equiv \widetilde{g}(x, y/\varepsilon)$, $y \in \Omega_\varepsilon(x)$.

The fundamental assumption of the asymptotic procedure is that family of fields are introduced:

a) for the displacements:

$$u_{i\varepsilon}(x, y, \mathbf{x}, t) = w_i(y, \mathbf{x}, t) + \varepsilon \widetilde{h}_\varepsilon(x, y) v_i(y, \mathbf{x}, t),$$

(14)

b) for the temperature:

$$\Theta_\varepsilon(x, y, \mathbf{x}, t) = \vartheta(y, \mathbf{x}, t) + \varepsilon \widetilde{g}_\varepsilon(x, y) \psi(y, \mathbf{x}, t),$$

(15)

where $y \in \Omega_\varepsilon(x), \mathbf{x} \in \Xi$ and functions $w_i, v_i, \vartheta, \psi$ are continuously bounded in $\overline{\Omega}$ together with their first derivatives. Formulas (14) and (15) will be called *the consis-*

tent asymptotic decomposition of the displacements u_i $(x, y, \mathbf{x}, t)$ and the temperature Θ $(x, y, \mathbf{x}, t)$, $y \in \Omega(x)$, $\mathbf{x} \in \Xi$ (cf. [1]).

Introduce denotations:

$$\overline{\partial \widetilde{h}_\varepsilon}(x, y) \equiv \varepsilon^{-1} \partial \widetilde{h}(x, \overline{y})|_{\overline{y} = y/\varepsilon}, \quad \overline{\partial \widetilde{g}_\varepsilon}(x, y) \equiv \varepsilon^{-1} \partial \widetilde{g}(x, \overline{y})|_{\overline{y} = y/\varepsilon}.$$

Hence, we can write:

$$\partial u_{i\varepsilon}(x, y, \mathbf{x}, t) = \partial w_i(y, \mathbf{x}, t) + \overline{\partial \widetilde{h}_\varepsilon}(x, y) v_i(y, \mathbf{x}, t) + \varepsilon \widetilde{h}_\varepsilon(x, y) \partial v_i(y, \mathbf{x}, t),$$

$$\partial_\alpha u_{i\varepsilon}(x, y, \mathbf{x}, t) = \partial_\alpha w_i(y, \mathbf{x}, t) + \varepsilon \widetilde{h}_\varepsilon(x, y) \partial_\alpha v_i(y, \mathbf{x}, t),$$

$$\partial \Theta(x, y, \mathbf{x}, t) = \partial \vartheta(y, \mathbf{x}, t) + \overline{\partial} \, \widetilde{g}_\varepsilon(x, y) \psi(y, \mathbf{x}, t) + \varepsilon \widetilde{g}_\varepsilon(x, y) \partial \psi(y, \mathbf{x}, t),$$ (16)

$$\partial_\alpha \Theta(x, y, \mathbf{x}, t) = \partial_\alpha \vartheta(y, \mathbf{x}, t) + \varepsilon \widetilde{g}_\varepsilon(x, y) \partial_\alpha \psi(y, \mathbf{x}, t),$$

where $y \in \Omega_\varepsilon(x)$; for an arbitrary but fixed $x \in \overline{\Omega}$.

Denoting $\phi(\cdot) \equiv (w_i(\cdot), \vartheta(\cdot))$, $\varphi(\cdot) \equiv (v_i(\cdot), \psi(\cdot))$, $i = 1, 2, 3$, and taking into account $\varepsilon \to 0$, since $y \in \Omega_\varepsilon(x)$, $x \in \overline{\Omega}$, we arrive at (cf. the book [1])

$$\phi(y, \mathbf{x}, t) = \phi(x, \mathbf{x}, t) + O(\varepsilon), \quad \partial_j \phi(y, \mathbf{x}, t) = \partial_j \phi(x, \mathbf{x}, t) + O(\varepsilon),$$

$$\varphi(y, \mathbf{x}, t) = \varphi(x, \mathbf{x}, t) + O(\varepsilon), \quad \partial_\alpha \varphi(y, \mathbf{x}, t) = \partial_\alpha \varphi(x, \mathbf{x}, t) + O(\varepsilon),$$

where $j = 1, 2, 3$, $\alpha = 1, 2$. Hence, Equations (14), (15) and (16) take the form:

$$u_{i\varepsilon}(x, y, \mathbf{x}, t) = w_i(x, \mathbf{x}, t) + O(\varepsilon),$$

$$\Theta_\varepsilon(x, y, \mathbf{x}, t) = \vartheta(x, \mathbf{x}, t) + O(\varepsilon),$$

$$\partial u_{i\varepsilon}(x, y, \mathbf{x}, t) = \partial w_i(x, \mathbf{x}, t) + \overline{\partial \widetilde{h}_\varepsilon}(x, y) v_i(x, \mathbf{x}, t) + O(\varepsilon),$$

$$\partial_\alpha u_{i\varepsilon}(x, y, \mathbf{x}, t) = \partial_\alpha w_i(x, \mathbf{x}, t) + O(\varepsilon),$$ (17)

$$\partial \Theta(x, y, \mathbf{x}, t) = \partial \vartheta(x, \mathbf{x}, t) + \overline{\partial \widetilde{g}_\varepsilon}(x, y) \psi(x, \mathbf{x}, t) + O(\varepsilon),$$

$$\partial_\alpha \Theta(x, y, \mathbf{x}, t) = \partial_\alpha \vartheta(x, \mathbf{x}, t) + O(\varepsilon).$$

Using a limit passage $\varepsilon \to 0$ terms $O(\varepsilon)$ in the above formulas are neglected.

5.2. Modelling procedure

We start with the extended action functional in the form (6) with Lagrangian $\Lambda(\cdot, \partial_j u_i, u_i, \partial_i \Theta, \Theta, p_i, f) \in HO_\delta^0(\Omega, \Omega)$, described by formula (7) and parameters $p_i(\cdot, \boldsymbol{\xi}, t)$, $f(\cdot, \boldsymbol{\xi}, t) \in HO_\delta^0(\Omega, \Omega)$, determined by (8). Since Lagrangian Λ is highly

oscillating in Ω there exists Lagrangian $\widetilde{\Lambda}(x,\cdot,\partial_j w_i, w_i, v_i, \partial_i \vartheta, \vartheta, \psi, p_i, f)$ for every $x \in \overline{\Omega}$, being a periodic approximation of Lagrangian Λ in $\Omega(x)$.

Denote by $\widetilde{\mathcal{L}}_\varepsilon$ a family of functions

$$\widetilde{\Lambda}_\varepsilon = \widetilde{\Lambda}(x, y/\varepsilon, \partial_j w_i, w_i, v_i, \partial_i \vartheta, \vartheta, \psi, p_i, f), y \in \Omega_\varepsilon(x), x \in \overline{\Omega},$$

which are Lagrangians in the action functionals:

$$A_{hg}^\varepsilon(w_i, v_i, \vartheta, \psi, p_i, f) = \iint\limits_{\Omega\,\Xi} \int_{t_0}^{t_1} (\widetilde{\Lambda}_\varepsilon(x, y/\varepsilon, \partial_j w_i, w_i, v_i, \partial_i \vartheta, \vartheta, \psi, p_i, f)\, dt d\xi dx.$$

Then, we use the asymptotic modelling procedure (also for terms p_i and f), in which for $\varepsilon \to 0$ functions $\widetilde{\Lambda}_\varepsilon$ of $y/\varepsilon, y \in \Omega_\varepsilon(x)$, tend weakly in $L_{loc}^\gamma(R^m)$, $\gamma \geq 1$, to

$$\Lambda_0(x, \partial_j w_i, w_i, v_i, \partial_i \vartheta, \vartheta, \psi, p_i, f) =$$
$$= \frac{1}{|\Omega|} \int\limits_{\Omega(x)} \widetilde{\Lambda}(x, y, \partial_j w_i, w_i, v_i, \partial_i \vartheta, \vartheta, \psi, p_i, f) dy, x \in \overline{\Omega}, \tag{18}$$

being referred to as *the averaged form of Lagrangian Λ under the asymptotic averaging*. Hence, we can introduce *the asymptotic action functional* defined by

$$A_h^0(w_i, v_i, \vartheta, \psi, p_i, f) = \iint\limits_{\Omega\,\Xi} \int_{t_0}^{t_1} \Lambda_0(x, \partial_j w_i, w_i, v_i, \partial_i \vartheta, \vartheta, \psi, p_i, f)\, dt d\xi dx.$$

Applying the asymptotic averaging with combining decompositions (14) and (15), formulas (17) and Lagrangian (18) we obtain

$$\begin{aligned}
\Lambda_0 &= \frac{1}{2}<k_{ij}>\partial_i \vartheta \partial_j \vartheta + \frac{1}{2}<k_{i1}\partial g>\partial_i \vartheta \psi + \frac{1}{2}<k_{1j}\partial g>\partial_j \vartheta \psi + \\
&+ \frac{1}{2}<k_{11}\partial g \partial g>\psi\psi + \frac{1}{2}<\rho>\dot{w}_i \dot{w}_j \delta_{ij} - \frac{1}{2}<c_{ijkl}>\partial_j w_i \partial_l w_k - \\
&- \frac{1}{2}<c_{ijk1}\partial h>\partial_j w_i v_k - \frac{1}{2}<c_{i1kl}\partial h>v_i \partial_l w_k - \frac{1}{2}<c_{i1k1}\partial h \partial h>v_i v_k + \\
&+ <p_i>w_i + <f>\vartheta,
\end{aligned} \tag{19}$$

with $<p_i>, <f>$ defined by the constitutive equations:

$$<f> = <c>\dot{\vartheta} + <T_0 b_{ij}>\partial_j \dot{w}_i + <T_0 b_{i1}\partial h>\dot{v}_i,$$
$$<p_i> = \partial<b_{ij}>\vartheta + <b_{ij}>\partial_j \vartheta. \tag{20}$$

Using *the extended principle of stationary action* (cf. the book [1]) to A_h^0 we arrive at the following system of Euler-Lagrange equations:

$$\frac{\partial}{\partial t}\frac{\partial \Lambda_0}{\partial \dot{w}_i} + \partial_j \frac{\partial \Lambda_0}{\partial \partial_j w_i} - \frac{\partial \Lambda_0}{\partial w_i} = 0, \quad \frac{\partial \Lambda_0}{\partial v_i} = 0,$$

$$\partial_j \frac{\partial \Lambda_0}{\partial \partial_j \vartheta} - \frac{\partial \Lambda_0}{\partial \vartheta} = 0, \quad \frac{\partial \Lambda_0}{\partial \psi} = 0,$$

(21)

which have slowly-varying coefficients.

6. Governing equations

6.1. Tolerance model equations

Combining Equations (13) with formulas (11) and (12) we arrive at the following form of averaged equations for thermoelasticity problems:

$$\partial_j(<c_{ijkl}>\partial_l w_k + <c_{ijk1}\partial h>v_k) - <\rho>\ddot{w}_i = \partial<b_{ij}>\vartheta + <b_{ij}>\partial_j\vartheta,$$

$$\underline{-\partial_\alpha(<c_{i\alpha k\beta}hh>\partial_\beta v_k)} + <c_{i1k1}\partial h\partial h>v_k + <c_{i1kl}\partial h>\partial_l w_k + \underline{<\rho hh>\ddot{v}_i} =$$

$$= -<b_{i1}\partial g>\vartheta + \underline{<b_{i\beta}gh>\partial_\beta\psi},$$

(22)

$$\partial_j(<k_{ij}>\partial_i\vartheta + <k_{1j}\partial g>\psi) = <c>\dot{\vartheta} + <T_0 b_{ij}>\partial_j\dot{w}_i + <T_0 b_{i1}\partial h>\dot{v}_i,$$

$$\underline{\partial_\alpha(<k_{\alpha\beta}gg>\partial_\beta\psi)} - <k_{i1}\partial g>\partial_i\vartheta - <k_{11}\partial g\partial g>\psi = \underline{<cgg>\dot{\psi}} + \underline{<T_0 b_{i\beta}hg>\partial_\beta\dot{v}_i},$$

where the underlined terms depend on the microstructure parameter *l*. It can be observed that one of the characteristic features of Equations (22) is that they have coefficients being slowly-varying functions in *x*, in contrast to Equations (1), with coefficients as non-continuous, highly oscillating and tolerance-periodic functions. The second feature is that these equations describe the effect of the microstructure size on thermoelasticity problems for composites under consideration.

Equations (22) together with micro-macro decompositions (3) and (4) constitute *the tolerance model of thermoelasticity problems for transversally graded laminates*.

It has to be emphasised that for the laminated layer we have to formulate boundary conditions for the macrodisplacements w_i, $i = 1, 2, 3$, and the macrotemperature ϑ on the edges $x = 0$, H and $x_\alpha = 0$, L_α, $\alpha = 2, 3$, but for the fluctuation amplitudes of displacements v_i, $i = 1, 2, 3$, and the fluctuation amplitude of temperature ψ − only on the edges $x_\alpha = 0$, L_α, $\alpha = 2, 3$. Solutions w_i, v_i, ϑ, ψ, obtained for the specific boundary/initial conditions, have a physical sense only if they hold the following conditions $w_i(\cdot, \mathbf{x}, t), v_i(\cdot, \mathbf{x}, t), \vartheta(\cdot, \mathbf{x}, t), \psi(\cdot, \mathbf{x}, t) \in SV_\delta^1(\Omega, \Omega)$. These conditions can be treated as *a posteriori* evaluation of tolerance parameter δ.

6.2. Asymptotic model equations

Combining Equations (21) with formulas (19) and (20) the following averaged equations of thermoelasticity problems can be derived:

$$\partial_j(<c_{ijkl}>\partial_l w_k + <c_{ijk1}\partial h>v_k) - <\rho>\ddot{w}_i = \partial<b_{ij}>\vartheta + <b_{ij}>\partial_j\vartheta + <b_{i1}\partial g>\psi,$$

$$\partial_j(<k_{ij}>\partial_i\vartheta + <k_{1j}\partial g>\psi) = <c>\dot{\vartheta} + <T_0 b_{ij}>\partial_j\dot{w}_i + <T_0 b_{i1}\partial h>\dot{v}_i,$$

$$v_k = -(<c_{i1k1}\partial h\partial h>)^{-1}(<c_{i1kl}\partial h>\partial_l w_k + <b_{i1}\partial g>\vartheta),$$

$$\psi = -<k_{i1}\partial g>(<k_{11}\partial g\partial g>)^{-1}\partial_i\vartheta,$$

$$(23)$$

with functional coefficients being slowly-varying in x, in contrast to Equations (1), which have non-continuous, highly oscillating and tolerance-periodic coefficients.

Equations (23) together with decompositions (14) and (15) constitute *the asymptotic model of thermoelasticity problems for transversally graded laminates*. These equations do not describe the effect of the microstructure size in contrast to Equations (22).

It can be observed that in the system of Equations (23) for the fluctuation amplitudes of displacements v_i, $i = 1, 2, 3$, and the fluctuation amplitude of temperature ψ we have only algebraic equations. Hence, for the laminated layer only boundary conditions for the macrodisplacements w_i, $i = 1, 2, 3$, and the macrotemperature ϑ on the edges $x = 0$, H and $x_\alpha = 0$, L_α, $\alpha = 2, 3$, have to be formulated.

7. Remarks

Summarizing, some general remarks can be formulated.

• The tolerance modelling, cf. the book edited by Cz. Woźniak et al. [1], makes it possible to replace the differential equations of thermoelasticity for transversally graded laminates with highly-oscillating, non-continuous coefficients by the differential equations with smooth, slowly-varying coefficients.

• The tolerance model equations describe the effect of the microstructure size.

• Using the consistent asymptotic modelling, proposed in the aforementioned book, we can derive instead of the tolerance model equations, the asymptotic model equations having simplified form, because they neglect the above effect.

• That is why both the obtained models can serve as proper tools for analysis of specific boundary value problems.

References

[1] Woźniak Cz., et al., (eds): *Mathematical modelling and analysis in continuum mechanics of microstructured media*, Publishing House of Silesian University of Technology, Gliwice, 2010.

[2] Suresh S., Mortensen A.: *Fundamentals of functionally graded materials*, The University Press, Cambridge, 1998.

[3] Reiter T., Dvorak G.J., Tvergaard V.: *Micromechanical models for graded composite materials*, J. Mech. Phys. Solids, Vol. 45, 1997, pp. 1281−1302.

[4] Bensoussan A., Lions J.L., Papanicolau G.: *Asymptotic analysis for periodic structures*, North-Holland, Amsterdam, 1978.

[5] Jikov V.V., Kozlov C.M., Oleinik O.A.: *Homogenization of differential operators and integral functionals*, Springer Verlag, Berlin-Heidelberg, 1994.

[6] Matysiak S.J.: *On the microlocal parameter method in modelling of periodically layered thermoelastic composites*, J. Theor. Appl. Mech., Vol. 33, 1995, pp. 481−487.

[7] Kim K.-S., Noda N.: *Green's function approach to three-dimensional heat conduction equation of functionally graded materials*, J. Therm. Stresses, Vol. 24, 2001, pp. 457−477.

[8] Ootao Y., Tanigawa Y.: *Transient thermoelastic analysis for a functionally graded hollow cylinder*, J. Therm. Stresses, Vol. 29, 2006, pp. 1031−1046.

[9] Aboudi J., Pindera M.-J., Arnold S.M.: *Higher-order theory for functionally graded materials*, Composites. Part B, Vol. 30, 1999, pp. 777−832.

[10] Bansal Y., Pindera M.-J.: *Efficient reformulation of the thermoelastic higher-order theory for functionally graded materials*, J. Therm. Stresses, Vol. 26, 2003, pp. 1055−1092.

[11] Woźniak Cz., Wierzbicki E.: *Averaging techniques in thermomechanics of composite solids. Tolerance averaging versus homogenization*, Wydawnictwo Politechniki Częstochowskiej, Częstochowa, 2000.

[12] Woźniak Cz., Michalak B., Jędrysiak J., (eds): *Thermomechanics of microheterogeneous solids and structures. Tolerance averaging approach*, Wydawnictwo Politechniki Łódzkiej, Łódź, 2008.

[13] Rychlewska J., Woźniak Cz.: *Boundary layer phenomena in elastodynamics of functionally graded laminates*, Arch. Mech., Vol. 58, 2006, pp. 1−14.

[14] Szymczyk J., Woźniak Cz.: *Continuum modelling of laminates with a slowly graded microstructure*, Arch. Mech., Vol. 58, 2006, pp. 445−458.

[15] Jędrysiak J., Radzikowska A.: *On the modelling of heat conduction in a non-periodically laminated layer*, J. Theor. Appl. Mech., Vol. 45, 2007, pp. 239−257.

[16] Jędrysiak J., Radzikowska A.: *Stationary heat conduction in a laminate with functionally graded macrostructure (FGM)*, Build. Phys. Theory Pract., Vol. 3, 2008, pp. 23−26.

[17] Michalak B., Woźniak M.: *On the heat conduction in certain functionally graded composites*, in: Selected Topics in the Mechanics of Inhomogeneous Media, ed. by Cz. Woźniak, R. Świtka, M. Kuczma, Zielona Góra, 2006, pp. 229−238.

[18] Michalak B., Woźniak Cz., Woźniak M.: *Modelling and analysis of certain functionally graded heat conductor*, Arch. Appl. Mech., Vol. 77, 2007, pp. 823−834.

**Tolerancyjne modelowanie zagadnień termosprężystości
w laminatach o poprzecznej gradacji własności**

Obiektem analizy jest wielowarstwowy kompozyt, wykonany z dwóch składników, które są nieperiodycznie rozmieszczone jako mikrolaminy wzdłuż pewnego kierunku. Przyjęto, że makrowłasności tego kompozytu zmieniają się w sposób ciągły w kierunku prostopadłym do lamin. W pracy zaproponowano dwa modele, opisujące problemy termosprężystości takich laminatów: *model tolerancyjny*, uwzględniający wpływ wielkości mikrostruktury, oraz *model asymptotyczny*, pomijający ten wpływ. Do wyprowadzenia równań obu modeli wykorzystano procedury uśredniające, zaproponowane w książce pod red. Cz. Woźniaka i in. [1], tj. modelowanie tolerancyjne oraz tzw. „konsystentne" modelowanie asymptotyczne.

Some problems of heat conduction for transversally graded laminates with non-uniform distribution of laminas

J. JĘDRYSIAK, A. RADZIKOWSKA

Department of Structural Mechanics, Technical University of Łódź,
al. Politechniki 6, 90-924 Łódź, Poland.

In this contribution a problem of heat conduction in laminates, made of two conductors non-periodically distributed as microlaminas along one direction, is investigated. A macrostructure of such laminate is assumed to be functionally graded along this direction. In order to analyse some effects of the microstructure on the heat conduction, the tolerance averaging technique is applied, cf. the book edited by Woźniak, Michalak and Jędrysiak [1].

1. Preliminaries

The main objects under consideration are laminates made of two conductors. These conductors are distributed non-periodically along a direction normal to laminas. Every lamina (called also *cell*) has the thickness λ. It consists of two sub-laminas. From the macroscopic point of view averaged (macroscopic) properties of these composites are continuously varied along this direction, cf. Figure 1a. However, the microstructure of this laminate can be defined by a uniform distribution function of laminas λ = const, cf. Figure 1b or by a non-uniform distribution function $-\lambda = \lambda(x)$, cf. Figure 1c. Laminates of this kind can be treated as made of *functionally graded materials* (*FGM*), cf. Suresh and Mortensen [2], and will be called *transversally graded laminates*.

Various thermomechanical problems of FGM-type laminates are analysed by using methods introduced for macroscopically homogeneous structures, as periodic laminates. Some of these methods are discussed in the book. We can distinguish these modelling techniques, based on *the asymptotic homogenization*, cf. the monograph by Jikov, Kozlov and Oleinik [3]. Heat conduction for periodic laminates is also analysed using *models with microlocal parameters*, cf. Matysiak [4]. However, the effect of the microstructure size on laminates is usually omitted in equations of these models. As an alternative approach for FG-type materials *the higher-order theory* was proposed by Aboudi, Pindera and Arnold [5] (with its reformulation by Bansal and Pindera [6]).

The aforementioned effect can be taken into account within *the tolerance averaging technique* (*the tolerance modelling*), proposed to the modelling non-stationary problems for periodic composites in the book by Cz. Woźniak and Wierzbicki [7], and

extended on FG-type materials in the books edited by Cz. Woźniak, Michalak and Jędrysiak [1] and by Cz. Woźniak et al. [8]. This technique was adopted to analyse various problems of FG-type materials and structures in a series of papers, e.g. for a heat conduction in transversally graded composites by Jędrysiak and Radzikowska [9–10] and in longitudinally graded composites by Michalak and M. Woźniak [11], Michalak, Cz. Woźniak and M. Woźniak [12]. Some additional examples of applications of this technique for composites and structures of this kind can be found in the books [1, 8].
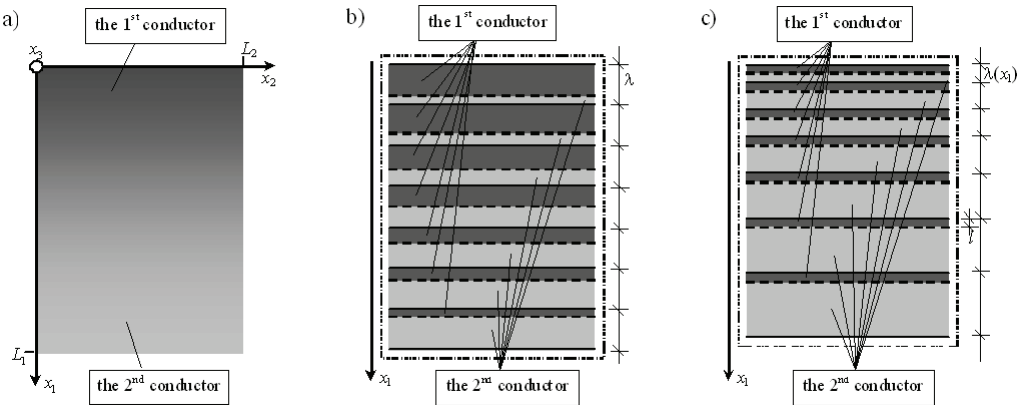
Fig. 1. A cross section of a transversally graded laminate: a) the macroscopic point of view, b) the microscopic point of view with a uniform distribution of laminas, c) the macroscopic point of view with a non-uniform distribution of laminas

The main aim of this contribution is to apply *the tolerance model equations of heat conduction for transversally graded laminates* (*TGL*) to analyse stationary heat conduction along the direction perpendicular to laminas. The TG-type laminate under consideration is assumed in the form of a laminated layer with a non-uniform distribution of laminas, cf. Figure 1c. Some effects of a cell distribution and material properties on basic unknowns of the applied model will be shown.

2. Modelling foundations

Let subscripts $i, j, \ldots$, related to the coordinate system Ox_1x_2, run over 1, 2. Introduce denotations: $x \equiv x_1$; t as the time coordinate; ∂_i as derivatives of x_i; and also $\partial \equiv \partial_1$. Let H be the layer thickness along the x-axis, and L be the length dimension along the x_2-axis. We assume that the layer under consideration occupies the region $\Omega \times \Xi$ on the plane Ox_1x_2, where $\Omega \equiv (0, H)$, $\Xi \equiv (0, L)$. This layer is made of two conductors distributed in m laminas with the varied thickness λ. Properties of these conductors are described by: specific heats c', c'' and heat conduction tensors with

components k'_{ij}, k''_{ij}, $i, j = 1, 2$. It is assumed that the 1st conductor has the constant thickness l (cf. Figure 1c), satisfying the condition $l << H$, and called *the microstructure parameter*. Every n-th lamina has the thickness λ_n (which is not constant). The n-th lamina consists of two homogeneous sub-laminas with thicknesses $\lambda'_n = l = \text{const}$ and $\lambda''_n = \lambda_n - l$, which is not constant, cf. Figure 1c. We can introduce material volume fractions in the n-th lamina defined as $v'_n \equiv l / \lambda_n, v''_n \equiv \lambda''_n / \lambda_n$. Sequence $\{v'_n\}$, $n = 1, ..., m$, is monotone and satisfies condition $|v'_{n+1} - v'_n| << 1$, for $n = 1, ..., m - 1$. Because $v'_n + v''_n = 1$ sequence $\{v''_n\}$ satisfies similar conditions. Sequences $\{v'_n\}$, $\{v''_n\}$, $n = 1, ..., m$, can be approximated by continuous functions $v'(\cdot)$, $v''(\cdot)$, describing the gradation of material properties along the x-axis. Similarly, the sequence $\{\lambda_n\}$ of laminas thicknesses can be approximated by the function $\lambda(x)$. The functions $v'(\cdot)$, $v''(\cdot)$ can be called *the fraction ratios of materials*. Let us also define *the non-homogeneity ratio* by $v(\cdot) \equiv [v'(\cdot) \, v''(\cdot)]^{1/2}$. For such laminates we cannot define a basic cell in Ω, but a certain non-uniform cell distribution in Ω can be introduced as $\Omega(x) \equiv (x - \lambda(x)/2, x + \lambda(x)/2)$. Hence, the function $\lambda(x)$ can be referred to as *the cell distribution function*. Moreover, these functions ($v'(\cdot)$, $v''(\cdot)$, $\lambda(\cdot)$) are assumed to be slowly-varying (cf. the book edited by Cz. Woźniak, Michalak and Jędrysiak [1]). Thus, the layer is called *the transversally graded laminated layer* (*the TGL layer*).

Let Θ denote the unknown temperature field. Moreover, the heat conduction problem in the TGL layer will be analysed in the framework of the Fourier's model, i.e. described by the following equation (without heat sources):

$$\partial_i(k_{ij}\partial_j\Theta) - c\dot{\Theta} = 0. \tag{1}$$

For the TGL layer all coefficients in Equation (1), i.e. $k_{ij} = k_{ij}(x)$, $c = c(x)$, are highly-oscillating, tolerance-periodic, non-continuous functions in x. Thus, this equation is not a good tool to analyse problems of heat conduction. Equation (1) can be replaced by differential equations with continuous, smooth, slowly-varying coefficients using *the tolerance modelling*, cf. the book edited by Cz. Woźniak et al. [8].

3. Tolerance modelling

3.1. Introductory concepts

Some basic concepts, used in the tolerance modelling, are: an averaging operator, a tolerance-periodic function, a slowly-varying function, a highly oscillating function. Definitions and explanations of these concepts can be found in the books – edited by Cz. Woźniak et al. [8] and by Cz. Woźniak, Michalak and Jędrysiak [1]. Below, some of them are reminded.

For an arbitrary integrable function f (which can also depend on x_2 and t), defined in $\overline{\Omega}$, the *averaging operator* is given by

$$< f >(x) = \lambda(x)^{-1} \int_{x-\lambda(x)/2}^{x+\lambda(x)/2} f(\xi)d\xi, \ x \in [\lambda(x)/2, H - \lambda(x)/2]. \tag{2}$$

It can be shown that for tolerance-periodic function f of x, its averaged value calculated from (2) is a slowly-varying function in x (cf. the books [1, 8]).

Denote by $\partial^k \phi$ the k-th gradient of function $\phi = \phi(x)$, $x \in \Omega$, $k = 0, 1$, $\partial^0 \phi \equiv \phi$; and by $\widetilde{\phi}^{(k)}(\cdot, \cdot)$ a function defined in $\overline{\Omega} \times R^m$.

Function $\phi \in H^1(\Omega)$ is called *the tolerance-periodic function* (with respect to Ω and tolerance parameter δ), $\phi \in TP^1_\delta(\Omega, \Omega)$, if for $k = 0, 1$ the following conditions hold

(I) $(\forall x \in \Omega)\, (\exists \widetilde{\phi}^{(k)}(x, \cdot) \in H^0(\Omega))\ [\| \partial^k \phi\big|_{\Omega_x}(\cdot) - \widetilde{\phi}^{(k)}(x, \cdot) \|_{H^0(\Omega_x)} \leq \delta]$,

(II) $\int_{\Omega(\cdot)} \widetilde{\phi}^{(k)}(\cdot, z)dz \in C^0(\overline{\Omega})$.

Function $\widetilde{\phi}^{(k)}(x, \cdot)$ is *the periodic approximation of $\partial^k \phi$ in $\Omega(x)$, $x \in \Omega$, $k = 0, 1$.

Function $\Phi \in H^1(\Omega)$ is called *the slowly-varying function* (with respect to Ω and tolerance parameter δ), $\Phi \in SV^1_\delta(\Omega, \Omega)$, if

(I) $\Phi \in TP^1_\delta(\Omega, \Omega)$,

(II) $(\forall x \in \Omega)[\widetilde{\Phi}^{(k)}(x, \cdot)|_{\Omega(x)} = \partial^k \Phi(x), \ k = 0, 1]$.

Thus, periodic approximation $\widetilde{\Phi}^{(k)}$ of $\partial^k \Phi(\cdot)$ in $\Omega(x)$ is a constant function for every $x \in \Omega$.

Function $f \in H^1(\Omega)$ is called *the highly oscillating function* (with respect to Ω and tolerance parameter δ), $f \in HO^1_\delta(\Omega, \Omega)$, if

(I) $f \in TP^1_\delta(\Omega, \Omega)$,

(II) $(\forall x \in \Omega)[\widetilde{f}^{(k)}(x, \cdot)|_{\Omega(x)} = \partial^k \widetilde{f}(x), \quad k = 0, 1]$.

Moreover, for every $\Phi \in SV^\alpha_\delta(\Omega, \Omega)$ function $\phi \equiv fF \in TP^\alpha_\delta(\Omega, \Omega)$ satisfies condition

(III) $\widetilde{\phi}^{(k)}(x, \cdot)\big|_{\Omega(x)} = \Phi(x)\partial^k \widetilde{f}(x)\big|_{\Omega(x)}$, $k = 1$.

If $\alpha = 0$ then we denote $\widetilde{\phi} \equiv \widetilde{\phi}^{(0)}$.

Let $h(\cdot)$ be a highly oscillating, continuous function, $h \in HO^1_\delta(\Omega, \Omega)$, defined on $\overline{\Omega}$. Its gradient $\partial^1 h$ is a piecewise continuous and bounded. Function $h(\cdot)$ is called *the fluctuation shape function* of the 1st kind, if it depends on l as a parameter and satisfies conditions:

(1º) $\partial^k h \in O(\tilde{l}^{1^\cdot k})$ for $k = 0, 1, \partial^0 h \equiv h$,

(2º) $<h>(x) \approx 0$ for every $x \in \Omega$.

By $FS_\delta^1(\Omega,\Omega)$ we denote a set of all fluctuation shape functions of the 1st kind. Condition (2º) can be replaced by $<ch>(x) \approx 0$ for every $x \in \Omega$, where c is a certain tolerance-periodic function and $c > 0$.

3.2. Modelling assumptions

The fundamental modelling assumptions are mentioned below.

The first assumption is *the micro-macro decomposition*, in which it is assumed

$$\Theta(x, x_2, t) = \vartheta(x, x_2, t) + h(x)\,\psi(x, x_2, t), \tag{3}$$

and $\vartheta(\cdot, x_2, t), \psi(\cdot, x_2, t) \in SV_\delta^1(\Omega,\Omega)$ for every t; $h(\cdot) \in FS_\delta^1(\Omega,\Omega)$. The basic unknown is function $\vartheta(\cdot, x_2, t)$ called *the macrotemperature*; an additional basic unknown is *the fluctuation amplitude* $\psi(\cdot, x_2, t)$; $h(\cdot)$ is the known *fluctuation shape function*. The function $h(\cdot)$ is assumed to be continuous, linear across every sub-lamina thickness and of an order $O(l)$, and to satisfy conditions (1º)–(2º), i.e. it can be given by:

$$h(x) = \begin{cases} -l\sqrt{3}\,\dfrac{v(\bar{x})}{v''(\bar{x})}[2\dfrac{x}{\lambda(\bar{x})} + v'(\bar{x})] \text{ for } x \in (-\tfrac{1}{2}\lambda(\bar{x}), -\tfrac{1}{2}\lambda(\bar{x}) + \lambda(\bar{x})v''(\bar{x})), \\ l\sqrt{3}\,\dfrac{v(\bar{x})}{v'(\bar{x})}[2\dfrac{x}{\lambda(\bar{x})} - v''(\bar{x})] \text{ for } x \in (\tfrac{1}{2}\lambda(\bar{x}) - \lambda(\bar{x})v'(\bar{x}), \tfrac{1}{2}\lambda(\bar{x})), \end{cases} \tag{4}$$

where $\bar{x}$ is a centre of $\Omega(\cdot)$, cf. the book [1]. The mean value of h in every lamina is equal to zero, since the non-homogeneity ratio $v(\cdot)$ is a slowly-varying function.

The second modelling assumption is called *the tolerance averaging approximation*, in which we assume that terms $O(\delta)$ are negligibly small, e.g. in formulae:

$$<\phi>(x) = <\bar{\phi}>(x) + O(\delta), <\phi\Phi>(x) = <\phi>(x)\Phi(x) + O(\delta)$$
$$<\phi\partial(h\Phi)>(x) = <\phi\partial h>(x)\Phi(x) + O(\delta),$$
$$x \in \Omega; \ 0 < \delta << 1; \quad \phi \in TP_\delta^1(\Omega,,), \ \Phi \in SV_\delta^1(\Omega,,) \ h \in FS_\delta^1(\Omega,,).$$

3.3. Modelling procedure

Following the book edited by Cz. Woźniak et al. [8], the modelling procedure is outlined here. Firstly, we formulate the extended action functional in the form

$$A(\Theta(\cdot), p(\cdot)) = \iint_{\Omega \Xi} \int_{t_0}^{t_1} \Lambda(z, \partial_i \Theta(z, \xi, t), \Theta(z, \xi, t), p(z, \xi, t)) dt d\xi dz, \tag{5}$$

where $\Lambda(\cdot, \partial_i \Theta, \Theta) \in HO_\delta^0(\Omega, \Omega)$, $p(\cdot, \xi, t) \in HO_\delta^0(\Omega, \Omega)$. The Lagrangian Λ is given by

$$\Lambda = \frac{1}{2} \partial_i \Theta k_{ij} \partial_j \Theta + p\Theta, \tag{6}$$

and the term p is determined by the constitutive equation

$$p = c\dot{\Theta}. \tag{7}$$

For Lagrangian (6) we can write the Euler-Lagrange equation

$$\partial_j \frac{\partial \Lambda}{\partial \partial_j \Theta} - \frac{\partial \Lambda}{\partial \Theta} = 0. \tag{8}$$

The extended principle of stationary action (cf. Part I of the book edited by Woźniak et al. [8]) leads from Equation (8) (combined with (6) and (7)) to the fundamental equation of the Fourier's heat conduction (1). In the next step, the tolerance modelling is applied to action functional (5). We substitute micro-macro decomposition (3) to (5) and use averaging operator (2) to this action functional. At the end we arrive at the tolerance averaging of functional $A(\Theta(\cdot), p(\cdot))$:

$$A_h(\vartheta, \psi, p) = \iint_{\Omega \Xi} \int_{t_0}^{t_1} < \Lambda_h > (x, \partial_i \vartheta, \partial_2 \psi, \vartheta, \psi, p) dt d\xi dx,$$

where the averaged Lagrangian $< \Lambda_h >$ takes the form

$$< \Lambda_h >= \frac{1}{2} (\partial_i \vartheta < k_{ij} > \partial_j \vartheta + \psi < \partial h k_{11} \partial h > \psi + \partial_2 \psi < k_{22} h^2 > \partial_2 \psi +$$
$$+ \partial_i \vartheta < k_{1i} \partial h > \psi + \psi < \partial h k_{j1} > \partial_j \vartheta) + < p > \vartheta + < ph > \psi, \tag{9}$$

and terms $<p>$, $<ph>$ are given by the constitutive equations:

$$< p >=< c > \dot{\vartheta}, \quad < ph >=< ch^2 > \dot{\psi}. \tag{10}$$

Applying the extended principle of stationary action to Lagrangian A_h the following system of equations is obtained:

$$\partial_i \frac{\partial < \Lambda_h >}{\partial(\partial_i \vartheta)} - \frac{\partial < \Lambda_h >}{\partial \vartheta} = 0,$$

$$\partial_2 \frac{\partial < \Lambda_h >}{\partial \partial_2 \psi} - \frac{\partial < \Lambda_h >}{\partial \psi} = 0,$$

(11)

with slowly-varying, functional coefficients.

4. Tolerance model equations

Combining Equations (11) with (9, 10), and using the smooth functional coefficients:

$$K \equiv< k_{11} >, \quad K_{22} \equiv< k_{22} >, \quad \widetilde{K} \equiv< k_{11}\partial h >, \quad \breve{K} \equiv< k_{11}\partial h\partial h >, \quad C \equiv< c >,$$

we arrive at the following form of averaged heat conduction equations:

$$\partial(K(x)\partial \vartheta) + K_{22}(x)\,\partial_{22}\vartheta - C(x)\dot{\vartheta} + \partial(\widetilde{K}(x)\psi) = 0,$$

$$\widetilde{K}(x)\partial \vartheta + \breve{K}(x)\psi + l^2(\nu(x))^2[C(x)\dot{\psi} - K_{22}(x)\partial_{22}\psi] = 0,$$

(12)

with some terms depending explicitly on the microstructure parameter *l*. Equations (12) have coefficients being slowly-varying functions in *x*, in contrast to Equation (1), which has functional, non-continuous, highly oscillating coefficients.

Equations (12) together with micro-macro decomposition (3) constitute *the tolerance model of heat conduction for transversally graded laminates*. These equations take into account the effect of the microstructure size on heat transfer for these composites. It can be observed that for the TGL layer under consideration boundary conditions for the macrotemperature ϑ have to be formulated on the edges $x = 0$, *H* and $x_2 = 0$, *L*, but for the fluctuation amplitude ψ only on the edges $x_2 = 0$, *L*. Moreover, solutions ϑ, ψ to the specific boundary/initial conditions have a physical sense only under conditions $\vartheta(\cdot, x_2, t), \psi(\cdot, x_2, t) \in SV_\delta^1(\Omega, \Omega), t \in (t_0, t_1)$, which can be *a posteriori* evaluation of tolerance parameter δ.

5. Applications: stationary heat conduction across laminas

Let us assume that Let the TGL layer under consideration be subjected to a thermal gradient in the direction parallel to the *x*-axis. Moreover, let the problem of the heat conduction be stationary. Thus, temperature Θ is a function of *x*, i.e. $\Theta = \Theta(x)$, and then the basic unknowns in the tolerance model are also functions only of *x*, i.e. $\vartheta = \vartheta(x)$, $\psi = \psi(x)$. Denote by $k \equiv k_{11}, k' \equiv k_{11}', k'' \equiv k_{11}''$ heat conduction coefficients in sub-laminas.

Introducing notations

$$K(x) \equiv v'(x)k' + v''(x)k'', \quad \widetilde{K}(x) \equiv 2\sqrt{3}v(x)(k' - k''), \quad \breve{K}(x) \equiv 12(v'(x)k'' + v''(x)k'),$$

Equations (12) take the form:

$$\partial[K(x)\partial\vartheta + \widetilde{K}(x)\psi] = 0,$$
$$\widetilde{K}(x)\partial\vartheta + \breve{K}(x)\psi = 0.$$

(13)

The fluctuation amplitude ψ can be calculated from Equation (13)$_2$:

$$\psi = -\widetilde{K}(x)[\breve{K}(x)]^{-1}\partial\vartheta.$$

(14)

Substituting (14) into Equation (13)$_1$ and denoting

$$K^{eff}(x) \equiv K(x) - [\widetilde{K}(x)]^2[\breve{K}(x)]^{-1}$$

(15)

we obtain the following equation:

$$\partial[K^{eff}(x)\partial\vartheta] = 0.$$

(16)

The above equation together with formula (14) for the fluctuation amplitude ψ and micro-macro decomposition (3), which takes the form

$$\Theta(x) = \vartheta(x) + h(x)\psi(x),$$

(17)

describes the stationary heat conduction across laminas in the TGL layer.

Equation (16) has slowly-varying coefficients, defined by known functions, e.g. by v', v'', v, h, cf. (4). Hence, integrating Equation (16) we can write the solution as:

$$\vartheta(x) = C_1 \int [K^{eff}(x)]^{-1} dx + C_2,$$

(18)

with constants C_1, C_2 determined by boundary conditions. For the considered layer with constant coefficients k', k'' and the fluctuation shape function given by (4) the averaged heat conduction coefficient K^{eff}, (15), is equal

$$K^{eff}(x) = k'k''[k' + (k'' - k')v'(x)]^{-1}.$$

(19)

For the macrotemperature ϑ we assume the following boundary conditions:

$$x = 0 : \vartheta(0) = T_0; \; x = H : \vartheta(H) = 0. \tag{20}$$

Denoting

$$f(x) = \int v'(x)dx$$

and combining the boundary conditions (20) with formulas (18)–(19) we arrive at constants C_1, C_2:

$$C_1 = T_0 \frac{k'k''}{(k'' - k')[f(0) - f(H)] - k'H}, \; C_2 = -T_0 \frac{k'H + (k'' - k')f(H)}{(k'' - k')[f(0) - f(H)] - k'H}. \tag{21}$$

Hence, the macrotemperature (18) has the form

$$\vartheta(x) = C_1[x(k'')^{-1} + (k'' - k')(k'k'')^{-1}f(x)] + C_2; \tag{22}$$

however, the fluctuation amplitude ψ can be written as

$$\psi(x) = \frac{\sqrt{3}}{6}(k'' - k')(k'k'')^{-1}v(x)C_1. \tag{23}$$

Combining (22) and (23) with formula (17) the temperature Θ is equal

$$\Theta(x) = \{x(k'')^{-1} + (k'' - k')(k'k'')^{-1}[f(x) + \frac{\sqrt{3}}{6}h(x)v(x)]\}C_1 + C_2. \tag{24}$$

Formula (24), with constants C_1, C_2 determined by (21) and the fluctuation shape function h given by (4), describes the "exact" distribution of the temperature in the TGL layer by the tolerance model.

6. Results

In this section some effects of conductor properties (heat conduction coefficients) and of a form of the cell distribution function on the macrotemperature and the fluctuation amplitude are presented.

Let the layer thickness H be coupled with the microstructure parameter l by the relation $H = 2(m - 1)l$ (m is the number of laminas). The cell distribution function is assumed in the following form:

1) the linear function (denoted by $\alpha = 1$)

$$\lambda(\bar{x}) = \bar{x}\frac{2(H - ml)}{H(m-1)} + l, \tag{25}$$

2) the square function (denoted by $\alpha = 2$)

$$\lambda(\bar{x}) = \bar{x}^2\frac{6m(H - ml)}{(m-1)(2m-1)H^2} + l, \tag{26}$$

3) the cubic function (denoted by $\alpha = 3$)

$$\lambda(\bar{x}) = \bar{x}^3\frac{4m(H - ml)}{(m-1)^2 H^3} + l, \tag{27}$$

where $\bar{x}$ is the centre of "cell". For a comparison it is also assumed a periodic laminate with the constant function $\lambda(x) = 2l$ (denoted by $\alpha = 0$). For the above functions the fraction ratios of materials are defined as:

$$v'(\bar{x}) = l(\lambda(\bar{x}))^{-1}, \;\; v''(\bar{x}) = 1 - v'(\bar{x}).$$
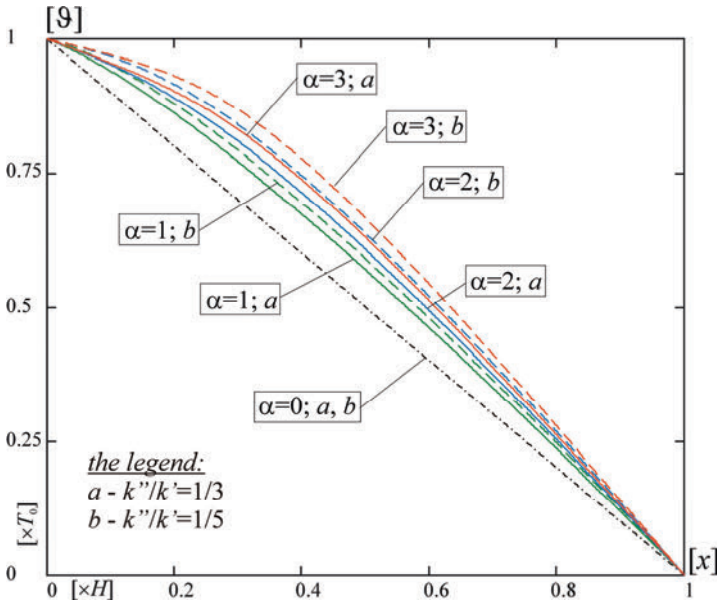
Fig. 2. Diagrams of the macrotemperature ϑ versus x-coordinate (for the linear ($\alpha = 1$), the square ($\alpha = 2$), the cubic ($\alpha = 3$) cell distribution function and the periodic distribution ($\alpha = 0$))
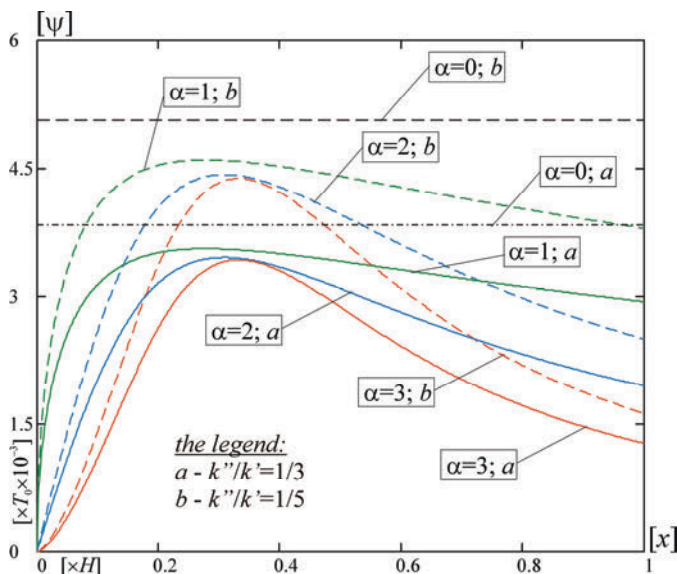
Fig. 3. Diagrams of the fluctuation amplitude ψ versus x-coordinate (for the linear ($\alpha = 1$), the square ($\alpha = 2$), the cubic ($\alpha = 3$) cell distribution function and the periodic distribution ($\alpha = 0$))

Some calculational results are shown in Figures 2–3. These plots are made for $m = 20$, thus the ratio $l/H = 0.026$. In Figure 2 there are presented curves of the macrotemperature ϑ given by formula (22) versus coordinate $x \in [0, H]$, but Figure 3 shows plots of the fluctuation amplitude ψ (by formula (23)) versus this coordinate. Diagrams in these figures are made for ratios $k''/k' = 1/3$ (*a*) and $k''/k' = 1/5$ (*b*).

Under the obtained results some remarks can be formulated.

1. Distributions of the macrotemperature in the TGL layer depend on the cell distribution functions, cf. Figure 2, i.e.:

    a) values of the macrotemperature are smallest for the linear function (25);

    b) values of the macrotemperature are biggest for the cubic function (27).

2. Values of the macrotemperature in the TGL layer depend on differences between values of heat conduction coefficients k', k'' of material properties, cf. Figure 2, i.e. these values increase with the decreasing of the ratio k''/k'.

3. The macrotemperature in the periodic layer (the case $\alpha = 0$, cf. Figure 2) is independent of differences between values of heat conduction coefficients k', k'' of material properties.

4. Distributions of the fluctuation amplitude in the TGL layer depend on the cell distribution functions, cf. Figure 3, i.e.:

    a) values of the fluctuation amplitude are smallest for the cubic function (27);

    b) values of the fluctuation amplitude are biggest for the linear function (25).

5. Values of the fluctuation amplitude in the TGL layer depend on differences between values of heat conduction coefficients k', k'' of material properties, cf. Figure 3, i.e. these values increase with the decreasing of the ratio k''/k'.

6. The fluctuation amplitudes in the periodic layer (the case $\alpha = 0$) depend on differences between values of heat conduction coefficients k', k'' of material properties and their values are bigger than those values for the TGL layer.

7. Remarks

The tolerance modelling, presented in the book edited by Cz. Woźniak et al. [8], applied to the heat conduction equation for transversally graded laminates (TGL), has made it possible to obtain the governing equations of *the tolerance model* for those laminates.

Summing up, some general remarks can be formulated:

- the tolerance modelling leads from the heat conduction differential equation with highly-oscillating, non-continuous coefficients to the system of differential equations with smooth, slowly-varying coefficients;
- the tolerance model equations describe the effect of the microstructure size;
- exact analytical solutions to these equations can be obtained for the stationary heat conduction.

Under the calculational results for the stationary heat conduction we can observe:

- Distributions of the macrotemperature and the fluctuation amplitude depend on:
  - the cell distribution functions in the TGL layer,
  - differences between heat conduction coefficients k', k''.

Some additional analyses of applications of the tolerance model to various problems of heat conduction for the transversally graded laminates will be shown separately.

References

[1] Woźniak Cz., Michalak B., Jędrysiak J., (eds): *Thermomechanics of microheterogeneous solids and structures. Tolerance averaging approach*, Wydawnictwo Politechniki Łódzkiej, Łódź, 2008.

[2] Suresh S., Mortensen A.: *Fundamentals of functionally graded materials*, The University Press, Cambridge, 1998.

[4] Jikov V.V., Kozlov C.M., Oleinik O.A.: *Homogenization of differential operators and integral functionals*, Springer Verlag, Berlin-Heidelberg, 1994.

[5] Matysiak S.J.: *On the microlocal parameter method in modelling of periodically layered thermoelastic composites*, J. Theor. Appl. Mech., Vol. 33, 1995, pp. 481–487.

[6] Aboudi J., Pindera M.-J., Arnold S.M.: *Higher-order theory for functionally graded materials*, Composites. Part B, Vol. 30, 1999, pp. 777–832.

[7] Bansal Y., Pindera M.-J.: *Efficient reformulation of the thermoelastic higher-order theory for functionally graded materials*, J. Therm. Stresses, Vol. 26, 2003, pp. 1055–1092.

[8] Woźniak Cz., Wierzbicki E.: *Averaging techniques in thermomechanics of composite solids. Tolerance averaging versus homogenization*, Wydawnictwo Politechniki Częstochowskiej, Częstochowa, 2000.

[9] Woźniak Cz., et al., (eds): *Mathematical modelling and analysis in continuum mechanics of microstructured media*, Publishing House of Silesian University of Technology, Gliwice, 2010.

[10] Jędrysiak J., Radzikowska A.: *On the modelling of heat conduction in a non-periodically laminated layer*, J. Theor. Appl. Mech., Vol. 45, 2007, pp. 239–257.

[11] Jędrysiak J., Radzikowska A.: *Stationary heat conduction in a laminate with functionally graded macrostructure (FGM)*, Build. Phys. Theory Pract., Vol. 3, 2008, pp. 23–26.

[12] Michalak B., Woźniak M.: *On the heat conduction in certain functionally graded composites*, in: Selected Topics in the Mechanics of Inhomogeneous Media, ed. by Cz. Woźniak, R. Świtka, M. Kuczma, Zielona Góra, 2006, pp. 229–238.

[13] Michalak B., Woźniak Cz., Woźniak M.: *Modelling and analysis of certain functionally graded heat conductor*, Arch. Appl. Mech., Vol. 77, 2007, pp. 823–834.

Pewne zagadnienia przewodnictwa ciepła laminatów o poprzecznej gradacji własności z nierównomiernym rozmieszczeniem lamin

W niniejszej pracy analizowany jest problem przewodnictwa ciepła w laminatach wykonanych z dwóch przewodników, rozmieszczonych nieperiodycznie w postaci mikrolamin wzdłuż pewnego kierunku. Przyjęto, że wzdłuż tego kierunku laminat ma makrostrukturę o funkcyjnej gradacji. W celu zbadania pewnych efektów, związanych z budową laminatu w przewodnictwie ciepła zastosowano technikę tolerancyjnego uśredniania, por. książka pod red. Cz. Woźniaka, Michalaka i Jędrysiaka [1].

The concept of the ideal indoor environment in multi-attribute assessment of dwelling-houses

D. KALIBATAS, E.K. ZAVADSKAS, D. KALIBATIENE

Vilnius Gediminas Technical University, Sauletekio al. 11, LT-10223 Vilnius, Lithuania.

This paper presents a multi-attribute assessment of an indoor environment of dwelling-houses, since it depends on a number of criteria, like temperature, humidity, noise, etc. There are a number of works, where a comparison of indoor environment of different dwelling-houses are analysed and the best alternative is determined. Only a few works compare a present state of an indoor environment of dwelling-houses with standards, like the Lithuanian hygienic norm or ISO EN 7730. In this paper, a multi-attribute assessment of indoor environment of dwelling-houses based on the concept of the ideal indoor environment is presented. This concept defines an optimal indoor environment of a dwelling-house according to the Lithuanian hygienic norm and some other regulations presented in the paper and is introduced to determine the deviation of each alternative (an indoor environment of a dwelling-house) from the optimal values. In the case study the TOPSIS method is used for the MADM of an indoor environment of dwelling-houses in Naujoji Vilnia, Vilnius, Lithuania.

Keywords: *indoor environment, multi-attribute decision making, the TOPSIS method*

1. Introduction

Nowadays there are plenty of dwelling-houses, which people use to live in. Some of them are characterized as suitable for leaving, others – are not suitable. Since the suitability of a dwelling-house for living depends on a number of attributes, like temperature, noise isolation, annual heat requirements, etc., a multi-attribute decision making (MADM) methods are used for their assessment. Different methods and attributes are proposed to assess dwelling-houses. However, not all authors take into account hygienic norms and different regulations during the assessment.

In this paper, an approach based on the concept of the ideal indoor environment is presented to determine the suitability of dwelling-houses for living. The concept of the ideal indoor environment presents the optimal indoor environment according to the Lithuanian hygienic norm HN 42:2004 [1–2] and ISO EN 7730 2005 [3]. The complementing of a set of alternatives (indoor environments of dwelling-houses) with the ideal indoor environment allows us to compare alternatives and to determine the deviation of each alternative from the ideal indoor environment.

The main problems solved in the paper are defining attributes and their significance for the assessment of dwelling-houses, determining the ideal indoor environment, adopting the TOPSIS method for the assessment of dwelling-houses according to the defined attributes and evaluating the deviation from the ideal indoor environment.

The paper is organised as follows. Section 2 presents the related work on a concept of indoor environment and the ideal indoor environment. Section 3 presents a description of the TOPSIS method applied to the assessment of dwelling-houses. Section 4 presents a case study of the assessment of dwelling-houses in Naujoji Vilnia, Vilnius, Lithuania. Finally, Section 5 concludes the paper.

2. The related work

From the perspective of an occupant of a building, the ideal situation is an indoor environment that satisfies all occupants (i.e. they have no complaints) and does not unnecessarily increase the risk or severity of illness or injury. The desire is that the air be perceived as fresh and pleasant, that it has no negative impact on occupants' health, and that the air is stimulating and promoting their work [4].

According to the Lithuanian hygienic norm (HN 42:2004) [1], balanced inner climate prevents from spreading of bacteria as well as human immune system and the inner surfaces of a building from vapour condensing and moulding.

Authors of [5] investigate an indoor environment of schools in Jordan according to environmental parameters such as air quality, air temperature, relative humidity, and acoustics. A cross multiple design strategy was adopted that included objective measurements (building physical measurements, monitoring and archival data) and subjective measurements (questionnaires, interviews and students' medical records). Seventeen schools were selected based on a multi-stage systematic sampling strategy. However, authors do not present one consistent method for evaluating an indoor air.

Authors of [6] and [7] analyse indoor air quality and ventilation efficiency according to Carbon dioxide (CO_2). However, other indicators are not taken into account.

Bluyssen in [8] states that over the last century, management of the indoor environment was focused only on its single components (thermal comfort, noise, light, air quality) and not attention was paid on interrelations between these components. Although standards and guidelines are met, the quality of the indoor environment, as experienced by the occupants, could be not acceptable and unhealthy, causing health and comfort problems. Nowadays, it is important to pay attention and evaluate such indoor air pollutants, like volatile organic compounds (VOC), VOC groups, ammonia, and formaldehyde in newly established residential buildings with low-emitting materials. The paper [8] presents contribution of pollutants from different structures (floor, walls, and ceiling) to indoor air concentration levels during the first year after the building was taken into use.

In [9] air quality was analysed according to the ratio of living room to kitchen (L/K) pollutant concentrations and the correlation of their levels to assess the transport of pollutants indoors. It was determined that among all the pollutants, SO_2 has the minimum 0.88 L/K ratio value, and maximum correlation value, $R_2 = 0.89$; on the other hand, PM_{10} has the maximum L/K ratio value, 1.20 and minimum R_2-value, 0.55, which means that PM_{10} is mostly influenced by activities and other factors that do not take place in the kitchen. Concentrations of SO_2 differed significantly de-

pending on the fuel type used for cooking with coal gas producing 87.6% higher SO_2 concentrations than natural gas. Concentrations of CO_2 and PM_{10} were the same regardless of gas type.

Authors of [10] analyse an importance of noise reduction for goodness of indoor being. Other pollutants and attributes of indoor environment, like dust [11], nitrogen oxides [12], energy saving [13], toxic moulds [14], lighting installations [15], housing environment [16], thermal environment [17–18], etc. are analysed, also. However, not all authors present a continuous method for evaluating an indoor environment. The deviation from hygienic norms is not mentioned in many researches, also.

Since in Lithuania there are two seasons – heating season and not-heating season – it is necessary to take into account heating costs, which indirectly influence an indoor environment of dwelling-houses. The passive house concept is used to define a house with minimal energy losses, what allow minimizing heating cost and environmental (outdoor and indoor) damage, and maximizing habitants' satisfaction of indoor environment. Unfortunately, not all dwelling-houses in Lithuania can be referred as passive houses. According to [19] and [20], annual heat requirement is ≤15 kWh/m^2/year (4.75 kBtu/sf/yr).

From the related work presented in this section, it can be seen that indoor environment of dwelling-houses is defined by a number of attributes. Therefore, in this research, we are going to apply MADM to evaluate an indoor environment of dwelling-houses. MADM methods are successfully applied for: risk analysis [21], transport system modelling [22], selection of pumps [23], assessment of building redevelopment in Lithuanian rural areas [24], the assessment of sustainability of a residential building [25], the facilities sector [26], evaluation of apartment blocks maintenance contractors [27], assessment of partnering relations in construction enterprises [28], evaluation of contracts for construction [29], design of coordinated energy and environmental policies [30], building refurbishment [31], renovation [32–34] and revitalization [35], selection the most appropriate and safe foundation instalment alternative for building [36], indoor environment analysis [37–40], etc.

In the next section, attributes for the assessment of indoor environment of dwelling-houses are selected and optimal values of chosen attributes are determined. These optimal values allow defining the concept of the ideal indoor environment.

3. A MADM method to the assessment of an indoor environment of dwelling-houses

3.1. Attributes of the assessment of an indoor environment

Based on the related work presented above, the attributes of evaluating an indoor environment of dwelling-houses are selected. They are as follows:
- air exchange, m^3/h,
- relative air humidity, percents,

- air temperature, °C,
- air velocity, m/s,
- price per $1m^2$, thousands of LT (1 EUR = 3.4528 LTL),
- noise isolation, dB,
- annual heat requirement, kWh/m^2/year.

42 experts were questioned to determine the significance of the presented attributes. The results of questioning were processed according to [41] and [42]. Figure 1 presents attributes and their weights (w_i), which equal to the sum of significance of a particular attribute divided to the sum of significance of all attributes. Significance is defined as an integer number from 1 to 7 (we have 7 attributes), where 7 is the most important and 1 is the least important. Moreover, a number can appear only once evaluating significance. The correctness of experts' answers was determined by defining their compatibility as presented in [41] and [42]. The result is acceptable.

New attributes, like chemical and biological agents, dusts, etc., can be included into the assessment. We are concentrated on the listed before seven attributes, since according to the experts they are the main in the assessment of indoor environment of dwelling-houses.
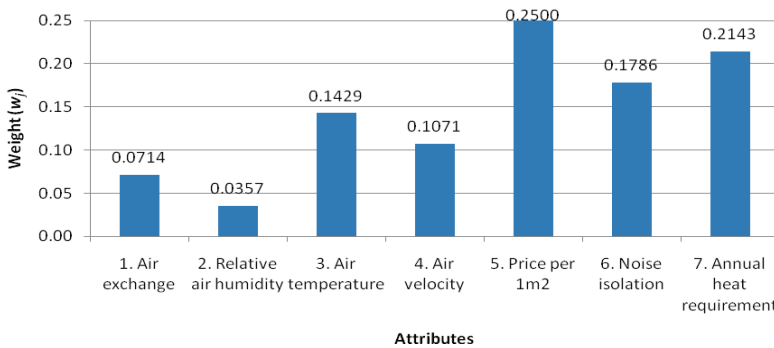
Fig. 1. Weights (w_i) of attributes

As can be seen from Figure 1, the fifth (price per $1m^2$) and seventh (annual heat requirement) attributes have the strongest impact on the assessment of dwelling-houses.

The data of measurements are given in a decision making matrix (Table 2), where columns contain attributes, rows contain dwelling-houses and cells of the matrix contain values of attributes for a particular dwelling-house.

3.2. The concept of the ideal indoor environment according to the selected attributes

The concept of the ideal indoor environment is defined by assigning optimal values to the selected attributes. These optimal values are taken from the Lithuanian hygienic

norm (HN 42:2004) and other standards, like [2], ISO EN 7730 2005 [3], [19] and [20]. Table 1 presents optimal values of the selected attributes.

Table 1. Optimal values for the selected attributes

Attribute	Measuring units	Optimal value
1. Air exchange	m^3/h	≤ 90
2. Relative air humidity	Percents (%)	50*
3. Air temperature	°C	22*
4. Air velocity	m/s	≥0.15* at cold season ≥0.25* at worm season
5. Price per 1m^2	×10^3 LT	minimal value of the attribute is taken
6. Noise isolation	dB	55**
7. Annual heat requirement	kWh/m2/year	≤ 15 kWh/m^2/year

* Average comfort values of air temperature, relative air humidity and air velocity according to the Lithuanian Technical regulations of construction "Heating, ventilation and air exchange" (STR 2.09.02:2005) [43].

** According to the Lithuanian Technical regulations of construction "Noise protection of inside and outside environment" (STR 2.01.07:2003) [44], an acceptable noise level of a transport vehicles outside the building is 55 dB.

Due to individual differences it may be very difficult to satisfy everybody in a space [2]. Individual control of the thermal environment or individual adaptation (clothing, activity) will, however, increase the level of acceptance.

3.3. The TOPSIS method

TOPSIS (for the Technique for Order Preference by Similarity to Ideal Solution) was developed by Hwang and Yoon in 1981 [45]. The basic idea of this method is that the selected alternative should have the shortest distance from the ideal solution and the farthest distance from the negative solution [46]. It evaluates the following decision-making matrix, which refers to *m* alternatives evaluated in terms of *n* criteria (1):

$$D = \left[x_{ij}\right] = \begin{matrix} a_1 \\ a_2 \\ \dots \\ a_m \end{matrix} \begin{bmatrix} x_{11} & x_{12} & \dots & x_{1n} \\ x_{21} & x_{22} & \dots & x_{2n} \\ \dots & \dots & \dots & \dots \\ x_{m1} & x_{m2} & \dots & x_{mn} \end{bmatrix} \tag{1}$$

where:

x_{ij} denotes the performance measure of the *i*-th alternative in terms of the *j*-th criterion,

a_i denotes alternatives.

Step 1: Construct the normalised decision matrix. The TOPSIS method first converts the various criteria dimensions to non-dimensional criteria. An element r_{ij} of the normalised decision matrix R is calculated as follows (2):

$$r_{ij} = \frac{x_{ij}}{\sqrt{\sum_{k=1}^{m} x_{kj}^2}}, \qquad k = 1, ..., m, \qquad j = 1, ..., n,$$
(2)

Step 2: Construct the weighted normalised decision matrix. A set of weights $W = (w_1, w_2, w_3, ..., w_n)$, (where $\sum w_i = 1$) defined by the decision maker is used with the decision matrix R to generate the weighted normalised matrix V as follows (3):

$$V = [w_i r_{ij}] = \begin{matrix} a_1 \\ a_2 \\ ... \\ a_m \end{matrix} \begin{bmatrix} w_1 r_{11} & w_2 r_{12} & ... & w_n r_{1n} \\ w_1 r_{21} & w_2 r_{22} & ... & w_n r_{2n} \\ ... & ... & ... & ... \\ w_1 r_{m1} & w_2 r_{m2} & ... & w_n r_{mn} \end{bmatrix},$$
(3)

Step 3: Determine the ideal and the negative solutions. The ideal, denoted as A^+, and the negative, denoted as A^-, alternatives are defined as follows (4) and (5):

$$A^+ = \{[(\max_i v_{ij} | j \in J), (\min_i v_{ij} | j \in J')], i = 1, ..., m\} = \{a_1^+, a_2^+, ..., a_n^+\},$$
(4)

$$A^- = \{[(\min_i v_{ij} | j \in J), (\max_i v_{ij} | j \in J')], i = 1, ..., m\} = \{a_1^-, a_2^-, ..., a_n^-\},$$
(5)

where $J = \{j = 1, 2, ..., n$ and j is associated with benefit criteria$\}$; $J' = \{j = 1, 2, ..., n$ and j is associated with cost/loss criteria$\}$.

The previous two alternatives are fictions. However, it is reasonable to assume that for the benefit criteria, the decision maker wants to have a maximum value among the alternatives.

Step 4: Calculate the separation measures for each alternative. The separation from the ideal solution is calculated by formula (5a). Similarly, the separation from the negative solution is calculated by formula (5b).

$$L_i^+ = \sqrt{\sum_{j=1}^{n} \left(v_{ij} - a_j^+\right)^2}, \qquad i = 1, ..., m,$$
(5a)

$$L_i^- = \sqrt{\sum_{j=1}^{n} \left(v_{ij} - a_j^-\right)^2}, \qquad i = 1, ..., m. \tag{5b}$$

Step 5: Calculate the relative closeness to the ideal solution. It is calculated as follows (6):

$$K_i^* = \frac{L_i^-}{L_i^+ + L_i^-}, \qquad i = 1, ..., m, \; K_i^* \in [0, 1]. \tag{6}$$

The option with K_i^* closest to 1 is closest to the ideal solution.

Step 6: Determine the rationality index. It is determined using formula as follows (7):

$$Z_{Ti} = \frac{K_i^*}{\max K_i^*}. \tag{7}$$

3.4. Applying TOPSIS to the assessment of an indoor environment of dwelling-houses

In this section, the overall description of the proposition by applying the TOPSIS method is present to the assessment of an indoor environment in dwelling-houses.

The main steps in utilizing TOPSIS are as follows:

1. Determine the relevant attributes and alternatives (dwelling-houses). Attributes used for the assessment of an indoor environment of dwelling-houses are: air exchange (m^3/h), relative air humidity (percents), air temperature (C), air velocity (m/s), price per 1 m^2 (thousands of LT), noise isolation (dB) and annual heat requirement (kWh/m^2/year).

2. Attach weights to the selected attributes.

3. Perform measurements to determine the values of the attributes.

4. Determine the ideal indoor environment by attaching optimal values to the selected attributes.

5. Apply the TOPSIS method to process the obtained measures.

6. Choose the rational indoor environment and compare it with the defined ideal indoor environment.

Note that during determining the ideal and the negative solutions (see Step 3 of the TOPSIS method) the ideal solution will be equal to the ideal indoor environment of a dwelling-house determined in Section 3.2.

The next section presents the case study of evaluating indoor environment of dwelling-houses in Naujoji Vilnia, Vilnius, Lithuania.

4. A case study: Assessment of dwelling-houses in Naujoji Vilnia

The proposed approach of MADM to the assessment of dwelling-houses based on the concept of the ideal indoor environment was applied to assess the 5 single flat houses situated in Naujoji Vilnia, Vilnius, Lithuania. The values of attributes were measured by Metrel device MI 6201 EU, having the calibration certificate. The data of measurements is presented in Table 2.

Table 2. Decision-making matrix of the 5 single flat houses situated in Naujoji Vilnia, Vilnius

House No	Attributes and their measuring units						
	Air exchange	Relative air hu-midity	Air temperature	Air velocity	Price per 1m^2	Noise isolation	Annual heat requirement
Measure	m^3/h	%	°C	m/s	×10^3 LT	dB	kWh/m^2/year
w_i	0.0714	0.0357	0.1429	0.1071	0.2500	0.1786	0.2143
1	21	65	16	0.10	7.00	57	125
2	22	69	17	0.15	6.15	49	133
3	29	68	17	0.09	3.63	56	127
4	22	55	18	0.07	7.06	48	130
5	33	73	16	0.12	6.78	54	120
	max	min/max	min/max	min/max	min	min	min
Optimal value	≤ 90	50	22	0.17	3.63	55	≤ 15

Table 3 presents the normalised values of attributes, calculated according (2).

Table 3. Normalised decision-making matrix of the 5 single flat houses situated in Naujoji Vilnia, Vilnius

House No	Attributes and their measuring units						
	Air exchange	Relative air humidity	Air temperature	Air velocity	Price per 1 m^2	Noise isolation	Annual heat requirement
Measure	m^3/h	%	°C	m/s	×10^3 LT	dB	kWh/m^2/year
w_i	0.0714	0.0357	0.1429	0.107100	0.2500	0.1786	0.2143
1	0.6364	0.7692	0.7273	0.588235	0.5186	0.1579	0.1200
2	0.6667	0.7246	0.7727	0.882353	0.5902	0.1837	0.1128
3	0.8788	0.7353	0.7727	0.529412	1.0000	0.1607	0.1181
4	0.6667	0.9091	0.8182	0.411765	0.5142	0.1875	0.1154
5	1.0000	0.6849	0.7273	0.705882	0.5354	0.1667	0.1250
	max	min/max	min/max	min/max	min	min	min
Optimal value	1	1	1	1	1	1	1

Table 4 presents the separation from the ideal solution L_i^+, calculated by formula (5a), the separation from the negative solution L_i^-, calculated by formula (5b), the relative closeness to the ideal solution K_i^*, calculated by formula (6), and the rationality index Z_{Ti}, calculated by formula (7).

Now it is possible to determine the deviation of each alternative (an indoor environment of a dwelling-house) from the optimal value. For this purpose the rationality index Z_{Ti} of the optimal value (the ideal solution) is compared with the rationality indexes of each alternative. The comparison is presented in Figure 2.

Table 4. Calculations by TOPSIS to the 5 single flat houses situated in Naujoji Vilnia, Vilnius

House No.	L_i^+	L_i^-	K_i^*	Z_{Ti}
1	0.0644	0.2704	0.8076	0.8076
2	0.0465	0.2657	0.8510	0.8510
3	0.1357	0.2424	0.6411	0.6411
4	0.0728	0.2682	0.7865	0.7865
5	0.0505	0.2694	0.8422	0.8422
Optimal value	0.2714	0.0785	1	1
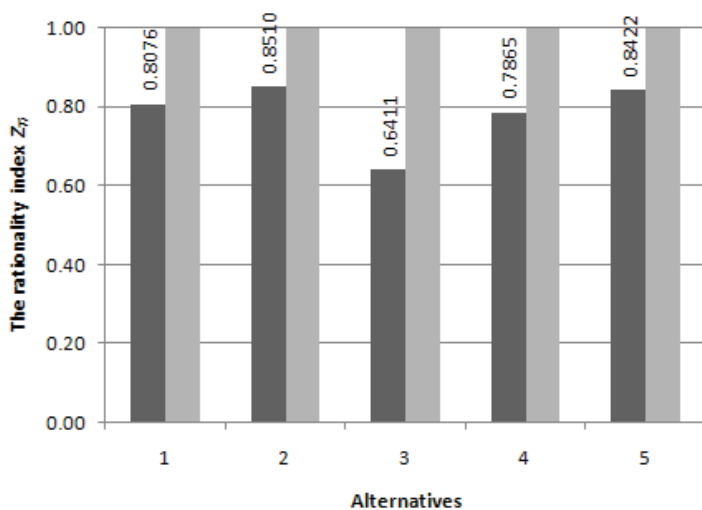
Fig. 2. The comparison of the rationality indexes Z_{Ti} of the 5 single flat houses in Naujoji Vilnia, Vilnius, Lithuania (dark columns) with the ideal indoor environment (light columns)

As can be seen from the comparison (Figure 2), the second and the fifth single flat houses have the best indoor environment compared to other houses. However, the indoor environment of all five houses does not meet the ideal environment. This is because of high annual heat requirements of each house.

5. Conclusions

The analysis of the related work on the assessment of an indoor environment of dwelling houses shows that a number of methods and models have been proposed to measure and analyse an indoor environment. In those works authors apply a particular

multi-attribute decision making method to assess indoor environment of chosen dwelling-houses and/or determine the best or the worst indoor environment. However, there is lack of works comparing a present state of an indoor environment of dwelling-houses with standards, like the Lithuanian hygienic norm or ISO EN 7730.

The proposed approach on multi-attribute decision making to the assessment of dwelling-houses including the ideal indoor environment allows to evaluate not only the current state of indoor environment of chosen dwelling-houses, but determine the deviation of each alternative (an indoor environment of dwelling-houses) from the optimal value.

In this paper, multi-attribute assessment of indoor environment by applying the TOPSIS method to analyse the results obtained in the investigation is presented. For the detailed study the following attributes were selected: air exchange (m^3/h), relative air humidity (percents), air temperature (C), air velocity (m/s), price per 1 m^2 (thousands of LT (1 EUR = 3.4528 LTL)), noise isolation (dB) and annual heat requirement (kWh/m^2/year).

The experimental data obtained by assessing five single flat houses situated in Naujoji Vilnia, Vilnius, Lithuania shows that the second and the fifth single flat houses have the best indoor environment. However, the indoor environment of all five houses does not meet the ideal environment, determined according to Lithuanian hygienic norm. A high annual heat requirement has a strong impact on indoor environment and is not acceptable in all five houses.

The results presented in this paper show that the proposed approach can be used to evaluate an indoor environment and to determine does it meet standards.

The next step of the research could be aimed at extending and verifying the proposed approach and defining the particular attributes to determine the validity of the method.

References

[1] HN 42:2004: *Microclimate of residential and administrative buildings* (in Lithuanian), Lithuanian hygienic norm. Zin., No. 105–3911, 2004.
[2] Olesen B.W.: *International standards for the indoor environment*, Indoor Air, Vol. 14, No. 7, 2004, pp. 18–26.
[3] ISO EN 7730 2005: *Moderate thermal environments. Determination of the PMV and PPD indices and specification of the conditions for thermal comfort*, International Standards Organisation, Geneva.
[4] Fanger P.O.: *What is IAQ?*, Indoor Air, Vol. 16, No. 5, 2006, pp. 328–334.
[5] Ali H.H., Almomani H.M., Hindeih M.: *Evaluating indoor environmental quality of public school buildings in Jordan*, Indoor and Built Environment, Vol. 18, No. 1, 2009, pp. 66–76.
[6] Hui P.S., Wong L.T., Mui K.W.: *Using carbon dioxide concentration to assess indoor air quality in offices*, Indoor and Built Environment, Vol. 17, No. 3, 2008, pp. 213–219.
[7] Hui P.S., Wong L.T., Mui K.W.: *Evaluation of professional choice of sampling locations for indoor air quality assessment*, Building and Environment, Vol. 42, No. 8, 2007, pp. 2900–2907.

[8] Bluyssen P.M.: *Management of the indoor environment: from a component related to an interactive top-down approach*, Indoor and Built Environment, Vol. 17, No. 6, 2008, pp. 483–495.

[9] Tian L., Zhang G., Zhang Q., Moschandreas D.J., Hao J., Lin J., Liu Y.: *The impact of kitchen activities on indoor pollutant concentrations*, Indoor and Built Environment, Vol. 17, No. 4, 2008, pp. 377–383.

[10] Kavraz M., Abdulrahimov R.: *A study comparing the noise reduction behaviour of variously shaped barriers of limited size in indoor spaces*, Indoor and Built Environment, Vol. 18, No. 6, 2009, pp. 541–552.

[11] Latif M.T., Othman M.R., Kim C.L., Murayadi S.A., Sahaimi K.N.A.: *Composition of household dust in semi-urban areas in Malaysia*, Indoor and Built Environment, Vol. 18, No. 2, 2009, pp. 155–161.

[12] Vilcekova S., Senitkova I.: *Modelling the occurrence of nitrogen oxides indoors*, Indoor and Built Environment, Vol. 18, No. 2, 2009, pp. 138–143.

[13] Yik F.W.H., Lun Y.F.: *Energy saving by utilizing natural ventilation in public housing in Hong Kong*, Indoor and Built Environment, Vol. 19, No. 1, 2010, pp. 73–87.

[14] Singh J., Yu C.W.F., Kim J.T.: *Building pathology, investigation of sick buildings – toxic moulds*, Indoor and Built Environment, Vol. 19, No. 1, 2010, pp. 40–47.

[15] Boyce P.R.: *Review: the impact of light in buildings on human health*, Indoor and Built Environment, Vol. 19, No. 1, 2010, pp. 8–20.

[16] Braubach M.: *Residential conditions and their impact on residential environment satisfaction and health: results of the WHO large analysis and review of European housing and health status (LARES) study*, Int. J. Environment and Pollution, Vol. 30, No. 3–4, 2007, pp. 384–403.

[17] Cheong K.W.D., Yu W.J., Kosonen R., Tham K.W., Sekhar S.C.: *Assessment of thermal environment using a thermal manikin in a field environment chamber served by displacement ventilation system*, Building and Environment, Vol. 41, 2006, pp. 1661–1670.

[18] Gulyas A., Unger J., Matzarakis A.: *Assessment of the microclimatic and human comfort conditions in a complex urban environment: modelling and measurements*, Building and Environment, Vol. 41, 2006, pp. 1713–1722.

[19] *What is a Passive House?*, Passive House Institute, 2010, http://www.passivehouse.us/passiveHouse/PassiveHouseInfo.html

[20] Ludeman C.: *Passive house (passivhaus) standard for energy efficient design*, 2008, http://www.100khouse.com/2008/04/10/passive-house-passivhaus-standard-for-energy-efficient-design/

[21] Zavadskas E.K., Turskis Z., Tamosaitiene J.: *Risk assessment of construction projects*, Journal of Civil Engineering and Management, Vol. 16, No. 1, 2010, pp. 33–46.

[22] Jakimavicius M., Burinskiene M.: *Assessment of Vilnius city development scenarios based on transport system modelling and multicriteria analysis*, Journal of Civil Engineering and Management, Vol. 15, No. 4, 2009, pp. 361–368.

[23] Ulubeyli S., Kazaz A.: *A multiple criteria decision-making approach to the selection of concrete pumps*, Journal of Civil Engineering and Management, Vol. 15, No. 4, 2009, pp. 369–376.

[24] Antucheviciene J., Zavadskas E.K., Zakarevicius A.: *Multiple criteria construction management decisions considering relations between criteria*, Technological and economic development of economy, Vol. 16, No. 1, 2010, pp. 109–125.

[25] Zavrl M.S., Zarnic R., Selih J.: *Multicriterial sustainability assessment of residential buildings*, Technological and economic development of economy, Vol. 15, No. 4, 2009, pp. 612–630.

[26] Brauers W.K., Zavadskas E.K.: *Robustness of the multi-objective MOORA method with a test for the facilities sector*, Technological and economic development of economy, Vol. 15, No. 2, 2009, pp. 352–375.

[27] Zavadskas E.K., Kaklauskas A., Vilutiene T.: *Multicriteria evaluation of apartment blocks maintenance contractors: Lithuanian case study*, International Journal of Strategic Property Management, Vol. 13, No. 4, 2009, pp. 319–338.

[28] Radziszewska-Zielina E.: *Methods for selecting the best partner construction enterprise in terms of partnering relations*, Journal of Civil Engineering and Management, Vol. 16, No. 4, 2010, pp. 510–520.

[29] Podvezko V., Mitkus S., Trinkuniene E.: *Complex evaluation of contracts for construction*, Journal of Civil Engineering and Management, Vol. 16, No. 2, 2010, pp. 287–297.

[30] Greening L.A., Bernow S.: *Design of coordinated energy and environmental policies: use of multi-criteria decision-making*, Energy Policy, Vol. 32, No. 6, 2004, pp. 721–735.

[31] Kaklauskas A., Zavadskas E.K., Raslanas S.: *Multivariant design and multiple criteria analysis of building refurbishments*, Energy and Buildings, Vol. 37, No. 4, 2005, pp. 361–372.

[32] Martinaitis V., Kazakevičius E., Vitkauskas A.: *A two-factor method for appraising building renovation and energy efficiency improvement projects*, Energy Policy, Vol. 35, No. 1, 2007, pp. 192–201.

[33] Martinaitis V., Rogoza A., Bikmaniene I.: *Criterion to evaluate the "two-fold benefit" of the renovation of buildings and their elements*, Energy and Buildings, Vol. 36, No. 1, 2004, pp. 3–8.

[34] Zavadskas E.K., Raslanas S., Kaklauskas A.: *The selection of effective retrofit scenarios for panel houses in urban neighborhoods based on expected energy savings and increase in market value: The Vilnius case*, Energy and Buildings, Vol. 40, No. 4, 2008, pp. 573–587.

[35] Zavadskas E.K., Antucheviciene J.: *Development of an indicator model and ranking of sustainable revitalization alternatives of derelict property: a Lithuanian case study*, Sustainable Development, Vol. 14, No. 5, 2006, pp. 287–299.

[36] Zavadskas E.K., Turskis Z., Vilutiene T.: *Multiple criteria analysis of foundation instalment alternatives by applying Additive Ratio Assessment (ARAS) method*, Archives of Civil and Mechanical Engineering, Vol. 10, No. 3, 2010, pp. 123–141.

[37] Kalibatas D., Turskis Z.: *Multicriteria evaluation of inner climate by using MOORA method*, Information Technology and Control, Vol. 37, No. 1, 2008, pp. 79–83.

[38] Mui K.W., Chan W.T.: *Building calibration for indoor air quality management*, Building and Environment, Vol. 41, 2006, pp. 877–886.

[39] Rutman E., Inard C., Bailly A., Allard F.: *A global approach of indoor environment in an air-conditioned office room*, Building and Environment, Vol. 40, 2005, pp. 29–37.

[40] Wong L.T., Mui K.W., Hui P.S.: *A statistical model for characterizing common air pollutants in air-conditioned offices*, Atmospheric Environment, Vol. 40, 2006, pp. 4246–4257.

[41] Kendall M.G.: *Rank correlation methods*, 4th ed., Griffin, London, 1970.

[42] Zavadskas E.K., Turskis Z., Ustinovichius L., Shevchenko G.: *Attributes weights determining peculiarities in multiple attribute decision making methods*, Inzinerine Ekonomika –Engineering Economics, Vol. 21, No. 1, 2010, pp. 32–43.

[43] STR 2.09.02:2005. *Heating, ventilation and air exchange*, Zin., 2005, No. 75–2729.

[44] STR 2.01.07:2003. *Noise protection of inside and outside environment*, Zin., 2003, No. 79–3614.

[45] Hwang C.L., Yoon K.: *Multiple attribute decision making – methods and applications. A state-of-the-art surwey*, Springer Verlag, Berlin, 1981.

[46] Triantaphyllou E.: *Multi-criteria decision making methods: a comparative study*, Springer, 2000.

Wieloatrybutowa ocena środowisk wewnętrznych domów zamieszkałych oparta na koncepcji idealnego środowiska wewnętrznego

Artykuł ten prezentuje wieloatrybutową ocenę środowisk wewnętrznych zamieszkałych domów. Zależy ona od wielu kryteriów, takich jak temperatura, wilgotność, hałas itp. Istnieje wiele prac, które porównują wewnętrzne środowiska różnych zamieszkałych domów i wybierają najlepszą możliwość. Tylko kilka z nich porównuje stan faktyczny środowisk wewnętrznych zamieszkałych domów z normami, takimi jak litewska norma „higieny" lub ISO 7730. W niniejszej pracy pokazano wieloatrybutową ocenę środowisk wewnętrznych domów zamieszkałych, opartą na koncepcji idealnego środowiska wewnętrznego. Koncepcja ta definiuje optymalne środowisko wewnętrzne domów zamieszkałych zgodnie litewską normą „higieny" i innymi regulacjami prezentowanymi w pracy i jest wprowadzona, aby wyznaczyć odchylenia każdej możliwości (środowiska wewnętrznego domów zamieszkałych) od wartości optymalnych. W analizowanym przypadku wykorzystano metodę TOPSIS do wieloatrybutowej oceny środowiska wewnętrznego domów zamieszkałych w Naujoji Vilnia w Wilnie na Litwie.

Impact and dynamic resistance of SFRCC modified by varied superplasticizers

J. KATZER

Koszalin University of Technology, ul. Śniadeckich 2, 75-453 Koszalin, Poland.

The paper presents results of examinations of steel fiber reinforced cement composites (SFRCC) modified by superplasticizers based on different chemical substances. The described SFRCC were made on the basis of fine aggregate cement matrix modified by steel fibers of an aspect ratio $l/d = 50$. Fine aggregate matrix composed of waste aggregate (obtained during hydroclassification) was modified by an addition from 0% to 2.8% (by volume) of hooked steel fibers and 1% of superplasticizer. After establishing basic parameters of fresh mix and hardened fiber reinforced composites, the main tests were a drop-weight test of the SFRCC plates and dynamic harmonic loading of beams. Results achieved this way allowed to specify the influence of the specific superplasticizer on the behaviour of SFRCC subjected to a dynamic force.

Keywords: *aggregate, cement, composite, fiber, waste*

1. Introduction

Development of modern civil engineering includes an urgent need to develop higher performance engineering materials characterized by high strength, toughness, energy absorption, durability, etc [1]. One of such still developing high performance engineering materials is steel fiber reinforced cement composite (SFRCC). This paper presents an experimental investigation carried out on three series of SFRCC. Steel fiber-reinforced cement composite is more difficult to mix and place than plain concrete. Adding any type of steel fiber to cement composite reduces fluidity of the mixture because of the needle-like shape and high specific surface of the fibers. The geometry and water requirements of SFRCC are an obstacle to its workability [2–4]. These factors lead to a reduction in consistency and the necessity to use superplasticizer. It is much more difficult to quantitatively investigate dynamic properties of material than to qualitatively study static or quasi-static properties [5–6]. Static and quasi-static properties of SFRCC are already well-known and described [7–10], but there is still lack of research programs concerning dynamic properties of such composites.

2. Materials and test method

Materials consisted of ordinary Portland cement with 28-day compressive strength of 32.5 MPa (CEM I 32.5), waste fine aggregate of maximum size 2 mm, tap water for mixing and curing and three superplasticizing admixtures. There were used: one su-

perplasticizer based on polycarboxylate, one superplasticizer based on polyether and one special multifunctional superplasticizer. All three superplasticizers, used in the research programme are commercially available products offered by large and well known admixture producers and can be classified by ASTM C-494 and ASTM C-1017 as high range water reducers.

Superplsticizers based on polycarboxylate were introduced into civil engineering in 1993 [11–12]. The performed dispersion mechanism of these superplasticizers is related to a steric hindrance effect produced by the presence of neutral side long graft chains of the polymer molecules. The graft chains on the surface of cement are hindered by themselves from flocculating into large and irregular agglomerates of cement particles. Superplsticizers based on polyether were introduced into civil engineering in 1997 [11–12]. The performed dispersion mechanism of these superplasticizers is similar to the mechanism of polycarboxylate superplasticizers. A polyether based superplasticizers are characterized by much longer side chains of ethylene oxide (130 moles) than polycarboxylate based superplasticizers (25 moles of ethylene oxide). This change creates a lower adsorption speed and reduces the typical retarding effect related to the early adsorption in comparison to polycarboxylate based superplasticizers. Special multifunctional superplasticizers were introduced into civil engineering in the beginning of the 21st century [11–12]. The action of used special multifunctional superplasticizer is twofold − traditional water reduction effect on the one side and the formation of pore closing crystals, on the other side. These active processes of the admixture are permanent and not reversible and achieved due to small addition of highly reactive and very fine silica fume. Raw silica fume is widely and successfully used all over the world as an additive to special concretes [5, 11, 13–15]. In recent years due to numerous technological and health concerns about proper shipping and unloading and process of batching of raw silica fume and restrict storage requirements, more and more admixture and additive producers switch to production either of silica fume paste or superplasticizer containing silica fume [16].

The superplasticizers are codified as PC3, PE and CRSP. The PC3 is a superplasticizer based on polycarboxylate, the PE superplasticizer is based on polyether, and the CRSP superplasticizer contains silica fume. The density of PC3, PE and CRSP superplasticizers was equal to 1.1 g/cm^3, 1.1 g/cm^3 and 1.45 g/cm^3 respectively. These superplasticizers (and their influence on properties of the fresh mix) were described in previous work [17]. The superplasticizing admixture was batched in quantity equal to 1% (by mass of cement). The water to cement ratio (w/c) was 0.50.

The waste fine aggregate used in the examinations was of glacial origin and was obtained as a by-product from the process of hydro-classification of natural all-in-aggregate. The main mineral component of the aggregate is quartz and crystalline rock, dominated by granite. As far as smoothness of the grain surface is concerned fine aggregate is composed of angular and partially subrounded grains. Main properties of used aggregate are presented in Table 1. This aggregate was described in detail in previous works [18–19].

Table 1. Physical features of waste fine aggregate

Feature	Symbol	Size
Loose bulk density	ρ_n^1	1631 kg/m^3
Compacted bulk density	ρ_n^z	1805 kg/m^3
Fineness modulus by Kuczyński	U_K	3.279
Fineness modulus by Hummel	U_H	66.4
Fineness modulus by Abrams	U_A	2.206
Cavity of loose aggregate	j_l	38%
Cavity of compacted aggregate	j_z	32%
Porosity	P	3.39%

Hooked steel fibers of a length equal to 50 mm and circular cross-section, with an aspect ratio $l/d = 50$ and breaking strength of 1100 MPa were used in this research study. The shape of applied steel fibers is presented in Figure 1. The mix was modified by the addition of steel fibers used of volume fractions varying between 0 and 2.8%. Mixing, vibrating and curing of SFRCC was applied according to the procedures described in [11, 14].
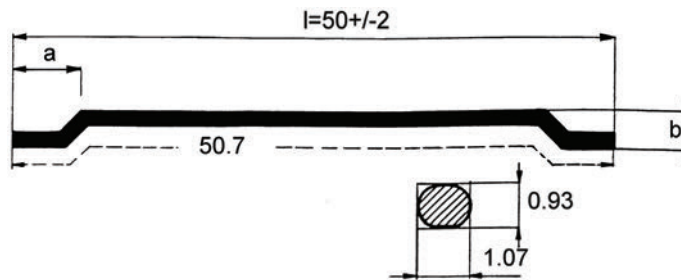
Fig. 1. Shape of applied steel fibers ($a = 5$ mm ± 2mm, $b = 3$ mm ± 1 mm)

The specimens were in a form of big beams, small beams and plates. Before testing, small beams (100 × 100 × 400 mm) were cut into three cube specimens. These specimens were used to determine the compression strength f_{cube} and density ρ. For the impact test, a drop-weight apparatus was used. A steel ball of 2381 g was falling onto the centre of a freely supported plate (250 × 250 × 50 mm) from a fixed height of 500 mm. Energy passed to the plate during one weight drop was equal to 11.7 J. Number of dropping the weight until the appearance of the first crack n_{crack} and until ultimate destroying the plate n_{max} was counted. Big beams (100 × 200 × 2000 mm) were exposed to an exciting harmonic force changeable in time. These beams were examined in the open air test facility consisted of two large concrete support blocks, and an electronically controlled inertial inductor comprising two counter-rotating cast steel discs was used to expose the beams to a time-varying harmonic force excitation. Six different attachment positions for the spinning elements enabled forces to be set with values equal to 100%, 85%, 70%, 55%, 40% and 25% of the maximum force. In this way six different levels of dynamic loading from Q_1 to Q_6 were easily achieved (for Q_1

from 44 N to 1097 N, for Q_2 from 70 N to 1755 N, for Q_3 from 96 N to 2414 N, for Q_4 from 123 to 3070, for Q_5 from 149 to 3730 N and for Q_6 from 175 to 4388 N). The applied inertial inductor is shown in Figure 2. Both the inertial inductor and whole test facility are described in detail in previous publications [6, 17].
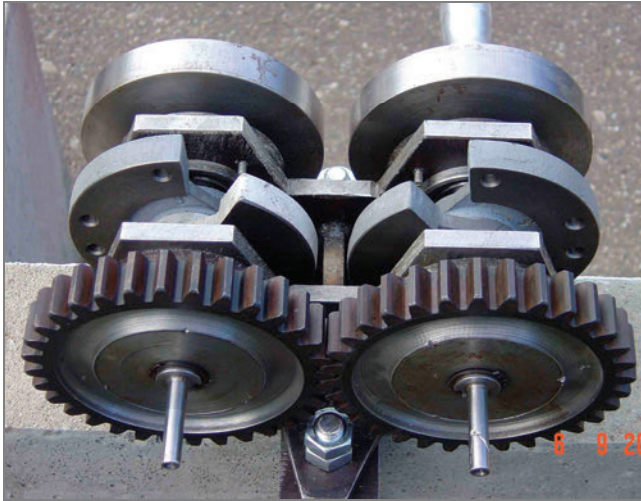

Fig. 2. Inertial inductor

All examined beams were dynamically loaded until failure or until execution all six levels of loading. Beam failure is taken as the condition when the first crack propagates through the beam cross-section. The moment was accompanied with an instant increase of vibration acceleration. Beams were loaded in cycles which lasted 225 seconds. At a given cycle of loading, the spinning disks of the inertial inductor were accelerated within 10 seconds to reach rounds generating exciting force of a frequency equal to 8 Hz. Then, within 5 seconds the first measurement of acceleration of vibration was made. Further on, within 5 seconds the rounds of spinning disks were increased by 2 Hz, and within the next 5 seconds new measurement of acceleration of vibration was carried out. This procedure was repeated until the rounds of spinning disks reached 50 Hz. The scheme of a single cycle of dynamic loading is shown in the Figure 3. In total, 15 mixtures were made, including 5 mixtures modified by superplasticizing admixture PC3, 5 mixtures modified by the PE, and 5 mixtures modified by the CRSP. These three groups of mixtures had the same contents (fine aggregate = 1780 kg/m^3, cement = 400 kg/m^3, water = 200 kg/m^3, superplasticizer = 4 kg/m^3). The only difference between them was the volume of the applied steel fiber.

The examination results were statistically processed, and values bearing the gross error were assessed on the basis of Grabbs criterion [20]. The objectivity of the experiments was assured by the choice of the sequence of the realization of specific experiments from a table of random numbers. All calculations connected with speci-

fying a correlation coefficient and graphic interpretation of the model was carried using a statistical computer program [21–22]. Polynomial fit was used to achieve contour plots. Fitted functions were characterized by a correlation coefficient equal to at least 0.9.
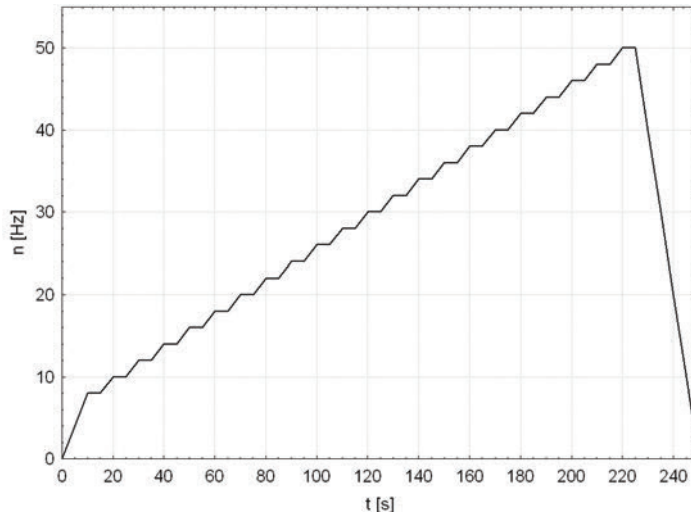

Fig. 3. Single cycle of dynamic loading

3. Test results

Workability is shown on a line plot in Figure 4 independently for each applied admixture in relation to the volume of batched steel fibers.
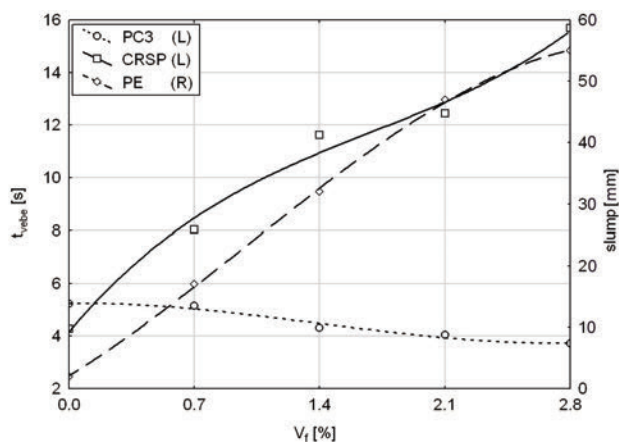
Fig. 4. Workability of fresh SFRCC

Mixtures modified by the PC3 and CRSP admixtures were examined according to Vebe procedure. Mixtures modified by the PE admixture were too liquid to warrant the use of the Vebe; instead the consistency was determined using the slump procedure. All three admixtures are shown to influence workability in different ways. The PC3 admixture enables to maintain constant workability at a level of $t_{\text{Vebe}} = 4.5 \pm 0.8$ seconds for all examined mixtures. In the case of the CRSP admixture, consistency becomes stiffer together with the increased addition of steel fibers. Unreinforced composite modified by CRSP was characterized by $t_{\text{Vebe}} = 4.3$ s, and the mixture with maximum addition of steel fibers was characterized by $t_{\text{Vebe}} = 15.7$ s. Admixture PE led to relatively high fluidity. As the quantity of batched fibers increases, the consistency becomes more and more liquid. Unreinforced composite is characterized by $h_{\text{slump}} = 2$ mm and the composite with the maximum addition of steel fibers is characterized by $h_{\text{slump}} = 55$ mm. This phenomenon is caused by high air content in fresh SFRCC. Effect of high airing of some fresh SFRCC will be discussed in a separate study.

Fig. 5. Compressive strength and density of SFRCC modified by different superplasticizers
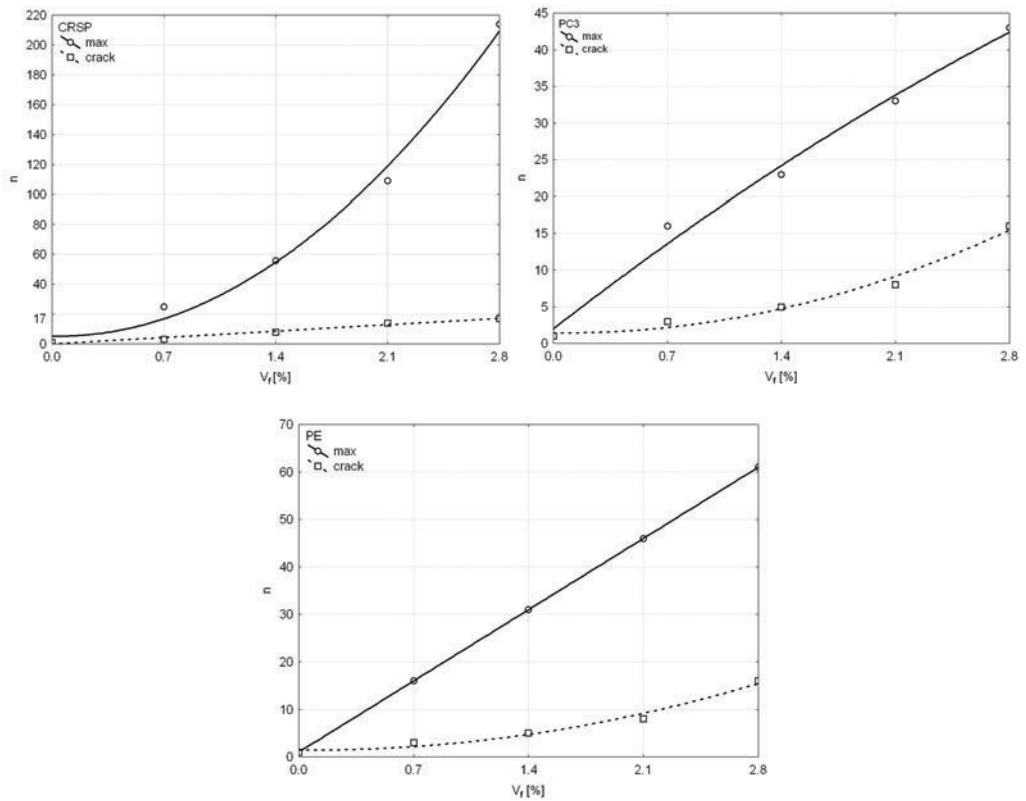
Fig. 6. Number of dropping the weight until the appearance of the first crack n_{crack}
and until ultimate destroying the plate n_{max} was counted

Compressive strength and density of the hardened SFRCC are shown on Figure 5 independently for each of the applied admixtures in relation to the volume of batched steel fibers. Compressive strength of cemen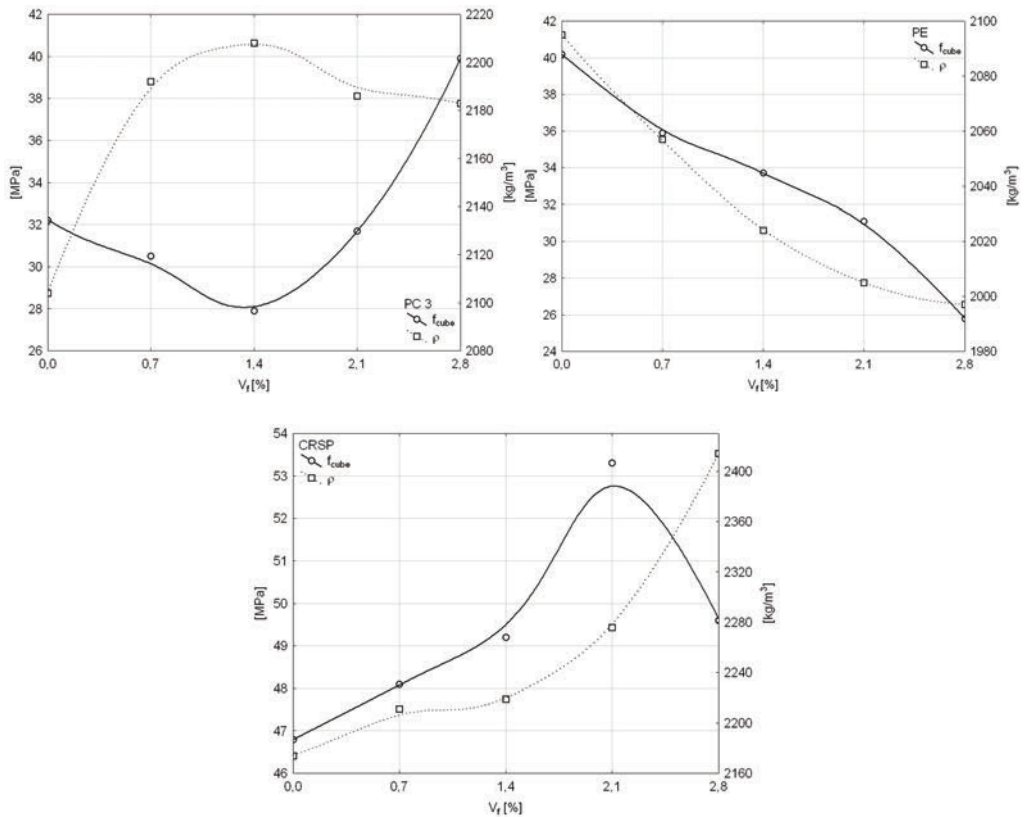t composites with the admixture PC3 decreased from f_{cube} = 32.20 MPa for unreinforced composite to a value of f_{cube} = 27.90 MPa at a V_f = 1.4%. Thereafter the strength increased again with further increase in the volume of fibers until it reaches f_{cube} = 39.90 MPa at the maximum addition of fibers. Unreinforced composite is characterized by a density ρ = 2104 kg/m^3. The density increased with an increase in the addition of fibers until it reaches ρ = 2208 kg/m^3 at V_f = 1.4%. Further dosing of fibers slightly decreased the density of composite which is characterized by ρ = 2183 kg/m^3 at a maximum addition of fibers. In case of composite modified by admixture PE, together with the increase of fiber content there is a decrease of both strength from f_{cube} = 40.20 MPa to f_{cube} = 25.80 MPa, and the density from ρ = 2095 kg/m^3 to ρ = 1997 kg/m^3. The addition of the admixture CRSP increased the density of composite from ρ = 2174 kg/m^3 for unreinforced one to ρ = 2414 kg/m^3 for composite modified by a maximum quantity of fibers. Compressive strength in-

creased from f_{cube} = 46.80 MPa for unreinforced composite to f_{cube} = 53.30 MPa for composite of fibre contents V_f = 2.1%. The number of dynamic loading until the appearance of the first crack n_{crack} is equal to 16 for all three superplasticizers. The number of dynamic loading until ultimate destroying the plate n_{max} is equal 43, 61 and 214 for PC3, PE and CRSP admixture respectively (Figure 6).
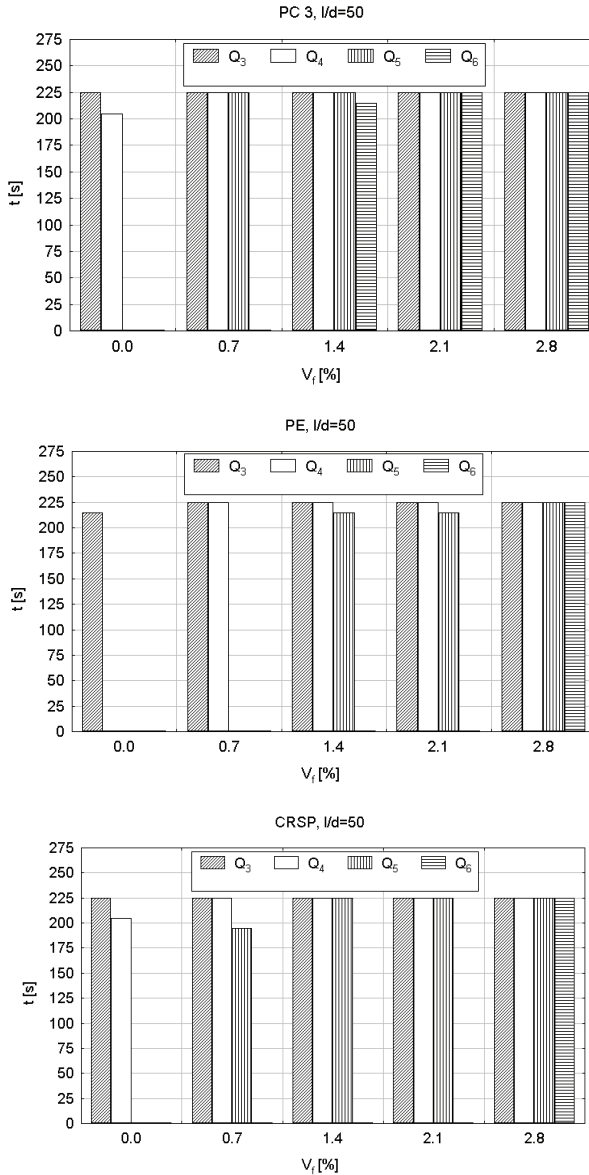

Fig. 7. Duration of cycles of loading of beams modified by different superplasticizers

The duration of a dynamic loading of a beam until its failure was taken as to estimate load-carrying ability. Because of the specificity of the examination connected with six separate cycles of loading from Q_1 to Q_6, time of loading was shown in a form of a column plot for each type of beams separately. None of the beams failed during the first two cycles of loading (from Q_1 to Q_2). Therefore, Figure 7, shows only the duration of loadings for cycles from Q_3 to Q_6. The maximum duration of a cycle of loading (Figure 3) was 225 seconds. Beams modified by the PC3 admixture were characterized by the highest resistance to dynamic loading. The addition of fibers ranging from 2.1% to 2.8% allowed the load-carrying ability of beams through 255 seconds during the cycles of loading Q_3, Q_4, Q_5, and Q_6. In case of beams modified by the PE and CRSP admixtures, only the maximum addition of fibers, of 2.8% enabled to maintain the load-carrying ability of beams subjected to the cycles of loading Q_3, Q_4, Q_5 and Q_6. Beams modified by the PE admixture were characterized by the overall smallest load-carrying ability under cycles of dynamic loadings.

4. Discussion and conclusions

The PC3, PE, and CRSP admixtures, represent three groups of most frequently used superplasticizers. Modifying the same cement composite mixtures by each of the mentioned superplasticizers allowed to achieve fiber-reinforced composites of entirely different features of density, strength and dynamic parameters. The main advantage to SFRCC beams mechanical properties resulting from the admixture of particular superplsticizer is the increase in number of impact loading until its failure and the increase in duration of a dynamic loading until its failure. The number of impact loading until the appearance of the first crack n_{crack} is the same for all free superplasticizers. The total number of a dynamic loading of all SFRCC plates modified by the CRSP admixture is the highest one. It is nearly four and five times higher then the number of a dynamic loading of plates modified by the PE and PC3 admixtures, respectively. The total duration of a dynamic loading of all SFRCC beams modified by the PC3 admixture is the highest one. It is nearly 13% and 24% higher then the duration of a dynamic loading of all beams modified by the CRSP and PE admixtures, respectively. The choice of superplasticizer is shown to have marked influence on strength and impact resistance of SFRCC.

References

[1] Luo X., Sun W., Chan S.: *Characteristics of high-performance steel fiber-reinforced concrete subject to high velocity impact*, Cement and Concrete Research, Vol. 30, No. 6, 2000, pp. 907–914.
[2] Maidl B.R.: *Steel fibre reinforced concrete*, Ernest&Sohn, Berlin, 1995.
[3] Johnston C.D.: *Fiber reinforced cements and concretes*, Gordon and Breach Science Publisher, Ottawa, 2001.

[4] Weiss H.J., Edgington J.: *On the workability of steel fiber mortar mix*, Archiwum Inżynierii Lądowej, Vol. XXXIII, No. 1, 1987, pp. 3–7.

[5] Nawy E.G.: *Fundamentals of high strength high performance concrete*, Longman, Harlow, Essex, England, 1996.

[6] Katzer J.: *Mechanical properties of fine aggregate SFRC beams under dynamic load*, Proceedings, 1st Central European Congress on Concrete Engineering "Fibre Reinforced Concrete in Practice", 8–9 September 2005, Graz, Austria, pp. 81–84.

[7] Katzer J., Piątek Z.: *Chosen Features of fine aggregate concrete modified by silica fume and steel fibre*, Proceedings, International Conference "Concrete and Concrete Structures", 28–29 April 1999, Žilina, Slovakia, pp. 41–46.

[8] Al-Khalaf M.N., Page C.L., Ritchie A.G.B.: *Effects of fibre surface composition on mechanical properties of steel fibre reinforced mortars*, Cement and Concrete Research, Vol. 10, No. 1, 1980, pp. 71–77.

[9] Cao J., Chung D.D.L.: *Improving the dispersion of steel fibers in cement mortar by the addition of silane*, Cement and Concrete Research, Vol. 31, No. 2, 2001, pp. 309–311.

[10] Kosa K., Naaman A.E., Hansen W.: *Durability of fiber reinforced mortar*, ACI Materials Journal, Vol. 88, No. 3, 1991, pp. 310–319.

[11] Colepardi M.: *The new concrete*, Grafiche Tintoretto, Italy, 2006.

[12] Spiratos N., et al.: *Superplasticizers for concrete*, Marquis, Quebec, Canada, 2006.

[13] Katzer J.: *Strength and watertightness of fiber reinforced concrete modified by silica fume*, e-Mat - Revista de Ciência e Tecnologia de Materiais de Construção Civil, Vol. 2, No. 2, 2005, pp. 157–161.

[14] Katzer J.: *Strength, deflection and watertightness of steel fiber reinforced concrete modified by silica fume*, West Indian Journal of Engineering, Vol. 30, No. 2, 2008, pp. 50–56.

[15] Katzer J.: *Permeability of SFRCC based on fine aggregate after pre-load cycles*, Proceedings, Brittle Matrix Composites 9, 25–28 October, 2009, Warsaw, Poland, pp. 139–148.

[16] FHWA-IF-05-016, Silica fume user's manual, Silica fume association, April, 2005.

[17] Katzer J.: *Dynamic properties of SFRM beams modified by varied superplasticizers*, Proceedings (Supplementary Papers), Eighth CANMET/ACI International conference on superplasticizers and other chemical admixtures in concrete, 29 October–1 November 2006, Sorrento, Italy, pp. 21–35.

[18] Katzer J.: *Beschreibung der granulometrischen Eigenschaften der Zuschlagstoffe Mittelpommerns mithilfe des Median-Korns*, BetonWerk International, No. 06, 2003, pp. 7–12.

[19] Katzer J., Kobaka J.: *The assessment of fine aggregate pit deposits for concrete production*, Kuwait Journal of Science and Engineering, Vol. 33, No. 2, 2006, pp. 165–174.

[20] Borovikov I.P., Borovikov V.P.: *STATISTICA data preparation and analysis*, Filini, Moscow, 1998.

[21] Afifi A.A., Clark V.: *Computer aided multivariate analysis*, Chapman & Hall, London, 1999.

[22] Lee-Ing T., Chung-Ho W.: *STATISTICA V5.5 and basic statistic analysis*, TasngHai Publisher, Taiwan, 2002.

Uderzeniowa i dynamiczna odporność fibrokompozytów cementowych modyfikowanych różnymi superplastyfikatorami

W referacie przedstawiono wyniki badań nad fibrokompozytami cementowymi wykonanymi na bazie drobnych kruszyw odpadowych. Do wykonania fibrokompozytów wykorzystano

włókna stalowe produkcji krajowej. Włókna dozowano w ilości od 0 do 2,8% (objętościowo). Badania obejmowały swym zakresem dwa etapy. Etap pierwszy stanowiły badania cech świeżej mieszanki (konsystencja) oraz badania stwardniałych fibrokompozytów wykonane w sposób statyczny (gęstość, wytrzymałość na ściskanie). Drugi etap stanowiły badania cech dynamicznych omawianych fibrokompozytów obejmujące swym zakresem badania uderzeniowe oraz badania przy obciążeniu harmonicznym. Badania przy obciążeniu harmonicznym prowadzono na polowym stanowisku laboratoryjnym przy wykorzystaniu próbek wielkowymiarowych o długości 2000 mm i przekroju 200 mm × 100 mm.

The formation of space bar structures supported by the system reliability theory

Z. KOWAL

Kielce Technological University, Al. Tysiąclecia P.P. 7, 25-314 Kielce, Poland.

This paper presents the estimation of the carrying capacity of space structures with the use of the reliability theory and quantile algebra. Structures with rectangular meshes with every other blank mesh are shown to be economically competitive in relation to traditional full-wall and lattice roof coverings. On the basis of the structure reliability theory it is shown that connections of bars with nodes ought to have a greater carrying capacity than that of bars so that change of mechanisms of destruction from elastic-plastic to elastic-brittle does not occur. Attention is drawn to the fact that structures which are accompanied by geometric invariability resulting from articulated connections of bars with nodes are safer and have a smaller mass than structures whose geometric invariability depends on the spatial stiffness of the connections of bars with nodes. Attention is drawn to the additional advantages of selected economically competitive structures, namely: the possibility of support in any nodes of the structure, a smaller labour outlay in designing, execution and assembly and the ease of the provision of technological equipment in the structural space, including suspension of fire shields.

Keywords: *space structures, reliability models, determination of reliability, formation of structures*

1. Introduction

The last twenty years have witnessed a setback in the implementation of space structures to the construction of large-span roofs. Many architects and designers (including many Poles: Makowski in England, Du Chateau in France and many others) were fascinated in the 1970s by the values of such structures and by the possibility of creating beautiful architectural forms, multi-series of shipped elements, productions of elements for storage, the possibility of assembly of even large structures without use of heavy equipment, provision of technological equipment inside the constructional space of the structure. However, conclusions about significant vandal resistance, reliability and resistance to local overloads of structural nodes were derived from the properties of regular space structures with triangular or square meshes and parallel bars of the upper layer in relation to sublayer bars (Figure 1). Attention was not paid to the fact that the geometric invariability and the carrying capacity of some geometrically regular structures is relative to the stiffness of connections of bars in nodes and is significantly lower than the carrying capacity of structures whose geometric invariability does not depend on the spatial stiffness of connections in nodes.

The fantasy of designers prompted them to develop ideas of turning upper meshes in relation to lower ones by 45°, using pentagonal and hexagonal as well as circular meshes, and introducing the concentration of blank meshes and other geometric conceptions. Innovative conceptions of structures were seldom preceded by model investigations which would disclose the occurrence of traps that radically reduced the carrying capacity of some structures. Large space regular structures with the every other rectangular or square blank mesh, shown in Figure 1a, have greater competitive, technical and operational values in relation to traditional girder-purlin roofs. The exemplary structure shown in Figure 1a has 168 bars and 10 support bars and 57 nodes. There are 7 supernumerary bars in the structure. The filling of blank meshes leads to the significant increase of the number of bars in the structure. 8 new bars are added to every additional node in the structure with square meshes. Increase in the number of supernumerary bars leads to the increment of the carrying capacity and vandal resistance of the roof, but also to the increase of labour intensity of the project. In hall roof covers with rectangular projection it is worthwhile to prefer structures with square or rectangular meshes. Structures with triangular meshes ought to be considered in halls with triangular or hexagonal projection, and in halls with rhombic projection, structures with rhombic or triangular meshes are recommended. 67 bars and 6 support bars as well as 22 nodes in the example of the structure shown in Figure 1b. The structure contains 7 supernumerary bars. Filling of blank meshes leads to increase in the number of bars by 6 for each new node.

Denotation in Figures: ———— upper belts, ———— crossheads, ---------- lower belts.
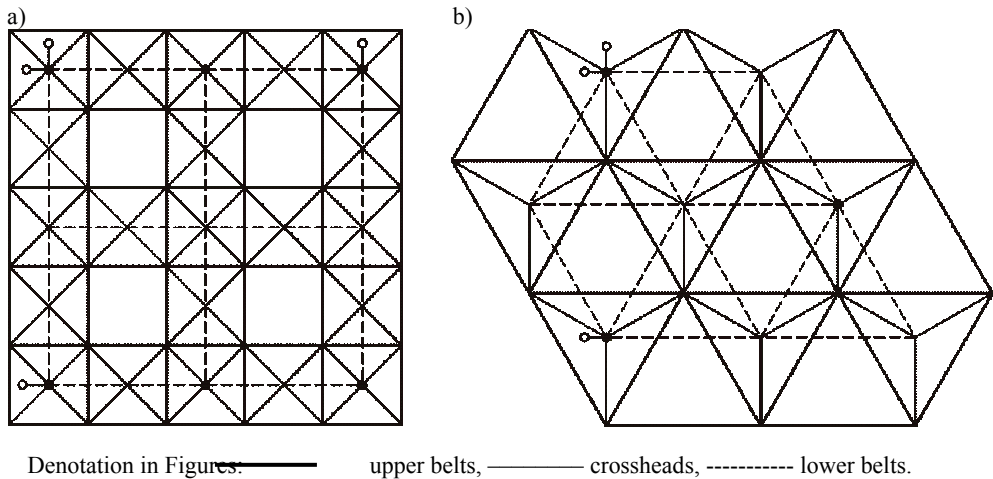
Fig. 1. Economical regular structures with square and triangular meshes

The advantage of rationally designed space structures in relation to traditional constructions from flat sheet-iron or trusses transformed into space constructions by means of concentrations is the possibility of the avoidance of failures resulting from

errors made in the concentration of the construction. It is estimated that about 70% of failures of large area structures results from the defective concentrating of traditional flat constructions into space constructions. In recent years there has been a significant increase of the number of failures and disasters caused by badly constructed and incorrectly calculated connections of bars with nodes. The formation and dimensioning of steel bars of spatial trusses and connections of bars with nodes from the condition of the maximum carrying capacity at the minimum of the construction mass can be improved by means of postulates, certainties and theorems resulting from the system reliability theory. It is also necessary to pay attention to the fact that the carrying capacity and costs of the execution of the system are influenced by the manner of the division of the construction into shipped elements and assembly units, the model of bars and connections with nodes and the number of geometrically similar and equal elements. A characteristic feature of construction and assembly solutions shown in Figures 1a and 2a is the possibility of their objective calculation and dimensioning on the basis of analogy to truss beams. Besides, it is easy to create geometrically invariable, safe assembly units. In the case of large area bar structures shown in Figure 2 it is advisable to create assembly segments with the width of at least B = 3a or with an odd number of meshes B = 5a, 7a, 9a.
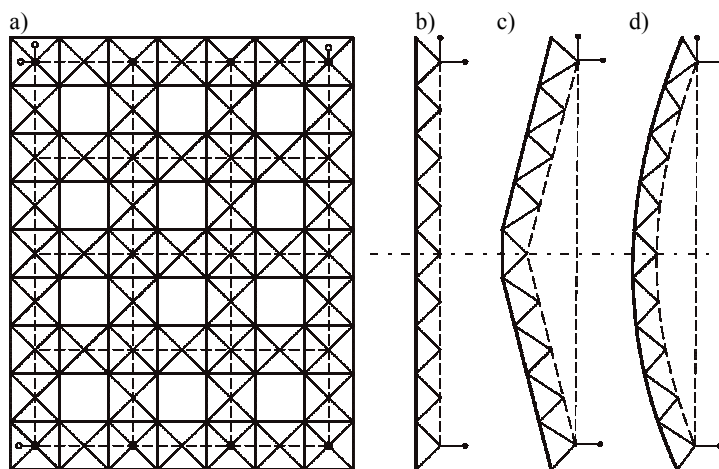
Fig. 2. Exemplary hall roof with the following structures:
b) flat, c) two slopes with a tie member, d) arched with a tie member

2. Measures of structure reliability

All mechanical and geometric magnitudes of both shipped elements and the whole construction are random. This statement has the weight of an axiom. In the USA is in use the correctly constructed Hasofer–Linda reliability index of the construction (Hasofer–Linda) counted on the basis quantile of the reserve of the carrying capacity of

the construction. The random reserve $Z(w)$ of the carrying capacity $N(w)$ is a difference of the random carrying capacity $N(w)$ of the structure and the random load $P(w)$ and is:

$$Z(w) = N(w) – P(w). \tag{1}$$

The expected carrying capacity reserve $E(Z)$ is:

$$E(Z) = E(N) – E(P). \tag{2}$$

The variance of the carrying capacity reserve is:

$$D^2(Z) = D^2(N) + D^2(P). \tag{3}$$

The standard deviation of the reserve of carrying capacity $D(Z)$ is:

$$D(Z) = [D^2(N) + D^2(P)]^{0.5}. \tag{4}$$

Quantile Z_k of the carrying capacity reserve is:

$$Z_k = E(Z) – \beta D(Z). \tag{5}$$

The (Hasofer-Lind) reliability index β is calculated from the formula:

$$\beta = [E(N) – E(P)]/D(Z). \tag{6}$$

Reliability index β is standardized in the USA although it is seldom applied in designing. On the basis of reliability index β we can calculate the probability of disaster or failure directly from tables, e.g. normal probability distribution. One of the objective causes of the difficulty in using of index β to the estimation of the reliability of systems, particularly in the designing of large-scale constructional systems is the fact that only some loads of the building can be approximated by means of normal distributions. Normal distributions characterize quite well the carrying capacity of the elements of steel structures, therefore, they are suitable for the estimation of quantiles of the carrying capacity of bar space structures. In the further part of this study we shall be concerned with the estimation of quantiles of the carrying capacity of space structures that characterize the computational carrying capacity of the construction.

In designing one does not use postulates, theorems and axioms resulting from the calculus of probability. This results in open and hidden economic losses. The overt losses include failures and disasters of constructions in consequence of significant inaccuracies made in designing, and the estimation of the safety of complex traditional constructions. The covert losses include too big sections of noncritical elements of constructions in relation to critical elements which participate in the initiation of the

disaster. For example, after the failure or disaster it is often found that the carrying capacity of connections placed in critical places of the construction is lower than that of the connected elements. In such cases connections and not bars are accountable for the carrying capacity of the bar system.

The safety of the construction according to European practice, conformable with the public intuition of safety, is calculated on the basis of the relation of computational carrying capacity to computational load $N_0/P_0 > 1$. Computational carrying capacity N_0 and computational load P_0 are reflected in standards by arbitrarily accepted quantiles N_k, P_k, which in the case of normal distributions of carrying capacity are calculated from formulas (7) and (8):

$$N_k = E(N) - t_N D(N), \tag{7}$$

$$P_k = E(P) + t_P D(P). \tag{8}$$

Safety calculated on the basis of the relation of the quantile of carrying capacity to the quantile of load $N_k/P_k > 1$ leads to the dependence: $[E(N) - E(P)] > t_N D(N) + t_P D(P)$. If there is no reason to differentiate index t_N of the quantile of carrying capacity and the indicator of the quantile of load t_P, we assume that $t_N = t_P = t$. Safety $N_k/P_k > 1$ is not equivalent to safety calculated from reliability index β. The equivalent index t of the quantile of the carrying capacity can be estimated from Equation (9):

$$t = [E(N) - E(P)] / [D(N) + D(P)]. \tag{9}$$

From the comparison of formulas (6) and (9) we have a formula (10) for the estimation of the equivalent index t. Index t is the indicator of the reliability of the carrying capacity of the construction:

$$\beta = t [D(N) + D(P)] / D(Z). \tag{10}$$

It results from the above analysis that we can convert safety estimated on the basis of the relation of quantiles $N_k / P_k > 1$ to the probability of safety $Pr\{N(w) > P(w)\}$.

The equivalent index of the quantile of the carrying capacity t is equal to or smaller than the index of the reserve of carrying capacity β. Therefore, we can safely distinguish the investigation of the reliability of the carrying capacity of the construction and separately investigate quantile N_k of the carrying capacity of the system. On this basis we can obtain the minimum mass of the construction while maintaining the standard reliability of the carrying capacity of the system.

The computational carrying capacity of the structure in the form of quantile N_k of the carrying capacity N_k can be determined by means of algebra quantiles. Then the difference in the estimation of the quantiles of the carrying capacity of structures statically determinate and the quantiles of the carrying capacity of structures statically

indeterminate is evident. In statically determinate structures with articulated nodes, all bars are connected in series. Minimum critical sets of parallelly connected bars and minimum critical sets with common bars occur in statically indeterminate structures.

3. Carrying capacity of statically determinate space bar structures

3.1. Estimation of the carrying capacity of bars and tie members connected in series with nodes

The carrying capacity of structures should be calculated on the basis of the carrying capacity of integrated elements. From the point of view of the theory of reliability three critical causative spots (Figure 3) occur: a bar and two connections of the bar with nodes. An economic solution is to utilize the carrying capacity of a bar in the carrying capacity of the structure in order to minimize the mass of the construction and to maximize the carrying capacity.

In the case of cylindrical and gable structures tie members with a significant length and connected in series tightening elements may occur (Figure 2). Bars and tie members are built from elastic-plastic materials. However, screwed or welded connections have a limited plastic formability in comparison with connected bars.
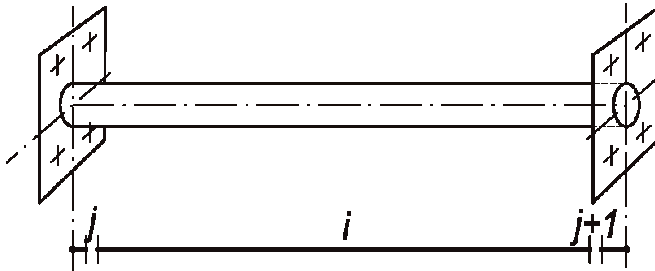
Fig. 3. Examples of a bar connected bar with nodes in series

In the tie member (Figure 4) occur n causative elements which are connected in series from the point of view of reliability. The carrying capacity of the tie member (11) can be estimated on the basis of the classical model of the reliability of the chain built from n elements. The number of elements in the string can be estimated on the basis of tension tests for steel or according to data provided by the manufacturer:

$$N(w) = \min N_i. \tag{11}$$

The carrying capacity of a causative bar should be estimated with regard to the carrying capacity of a bar and two connections with nodes. Reliability p, understood as the probability of not destruction of the tie member, is estimated as the product of the

safety n of causative elements which appear in the tie member from the well-known formula (12):

$$p = \Pi p_i = \Pi Pr \{N_i(w) > P\}. \tag{12}$$

Figure 4 illustrates the relation $k_s = N_k/N_{1k}$ of quantile N_k of the carrying capacity of the tie bar composed of n causative elements (links) to quantile N_{1k} of the carrying capacity of the single causative element on the level of significance $p = 0.99865$ for $t = 3$.
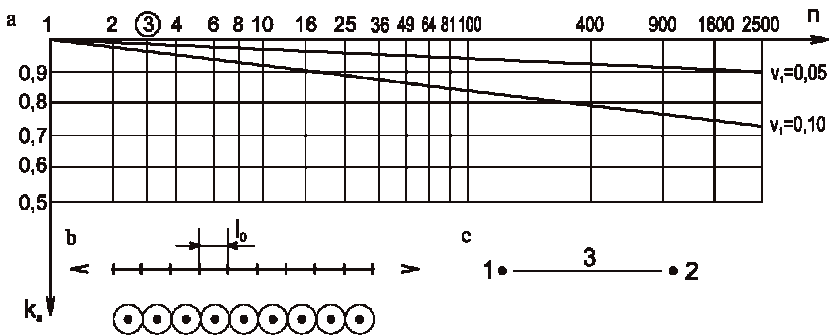
Fig. 4. Coefficients of the statistical weakening k_s of the construction with elements connected in series: b) schema of the tie bar, c) schema of a bar

Bars connected with two nodes occur most often in structures (Figure 4c). The random carrying capacity $N_i(w)$ of an integrated causative bar is:

$$N_i(w) = \min[N_1(w), N_3(w), N_2(w)]. \tag{13}$$

One ought to take into consideration $N_3(w)$ the carrying capacity of the bar itself and the carrying capacities $N_1(w)$ and $N_2(w)$ of connections. Safety p_i of the causative element will be estimated as the product of safety p_3 of the bar itself and p_1 and p_2 of connections (Figure c) from formula (14):

$$p_i = p_1 p_3 p_2. \tag{14}$$

In order to utilize the carrying capacity N_3 of bars and to protect the elastic plastic model of the destruction of the construction, the following conditions must be fulfilled:

$$p_1 \geq p_3 \text{ and } p_2 \geq p_3, \tag{15}$$

$$N_1 \geq N_3 \text{ and } N_2 \geq N_3. \tag{16}$$

The following postulate results from the economic requirement of the utilization of the carrying capacity of bars in the formation of the carrying capacity of the bar constructional system: one ought to preserve the elastic-plastic model of the destruction of the integrated causative element created by the bar and not by connections.

The elastic plastic model of the causative element can be transformed into the elastic-brittle model in consequence of the too small carrying capacity of connections (cracking of connections). Therefore, the carrying capacity of the connection should be greater than that of a bar attached to the node. A few percent increase of the carrying capacity is taken into account. This can be read from the graph in Figure 4. The excessively wide spread practice of the dimensioning of connections for sectional forces and not for the carrying capacity of connected bars leads to a carrying capacity of the system lower than it would result from the carrying capacity of bars. Connections of bars with a smaller carrying capacity than that of bars are a major factor which triggers mechanisms of the destruction of the construction due to the occurrence in connections of welding or assembly stresses. In connections of compressed bars one ought to pay attention to the critical carrying capacity of sheet metal unbraced elements of the node and connection.

3.2. Statically determinate space structures

Axiom 2. All causative elements in statically determinate bar structures are connected in series from the point of view of reliability. The causative element of the statically determinate structure is such an element which, when damaged, will cause the whole structure to be damaged. Causative elements in structures are bars integrated with connections of bars with nodes. The random limit carrying capacity N of statically determinate structures is determined from carrying capacity N_i of bars with weight α_i in the system of formulas:

$$N(w) = \min \alpha_i N_i(w), \text{ within the limit from } i = 1 \text{ to } n, \tag{17}$$

where n is the number of integrated causative elements (bar with connections) in the structure.

Integrated causative elements will be henceforth called bars and the random carrying capacity i of this bar will be denoted N_i instead of $N_i(w)$.

One ought to mention that the standard computational carrying capacity of elements is a quantile with an unknown significance level but sufficient in practice. Weight α_i and the carrying capacities of a bar in the construction is calculated on the basis of the relation of load P to force S_i of generated by load P in the i-th bar from the formula:

$$\alpha_i = P/S_i. \tag{18}$$

Coefficient α_i determined the affiliation of the carrying capacity of the i-th bar to the set of the carrying capacity of bars which determine the carrying capacity of the structure according to the criterion (20).

Reliability **p**, understood as the probability of not occurrence of disasters is calculated as the product of the safety n of integrated causative elements from the well-known formula:

$$p = \Pi\, p_i = \Pi\, Pr\, \{\alpha_i N_i > P\}. \tag{19}$$

It results from formula (19) that the quantile of the carrying capacity of the statically determinate construction is smaller than the quantile of weighed carrying capacity of the weakest element:

$$N_k(t) < \min \alpha_i\, N_{ki}(t). \tag{20}$$

The quantile of the carrying capacity of the i-th (single) bar is estimated from the formula:

$$N_{ki} = E(N_i) - t\, D(N_i). \tag{21}$$

In the case of the normal distribution of the carrying capacity of elements, the probability of safety (19) is read from tables of normal distribution on the basis of parameter t. An equivalent quantile of the carrying capacity of the element is the standard computational carrying capacity of the element. A conclusion drawn in the designing practice of bar constructions from formula (11), that the computational carrying capacity of bar systems determined on the basis of the standard computational carrying capacity of the weakest element has the same safety as the weakest causative element, is not correct because $N_k < N_0$. However, it is justified to formulate theorem 2: along with the increasing number n of causative elements in the statically determinate structure, with the standard safety p_i of elements, the quantile of the carrying capacity N_k decreases on the standard security level p of the construction. It results from theorem 2 (in the meaning of the standard) that the probability of fulfilling the computational carrying capacity of the construction is smaller than the probability of fulfilling the computational carrying capacity of the weakest causative element in the structure. The evidence of theorem 2 results directly from formula (19). Theorem 2 can be treated as an axiom. The use of theorem 2 can be shown by an example.

Example. If 10 bars occur in a statically determinate isostatic truss, safety diminishes by one class in relation to the safety of a single element, e.g. from class 6 ($p = 0.999999$) to class 5 ($p = 0.99999$). With 100 bars it diminishes to class 4 ($p = 0.9999$), and with 1000 bars to class 3 ($p = 0.999$). There may be several hundred or even several thousand bars in structures. In order to maintain in the practice the (implicit) standard (computational) safety of the structure one ought to increase the

computational carrying capacity N_{0i} of causative elements, for example, by means of the coefficient of the consequence of destruction. The more causative elements in statically determinate construction the greater are consequences of its destruction. The increase of the safety of a statically determinate structure by one class requires a few percent increase of the carrying capacity of elements. This increase can be estimated on the basis of graphs shown in Figure 4. One ought to mention that the above conclusions also refer to classical girder-purlin roofing structures of halls. In statically determinate bar constructions the number of bars corresponds to the number of kinematically admissible mechanisms of destruction.

3.3. Spatial trusses with separate nodes

The distinction of nodes as separate shipped elements favours the classification of nodes and connections of bars with nodes. Typical nodes are usually designed and executed more carefully. The significant number of nodes that occur in great structural systems allows examining them by destruction methods. Then the postulate is fulfilled that the carrying capacity of the node should be greater than the carrying capacity of attached causative elements (bars integrated with connections). One ought, however, to pay attention to the necessity of theoretical, and if need be, experimental, examination of the carrying capacity of nodes for loads greater than that of the carrying capacity of causative bars. The literature offers several dozen proposals of the construction of nodes. Many of them do not fulfil the expectation of a carrying capacity of connections greater than that of bars in concrete project realizations.

4. Statically indeterminate bar structures

Figure 5 shows examples of the use of statically indeterminate space structures with every other blank mesh, which is a profitable alternative because it does no not have many defects of great area classical roofing systems with the girder-purlin or steel-sheet-purlin constructions. An exemplary cut-out segment B = 7a of the structure in Figure 5, supported in lower nodes on two parallel edges, contains: 7×9 square meshes, 104 nodes and 320 bars as well as support bars. Supernumerary bars are included in many minimum critical dependent sets with common bars. In the case of the filling of blank meshes, each new node includes 8 bars of which $8 - 3 \times 1 = 5$ are supernumerary bars. It should be mentioned that in statically indeterminate structures there also appear bars integrated in series with connections described in section 3.1; they are further referred to as bars.

Supernumerary bars increase the carrying capacity and the reliability of statically indeterminate space structures. Supernumerary bars ought to be detected under the assumption that articulated connections of bars with nodes occur in the analyzed structure. Such a procedure makes it possible to detect structures with latent defects, whose geometric invariability results from the stiffness of nodes and not from at least

statically determinate set of bars. 3*w* of minimal critical sets of bars occur in statically indeterminate space structures with full triangular, rectangular or rhombic meshes (where: *w* – the number of nodes, *n* – 3*w* – the number of elastic-plastic supernumerary bars). If we fulfil the postulate: all integrated causative bars in minimum critical sets are elastic-plastic, then in such sets the theorem is true about the rank of the axiom: a minimum critical set of causative elements is a set in which if at least one element is causative, then the whole set is causative. Redistribution of stresses occurs in critical sections and sectional forces between elements of such sets. Note: the minimum critical set cannot be diminished because it is tantamount with the removal of the bar from the structure.
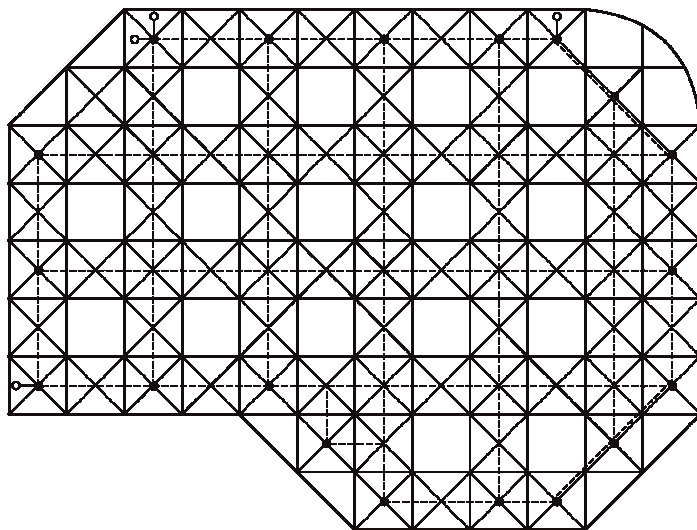

Fig. 5. The example of the structure with irregular projection supported on an irregular basis

If connections of bars with nodes have a smaller carrying capacity than bars in the minimum critical set, they can change the elastic-plastic mechanism of the destruction of the system into the brittle-plastic mechanism. Then the statically correct redistribution of forces between bars in minimum critical sets of elements does not occur because the fractured bars are eliminated from the minimum critical set. Brittle-plastic destructions of a bar in a small minimum critical set of causative elements can trigger an avalanche of destructions of other elements up to the destruction of the whole set. It should be added that loads from damaged elements are transferred dynamically and not statically to causative elements. The destruction of any minimum critical sets means the disaster of the system.

Conclusion: The change of elastic-plastic causative elements into brittle-plastic elements leads to a significant decrease of the carrying capacity and the safety of the structure in relation to the structure built from elastic-plastic causative elements.

The random carrying capacity N of the minimum critical set m of elastic-plastic elements is equal to the weighed sum of random carrying capacities $\alpha_i N_i$ of elements:

$$N = \Sigma \, \alpha_i \, N_i. \tag{22}$$

Weight $\alpha_i = P/S_i$ of a bar in the minimum critical set is determined from formula (18). In this instance weight α_i is a coefficient which denotes the inclusion of the carrying capacity of an i-th bar to the minimum critical set of bars which determine the carrying capacity of the structure. In every structure $m = 3w$ of minimum critical sets of bars occurs in every structure. The expected carrying capacity of the minimum critical set m of elements

$$E(N) = \Sigma \, \alpha_i \, E(N_i). \tag{23}$$

Variance $D^2(N)$ of the carrying capacity of the minimum critical set of bars is determined from the formula:

$$D^2(N) = \Sigma \, \alpha_i^2 \, D^2(N_i). \tag{24}$$

The standard deviation of the carrying capacity of the minimum critical set is determined from the formula:

$$D(N) = [D^2(N)]^{0.5}. \tag{25}$$

The coefficient of variability v of the minimum critical set is determined from the formula:

$$v = D(N)/E(N). \tag{26}$$

In the case of minimum critical sets containing m elements with equal coefficients of variability $v_i = v_1$, the coefficient of variability v of the carrying capacity of the set decreases and for "equal" elements in the minimum critical set it is:

$$v = D(N)/E(N) = v_1/m^{0.5}. \tag{27}$$

The quantile of the carrying capacity N_k of the set m of paralelly connected causative elements (from the point of view of reliability) with random carrying capacities is determined from formula (28):

$$N_k = E(N) - t \, D(N) = E(N) \, (1 - tv). \tag{28}$$

Note: quantiles of the carrying capacity of elements occurring in minimum critical sets must not be added algebraically with the exception of mean values. One ought to apply quantile algebra according to the example shown below.

Example. Calculate the quantile of the carrying capacity of the minimum critical set with the number $m = 4$ of four parallelly connected bars with parameters: $E(N_i) = E(N_1)$, $D(N_i)$, $v_1 = D(N_1)/E(N_1) = 0.06$, $t_1 = 3$. The quantile of the carrying capacity of one element is: $N_{1k} = E(N_1) (1 - t_1 v) = 0.82 E(N_1)$. The average carrying capacity of the minimum critical set is: $E(N) = 4E(N_1)$. The coefficient of variability v of the carrying capacity of the minimum critical set is: $v = v_1 / m^{0.5} = 0.06 / 2 = 0.03$. The quantile of the carrying capacity of the minimum critical set of 4 elements of the set of 4 bars with equal expected carrying capacity is $N_k = 4E(N_1) - 2t \, D(N_1) = 4E(N_1)[1 - 3 \times 0.03] = 0.91 \times 4E(N_1)$. The relation of the carrying capacity of quantile N_k of the minimum critical set to 4 quantiles N_k of the carrying capacity of bars is: $N_k/4 \, N_{1k} = 0.91/0.82 = 1.11$.

Conclusion: the quantile of the carrying capacity on the level $p(t = 3) = 0.99865$ of the set of four bars is greater by 11% than the sum of the quantiles of separate bars. The safety of the set of 4 bars $p(2t_1 = 6) > 0.999\ 999\ 9$.

In the case $t_1 = 2.5$ the quantile of the carrying capacity of 1 element is: $N_{1k} = E(N_1) (1 - tv) = 0.85 E(N_1)$. The safety of a separate bar is $p(t = 2.5) = 0.993\ 791$. The quantile of the carrying capacity of minimal critical sets of 4 bars is: $N_k = 4E(N_1)[1 - 2.5 \times 0.03] = 0.925 \times 4E(N_1) = 3.7 \, E(N_1)$.
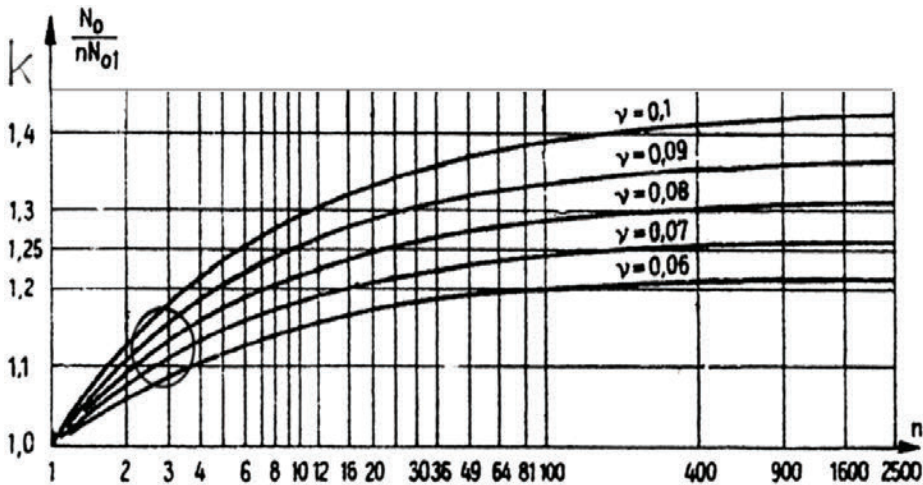

Fig. 6. Coefficients $k = N_k/mN_{1k}$ of the increase of quantiles N_k of the carrying capacity of the sets of n elements connected parallelly in relation to the sum nN_{1k} of the quantiles of the carrying capacity of separate bars

The relation of the carrying capacity of quantile N_k of minimum critical sets to 4 quantiles N_{k1} of the carrying capacity of separate bars is: $N_k/4 \, N_{1k} = 0.925/0.85 = 1.088$. The safety of the set of 4 bars is $p(t = 2t_1) = 0.999\ 999\ 7$, and failure rate $q = 1 - p$ is repeatedly smaller than that of a single bar.

Significant conclusions concerning the carrying capacity and reliability of statically indeterminate bar constructions result from quantile algebra. The following theorem has a weight of an axiom: the quantile of the carrying capacity of a set of parallelly connected elastic-plastic bars on the standard level of significance t is greater than the algebraic sum of standard (computational) quantiles of the carrying capacity of elements. It can be expressed as follows: safety p of the minimum critical set m of elastic-plastic bars under load mP is greater than safety p of a separated bar under load P and its failure rate $q = 1 - p$ is repeatedly smaller.

Figure 6 shows graphs of the relation of quantiles of the carrying capacity of critical minimum sets built from m equal causative elements to m quantiles of the carrying capacity of single bars for different coefficients of variability v_1 from 0.06 to 0.1 of the carrying capacity of single causative elements.

In an elastic-plastic structure, dimensioned in compliance with standards, supernumerary bars increase the carrying capacity of the construction above the carrying capacity anticipated on the basis of standards. Besides, they increase vandal resistance of the system. Increase of safety m of parallelly connected bars under load mP is greater than safety decrease m of elements connected in series (graph in Figures 4 and 6).

4.1. Structures that have minimum critical dependent sets with common bars

Mutually dependent minimum critical sets of bars occur in the majority of bar space structures (particularly in regular structures). The dependence of sets results from the occurrence of the same bars in different minimum critical sets. The exact estimation of the carrying capacity and reliability of such systems is very difficult. However, a very good estimation from below of the carrying capacity and reliability of the construction can be obtained with the use of the method of dependent set separation (Figure 7) and next by connection in series of separated minimum critical sets. An observation was used for the estimation of reliability on the basis of dependent set separation that the parallel connection of elements increases safety more effectively than it is diminished by connection in series. One can observe it when comparing graphs in Figures 4 and 6 with equal variability coefficients v of steel bars connected parallelly and in series. One ought to use elements of quantile algebra shown in previous sections to the estimation of the carrying capacity and reliability on the basis of the system transformed in such a manner. Figure 7 illustrates the dependence between minimum critical sets arranged in circles in which common bars occur. The dependence results from common elements occurring simultaneously in different minimum critical sets. The example in Figure 7a contains 11 real bars collected in 4 dependent sets. After separating dependent sets and connecting them in series (Figure 7b) the number of elements increases to 16.

One ought to mention that together with mathematicians from Wrocław University 3 dependent sets were theoretically solved [10]. During the tests of a great number of

dependent sets, we observed the technical usefulness of the method of the separation of dependent sets [16] to the safe estimation of the quantiles of the carrying capacity of systems characterized by sets with common elements was.
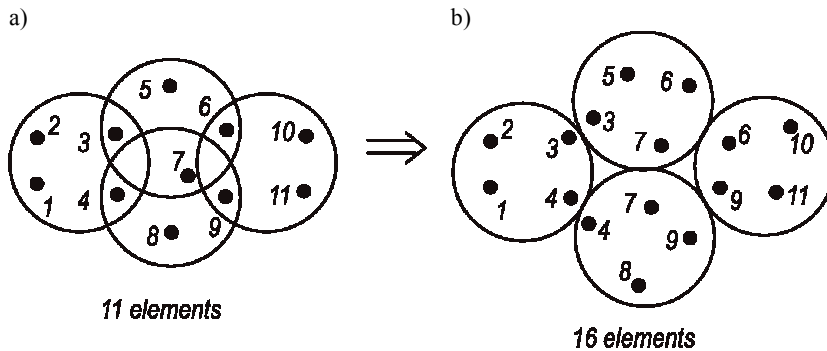

Fig. 7. Example of the separation of minimum critical dependent sets
and the connection of separated sets in series

4.2. The effect of load programs on the carrying capacity and reliability of bar structures

In practice we have a small chance to construct an isostatic space structure with uniform safety of causative elements. It is possible theoretically in the case of the occurrence of one load programme. In practice there are more load programmes that vary in time. Besides, the manufacturing programme includes a discrete change of the parameters of steel bar section. The dimensioning of the elements of the structure in the case of many load programmes leads to the differentiation of the safety of causative elements and to the increase of the carrying capacity and reliability of bar space structures as well as the decrease of the range of failure or disaster.

A conclusion can be drawn from many analyses and experimental research: The basic criterion of the quality of bar space structures is the behaviour of the geometric invariability of the structure in the foundation of articulated nodes. In practice nodes and stiff connections are most frequently applied. Generally, they are cheaper and they increase the carrying capacity and the reliability of structures. It is worthwhile to add that the detection of the "trap" of the geometric variability of the innovative structure is relatively easily achieved on the common geometric model of a designed structure which is subjected to dissymmetrical load. In every case the economically useful bar structure should fulfil the necessary condition $n - 3w > 0$.

5. General conclusion

Large space regular structures with every other square or rectangular mesh and parallel bars of the upper layer in relation to the lower layer are technically and eco-

nomically competitive in relation to traditional girder-purlin roofing. Regular space structures with full triangular or rectangular meshes are characterized by a greater vandal resistance, but they also tend to be more labour consuming. Structures with triangular meshes are suitable for roofing with triangular, hexagonal or rhombic projections as well as their combinations. Both structures with rectangular and triangular meshes are suitable for covering spaces with irregular projection as well as those which require an irregular layout of columns.

Structures with triangular or rectangular meshes with parallel upper and lower strips are vandal resistant. Every other mesh can be blank in such structures. The can also be curved cylindrically by shortening lower strips or they can be used to gable roofs. The local occurrence of a greater number of blank meshes in regular structures with square meshes is subject to limitations resulting from the local geometric variability of meshes surrounding the removed meshes. An example of the geometrically invariable structure with every other blank mesh is shown in Figures 1 and 2.

The use of screwed or welded connections of bars with nodes with a carrying capacity lower than that of bars also favours the change of elastic-plastic mechanisms of the destruction to elastic-brittle mechanisms. Then the carrying capacity of connections and not the carrying capacity of bars is accountable for the carrying capacity and reliability of a structure.

6. Detailed conclusions

1. The basic criterion of the quality of space structures from the point of view of obtaining the greatest carrying capacity at the least mass of material is the behaviour of the geometric invariability of the structure in the foundation of articulated nodes.

2. An economic necessity is the utilization of the carrying capacity of bars integrated with the carrying capacity of connections in the formation of the carrying capacity of space structures. Therefore, connections of bars with nodes ought to be designed for the carrying capacity of bars and not for sectional forces, and the carrying capacity of the connection ought to be greater at least by min 5% than the carrying capacity of bars attached to nodes.

3. With the increase of the number of bars in a statically determinate structure the computational carrying capacity of the structure decreases. In the case of connections of bars with nodes whose carrying capacity is lower than that of bars, the number of causative elements, which will occur in the calculation of the system reliability, increases three times.

4. Supernumerary bars create parallel connections from the point of view of reliability, and increase the carrying capacity of steel structures. Parallel connections increase the safety of space structures more effectively than the series connections decrease them.

5. In the case of many static load programmes the safety and the carrying capacity of bar space structures is increased.

6. The quantile of the carrying capacity of parallelly connected bars is greater than the sum of weighed carrying capacities of computational separate elements. The safety of the minimum- critical set of elastic-plastic bars is greater than the safety of bars separated.

7. Elastic-plastic supernumerary bars $n_n = n - 3w >$ increase the reserve of the carrying capacity of structures and simultaneously they increase vandal resistance of the system.

8. Separation of nodes as distinct shipped elements favours the typification of nodes and connections of bars with nodes. A significant number of nodes in large constructional systems allows for their examination with destructive methods.

References

[1] Biegus A., Kowal Z.: *Badania modelowe struktury przestrzennej o oczkach warstwy górnej obróconych o 45° względem konturu*, XXI KN-KILW PAN i KN PZITB, Kraków–Krynica, 1975, T. II, pp. l25–135.

[2] Biegus A., Kowal Z.: *Badania modelowe sił wewnętrznych w prętach struktur z płytową warstwą zewnętrzną*, VII Symp. Mechaniki Ciała Stałego PTMTS, Warszawa, 1976, pp. 43–53.

[3] Biegus A., Kowal Z.: *Badania modelowe struktury przestrzennej z oczkami pustymi*, PN Instytutu Budownictwa PWr., No. 20, 1976.

[4] Biegus A., Kowal Z., Woźniak J.: *Prętowe przestrzenne przekrycie czterospadkowe hal o dużych rozpiętościach*, XXII KN KILiW PAN i KN PZITB, Krynica, 1976, Referaty, T. II, pp. 493–503.

[5] Biegus A., Kowal Z.: *Badania modelowe losowych sił wewnętrznych w „zerowych" prętach struktur przestrzennych*, XXIII KN KILiW PAN i KN PZITB, Krynica, 1977, pp. 29–35.

[6] Biegus A., Kowal Z.: *Badania modelowe sił wewnętrznych w strukturze prętowo płytowej*, Rozprawy Inżynierskie (Engineering Transactions) Vol. 27, No. 1, 1979, pp. 69–80.

[7] Biegus A., Kowal Z.: *Strukturalne przekrycie hali lokomotywowni*, Przegląd Budowlany, 8/79.

[8] Bogucki W., et al.: *Poradnik projektanta konstrukcji metalowych*, Arkady, 1980, T. 2.

[9] Chodor L., Dziubdziela W., Kowal Z.: *Współczynnik bezpieczeństwa konstrukcji poddanej wielookresowym obciążeniom stochastycznym*, XXXV KN KILW PAN i KN PZITB, Krynica, 1989, pp. 19–24.

[10] Dziubdziela W., Kopociński B., Kowal Z.: *Ultimate bearing capacity of structural systems with minimal critical sets having joint elements in pairs*, Archives of Mechanics, Vol. 25, No. 5, 1973, pp. 719–731.

[11] Dziubdziela W., Kopociński B., Kowal Z.: *Losowa nośność graniczna konstrukcji o trzech minimalnych zbiorach krytycznych mających elementy wspólne*, AIL 1/1974, pp. 123–134.

[12] Dziubdziela W., Kowal Z.: *Evaluation of the reliability of structural systems with critical sets having joint elements in common*, Rozprawy Inżynierskie Vol. 26, No. 3, 1978, pp. 553–559.

[13] Dudziak-Owca H., Kowal Z.: *Koncepcja systemu przekryć walcowych postaci zredukowanych struktur prętowych*, Przegląd Budowlany, No. 1/80.

[14] Dziubdziela W., Kowal Z.: *Oszacowanie kwantyli ciągów wielookresowych maksymalnych obciążeń konstrukcji*, Archiwum Inż. Lądowej, 1/1989, pp. 299–311.

[15] Dziubdziela W., Kowal Z.: *Estimation of life time quantiles of structures under loading with random number of cycles*, 3rd International Conference Innovation and Reliability in Automotive Design and Testing, Firenze, Italy, April 8–10, 1992, Vol. 2, pp. 1223–1229.

[16] Dziubdziela W., Kowal Z.: *Safety of structures subjected to multi-periodical wind loads,* EECWE-94, East European Conference on Wind Engineering, July, 1994, Warsaw, Vol. 1, pp. 179–188.

[17] Dziubdziela W., Kowal Z.: *Quantils of random limit load capacity and reliability of systems characterized by binarily correlated critical sets*, Construction Safety and Loss Control, U. of Florida, 12–14 October 1994.

[18] Kopociński B., Kowal Z.: *Losowa nośność graniczna konstrukcji o dwóch minimalnych krytycznych zbiorach elementów mających elementy wspólne*, Arch. Inż. Ląd., 4/1972, pp. 103–115.

[19] Kowal Z., Seidel W.: *An attempt of measurement of random internal forces in bars of a regular space structure*, 2nd International Conference on Space Structures, University of Surrey, Guildford, Great Britain, 1975, Raports, pp. 762–766.

[20] Kowal Z., Seidel W.: *Doświadczalna analiza losowych sił wewnętrznych w strukturze o diagonalnych prętach warstwy dolnej*, AIL 3/1976, pp. 428–436.

[21] Kowal Z.: *Zuverlassigkeit von Konstruktionssystemen*, Wissenschaftliche Zeitschrift der Technischen Universitat Dresden, 25/1976, H. 1/2, pp. 265–270.

[22] Kowal Z., Polak M., Szpila E., Wydra S.: *System przekryć przestrzennych „ZACHÓD”*, Inż. i Bud., 11/1976, pp. 421–424.

[23] Kowal Z., Surkont B.: *Wyznaczanie losowych przemieszczeń i sił wewnętrznych w lepkosprężystych strukturach przestrzennych*, VII Sympozjum poświęcone reologii PAN I PTMTS, PWr. Wrocław, 1978, pp. 146–156.

[24] Kowal Z., Paczkowski W., Poluchowska B.: *Losowe przemieszczenia węzłów i siły wewnętrzne w prętowych strukturach przestrzennych obciążonych w węzłach siłami losowymi*, AIL 2/1978, pp. 191–204.

[25] Kowal Z.: *Parametry losowej wytrzymałości krytycznej prętów ściskanych i współczynniki wyboczenia*, AIL 1/1981, pp. 79–88.

[26] Kowal Z.: *O szacowaniu bezpieczeństwa konstrukcji*, Konwersatorium Mechanika Stochastyczna, Szklarska Poręba–Wrocław, maj 1994, pp. 17–30.

[27] Kowal Z.: *Statystyczne osłabienie i wzmocnienie konstrukcji*, Inż. i Bud., 7–8/1995, pp. 392–394.

[28] PN-EN 1993. *Projektowanie konstrukcji stalowych*.

Kształtowanie prętowych struktur przestrzennych wspomagane teorią niezawodności systemów

W pracy pokazano szacowanie nośności struktur przestrzennych wspomagane teoria niezawodności i algebrą kwantyli. Wskazano struktury o oczkach prostokątnych z co drugim oczkiem pustym jako ekonomicznie konkurencyjne w stosunku do pełnościennych i kratowych przekryć tradycyjnych. Z analizy niezawodności konstrukcji wynika, że połączenia prętów z węzłami powinny mieć większą nośność aniżeli pręty, aby nie dochodziło do zmiany mechanizmów zniszczenia ze sprężysto-plastycznego w sprężysto-kruchy. Zwrócono uwagę, że struktury, któ-

rym towarzyszy geometryczna niezmienność wynikająca z przegubowych połączeń prętów z węzłami są bezpieczniejsze i mają mniejszą masę aniżeli struktury, których geometryczna niezmienność zależy od przestrzennej sztywności połączeń prętów z węzłami. Zwiększa to zalety struktur ekonomicznych a mianowicie: możliwości podpierania w dowolnych węzłach konstrukcji, mniejszy nakład pracy na projektowanie, wykonanie i montaż oraz łatwość prowadzenie wyposażenia technologicznego w przestrzeni konstrukcyjnej przekrycia w tym podwieszania osłon przeciwpożarowych oraz sieci oświetleniowych i sygnalizacyjnych.

Joining the car-body sheets using clinching process with various thickness and mechanical property arrangements

J. MUCHA

Rzeszow University of Technology, W. Pola 2, 35-959 Rzeszów, Poland.

L. KAŠČÁK, E. SPIŠÁK

Technical University in Košice, Mäsiarska 74, 040 01 Košice, Slovakia.

The clinching joints are more and more used when assembling sheet plate elements, especially in an automotive industry. The clinching joint is created by local stamping of joined sheets without heat effect on the material structure.

This paper presents the analysis of effect of the thickness layout change and sheet type and die on the joint strength change. The shearing strength analysis of created joints has been presented. The shearing test results of the clinching joint have been compared with results achieved for spot welding joints of similar joint diameter.

Keywords: *clinching, joining under pressure, sheet metal, mechanical properties*

1. Introduction

Traditionally, resistance welding and fusion welding have been used in the automotive industry. Welding demands localized heating of the material, which may lead to changes in the mechanical properties of the materials [1]. When searching for new solutions to replace the spot welding (SW) process, well known press joining technology capabilities have been recognized. It is not always possible to achieve the required quality of joints in automotive industry when classical methods of joining like resistance spot welding and laser brazing are used. The clinching by stamping is one of these technologies [2–3]. Although clinching has been known for many years, only in recent years can increased industrial interest in clinching be noticed since the technique was successfully applied to complement or even replace other joining techniques such as, for example, spot welding [4–7].

A fundamental difference of clinching, in relation to traditional sheet metal forming, is that there is a deliberate forging of the adjacent sheets between the die and the punch at the bottom of the joint. The clinching technique has become an increasingly popular alternative to traditional spot welding due to the growing use of alternative materials which are difficult or impossible to weld [8]. This technology may be used when joining galvanized, painted or organically plated materials.

Although mechanical clinching has a low running cost, its joining range of e.g. aluminium alloy with high-strength steel is small because of the low ductility of high-strength steel. Specifically in the clinching process of high-strength steel, defects occur in high-strength steel due to its low ductility [9–10]. There have been studies on various methods for heating up the magnesium components including heating up components in a furnace or with hot air and applying inductive techniques [11]. The use of clinching technology in the assembly process is justified by the capability of its adaptation that the tool access is guaranteed to achieve the tool adequate support rigidity and its retraction after the process. This technology must be used in the open design components. Another disadvantage of this technology is visible flash, which protrudes over the sheet surface.

The clinch joints (therein clinch round press joints – RPJ) are a group of rapidly developing pressed cold joining technologies [12–15]. They are successfully used in the automotive industry (Figure 1). Currently there are performed researches on introducing pressed joints when assembling car body crush zone elements [16–19].

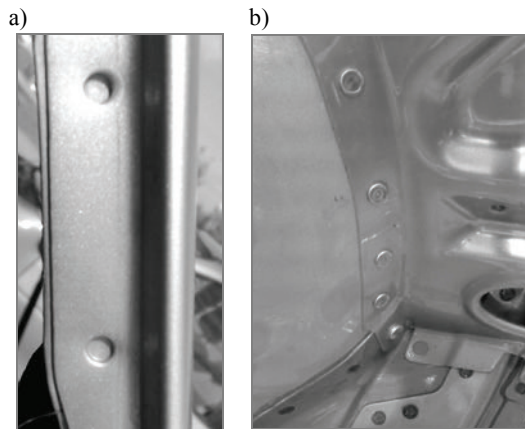a)   b)

Fig. 1. The example of the clinching joint: a) the side part of hood, b) the inside of the car

The clinching assembly technology is already used in some industry branches, especially in the automotive industry by car manufacturers and part vendors.

2. Material and experimental procedure

The experimental tests of clinching and spot welding have been performed for three material types with and without the galvanized coating. The analysis of effect of sheet arrangement change on die when joining has been performed. The purpose of this experiment was to determine the effect of joint type on joint strength. The real strength of the joint can only be defined by the use of destructive testing. The shearing test is the most popular joint strength test. Thus the maximum cutting force has been determined

as a priority strength index. Shear strength testing is based on obtaining both the displacement of the joint and the existing load.

2.1. Material properties

The examined sheet plates are used in Volkswagen Group car assembly plant, Skoda Mlada Boleslav in Bratislava. The joint specimens were made of DD13, DD14 and DX53D+Z sheet material. The last one had the galvanized coating of 22 μm thickness (~340 g/m^2). The sheet surface is uniform and its uniformity features good protection capabilities (e.g. painting). Moreover, the galvanized coating is lead-free, providing with good anti-corrosion features and preventing galvanic layer fracturing when straining. The presented materials are used to manufacture car body elements. The basic mechanical properties and the chemical composition of the material have been presented in Table 1 and Table 2.

Table 1. Mechanical properties of sheet

Material		Parameter			
		t [mm]	R_e [Mpa]	R_m [Mpa]	A_{80} [%]
DD13*	1	0.7	179	315	44
	2	0.8	193	324	41
DD14*	1	0.62	153	270	46
	2	0.7	162	279	42
	3	0.8	167	281	44
	4	0.9	175	285	42
DX53D + Z**	1	0.98	239	341	36

* EN 10111:2008, ** EN 10142:2000

Table 2. Chemical composition of sheet

Material	Chemical composition, %								
	C	Mn	Si	P	S	Al	Ti	V	Nb
DD13	0.03	0.2	0.006	0.008	0.008	0.042	–	–	–
DD14	0.05	0.27	0.01	0.013	0.014	0.039	–	–	–
DX53D + Z	0.07	1.54	0.4	0.01	0.0032	0.052	0.013	0.07	0.051

Galvatite (DX53D+Z) for cold forming offers a range that extends from bending and profiling qualities to extra deep drawing qualities. Galvatite for cold forming complies with European standard EN 10142:2000 shown in Table 1 below. Typical applications:
- automotive components and body panels,
- tubes,
- domestic appliances,
- steel furniture,
- electrical goods,

- domestic heating,
- drums,
- building components,
- components for agricultural machinery.

The zinc coating (*Z*) is produced in a continuously operating line, where the zinc crystallizes into a smooth layer with minimized spangle. The grain size may vary according to the coating conditions.

2.2. Apparatus and experimental procedures

Five specimens of both spot weld and clinching joints have been prepared for each sheet thickness and material type. The sheet metal joining process has been conducted in the laboratory environment using own tools. The tools used in experimental analysis of pressed joints, i.e. the punch and die with specified impression, were constant (Figure 2). The tool geometry enabled joining of sheet plates of various thickness arrangements with no fractures within joint area.
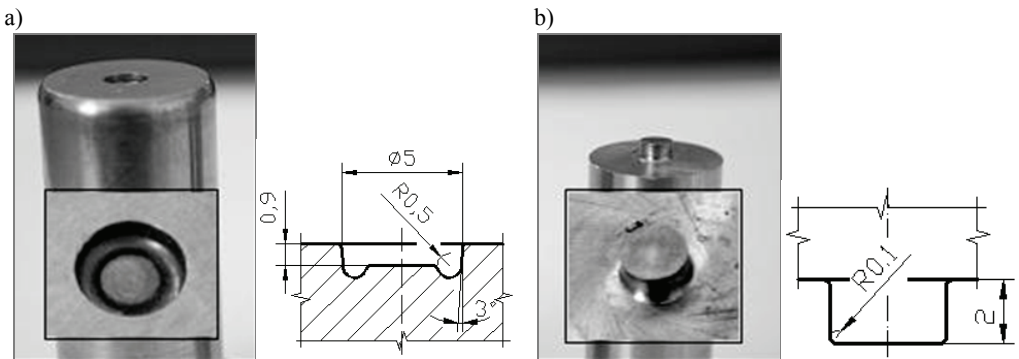

Fig. 2. Clinching joint tools and their main dimensions: a) die, b) punch
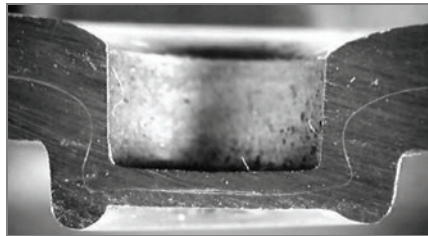

Fig. 3. The sheet joint cross-section (*X* – overpress bottom thickness)

When creating a joint, the last joint forming phase (final restriking) is of high importance, as the lock (sheet material clinching – this area is indicated in Figure 3) is

being created in this place. Depending on the sheet thickness and the thickness arrangement, the forming force was in the range 14–19 kN.

The valid joint is a joint without punctures or tensile failures of joined sheets in a location of a joint (Figure 4). The visible tensile failures are proof that the forming limit of the material in a joint has been exceeded. No gap may exist between joined elements. No gap is an indication of a valid joint.
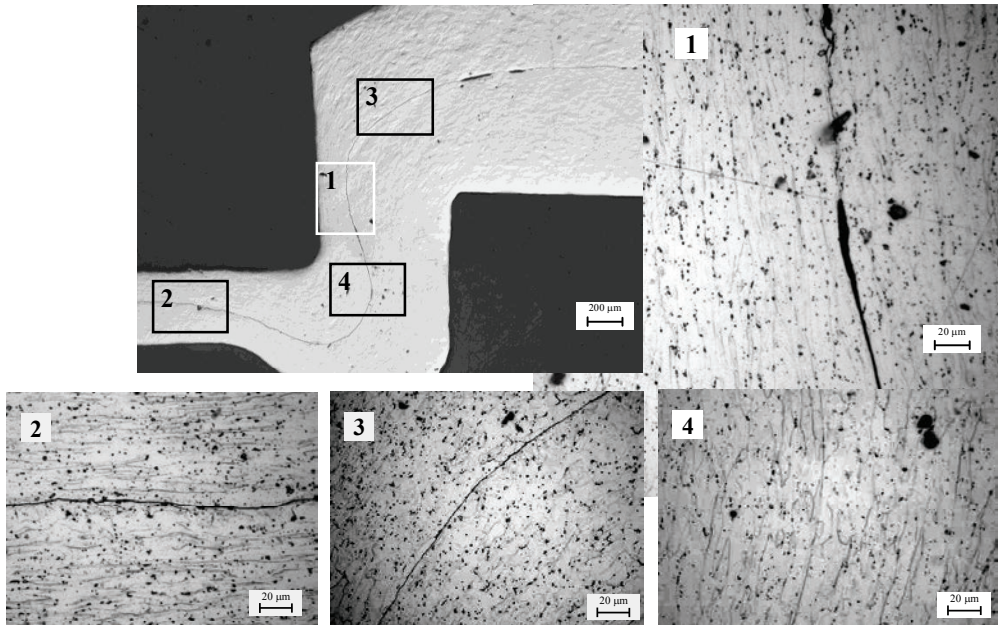

Fig. 4. The microstructure of properly created clinching joint

The spot weld (SW) joints have been additionally made in order to compare the strength of the clinch round press joints (RPJ) results. The parameters have been selected according to valid sheet recommendations in order to achieve the active weld diameter (d_z), of which is size is similar to the clinching joint diameter. The spot weld joint should feature proper macrostructure, i.e. the fusion of sheet material (merge area) – see Figure 5.

When spot welding the pressed sheets using electrodes, the heat generated melts the sheets being joined (Figure 6):

$$Q\ (t_w) = \int_0^{t_w} I_w(t_w) \cdot R \cdot dt_w, \tag{1}$$

where:

t_w – welding time,

Q – generated heat,

I_w – welding current,

R – electrical resistance of welding circuit.
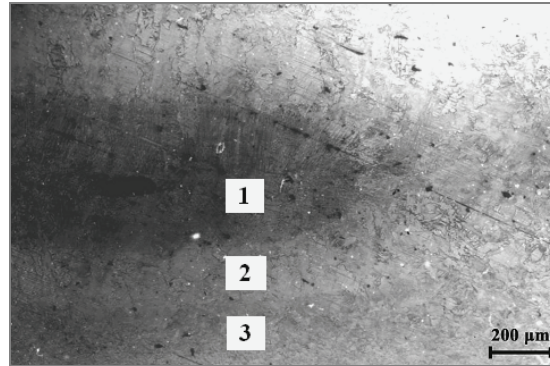

Fig. 5. The weld macrostructure in the point sheets joint
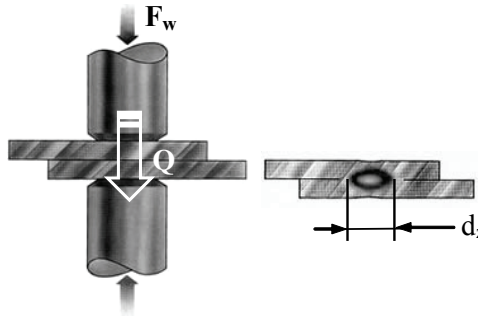("1" – fusion point, "2" – heat effect zone, "3" – native material)

Fig. 6. Schematic view of the spot welding process

The spot welding parameters have been assumed according to the sheet joint recommendations:

– non-galvanized sheet – pressure force F_w = 2.0 kN, short circuit time t_w = 0.16 s, current I_w = 8 kA;

– galvanized sheet – F_w = 2.2 kN, t_w = 0.18 s, I_w = 9 kA, (when arranging DX53D+Z with DD14 of thickness 0.62 – F_w = 2.0 kN, t_w = 0.16 s);

presented in the document: IIW Doc.III-WG12-92/1: „*Procedure for spot welding of uncoated and coated low carbon steels*".

Properly prepared clinching joint and spot weld joint specimens (Figure 7) have been tested for shearing strength until material separation.
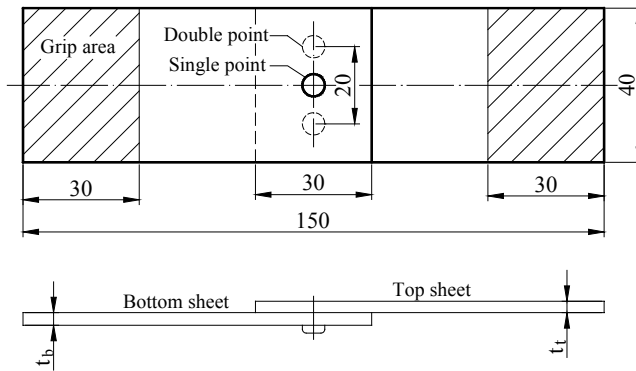
Fig. 7. Specimen geometry

The shearing strength tests have been performed using tensile testing machine TIRAtest2300. The force measurements have been performed using the strain gauge head with measuring range of 0.08–100 kN, at traverse speed of 8 mm/min.

3. Results and discussion

The sheet thickness arrangement is an important factor for joint forming and its final strength when creating clinching joints. In conducting joint shear test for various sheet thickness arrangements of a material DD14 obtained various forms of joint separation (Figure 8). The material separation may be caused by "breaking of created necking" of upper sheet material (Figure 8a); by a partial material ductile failure in the necking area with "separation" (Figure 8b) or by complete "separation" with no joint material cohesion loss (Figure 8c).

Some part of material is being pressed into the die groove when creating the lock during the joint forming (see area in Figure 3). The proper groove size enables the material displacement and creation of desired lock (Figure 9). Changing the sheet arrangement in relation to die causes significant change of maximum shearing force value, which destroys the joint.
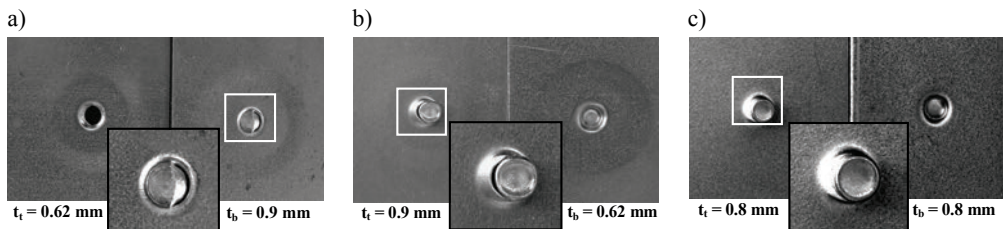

Fig. 8. The example of DD14 sheet material separation (the clinching joint):
a) $t_t = 0.62/t_b = 0.9$, b) $t_t = 0.9/t_b = 0.62$, c) $t_t = 0.8/t_b = 0.8$

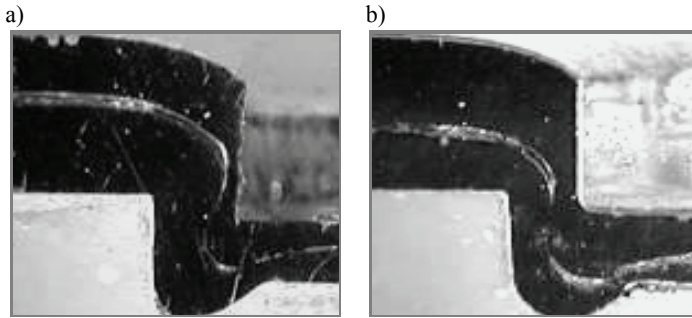a)   b)

Fig. 9. Critical area in press joint (DD14 sheet material):
a) sheet of 0.9 mm on the die side b) sheet of 0.62 mm on the die side

For example (see Figure 10), for sheet arrangement $t_t = 0.62$ mm/$t_b = 0.9$ mm, the force $F_{t\max} = 780$ N, but for $t_t = 0.9$ mm/$t_b = 0.62$ mm, the force $F_{t\max} = 1272$ N – this means increase by 63% in relation to previous sheet thickness arrangement.
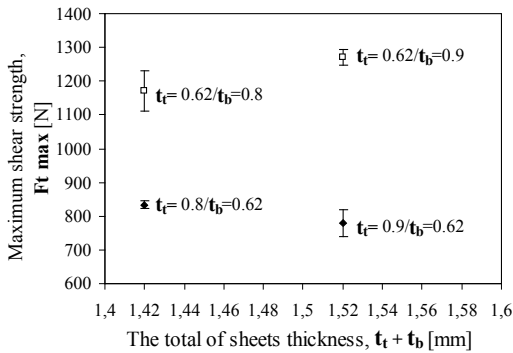

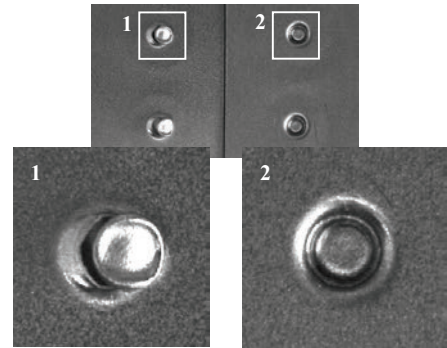Fig. 10. The effect of sheet thickness change on maximum joint shearing force for DD14 material

Fig. 11. Double joint after separation

The tests have been performed for identical thickness of the upper sheet ($t_t = 0.8$ mm) and lower sheet ($t_b = 0.8$ mm) in order to demonstrate the effect of joint number change under load. The Figure 11 presents the example destruction of joint, made of DD14 sheet with arrangement $t_t/t_b = 0.8/0.8$ mm.

The effect of joined sheet thickness arrangement change (material DD13 and DD14) for single and double joint on maximum shearing force has been presented in Figures 12a and 12b.

For single joint, when changing the sheet thickness from $t_t/t_b = 0.8/0.8$ to $t_t/t_b = 0.8/0.7$, the maximum shearing force ($F_{t\max}$) has dropped by 13% for DD14 sheet material and by 10% for DD13 material (see Figure 12).
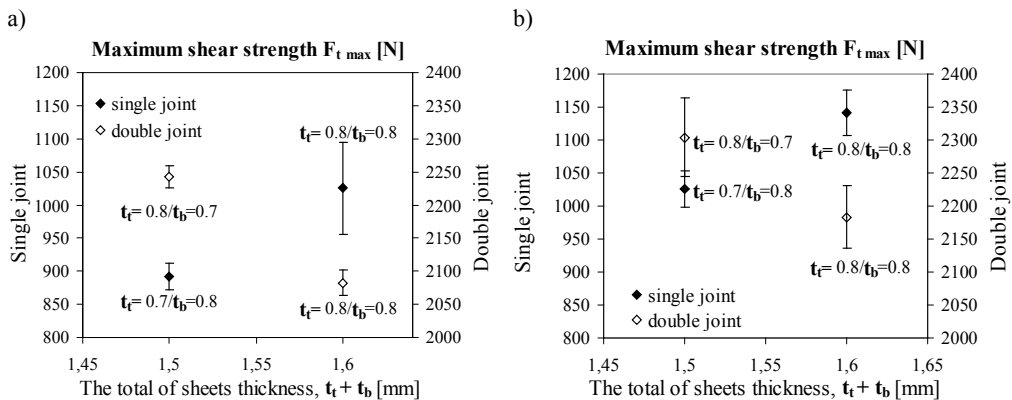
a)   b)

Fig. 12. The effect of sheet thickness arrangement and joint number on maximum
joint shearing force for: a) DD14 material, b) DD13 material

Increasing the joint number both for DD13 and DD14 sheet material results in ~100% increase of maximum strength – for $t_t/t_b = 0.8/0.8$. The situation is different when increasing the joint number to 2 and simultaneously changing the sheet thickness from $t_t/t_b = 0.7/0.8$ to $t_t/t_b = 0.8/0.7$. This results in maximum strength increase to 151% for DD14 material and 125% for DD13 material.

In order to present effect of various materials (DD13 and DD14) more clearly, the single joint results have been put together on a single chart (Figure 13). The increase of upper sheet thickness by 14.5% increases the maximum shearing force by 15% of joint made of steel sheets (material DD14) – Figure 13. This directly increases the joint strength. Similar situation occurs for DD13 material joint. The sheet joints made of DD13 have featured higher average force results comparing to DD14, by 15% for $t_t/t_b = 0.7/0.8$ and by 11% for $t_t/t_b = 0.8/0.8$. All diagrams present the average value taken from five tests.

The effects of different thickness arrangement for DX53D + Z material have been presented on Figure 14. For this material, the sheet thickness difference was increased in order to emphasize the joined layer arrangement change effect. For single joint with $t_t/t_b = 0.62/0.98$ arrangement, the upper sheet thickness was about 63.3% of the bottom sheet thickness. For such a thickness arrangement, the average value of force ($F_{t\max}$) was 547 N. The increase of upper sheet thickness ration by 18.3% (from 63.3% to 81.6%) resulted in the maximum shearing force increase by 72.4%. Changing the thickness arrangement (total layer thickness = constant) from $t_t/t_b = 0.62/0.98$ (single joint) to $t_t/t_b = 0.98/0.62$ (double joint) results in force increase by 393.6%, that is by 196.8% per single merge point. On the other hand, increasing the thickness ratio (for double joint) of bottom sheet by 18.3% results in $F_{t\max}$ decrease by 6.1% (Figure 14).

The spot welding process is very fast and effective method of permanent sheet joining. The sheet specimens joined during experiment have been tested for shearing strength. The example results have been presented on Figure 15. For all thickness com-

binations and all sheet material types, the achieved $F_{t\max}$ value was several times higher than for redrawing joints. For $t_t/t_b = 0.8/0.8$ arrangement and DD14 and DD13, $F_{t\max}$ value was 3520 N and 3800 N. Whereas the achieved force was 1025.35 N and 1141.15 N for redrawing joints, that is 30% and 29% of force value for spot welded joints, respectively. Decreasing of bottom sheet thickness from 0.8 mm to 0.62 mm (for $t_t = 0.8 =$ constant, DD14 material) resulted in force decrease by 21% for spot welded joints (Figure 15). For redrawing joints, $F_{t\max}$ force decrease was 18.6% (Figure 10 and 13). For other thickness arrangements of DD14 material and spot welded and redrawing joints, the differences occurred at similar maximum shearing force levels.
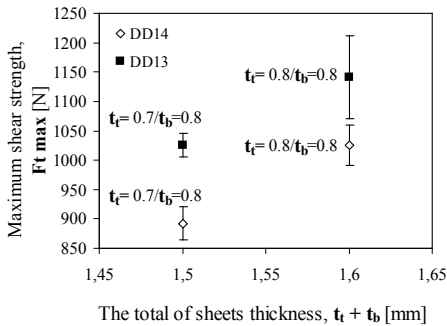

Fig. 13. The effect of upper sheet thickness on maximum joint shearing force – single joint
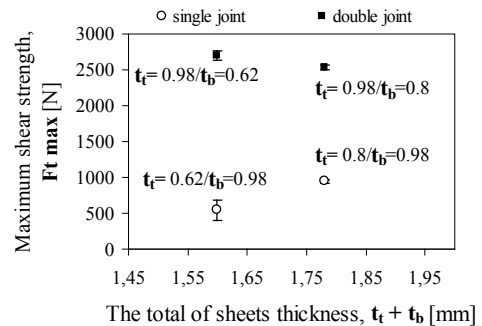
Fig. 14. The effect of sheet thickness arrangement and joint number on maximum joint shearing force for DX53D+Z material

The spot weld elements have been separated during the strength test, but no material separation occurred in the spot weld area (Figure 16). This proves the spot weld elements have been properly joined. Note the separation method, as this causes high values of the maximum shearing force of joint. When loading the spot welded joints, the material separation beginning occurs on the melted material boundary, and then the separation line runs in parallel to the displacement, which forces the joint deformation (Figure 16a).

For all thickness combinations and material types, the material separation was caused by the material cohesion loss in the joint area. When different materials were joined together, the material break out occurred on the weaker material side (Figure 16b), and in all other cases on the thinner material side.

Unconformities which can appear in spot welds cause the spot welds can have less strength and can lead into total destruction of manufacturing parts of cars bodies [20]. The typical unconformities of spot welds are:
- cold weld,
- bad shape of welding nugget,
- deep indentation of welding electrodes in sheets,

- cracks inside/around welding nugget,
- small-diameter nugget.
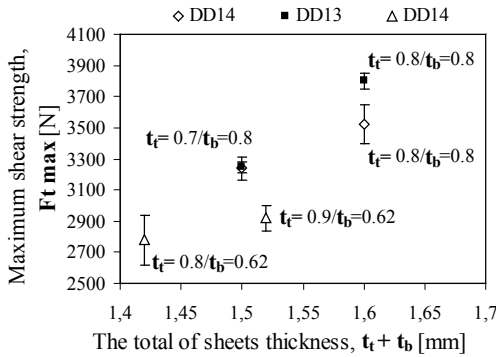
Fig. 15. The effect of sheet thickness on maximum spot welding joint shearing force – the weld diameter $d_{z(śr)} = 3.65–4.06$
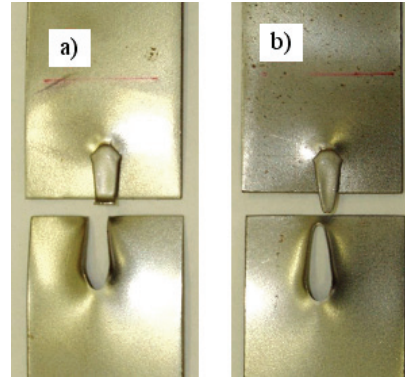
Fig. 16. The example of the spot welding joint material separation: a) DD13 ($t_t = 0.8/t_b = 0.8$), b) DX53D+Z / DD14 ($t_t = 0.98/t_b = 0.8$)

The diagram 17 presents the maximum force, which destroys the spot weld and clinching joints for joined sheets DD14 and DX53D+Z. Relatively good results have been achieved by increasing the clinching joints from one to two. However, such joints still feature lower strength than spot weld joints. Note that the clinching joint strength can be increased by increasing the joint diameter.

Fig. 17. The comparison of maximum shearing force for various joint arrangements
(SW – spot welding, RPJ – clinch round press joints)

When joining materials with $t_t/t_b = 0.98/0.62$ arrangement and DX53D+Z/DD14 using spot welding method, the maximum shearing force achieved was 3234 N. Whereas $F_{t\max}$ was by 59% lower for a single redrawing joint. When two merge points were used, the force was lower only by 30%. Changing the thickness arrangement and material to $t_t/t_b = 0.62/0.98$ and DD14/DX53D+Z results in force decrease from 1325 N to 547 N.

4. Conclusions

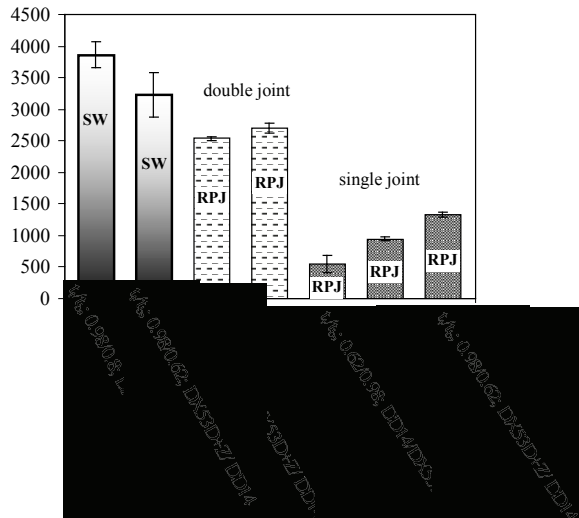The clinching technique has become an increasingly popular alternative to traditional spot welding due to the growing use of alternative materials which are difficult or impossible to weld. New sheet material and sheet combinations are constantly introduced in the automotive industry. As a consequence of this, new joining technologies are developed and old technologies are optimised. The simplicity of joint and the methods of its creation enable using such a joint both in series and make-to-order production. The customized robots (manipulators) combined with simple presses for simple shape parts are used in series production. The specialized assembly stations for clinching joints are used to create more complex parts. This paper presents the practical application of joining sheet plates (material DD13, DD14, DX53D+Z), which are used when manufacturing motor-car body components.

From the tests the following conclusions can be drawn:

1. In presented case, the joint load-carrying ability is lower. The strength compensation (increase) may be introduced by increasing the joint diameter or joint number. This fact has been accounted for in many modern motor-car body designs.

2. When joining the same materials, DD13 joints were by 11%–15% more strength that these made of DD14.

3. The sheet thickness arrangement in relation to die is a very important parameter when designing the clinching joints. This directly influences the final joint load-carrying ability.

4. Changing the sheet arrangement for joined material e.g. DD14 from $t_t/t_b = 0.62/0.98$ to $t_t/t_b = 0.98/0.62$ results in 63% change of $F_{t\max}$.

5. For all prepared joints, the highest value of shear test was achieved for spot welded joint – $F_{t\max} = 3860$ N.

6. In case of the clinching joint, the destruction occurs in form of a local deformation (crushing or partial fracture and tear-up of overpressed lock). The properly made weld is left intact, but the sheet plate is being torn.

References

[1] Spišák E., Kaščák L., Slota J.: *Strength analysis of joints made with resistance spot welding and press joining* (in Slovak), Acta Mechanica Slovaca, Vol. 7, No. 2, 2003, pp. 45–50.

[2] Varis J.P.: *The suitability of clinching as a joining method for high-strength structural steel*, Journal of Materials Processing Technology, Vol. 132, No. 1–3, 2003, pp. 242–249.

[3] Di Lorenzo G., Landolfo R.: *Shear experimental response of new connecting systems for cold-formed structures*, Journal of Constructional Steel Research, Vol. 60, No. 3–5, 2004, pp. 561–579.

[4] Varis J.P.: *Ensuring the integrity in clinching process*, Journal of Materials Processing Technology, Vol. 174, No. 1–3, 2006, pp. 277–285.

[5] Tubielewicz K., Turczyński K.: *Use of cold-pressed sheet joints in the construction of building platforms* (in Polish), Przegląd Mechaniczny, Vol. 77, No. 12, 2008, pp. 19–24.

[6] Varis J.P., Lepistö J.: *A simple testing-based procedure and simulation of the clinching process using finite element analysis for establishing clinching parameters*, Thin-Walled Structures, Vol. 41, No. 8, 2006, pp. 691–709.

[7] Oudjene M., Ben-Ayed L.: *On the parametrical study of clinch joining of metallic sheets using the Taguchi method*, Engineering Structures, Vol. 30, No. 6, 2008, pp. 1782–1788.

[8] Mucha J.: *Up to date metal sheet joining methods (Clinching)* (in Polish), Mechanik, Vol. 80, No. 11, 2007, pp. 932–939.

[9] Abe Y., Matsuda A., Kato T., Mori K.: *Plastic joining of aluminium alloy and high strength steel sheets by mechanical clinching*, Steel Research International, Vol. 79, 2008, pp. 649–656.

[10] Lee Ch.-J., Kim J.-Y., Lee S.-K., Ko D.-Ch., Kim B.-M.: *Parametric study on mechanical clinching process for joining aluminum alloy and high-strength steel sheets*, Journal of Mechanical Science and Technology, Vol. 24, No. 1, 2010, pp. 123–126.

[11] Neugebauer R., Kraus C., Dietrich S.: *Advances in mechanical joining of magnesium*, CIRP Annals – Manufacturing Technology, Vol. 57, No. 1, 2008, pp. 283–286.

[12] Mucha J.: *Some aspects of designing process self piercing riveting.* Archives of Mechanical Technology and Automation, Vol. 29, No. 4, 2009, pp. 91–101.

[13] Kaščák L., Spišák E.: *Analysis of properties of press joints through three sheets* (in Slovak), Acta Mechanica Slovaca, Vol. 14, No. 2-B, 2008, pp. 1–6.

[14] Mucha J., Bartczak B.: *Thoughts on the effective modelling of the process of joining thin sheets using the clinching method*, Obróbka Plastyczna Metali, Vol. 21, No. 2, 2010, pp. 105–117.

[15] Tubielewicz K., Turczyński K., Chmielik P.: *Kształtowanie połączeń plastycznych w pracach montażowych* (in Polish), Technologia i Automatyzacja Montażu, Vol. 61, No. 2, 2010, pp. 11–15.

[16] Lee M.H., Kim H.Y., Oh S.I.: *Crushing characteristic of double hat-shaped members of different materials joined by adhesive bonding and self-piercing rivet*, International Journal Automotive Technology, Vol. 7, No. 5, 2006, pp. 565–570.

[17] Lee M.H., Kim H.Y., Oh S.I.: *Crushing test of double hat-shaped members of dissimilar materials with adhesively bonded and self-piercing riveted joining methods*, Thin-Walled Structures, Vol. 44, No. 4, 2006, pp. 381–386.

[18] Gronostajski Z., Polak S.: *Quasi-static and dynamic deformation of double-hat thinwalled elements of vehicle controlled body crushing zones joined by clinching*, Archives of Civil and Mechanical Engineering, Vol. 8, No. 2, 2008, pp. 57–65.

[19] Lee Ch.-J., Kim J.-Y., Lee S.-K., Ko D.-Ch., Kim B.-M.: *Design of mechanical clinching tools for joining of aluminium alloy sheets*, Materials and Design, Vol. 31, No. 4, 2010, pp. 1854–1861.

[20] Papkala H., Pietras A., Zadroga L.: *Zgrzewanie rezystancyjne punktowe blach ocynko-wanych* (in Polish), Przegląd Spawalnictwa, Vol. 76, No. 5–7, 2004, pp. 51–57.

Łączenie za pomocą przetłaczania blach stosowanych w przemyśle samochodowym dla różnych aranżacji grubości i własności mechanicznych

Połączenia przetłoczeniowe w coraz większym stopniu wykorzystywane są do montażu elementów z blach, a szczególnie w przemyśle samochodowym. Wykonywanie połączenia zaciskowego realizowana jest przez proces miejscowego wytłaczania łączonych blach na zimno bez efektu cieplnego oddziaływania na strukturę materiału.

W pracy przedstawiono analizę wpływu zmiany aranżacji grubości i rodzaju materiału blach względem matrycy na efekt zmiany wytrzymałości połączenia. Przedstawiono analizę wytrzymałości na ścinanie wytworzonych złączy. Wyniki testów ścinania połączeń przetłocze-niowych porównano do wyników uzyskanych dla połączeń zgrzewanych o podobnej średnicy punktu spojenia elementów.

AFM surface investigation of Inconel 825 with multi wall carbon nano tube in electrical discharge machining process using Taguchi analysis

S. PRABHU

Assistant professor (Sr.G), School of Mechanical Engineering, SRM University, Chennai-603203, India, prabhume@yahoo.co.in

B.K. VINAYAGAM

Professor & Head, Department of Mechatronics Engineering, SRM University, Chennai-603203, India, bkvei23@yahoo.com

Demand for better surface finish has been increasing recently for super alloys. Carbon nano tube (CNT) is mixed with dielectric fluid in EDM process because of high thermal conductivity. The analysis of surface characteristics like surface roughness, micro cracks of Inconel-825 is carried out and an excellent machined nano finish can be obtained by setting the machining parameters at optimum level. The Taguchi design of experimental technique is used to optimize the machining parameters and an L9 orthogonal array is selected. The predicted surface roughness was estimated using S/N ratio and compared with actual values. ANOVA analysis is used for finding the significant factors affecting the machining process in order to improve the surface characteristics of Inconel-825 material. Taguchi design of experiments were used to identify the best experiment which optimize the surface roughness to nano level and meet the demand of high surface finish and accuracy to great extent. AFM analysis using CNT improves the surface characteristics like surface morphology, surface roughness and micro cracks from micro level to nano level. The regression analysis are used to predict the error between actual and regression values of surface roughness using carbon nano tube as dielectric fluid in EDM process.

Keywords: *multi wall carbon nano tube, electric discharge machining process, surface roughness, Taguchi method, ANOVA analysis, atomic force microscope, regression analysis*.

1. Introduction

Nano level surface finish has become an important parameter in several industries like semiconductor, optical, electrical and mechanical industries. Most of the materials used in these industries are either super alloys or some other difficult to machine materials like ceramics, glass and silicon wafers. Manufacturing processes such as micro moulds, micro holes etc on these materials would be almost impossible owing to high tool wear rate and expenses involved. Hence certain Non Traditional Machining techniques are involved in order to meet the present demand for high accuracy. Electrical Discharge Machining is one of the most widely accepted methods involved in production of complicated shapes and apertures of high accuracy. Hard and brittle materials

can be easily machined using the EDM process. The tool and work piece are separated by a very small gap and submerged in dielectric fluid. During the discharge temperature as high as 40 000 K can be produced, this melts and vaporizes the required region while the top surface re solidifies and cools at a very fast rate. This is how we can do the otherwise very cumbersome machining quite easily.

1.1. Literature review

Y.H. Guu et al. [1] proposed the electrical discharge machining (EDM) of AISI D2 tool steel was investigated. The surface characteristics and machining damage caused by EDM were studied in terms of machining parameters. Based on the experimental data, an empirical model of the tool steel was also proposed. Surface roughness was determined with a surface profilometer. S. Prabhu et al. [2] proposed the nano surface finish of AISI D2 tool steel material using multi wall carbon nano tube (MWCNT) in electrical discharge machining process (EDM). The surface morphology, surface roughness and micro cracks are determined using an atomic force microscope (AFM). I. Puertas et al. [3] carried out on the influence of the factors of intensity (I), pulse time (ti) and duty cycle (η) over the listed technological characteristics. The ceramic used in this study was a cemented carbide or hard metal such as 94WC–6Co. Y.H. Guu et al. [4] presents the effects of titanium nitride (TiN) coating by physical vapor deposition (PVD) on the fatigue life of AISID2 tool steel, which was electrical discharge machined (EDM) at various machining parameters, such as pulse current and pulse-on duration. Surface hardness, surface roughness, residual stress and fatigue strength were measured. Y.H. Guu [5] proposed the surface morphology, surface roughness and micro-crack of AISI D2 tool steel machined by the electrical discharge machining (EDM) process were analyzed by means of the atomic force microscopy (AFM) technique. K.R. Mahajan et al. [6] presents the basic principles of designing a knowledge based system for automated EDM electrode design. Electric discharge machining (EDM) electrode design has always been an important activity in the die and mould making sector. A.G. Mamalis et al. [7] written to give a consolidated view of the synthesis, the properties and applications of carbon nanotubes, with the aim of drawing attention to useful available information and to enhancing interest in this new highly advanced technological field for the researcher and the manufacturing engineer. P. Pecas et al. [8] presented electrical discharge machining using simple and powder-mixed dielectric: The effect of the electrode area in the surface roughness and topography. (PMD-EDM) EDM technology with powder mixed dielectric and to compare its performance to the conventional EDM when dealing with the generation of high-quality surfaces. Y.S. Wong et al. [9] presented Near-mirror-finish phenomenon in EDM using powder-mixed dielectric. A study of the near-mirror-finish phenomenon in electrical discharge machining (EDM) when fine powder is introduced into the dielectric fluid as a suspension at the tool–work piece or inter-electrode gap during machining.

1.2. Electric Discharge Machining (EDM) process

Electric discharge machining (EDM) shown in Figure 1 is an important non-traditional manufacturing method, developed in the late 1940s, has been accepted worldwide as a standard process in manufacture of forming tools to produce plastics mouldings, die castings, forging dies etc. New developments in the field of material science have led to new engineering metallic materials, composite materials, and high tech ceramics, having good mechanical properties and thermal characteristics as well as sufficient electrical conductivity so that they can readily be machined by spark erosion. The recent developments in the field of EDM have progressed due to the growing application of EDM process and the challenges being faced by the modern manufacturing industries, from the development of new materials that are hard and difficult-to-machine.
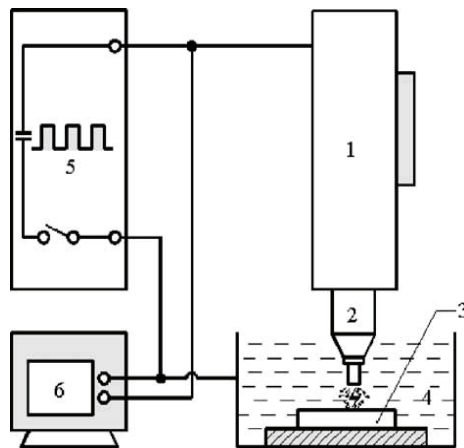

Fig. 1. Schematic diagram of the sinker EDM process (1 – servo-control, 2 – electrode, 3 – specimen, 4 – dielectric fluid, 5 – pulsed generator, 6 – oscilloscope)

The SD 35-5030 Model was used to machine the Inconel-825 Material with Multi wall carbon nano tube is mixed as dielectric fluid to analyse the surface characteristics.

1.3. Multi wall Carbon nano tubes (MWCNTs)

Carbon nanotubes which are related to graphite. In conventional graphite, the sheets of carbon are stacked on top of one another, allowing them to easily slide over each other. That is why graphite is not hard, but it feels greasy, and can be used as a lubricant. When graphene sheets are rolled into a cylinder and their edges joined, they form MWCNTs (Table 1).The sources of Carbon nano tubes are received from Cheap tubes Inc., USA.

Table 1. Specification of MWCNTs

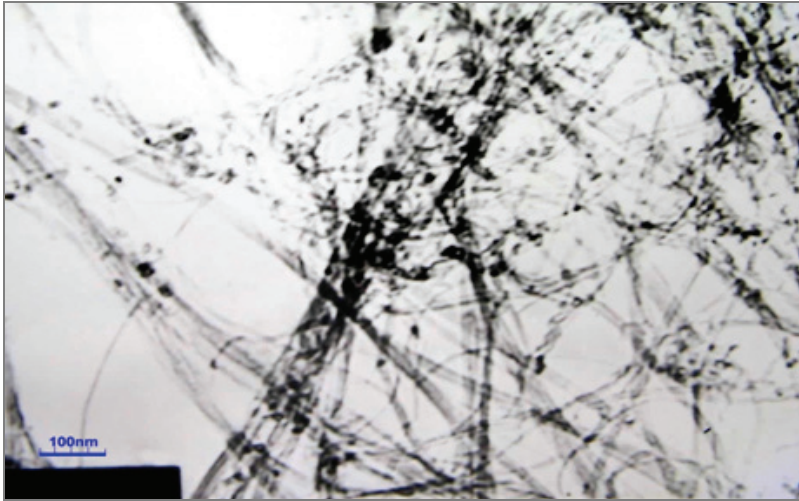| OD	10 nm to 20 nm
Length	10 μm to 30 μm
Purity	>95 wt%
Ash	<1.5 wt%
Specific surface area	>233 m^2/g
Electrical conductivity	>10−2 S/cm

Fig. 2. A TEM image of our MWNTs 95 wt% < 8 nm OD

1.4. Inconel 825

Inconel 825 is a high performance alloys, mainly Nickel Alloy and also Cobalt and Titanium. Inconel 825 might be used in any environment that requires resistance to heat and corrosion. They have good resistance to oxidation and corrosion at high temperatures. Inconel 825 typically finds application in Furnace components, chemical processing, Food processing industry and nuclear engineering. The Chemical composition and Mechanical properties of Inconel 825 material was tested according to CML/WP/036 & IS: 1056 standards in Mettex lab, Chennai.

Table 2. The Chemical composition of Inconel-825

Elements	C	Si	Cu	Mn	Mo	Cr	Ni	Al	S	Ti	Fe
Wt.%	0.05	0.5	1.5−3.0	1.0	2.5−3.5	19.5−23.5	38−46	0.2	0.03	0−1.2	22

Table.3 Mechanical properties of Inconel-825

Tensile strength	655 MPa
Hardness [HRB]	83−85

1.5. Surface roughness tester (T500)

Model Hommel Tester T500 surface roughness tester is a multi-application measuring instrument for component surface quality evaluation. It is capable of checking the work piece surface roughness on plane, cylinder, groove and bearing raceway.

1.6. Atomic force microscope (AFM)

AFM is a device used to view the object to the nanometer scale with the aid of atomic forces. This is used to obtain 3D topological view of the surface. Work piece is placed on the scanner. A cantilever beam is coated with gold of 0.8 nm having a silicon tip of 0.2 to 0.5 nm diameter is made to move over the top surface of the work piece. Contact type mode is used to measure the work piece surface.
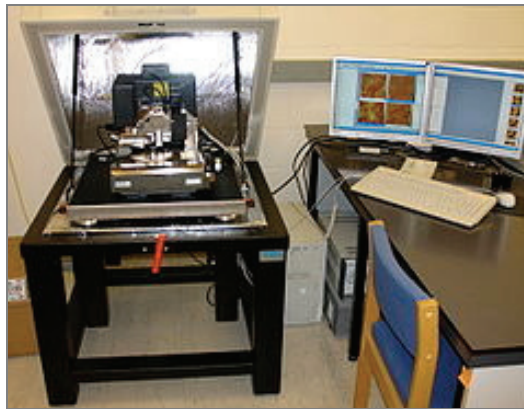

Fig. 3. Atomic force microscope

AFM Tip made − Silicon
Tip Radius − 5 nm
Force – 1.1 N/m
Cantilever thickness – 0.8 μm
Resonant frequency − 140 kHz

By using AFM the surface roughness of the machined work piece can be calculated from following formulas

$$Ra = \sum_{n=1}^{n} (Zn - Z)/N, \tag{1}$$

$$R_{Rms} = \frac{\sqrt{\sum_{N=1}^{N} (Zn - Z)^2}}{(N-1)}, \tag{2}$$

where:

    Zn − height of the data points,

    Ra − Surface roughness,

    Z − Mean height,

    N − Number of data points,

    Rms − Rms method of surface roughness,

    Ra is used to find out the surface finish of Rough surface when $RRms$ is used to find the surface finish of smooth surface.

Mean height can be calculated from

$$Z = \frac{1}{N} \sum_{n=1}^{n} Zn. \tag{3}$$

1.7. Taguchi method

This method is very effective to deal with responses influenced by multi-variables and powerful Design of Experiments tool, which provides a simple, efficient and systematic approach to determine optimal machining parameters. Compared to the conventional approach to experimentation, this method reduces drastically the number of experiments that are required to model the response functions. Traditional experimentation involves one-factor-at-a-time experiments, wherein one variable is changed while the rest are held constant. The main effect is the average value of the response function at a particular level of a parameter. The effect of a factor level is the deviation it causes from the overall mean response. The Taguchi method is devised for process optimization and identification of optimal combinations of factors for given responses. The steps involved are:

1) Identify the response functions and the process parameters to be evaluated.

2) Determine the number of levels for the process parameters and possible interaction between them.

3) Select the appropriate orthogonal array and assign the process parameters to the orthogonal array and conduct the experiments accordingly.

4) Analyze the experimental results and select the optimum level of process parameters.

5) Verify the optimal process parameters through a confirmation experiment.

2. Research methodology

The specimen of Inconel 825 (Nickel alloy) material is machined using several conventional methods such as turning, parting and grinding. The specimens were made to a size of diameter 20 mm and length 15 mm. Both the faces of the raw material are to be ground to get a smooth surface. This Smoothed specimen is heated to 1030 °C at a heating rate of 200 °C/min in muffle furnace. It was kept for one hour

and then quenched. After quenching, the specimens were tempered at 520 °C for two hours and then air cool. The hardness obtained for the specimen is 83-85HRC. Table 1 lists the chemical composition (wt.%) of the material. The EDM specimens were sparked on a die-sinking EDM machine model type SD35 – 5030. The experiment was carried out in kerosene dielectric covering the work piece by 20 mm. A cylindrical copper rod machined was used as the electrode for sparking the work piece. The copper electrode was the negative polarity and the specimen was the positive polarity during the EDM process. During EDM, the primary parameters are pulsed current, pulse-on duration, and pulse-off duration.

Table 4. Shows the electrical discharge machining conditions

Work material	Inconel 825
Dielectric	Kerosene
Electrode material	Copper
Pulsed current	2, 5, 10 A
Pulse-on duration	3,5, 8 μs
Pulse voltage	80 V

During the EDM process, the varying pulse-off duration setting from 1 μs to 7 μs could effectively control the flushing of the debris from the gap, giving machining stability. Hence, the effect of the pulse-off duration on the machined characteristics was not considered in the present work. After each experiment, the machined surface of the EDM specimen was studied like surface roughness, micro crack and morphology by means of Atomic force microscope. The dielectric fluid was mixed in a proportion of 10 gram of MWCNT for 1 Lit of kerosene. A separate tank was made to hold the dielectric fluid containing MWCNT in which the specimen was placed. The sparking was carried out in this setting Figure 4. Different samples were examined.
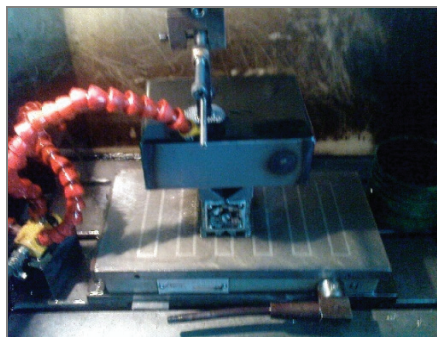

Fig. 4. EDM set up using SWCNT

The studies of process parameters which influence the objective function and which parameters will impact largely to this machining process is analyzed. The parameters control factors and their levels are identified Table 5. Here three levels and

three parameters are taken so based on Taguchi design of experiments L9 orthogonal array was taken Table 6. So totally nine experiments were conducted. The surface roughness of Inconel 825 with and with out carbon nano tubes and S/N ratio values are tabulated in Table 7.

Table 5. Identifying control factors and their levels

Item	Control Factor	Units	Level 1	Level 2	Level 3
A	Pulse current (I)	Amp	2	5	10
B	Pulse duration (τ)	μs	3	5	8
C	Pulse voltage (V)	Voltage		80	

Table 6. L9 orthogonal array

Exp. no	A	B
1	1	1
2	1	2
3	1	3
4	2	1
5	2	2
6	2	3
7	3	1
8	3	2
9	3	3

Table .7 Surface roughness and S/N ratio value

Exp. no.	Coded Values		Actual Values		Without carbon nano tubes Surface roughness (Ra)(y) μm	With carbon nano tubes Surface roughness (Ra)(y) μm	S/N ratio Without nano tubes	S/N ratio With nano tubes
	A	B	A	B				
1	1	1	2	3	2.77	2.59	−8.84	−8.26
2	1	2	2	5	2.54	1.85	−8.09	−5.34
3	1	3	2	8	3.15	2.31	−9.96	−7.27
4	2	1	5	3	5.83	6.19	−15.31	−15.83
5	2	2	5	5	8.87	4.19	−18.95	−12.44
6	2	3	5	8	9.79	1.96	−19.81	−5.84
7	3	1	10	3	10.87	10.11	−20.72	−20.09
8	3	2	10	5	10.14	10.97	−20.12	−20.80
9	3	3	10	8	10.42	9.52	−20.35	−19.57
Mean (μ)							−15.79	−12.82

3. Results and Discussions

3.1. Surface roughness

To determine the effect of the carbon nanotubes on the surface roughness of the Inconel 825, the surface profiles of the EDM machining work piece were measured by Surface roughness tester (Hommel Tester T500).
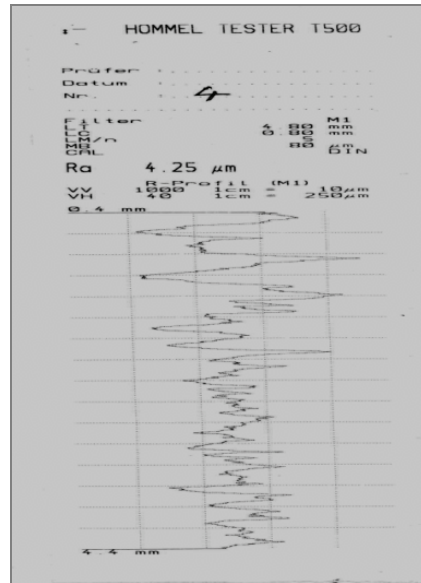
Fig. 5. Surface roughness (Ra) value for pulse current 2 Amp, Pulse duration 5 micro seconds,
Pulse voltage 80 v without carbon nano tubes

The surface roughness of the Inconel was machined by using Multi wall carbon nano tubes to improve the surface finish to nano level.

3.2. Signal to noise ratio

S/N Ratio calculated based on quality of the characteristics. The objective function of this method is to improve the surface finish of EDM machining process using Nano tubes. The Smaller the best S/N Ratio is calculated. The formula used for calculating the S/N ratio is given below:
Smaller the best

$$\frac{S}{N}ratio(\eta) = -10\log10\frac{1}{n}\sum_{i=1}^{n}y^2,\qquad(4)$$

where:
  n − no of experiments,
  y − no of response value.

Table 8. Determining the factor effects of S/N ratio without nanotubes

Factor	Level 1	Level 2	Level 3	Delta	Rank
A-Pulse current	−8.971	−18.029	−20.401	11.430	1
B-Pulse duration	−14.963	−15.725	−16.713	1.751	2

From the Figure 6 Level 1 of A and Level 1 of B gives the maximum effect of improving Surface roughness. Naturally A1 and B1 is the best combination i.e. a Pulse current 2 Amp, and Pulse duration of 3 µs will give the minimum of Surface roughness. From the factor effect graph shows that pulse current giving more impact to improve the surface finish.
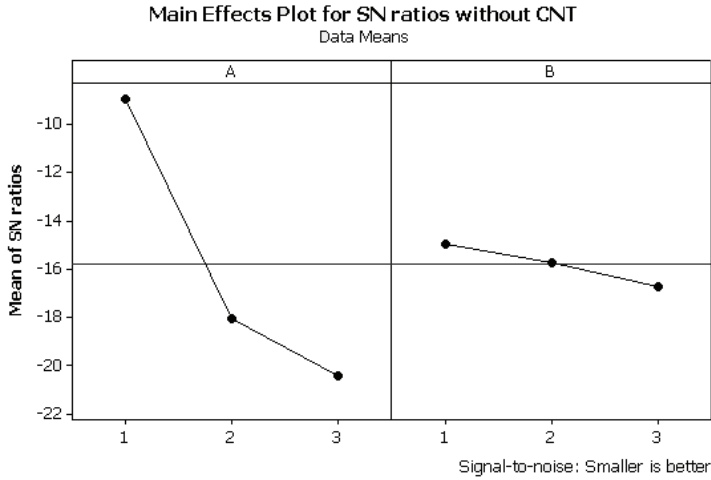

Fig. 6. Factor effect diagram for S/N Ratio without nano tube

The based on experiments, the optimum level setting of parameters is A1B1.
The predicted S/N ratio η' using the optimal levels of the machining parameters can be calculated as:

$$\eta' = \eta_m + \sum_{i=1}^{p} \eta_i - \eta_m, \tag{5}$$

where:

η_m – total mean of S/N Ratio,

η_i – mean of S/N Ratio at the optimum level,

p is the number of main machining parameters that significantly affect the performance.

From the definition without carbon nano tubes S/N Ratio $(\eta) = -8.13305$.

So predicted Surface roughness without carbon nano tubes Ra $(y) = 2.55$ µm.

Table 9. Determining the factor effects of S/N ratio with nanotubes

Factor	Level 1	Level 2	Level 3	Delta	Rank
A-Pulse current	−6.961	−11.374	−20.157	13.197	1
B-Pulse duration	−14.732	−12.864	−10.897	3.835	2

From the Figure 7 Level 1 of A and Level 3 of B gives the maximum effect of improving Surface roughness. Naturally A1, B3 is the best combination i.e. a Pulse current 2 Amp, and Pulse duration of 8 µs will give the minimum of Surface roughness. From the factor effect graph shows that pulse current giving more impact to improve the surface finish.
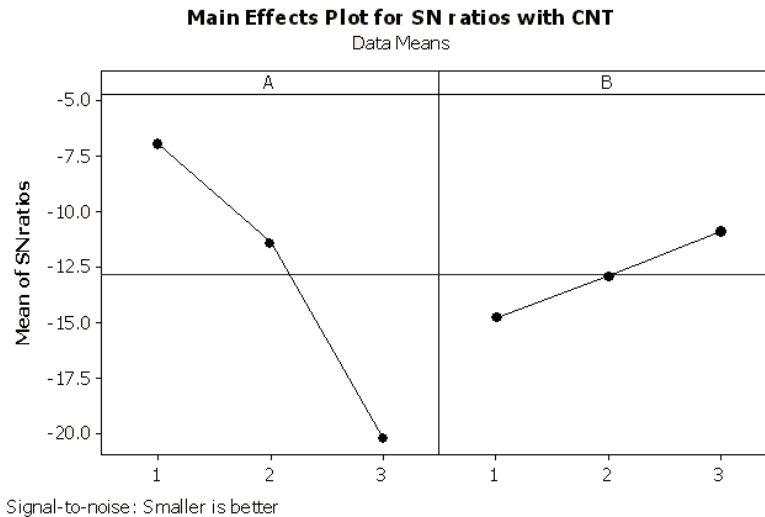

Fig. 7. Factor effect diagram for S/N Ratio with nano tubes

The based on experiments, the optimum level setting of parameters is A1B3.
Predicted Surface roughness without carbon nano tubes (Ra) = 2.55 µm.
Predicted Surface roughness with carbon nano tubes (Ra) = 1.783 µm.
Actual Surface roughness without carbon nano tubes (Ra) = 2.77 µm.
Actual Surface roughness with carbon nano tubes (Ra) = 1.83 µm.

3.3. Confirmation test

The confirmation experiment is the final step in the first iteration of the design of experiment process. The purpose of the confirmation experiment is to validate the conclusions drawn during the analysis phase. The confirmation experiments were conducted by setting the process parameters at optimum level. Pulse current 2 amp, and Pulse duration of 3 µs as optimum parameters and the actual surface roughness was obtained without carbon nano tubes is 2.77 µm compared to predicted surface roughness 2.55 µm. Similar way with carbon nano tubes the confirmation test is carried out with Pulse current 2 amp, and Pulse duration of 8 µs as optimum parameters and the actual surface roughness was obtained with carbon nano tubes 1.83 µm compared to predicted surface roughness 1.783 µm.

3.4. The relationship between surface roughness *Ra* and machining parameter (*I*, *τ*, *V*) with and without using carbon nano tube

Empirical expressions have been developed to evaluate the relationship between input and output parameters. The average output values of Surface roughness have been used to construct the empirical expressions. The empirical model was developed based on relationship between surface roughness with pulse current, pulse on duration and pulse voltage in EDM machining process.
The empirical model was

$$Y = A(X1)^a(X2)^b,$$ (6)

where:
    Y – surface roughness (μm),
    A – coefficient,
    *X*1 – pulse current (Amp),
    *X*2 – pulse duration (μs),
The above non linear equation is converted to linear form by

$$\mathrm{Log}(Y) = \mathrm{Log}A + a\,\mathrm{Log}(X1) + b\,\mathrm{Log}(X2).$$ (7)

Now the above Equation (2) can be written as

$$\hat{Y} = \beta 0 + \beta 1 \cdot 1 + \beta 2 \cdot 2,$$ (8)

where $\hat{Y}$ true value of dependent machining output on a logarithmic scale, *X*1 and *X*2 are the logarithmic transformation of the different input parameters β0, β1 and β2 are corresponding parameters to be estimated. Minitab 15 software has been used to estimate the parameters of the above first order model using the data shown in Table 1a and b are coefficients determined by regression analysis.

3.5. The developed empirical model for surface roughness without carbon nano tubes

$$Ra = A\,(I)^a(\tau)^b,$$ (9)

where:
    A = 0.66,
    a = 0.907,
    b = 0.255.
The regression analysis of the experimental data yields the semi empirical model

$$Ra \text{ without CNT} = 0.66\,(I)^{0.907}(\tau)^{0.255}.$$ (10)

3.6. The developed empirical model for surface roughness with carbon nano tubes

$$Ra = A \, (I)^a (\tau)^b, \tag{11}$$

where:
    $A = 1.58,$
    $a = 1.02,$
    $b = -0.341.$
The regression analysis of the experimental data yields the semi empirical model

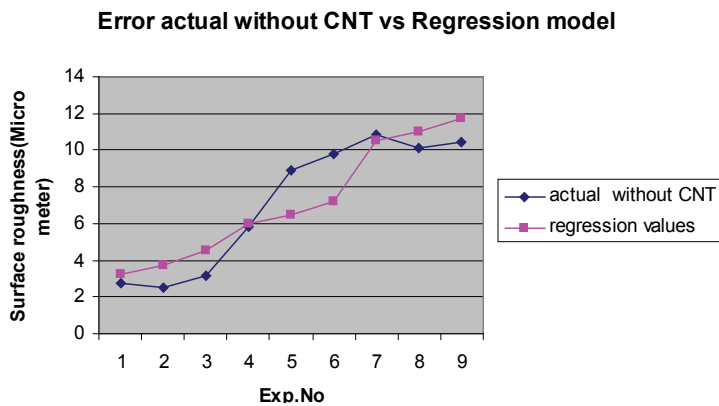$$Ra \text{ with } CNT = 1.58 \, (I)^{1.02} \, (\tau)^{-0.341}. \tag{12}$$

Error actual without CNT vs Regression model

Fig. 8. Error showing actual *Vs* regression Surface roughness without CNT
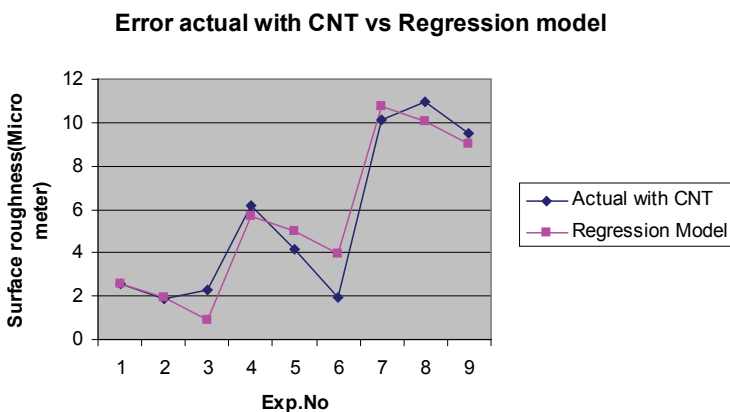
Error actual with CNT vs Regression model

Fig. 9. Error showing actual *Vs* predicted Surface roughness with CNT

Results of regression analysis are compared with experiments in Table 7 for 9 check sets. The comparison results are depicted in Table 10. This method is suitable for estimating surface roughness in an acceptable error ranges. The model generation of regression model took just a couple of seconds. From the results, an error of measurements occurs in surface roughness with nanotubes is less than without nanotubes used with dielectric fluid in EDM machining process.

Table 10. Comparison of regression model with experiment measurements for with and without using nanotubes

Exp. No	Without nano tubes surface roughness (μm)			With Nano tubes surface roughness (μm)		
	Experimental measurements	Regression model	Error	Experimental measurements	Regression model	Error
1	2.77	3.239	−0.469	2.59	2.597	−0.007
2	2.54	3.749	−1.209	1.85	1.915	−0.065
3	3.15	4.514	−1.364	2.31	0.892	1.418
4	5.83	5.96	−0.13	6.19	5.657	0.533
5	8.87	6.47	2.4	4.19	4.975	−0.785
6	9.79	7.235	2.555	1.96	3.952	−1.992
7	10.87	10.495	0.375	10.11	10.757	−0.647
8	10.14	11.005	−0.865	10.97	10.075	0.895
9	10.42	11.77	−1.35	9.52	9.052	0.468

3.7. ANOVA analysis

The purpose of analysis of variance is to find the significant factors affecting the machining process to improve the surface characteristics of Inconel 825 material in EDM machining process. ANOVA gives clearly how the process parameters affect the response and the level of significance of the factor considered. The ANOVA table for surface roughness of with and without carbon nano tubes is calculated.

The R^2 value of developed empirical model for surface roughness with nanotube is 94.86%. The high R^2 value indicates that better the model fits your data. Here 0.003 p value of pulse current factor is significant. The main output from an analysis of variance study ANOVA arranged in a Table 11 and 12.

Table 11. Shows the results of ANOVA for the surface roughness without carbon nano tubes

Machining parameters	Degree of freedom (f)	Sum of Squares (SSA)	Variance (VA)	FAo	P	Contribution (%)
A	2	92.527	46.264	28.36	0.004*	91.08
B	2	2.526	1.263	0.77	0.520	2.48
Error	4	6.525	1.631			6.44
Total	8	101.578				100

*Significant

S = 1.27719, R-Sq = 93.58%, R-Sq(adj) = 87.15%.

Table 12. Shows the results of ANOVA for the surface roughness with carbon nano tubes

Machining parameters	Degree of freedom (f)	Sum of Squares (SSa)	Variance (Va)	FAo	P	Contribution (%)
A	2	103.722	51.861	35.38	0.003*	90.98
B	2	4.435	2.217	1.51	0.324	3.88
Error	4	5.863	1.466			5.14
Total	8	114.020				100

*Significant

$S = 1.21069$, R-Sq = 94.86%, R-Sq(adj) = 89.72%.

List the sources of variation, their degrees of freedom, the total sum of squares, and the mean squares. The analysis of variance table also includes the F-statistics and p-values. Use these to determine whether the predictors or factors are significantly related to the response. Larger FAo value indicates that the variation of the process parameter makes a big change on the surface roughness.

3.8. Surface morphology

During the EDM process, the primary parameters were pulsed current and pulse-on duration, both of which are settings of the power supply. In order to assess the surface measurement results, an AFM study of the surface morphology of the EDM machined surface was conducted. Figure 10, 11 shows the three-dimensional AFM images of the machined surface obtained from the EDM specimens, where Ip is the pulsed current, and t_{on} denotes the pulse-on duration. The darker contrast corresponds to the lower areas of the surface, and the brighter corresponds to the higher.
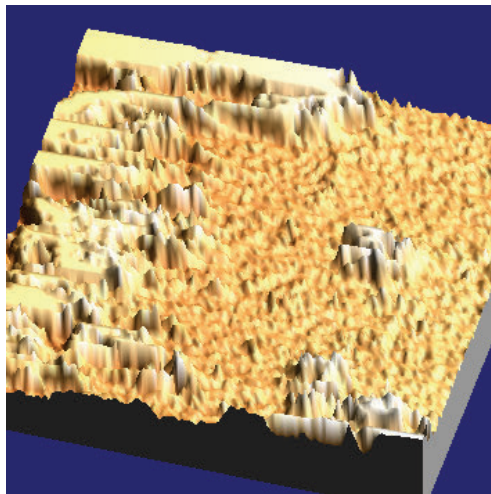

Fig. 10. 3D AFM image of sample 1 for 2 amps current with scanning area 10.5 μm × 10.5 μm with CNT

It is clear that the surface micro geometry characteristics include machining damages such as ridge-rich surfaces, micro-voids, and micro-cracks. The ridge-rich surface was formed by material melted during EDM, and blasted out of the surface by the discharge pressure. However, the surface immediately reached the solidification temperature being cooled by the surrounding working fluid. The micro-voids can be attributed to the gas bubbles expelled from the molten material during solidification. The micro-cracks were the result of the thermal stresses. The primary causes of the residual stress in the machined surface were the drastic heating and cooling rate and the non-uniform temperature distribution. In addition, the morphology of the EDM surface was dependent on the applied discharge energy. When applying the smaller pulsed current the surface characteristics have minor hillocks and valleys. When the pulsed current and pulse-on duration increased the machined surface exhibited a deeper crack or void and more pronounced defects.
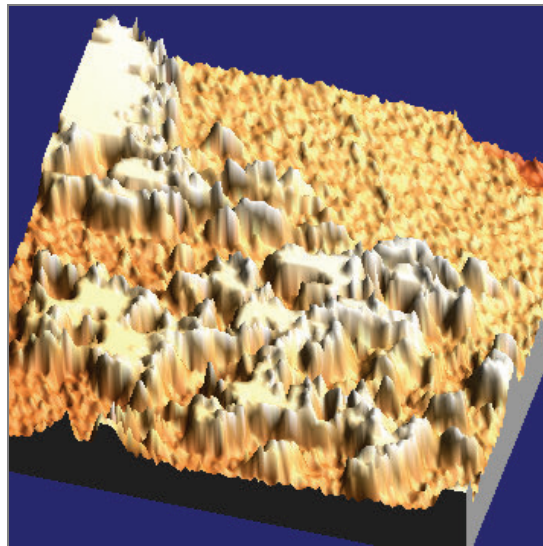

Fig. 11. 3D AFM Image samples 2 for 2 amps current
with scanning area 10.5 μm × 10.5 μm without CNT

3.9. Surface roughness

EDM erodes surfaces randomly. To determine the effect of the EDM process on the surface roughness of the tool steel, the surface profiles of the EDM specimens were measured by AFM. The average surface roughness, *Ra*, of the machined specimen was calculated from the AFM surface topographic data in a scanning area of 10.5 μm × 10.5 μm and the Figure 12–15 shows the measurement results. The surface roughness on the machined surface varied from 0.2 to 1.15 μm for a scanning area of 8 μm × 8 μm.
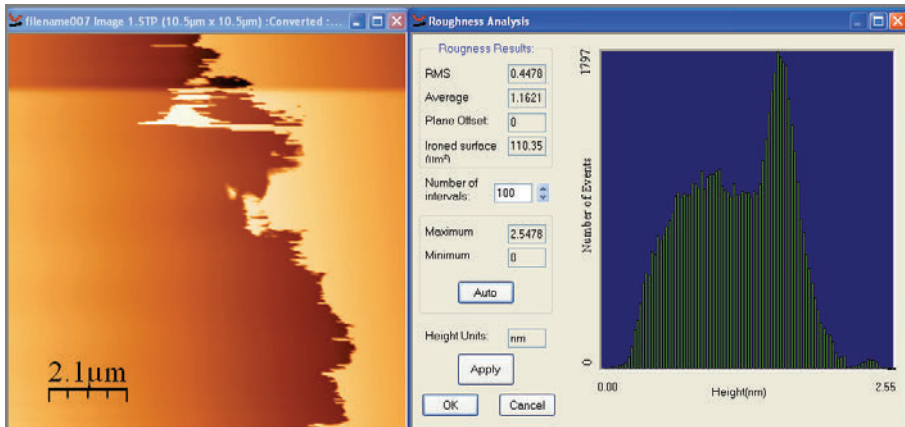
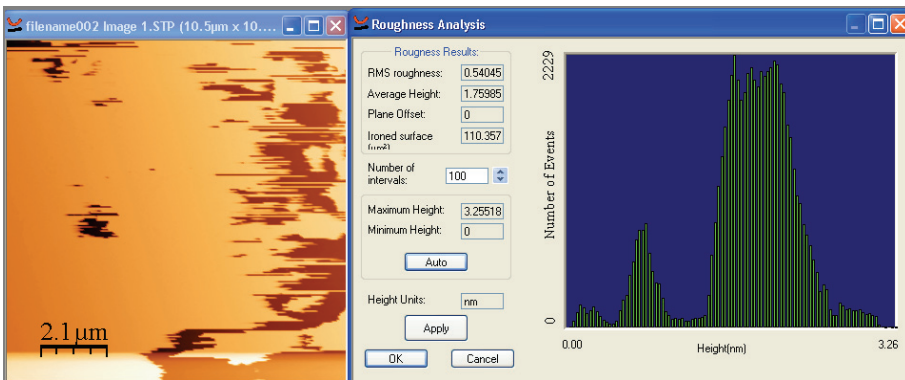Fig. 12. AFM Image and its results for 2 amps with CNT

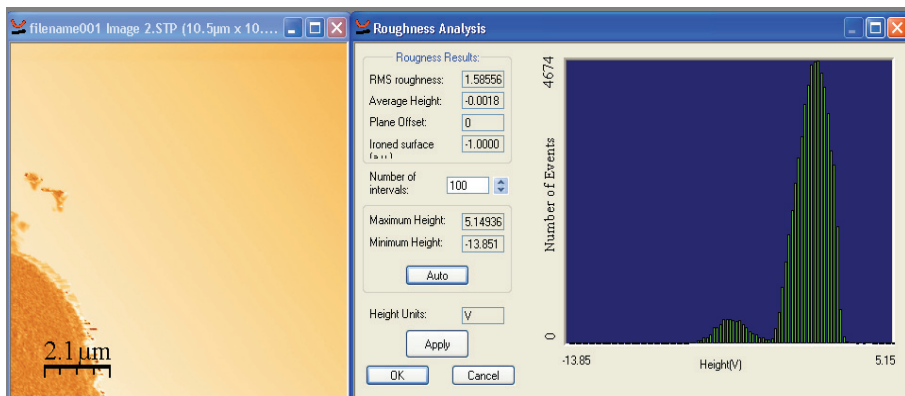Fig. 13. AFM Image and its results for 2 amps without

Fig. 14. AFM Image and its results for 5 amps with CNT
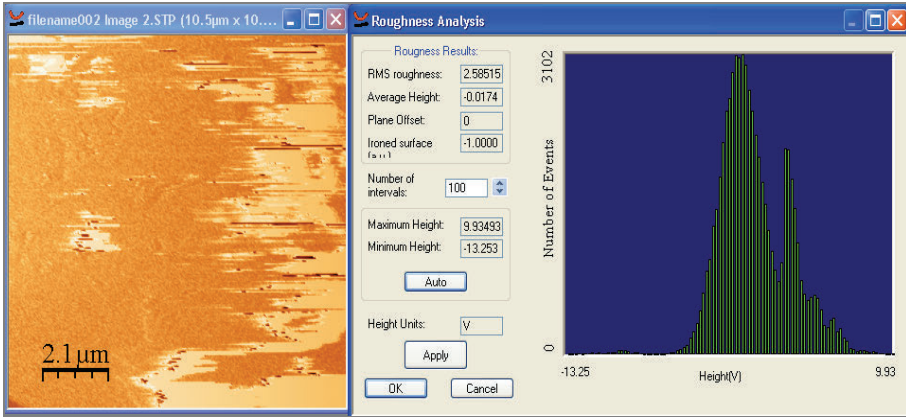
Fig. 15. AFM Image and its results for 5 amps without CNT

3.10. Micro cracks

In order to measure the maximum depth of the micro-cracks of the EDM specimen, the AFM was used to measure the object generating the line diagram of the cross section shown in Figures 16 and 17.
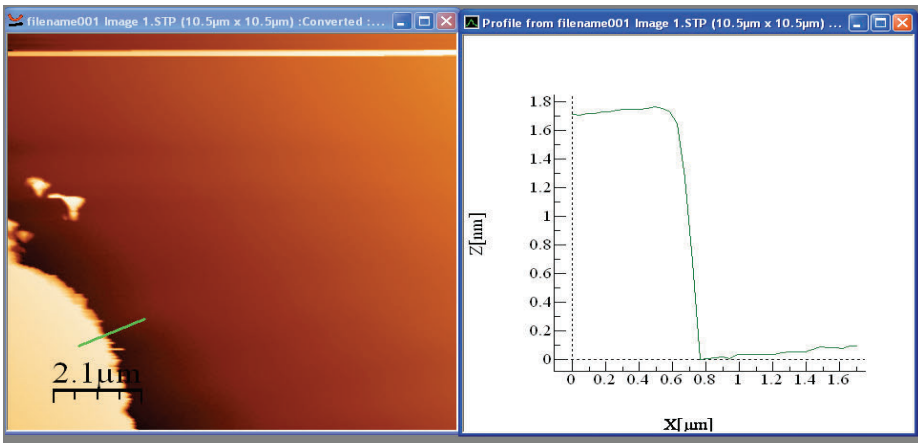
Fig. 16. Line profile of an AFM Image for 2 amps without CNT

The above line profile AFM image Figure 14 shows the micro cracks for the specimen sparked without CNT. The parameters used are current 0 amps, pulse on duration 8 µs and pulse off duration 7 µs.

$$D_{max} = h_{max} - h_{min} \tag{13}$$

where:

D_{max} – the maximum depth,

h_{max} and h_{min} – the maximum height and the minimum height of the section profile.

$D_{max} = 1.7$ nm.

Fig. 17. Line profile of an AFM Image for 2amps with CNT

$D_{max} = h_{max} - h_{min} = 1.6–0.25$

$D_{max} = 1.575$ nm.

Fig. 18. Line profile of an AFM Image for 5amps with CNT

$D_{max} = h_{max} - h_{min} = 1.7–0.1$

$D_{max} = 1.69$ nm

Fig. 19. Line profile of an AFM Image for 5amps without CNT

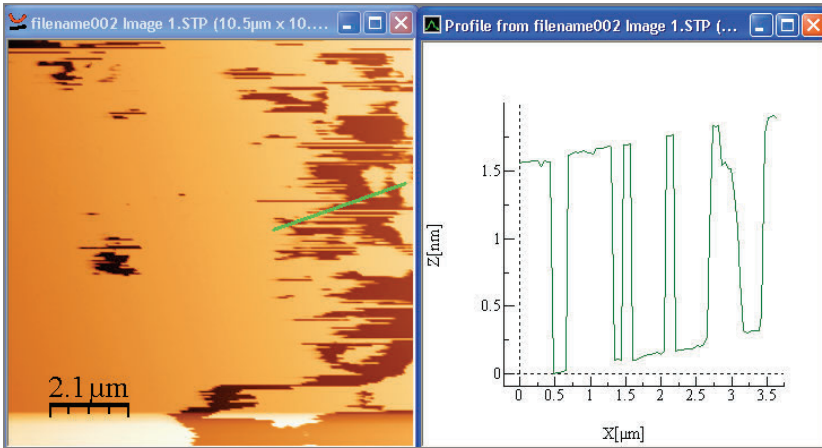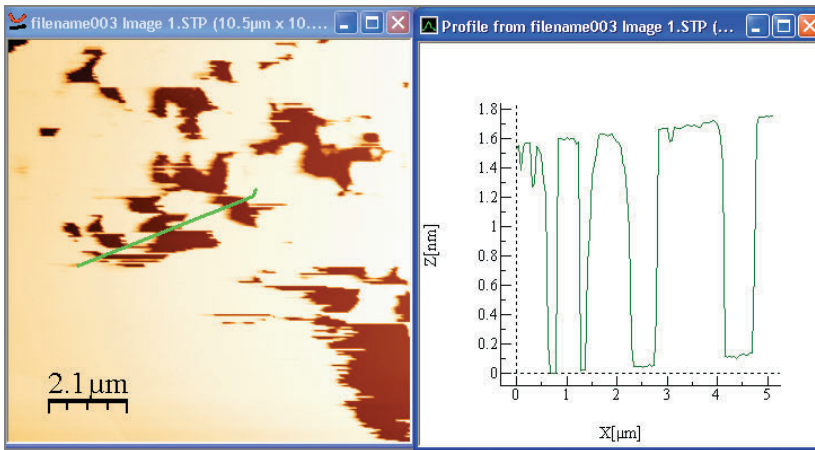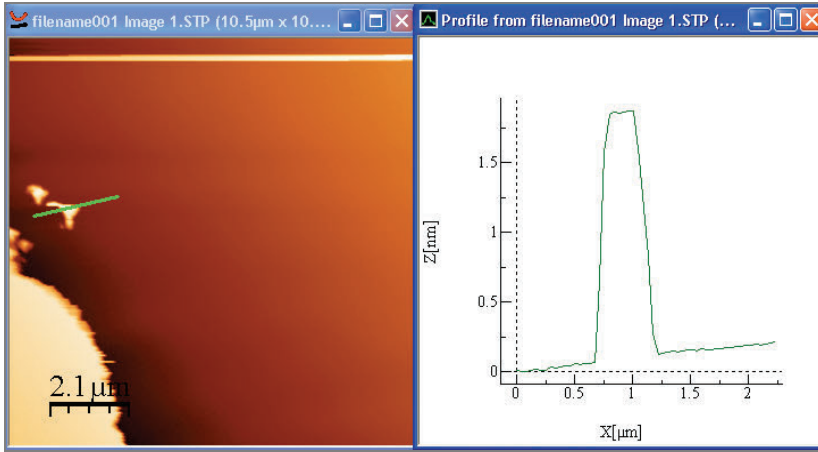$D_{max} = h_{max} - h_{min} = 1.8–0.25$

$D_{max} = 1.775$ nm.

A dotted line in the surface topography shows the position of the cross-section profile. The maximum depth of the micro-cracks can be determined from the distance between the highest peak and the lowest valley. The maximum depth of the micro-cracks is defined as.

The machined damages layer generated by the EDM process produces a harmful influence decreasing the service strength and life of the virgin material. This damage layer should be removed before being put to use. It is therefore recommended that the EDM specimen should be polished down to at least the maximum depth of the micro-cracks in order to improve its service life.

Table 13. Comparison results of with and without using CNT

	Without using CNT		With using CNT	
Current	2 amps	5 amps	2 amps	5 amps
Surface roughness in nm.	0.4478	2.58	0.540	1.585
Maximum depth of cracks in nm.	1.7	1.775	1.575	1.69

4. Conclusions

The experimental results indicate that the surface roughness after EDM is determined. Variation in the results is also achieved using multiwall CNTs. An excellent machined finish is obtained by setting the machine parameters to the best experiment analyzed by Taguchi method. Further AFM analysis was carried out to predict the surface characteristics with and without using carbon nano tube as dielectric fluids. It

is clear that the specimens sparked using CNTs have better surface finish, reduced micro cracks and better surface morphology as compared with specimens sparked without CNTs.

References

[1] Guu Y.H., Hocheng H., Chou C.Y., Deng C.S.: *Effect of electrical discharge machining on surface characteristics and machining damage of AISI D2 tool steel*, Materials Science and Engineering, A358, 2003, pp. 37–43.

[2] Prabhu S., Vinayagam B.K.: *Nano surface finish of AISI D2 tool Steel using multi wall carbon nano tube in Electrical Discharge Machining*, International journal of engineering research and technology, Vol. 1, No. 1, 2008, pp. 1–14.

[3] Puertas I., Luis C.J., Álvarez L.: *Analysis of the influence of EDM parameters on surface quality, MRR and EW of WC–Co*, Journal of Materials Processing Technology, Vol. 153–154, 2004, pp. 1026–1032.

[4] Guu Y.H., Hocheng H.: *Improvement of fatigue life of electrical discharge machined AISI D2 tool steel by TiN coating*, Materials Science and Engineering, A318, 2001, pp. 155–162.

[5] Guu Y.H.: *AFM surface imaging of AISI D2 tool steel machined by the EDM process*, Applied Surface Science, Vol. 242, 2005, pp. 245–250.

[6] Mahajan K.R., Knoppers G.E., Oosterling J.A.J., van Luttervelt C.A.: *Knowledge based design of EDM electrodes for mould cavities pre-machined by high-speed milling*, Journal of Materials Processing Technology, Vol. 149, 2004, pp. 71–76.

[7] Mamalis A.G., Vogtlander L.O.G., Markopoulos A.: *Nanotechnology and nanostructured materials: trends in carbon nanotubes*, Precision Engineering, Vol. 28, 2004, pp. 16–30.

[8] Pecas P., Henriques E.: *Electrical discharge machining using simple and powder-mixed dielectric: The effect of the electrode area in the surface roughness and topography*, IDMEC, Instituto Superior T´ecnico, TULisbon, Av. Rovisco Pais, 1049-001 Lisbon, Portugal.

[9] Wong Y.S., Lim L.C., Iqbal Rahuman, Tee W.M.: *Near-mirror-finish phenomenon in EDM using powder-mixed dielectric*, Journal of Materials Processing Technology, Vol. 79, 1998, pp. 30–40.

[10] Ho K.H., Newman S.T.: *State of the art electrical discharge machining*, International Journal of Machine Tools and Manufacture, Vol. 43, 2003, pp. 1287–1300.

[11] Singh S., Maheshwari S., Pandey P.C.: *Some investigations into the electric discharge machining of hardened tool steel using different electrode materials*, Journal of Materials Processing Technology, Vol. 149, 2004, pp. 272–277.

[12] Luis C.J., Puertas I., Villa G.: *Material removal rate and electrode wear study on the EDM of silicon carbide*, Journal of Materials Processing Technology, Vol. 164–165, 2005, pp. 889–896.

[13] Wilson M., Chapman and Hall: *Nanotechnology: basic science and emerging technologies*, 2002, ISBN 1-58488-339-1.

[14] Harris P.F.: *Carbon nanotubes and related structures: new materials for the twenty-first century*, Cambridge University Press, 1999, ISBN 0-521-55446-2.

[15] Saito R.: *Physical properties of carbon nanotubes*, Imperial College Press, 1998, ISBN 1-86094-093-5.

[16] Chow H.M., Yan B.H., Huang F.Y., Hung J.C.: *Study of added powder in kerosene for the micro-slit machining of titanium alloy using electro-discharge machining*, Journal of Materials Processing Technology, Vol. 101, 2004, pp. 95–103.

[17] Hayakawa S., Takahasi M., Itoigawa F., Nakamura T.: *Study on EDM phenomena with in-process measurement of gap distance*, Journal of Materials Processing Technology, Vol. 149, 2004, pp. 250–255.

[18] www.cheaptubes.com

Analiza powierzchni Inconelu 825 obrabianego obróbką elektroerozyjną z zastosowaniem nanorurek węglowych, wykorzystując metodę Taguchi

Wymagania dotyczące końcowej jakości powierzchni stopów typu Inconel 825 są bardzo wysokie. Zastosowanie nanorurek węglowych w dielektryku w procesie obróbki elektroerozyjnej pozwalają znacznie poprawić jakość powierzchni obrabianych materiałów. W pracy zastosowano metodę Taguchi w celu określenia optymalnych parametrów procesu.

Influence of the geometry of the arrangement inductor – crucible to the velocity of the transport of mass in the liquid metallic phase mixed inductive

R. PRZYŁUCKI, S. GOLAK, B. OLEKSIAK, L. BLACHA

Silesian Technical University, Krasińskiego 8, 40-019 Katowice, Poland.

The mutual reactions between the gaseous phase and liquid metals or their alloys are of particular importance for the processes of metal smelting and refining. A comprehensive kinetic analysis of such processes requires extensive knowledge of the mass transfer phenomena taking place in both the aforementioned phases. This results from the fact that in heterogeneous systems, the components of the individual phases react with one another only after penetrating the interface. The parameter characterising the mass transfer velocity in the given phase is the so-called mass transfer coefficient. Knowing its value with reference to both phases as well as knowing the constant velocity of the reaction taking place in the interfacial area enables calculation of the general mass transfer coefficient values characteristic for the given process but also identification of the stages determining the coefficient. Some of the metallurgical aggregates whose design evolution is currently widely discussed are vacuum induction furnaces used for smelting of metals and alloys as well as for their refining. Intensive mixing of the metallic bath, which occurs in the said aggregates, causes an increase in the mass transfer velocity in the metal, and therefore, it can determine various parameters, such as the evaporation process rate for the bath volatile contaminants. This article is an analysis of the results obtained under the tests aimed at determination of the influence exerted by the melting pot position against the inductor in an induction furnace on the mass transfer coefficient for liquid metallic phase.

Keywords: *metallurgy, barbotage, copper, refining, alloy*

1. Introduction

The mutual reaction between the gaseous phase and liquid metals or their alloys is of particular importance for the processes of metal smelting and refining. A comprehensive kinetic analysis of such processes requires extensive knowledge of the mass transfer phenomena taking place in both the aforementioned phases. This results from the fact that in heterogeneous systems, the components of the individual phases react with one another only after penetrating the interface. The parameter characterising the mass transfer velocity in the given phase is the so-called mass transfer coefficient. Knowing its value with reference to both phases as well as knowing the constant velocity of the reaction taking place in the interfacial area enables calculation of the general mass transfer coefficient values characteristic for the given process but also identification of the stages determining the coefficient. One of the metallurgical aggregates

whose design evolution is currently widely discussed is a vacuum induction furnace used for smelting of metals and alloys as well as for their refining. Intense mixing of the metallic bath, which occurs in the said aggregates, causes an increase in the mass transfer velocity in the metal, and therefore, it can determine various parameters, such as the evaporation process rate for the bath volatile contaminants. This article is an analysis of the results obtained under the tests aimed at determination of the influence exerted by the melting pot position against the inductor in an induction furnace on the mass transfer coefficient for liquid metallic phase.

2. Mass transfer in liquid phase

The hydrodynamic model applied to describe the phenomenon of mass transfer for an induction-stirred liquid metallic phase developed by Machlin. The model was based on the Higbie penetration model. Under this model, commonly referred to as a "streamline flow model", it was assumed that the liquid elements move as a rigid solid body along the contact surface between the bath and the gas, or between the bath and the melting pot, and the velocity gradient normal towards the surface is close to zero. In accordance with Machlin's theory, the mass transfer coefficient is described by the following dependence [1]:

$$\beta_l = \left(\frac{8 D_{AB} \cdot v_m}{\pi \cdot r_m} \right)^{0.5}.$$

(1)

Machlin's model was frequently used in kinetic analyses of the evaporation process for volatile contaminants of iron as well as copper or lead [2–4].

Assuming that one applies dependence (1) to calculate the value of coefficient β_l, a particularly important aspect would be the correct determination of the metal's velocity near the surface. According to Machlin, this value depends to a slight extend on the electric parameters of the furnace as well as on its dimensions, and for the aggregates of the capacity up to 1 Mg of metal, it amounts ca. $0.1 \text{ m} \times \text{s}^{-1}$. However, it has occurred that the nature of the metal motion in an induction furnace as well as its circulation and intensity are the functions of numerous variables, such as the furnace geometry, density of the power emitted or frequency of the current [5–8].

3. Determination of the metal velocity field

In order to determine the value of velocity v_m, one can apply a numerical method based on the so-called electromagnetic flow model [9–10]. The model comprises the following two subsequent elements:
- analysis of the electromagnetic field generated in the liquid metal,
- analysis of the velocity field occurring in the liquid metal.

Let us then elaborate on the last method, by applying it to determine the velocity of a liquid, inductively stirred Cu-Pb alloy in a JS5/III induction furnace manufactured by Leybold Heraeus.

The basic furnace operating parameters as well as the physical and chemical quantities characterising the liquid metal, which were used in the respective calculations, have been summarised in Table 1 below.

Table 1. Furnace operating parameters and selected properties of the Cu-Pb alloy

Furnace operating parameters		Liquid metal properties (Cu alloy + 2% wt. of Pb)	
Frequency	3 kHz	Temperature	1.473 K
Power	20 kW	Metal density	7.9 Mg×m^3
Melting pot internal diameter	0.1 m	Metal viscosity	0.0015 Pa×s
Inductor current intensity	155 A	Specific conductance	1.25×10^{-6} H×m
		Electric conductivity	4×10^6 S×m^{-1}

The electromagnetic field calculations were conducted in two dimensions, by applying a commercially available numerical programme, Flux. The programme was supplemented with certain procedures enabling determination of the mean value for the period of the forces volumetric density. In the model assumed for the electromagnetic field analysis, the melting pot was disregarded due to its negligible (as compared with the winding and the charge) specific conductance. And since such a system is axial-symmetrical in nature, the analytical model was limited to half of the geometry. Figure 1 is the analytical model diagram. The respective computational areas as well as the model boundaries have been marked as well.
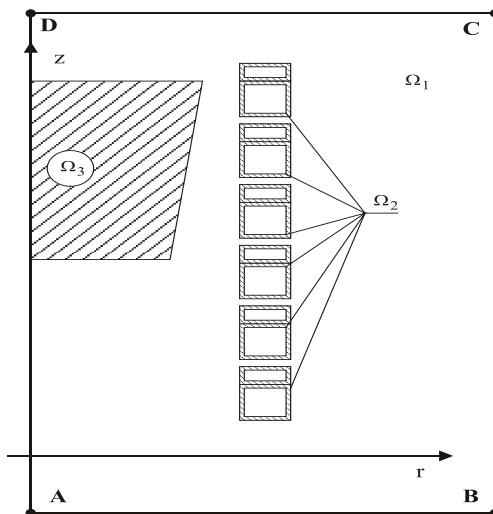

Fig. 1. Computational model of the electromagnetic part of calculations:
Ω_1 – air, Ω_2 – inductor winding, Ω_3 – charge material (liquid metal)

In the individual computational areas, the following differential equations of magnetic potential were solved for sinusoidal input functions:

$$\Omega_1: \quad \nabla \times \left(\frac{1}{\mu} \nabla \times \mathbf{A} \right) = 0, \tag{2}$$

$$\Omega_2: \quad \nabla \times \left(\frac{1}{\mu} \nabla \times \mathbf{A} \right) + j\omega\sigma\mathbf{A} = \mathbf{J}_{\dot{z}}, \tag{3}$$

$$\Omega_3: \quad \nabla \times \left(\frac{1}{\mu} \nabla \times \mathbf{A} \right) + j\omega\sigma\mathbf{A} = 0, \tag{4}$$

where j is imaginary unit, ($j = \sqrt{-1}$).

At the boundaries of the computational area: $\overline{AB}, \overline{BC}, \overline{CD}, \overline{DA}$, the Dirichlet boundary condition of $A = 0$ was assumed.

The components of the volumetric density of electromagnetic forces (mean values for the whole period) were calculated according to the vector potential based on formulas 5 and 6.

$$f_r = \frac{1}{2} \left\{ \mathrm{Re}(\underline{J}) \mathrm{Re}\left(\underline{B}_{\dot{z}}\right) + \mathrm{Im}(\underline{J})(\underline{B}_{\dot{z}}) \right\}, \tag{5}$$

$$f_z = -\frac{1}{2} \left\{ \mathrm{Re}(\underline{J}) \mathrm{Re}\left(\underline{B}_r\right) + \mathrm{Im}(\underline{J})(\underline{B}_r) \right\}, \tag{6}$$

where $J = j \times \omega \times \sigma \times A$.

Components of the forces were determined in area Ω_3 for a uniform, rectangular mesh of 181×199 nodes (in line with axes r and z respectively).

The areas of flows were calculated numerically using the Fluent 6.2 software. The model entailed axial symmetry of the system. A two-dimensional, structural mesh of 181 cells in the radial direction and 199 cells in the axial direction was applied.

Specific boundary conditions were introduced into the model in the form of two walls (the melting pot's bottom and generator) without any skid (i.e. with a zero velocity by the wall), an axis of symmetry and a free surface of the metal simulated by a wall free of friction with the liquid (Figure 2).

The impact of the electromagnetic field forces was introduced into the model by setting user defined functions. The functions used the field of force previously established by means of the Flux2D programme. Since the structure of the force field mesh developed using Flux2D differed from the mesh of the flow model, it was necessary to

interpolate the results. However, as the meshes only differed in the radial direction and the input mesh of forces was denser than the mesh of flows, the interpolation error could be considered negligibly small.
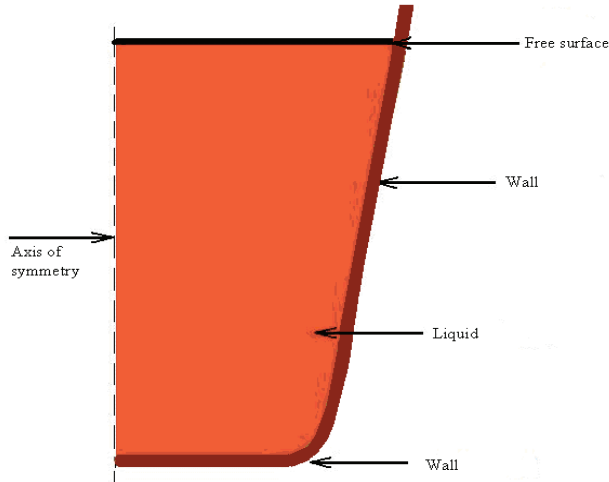

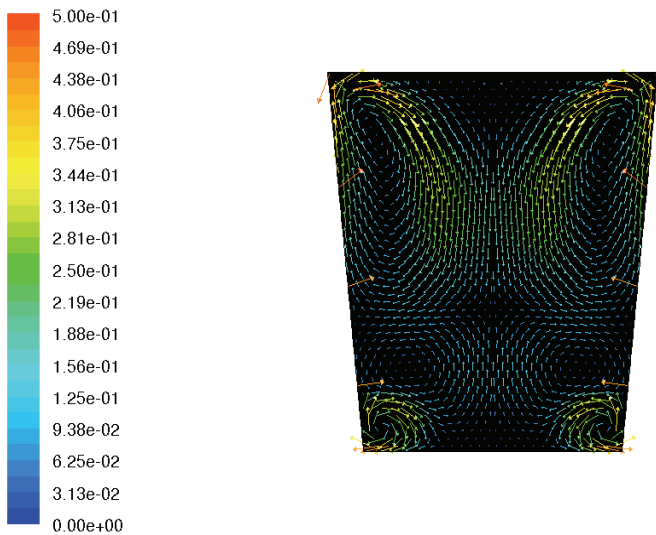Fig. 2. Boundary conditions in the flow model

Fig. 3. Velocity field obtained for a melting pot located in the inductor centre (variant 1, Table 2)

In order to calculate the velocity and turbulence, a second order discretisation was applied [11]. The pressure was determined based on the standard method proposed by

Rhie and Chow [12]. The analysed method of calculating the velocity of induction-stirred liquid metal was also applied to liquid Fe-Cu alloys [4].
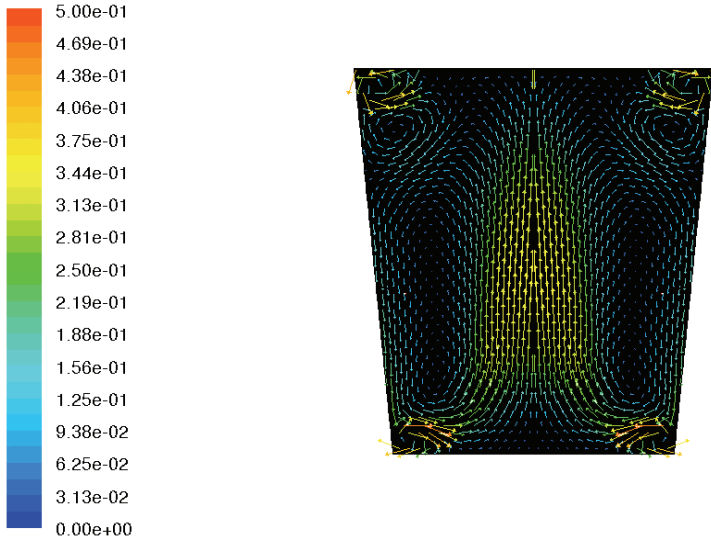

Fig. 4. Velocity field obtained for a melting pot located in the inductor upper section
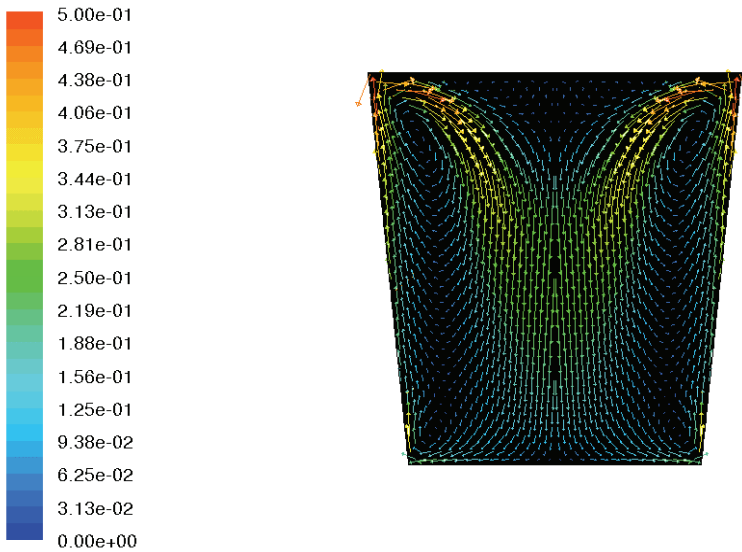(liquid's upper surface = inductor's upper surface)

Fig. 5. Velocity field obtained for a melting pot located in the inductor lower section
(liquid's bottom surface = inductor's bottom edge)

Table 2 provides a summary of the liquid metal velocity values obtained as a result of the calculations conducted for various melting pot's positions against the inductor.

Table 2. Liquid metal velocity on various melting pot's positions in the furnace against the inductor

Melting pot's position	Distance between the liquid metal's lower surface and the inductor's lower edge mm	Mean velocity throughout the volume m × s⁻¹	Mean velocity on the surface m × s⁻¹
1	0	0.149	0.259
2	37	0.143	0.234
3	69	0.133	0.215
4	74	0.130	0.211

1 – liquid's bottom surface = inductor's bottom edge,
2 – melting pot arranged in the centre of the inductor,
3 – basic arrangement (upper surface of the liquid 5 mm below the inductor's upper edge),
4 – liquid's upper surface = inductor's upper edge.

The dependence depicted in Figure 6 implies that as the distance between the bottom surface of the metal inside the melting pot and the inductor's bottom edge increases, the metal velocity near the surface decreases. This means that by changing the melting pot's position against the inductor, one influences the metal mean velocity near the surface, and consequently, also the mass transfer between the liquid and gaseous phase.
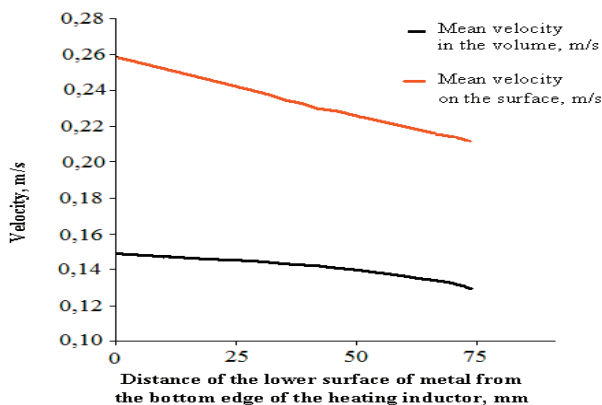
Fig. 6. Influence of arranging the crucible with regard to the head inductor to the velocity of metal by the surface

4. Determination of the mass transfer coefficient value for the liquid phase

Based on dependence (1) as well as the values calculated for velocity v_m, the respective values of mass transfer coefficient β_l were estimated for various arrangements of the melting pot with reference to the inductor. The results obtained have been summarised in Table 3 and depicted in Figure. 7.

Table 3. Value of coefficient β_l determined for various melting pot's positions against the inductor (Cu-Pb alloy, < 2% Pb)

Melting pot's position	Mass transfer coefficient for the liquid phase $\beta_1\ m \times s^{-1}$
1	5.16×10^{-4}
2	4.90×10^{-4}
3	4.70×10^{-4}
4	4.65×10^{-4}

1 – liquid's bottom surface = inductor's bottom edge,
2 – melting pot arranged in the centre of the inductor,
3 – basic arrangement (upper surface of the liquid 5 mm below the inductor's upper edge),
4 – liquid's upper surface = inductor's upper edge.
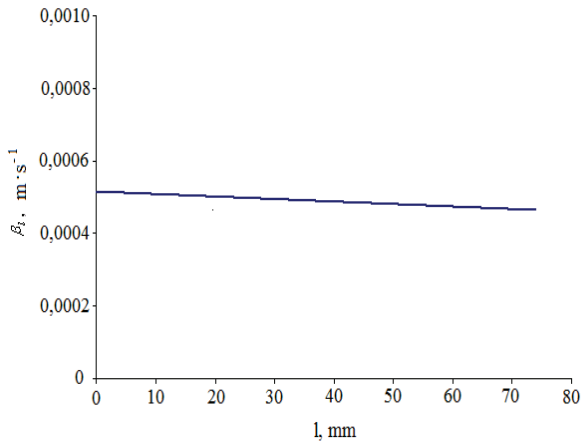
Fig. 7. Influence of the melting pot's arrangement on the mass transfer coefficient for
the inductively stirred metallic liquid phase
(*l* – distance between the lower metal surface and the bottom inductor edge)

5. Conclusions

The tests conducted implied an influence exerted by the melting pot arrangement against the inductor on the mass transfer coefficient for the induction-stirred liquid metallic phase. Using a numerical method based on the so-called electromagnetic flow field enabled determination of the metal velocity near the surface and the mean velocity deeper in the metal. The larger the distance between the lower surface of the liquid metal and the inductor's bottom edge is, the lower the value of mass transfer coefficient β_l is.

References

[1] Poirier D.R., Geiger G.H.: *Transport phenomena in materials processing*, TMS Warrendale, 1994.

[2] Ozberk E., Guthrie R.: *A kinetic model for the vacuum refining of inductively stirred copper melts*, Vol. 17B, 1986, pp. 87–103.

[3] Łabaj J., Botor J., Sosnowski R.: *Kinetik der Zinkverdampfung aus Zn-Ag-Pb Legierungen bei Unterdruck*, Archives of Metallurgy, Vol. 47, No. 3, 2002, pp. 307–320.

[4] Łabaj J.: *Kinetyka parowania miedzi z ciekłego żelaza*, Wyd. Oldprint, Katowice, 2010.

[5] Szekely J., Chang W.: *Turbulent electromagnetically driven flow in metals processing*, Ironmaking and Steelmaking, Vol. 3, 1977, pp. 196–204.

[6] Szekely J., Chang W., Ryan R.E.: *Turbulent electromagnetically driven flow in metals*, Metall. Trans. B, Vol. 8B, 1977, pp. 333–338.

[7] Tarapore E.D., Evans J.W.: *Fluid velocities in induction melting furnaces. Part I. Theory and laboratory experiment*, Metall. Trans. B, Vol. 7B, 1976, pp. 343–351.

[8] Tarapore E.D., Evans J.W., Langfeld J.: *Fluid velocities in induction melting furnaces. Part II. Large scale experiments and calculations*, Metall. Trans. B, Vol. 8B, 1977, pp. 179–184.

[9] Golak S., Przyłucki R.: *A simulation of the coupled problem of magnetohydrodynamics and a free surface for liquid metals*, Transactions on Engineering Science, WIT, Vol. 63, 2009.

[10] Golak S.: *Application of image analysis for the measurement of liquid metal surface. Transactions on modelling and simulation*, WIT, Vol. 48, 2009.

[11] Barth T.J., Jespersen D.: The *design and application of upwind schemes on unstructured meshes*, Technical Report AIAA-89-0366, AIAA 27th Aerospace Sciences Meeting, Reno, 1989.

[12] Rwie C.M., Chow W.L.: *Numerical study of the turbulent flow past an airfoil with trailing-edge separation*, AIAA Journal, No. 21, 1983, pp. 1525–1153.

Wpływ geometrii układu cewka–tygiel na szybkość transportu masy w ciekłej fazie metalicznej mieszanej indukcyjnie

Pełna analiza kinetyczna procesów chemicznych zachodzących w klasycznych układach metalurgicznych ciekły metal–faza gazowa wymaga znajomości zjawisk transportu masy, z którymi mamy do czynienia w obu fazach. Wynika to z faktu, że w układach heterogenicznych składniki poszczególnych faz reagują ze sobą tylko po przedostaniu się do granicy międzyfazowej. Parametrem charakteryzującym szybkość transportu masy w danej fazie jest tzw. współczynnik transportu masy. Jego znajomość w odniesieniu do obu faz, jak i znajomość stałej szybkości reakcji zachodzącej na powierzchni międzyfazowej pozwala na wyznaczenie wartości ogólnego współczynnika transportu masy charakteryzującej dany proces a także określenie etapów determinujących go. Jednymi z agregatów metalurgicznych, których rozwój konstrukcyjny jest obecnie szeroko obserwowany są próżniowe piece indukcyjne wykorzystywane do wytapiania metali i stopów, jak i ich obróbki rafinacyjnej. Poniżej przedstawiono wyniki badań, których celem było określenie wpływu geometrii układu cewka–tygiel na szybkość transportu masy w ciekłej fazie metalicznej mieszanej indukcyjnie.

Numerical homogenization by using the fast multipole boundary element method

J. PTASZNY, P. FEDELIŃSKI

Silesian University of Technology, Konarskiego 18A, 44-100 Gliwice, Poland.

The paper concerns the numerical homogenization of non-homogeneous linear-elastic materials by using the fast multipole boundary element method (FMBEM). Application of the FMBEM allows for the analysis of structures with larger number of degrees of freedom (DOF) in comparison to the conventional collocation BEM, which has at least the quadratic complexity. The FMBEM is convenient in the numerical homogenization by modelling of complex representative volume elements. In this article two examples of homogenization are presented. The first one concerns a porous material, and the second one – a composite material. The obtained results are in good agreement with analytical, semi-empirical and empirical models, and also with numerical results presented by other authors.

Keywords: *numerical homogenization, fast multipole boundary element method, effective elastic constants*

1. Introduction

The design of elements made of non-homogeneous materials (e.g. porous or composite ones) requires the knowledge of effective (homogenized) elastic constants. For the determination of the properties one can apply analytical, empirical or numerical methods. In the analytical methods some assumptions are made and thus the area of application is limited to relatively simple geometry of microstructure and a small volume fraction of pores, inclusions, etc. The empirical methods require the preparation of specimens which are subsequently tested for the searched properties. This results in relatively high costs. A meaningful alternative for the above described methods is the numerical analysis by using the representative volume element (RVE) concept [1].

There are several methods (or groups of methods) used for the numerical analysis of physical structures and phenomena, i.e.: the finite difference method (FDM), the finite element method (FEM), the boundary element method (BEM) and the group of meshless methods. From the point of view of geometry modelling (irregular boundaries, multiply connected domains and subdomains), which is important in the context of the numerical homogenization, the FEM and the BEM can be considered more effective than other methods. Furthermore, the BEM can be more efficient than the FEM because in many cases it requires only the discretization of boundaries of the analyzed domain. However, the complexity of the conventional collocation BEM is $O(N^2)$, where N is the number of degrees of freedom (DOF) of the analyzed structure. This

affects the possible maximum size of analyzed structures, which usually does not ex-
ceed several thousands of DOF. The analysis of large structures by the BEM can be
extremely time-consuming. In order to reduce the complexity the fast multipole
method (FMM) can be used [2]. The fast multipole BEM (FMBEM) has the linear
complexity and can be applied to the analysis of much complex structures in relation
to the conventional BEM.

Several authors performed the static analysis of linear-elastic structures with holes,
inclusions or cracks, which modelled RVEs or unit cells of non-homogeneous materi-
als, by using different versions of the BEM. Firstly a short review of selected papers
concerning the conventional BEM applications will be given. Eischen and Torquato
[3] analyzed 2-D unit cells containing inclusions forming the hexagonal array. The
effective material properties for a number of inclusion-matrix elastic constants' ratios
and volume fractions of inclusions were given. Hu et al. [4] analyzed perforated plates
with randomly or normally distributed identical holes by the conventional BEM. Ef-
fective moduli of the structures were determined and compared to values obtained by
several analytical models. Due to a relatively large number of degrees of freedom
(about 8 000) a special technique, consisting in the processing of the main matrix of
the system of equation partially, was applied to overcome the limitation of the com-
puter memory. Yao et al. [5] proposed a BEM formulation for the linear-elastic analy-
sis of plates containing many identical inclusions. Yang and Qin [6] used the concept
of unit cell for the determination of effective elastic constants of composites, modelled
as 2-D structures containing rigid circular inclusions. The results were compared to
finite element method results.

The structure size limitation encountered in the analysis by the conventional
collocation BEM pulled researchers to use improved versions of the BEM, with reduced
complexity. One of the first papers concerning the analysis of non-homogeneous
structures by a multipole BEM was by Yamada and Hayami [7]. They applied
a multipole BEM code based on the algorithm of complexity O ($N \log N$), using the
multipole expansion only (without the local one), to the analysis of a rectangular plate
with many holes. They analyzed structures with up to 900 constant elements. For such
numbers of DOF, the multipole algorithm appeared to be less effective than the
conventional one. Greengard and Helsing [8] applied the Sherman formulation for the
analysis of linear-elastic unit cells containing inclusions of different shapes. They
assumed periodic boundary conditions to determine effective elastic constants of the
material. Helsing [9] applied the FMBEM and the complex potential formulation to
the determination of effective elastic properties of 2-D RVEs containing many cracks.
Helsing and Jonsson [10] proposed a new complex potential BEM formulation. They
applied the new method in combination with the FMM to the evaluation of effective
properties of 2-D structures containing many circular and elliptic holes. Yao et al. [11]
applied their formulation for many identical inclusions with the FMBEM, introduced
in [5], to the evaluation of elastic constants of composites with the direct bonding
between inclusions and matrix, and also with interphases between inclusions and

matrix. Wang et al. in [12] described several techniques for the preconditioning of the FMBEM system of equations for structures with many inclusions or cracks. Liu [13] applied the FMBEM using the constant boundary elements. The stress results for a plate with one hole were investigated. Also, effective Young's moduli for plates with many uniformly and randomly distributed identical holes were determined. Ptaszny and Fedeliński [14] applied a FMBEM code using the three node quadratic boundary elements. In the paper, an analysis of structures similar to those described in [13], was performed. Effective properties of perforated plates were determined and compared to results obtained by an analytical model. An influence of the number of expansion terms on the stress results was investigated. Also, an influence of boundary conditions on the convergence of the iterative solution process was shown. The application of the higher-order isoparametric elements resulted in a lower number of DOF and expansion terms, in comparison to the constant element version presented most frequently by other authors.

In this work the authors' results of homogenization of porous and composite materials, compared to empirical, semi-empirical and analytical models, are presented. The version of the FMBEM with the quadratic boundary elements is applied. The present article is an expansion of the previous work [14]. Here the analysis is performed for different values of porosity or volume fraction of filler respectively, with fixed parameters of the FMBEM. The comparison of different models confirms validity of the developed numerical method for a broader range of different materials.

This article is organized as follows. In Section 2 the fundamental principles of numerical homogenization are presented. In Section 3 the FMBEM algorithm is briefly described. Section 4 contains two examples of the numerical homogenization. The first example concerns the determination of the effective Young's modulus of sintered alumina, which is a porous material. The second example concerns the determination of the effective transverse Young's modulus of a glass/epoxy fiber-reinforced composite. Section 5 contains conclusions.

2. Numerical homogenization

Behaviour of non-homogeneous structures is described by differential equations with discontinuous coefficients. In general, homogenization consists in the determination of smooth coefficients of partial differential equations which can be applied to the prediction of structure response on the macroscopic scale. In the case of linear-elastic structures the result of homogenization are the effective elastic constants. The commonly used homogenization approach is the determination of constitutive relation between averaged field variables (e.g. stresses and strains). The volume averaging is carried out over a statistically representative volume element (RVE) [1]. This requires the analysis of a given boundary value problem on the micro-scale, described by the RVE, which can be performed by using a numerical method.

To apply the RVE method one has to take into consideration the following principles:

I. The separation of scales principle:

$$L_1 >> L_2 >> L_3,$$ (1)

where L_1, L_2, and L_3 are the characteristic lengths of the structure, the RVE, and a microstructure constituent respectively.

II. The averaging theorem:

$$\langle \cdot \rangle = \frac{1}{|\Omega_0|} \int_{\Omega_0} \cdot \, d\Omega_0,$$ (2)

where $\langle \cdot \rangle$ denotes the average of a given field over the volume Ω_0 of the RVE.

III. The Hill-Mandel condition:

$$\langle \sigma_{ij} \varepsilon_{ij} \rangle = \langle \sigma_{ij} \rangle \langle \varepsilon_{ij} \rangle.$$ (3)

where σ_{ij}, ε_{ij} are micro stress and strain tensors respectively. This condition imposes the equality of the averaged micro-scale energy density and the macro-scale energy density at the selected point of macro-structure corresponding to the RVE.

IV. The boundary conditions satisfying the Hill-Mandel condition. The most frequently applied conditions are:

– Linear displacements (the Voigt assumption):

$$u_j \big|_{\partial \Omega_0} = \varepsilon_{ij} x_i \Rightarrow \langle \varepsilon_{ij} \rangle = \varepsilon_{ij}.$$ (4)

– Uniform tractions (the Reuss assumption):

$$t_j \big|_{\partial \Omega_0} = \sigma_{ij} n_i \Rightarrow \langle \sigma_{ij} \rangle = \sigma_{ij}.$$ (5)

– Periodic boundary conditions:

$$u_j^+ - u_j^- = \langle \varepsilon_{ij} \rangle \cdot \left(x_i^+ - x_i^- \right), \quad t_i^+ = -t_i^-, \quad \forall \mathbf{x} \in \partial \Omega_0 : n_i^+ = -n_i^-.$$ (6)

In the above formulas the symbols denote: u_j, t_j – displacements and tractions, x_i – coordinates of a point in the RVE, $\partial \Omega_0$ – the external boundary of the RVE, n_i – coordinates of outward unit vector normal to $\partial \Omega_0$. The superscripts "+" and "–" indicate quantities defined at mutually opposite faces of the RVE.

V. The constitutive equation for the homogenized material, which is the relation between the averages:

$$\left\langle \sigma_{ij} \right\rangle = c'_{ijkl} \left\langle \varepsilon_{kl} \right\rangle, \tag{7}$$

where c'_{ijkl} is the tensor of the effective elastic constants.

The Hill–Mandel condition (3) determines the size of RVE. The size should be large enough to assure small boundary field fluctuations in reference to the averaged values. The larger is the RVE size, the more accurate are the results of homogenization, assuming the principle of separation of scales (1) is satisfied. Results obtained by different authors (e.g. [4], [14]) show that the RVE models should contain at least one hundred inhomogeneities to provide acceptable results, when using the uniform tractions, linear displacements, or mixed displacement-traction boundary conditions.

3. The fast multipole boundary element method

The boundary integral equation of linear elasticity is obtained from Somigliana's identity [15]. It contains single and double layer potentials, which are integrals along the boundary of analyzed structure, with the fundamental solutions of elasticity as kernels. The kernels are multiplied by the boundary tractions or displacements, respectively. The boundary is discretized by using elements, along which the boundary values are approximated by shape functions. The boundary integral equation has to be satisfied for each boundary node as the collocation point. Thus, a system of algebraic equations is obtained, which can be written in the matrix form:

[H]{U} = [G] {T}. $\tag{8}$

The matrices [**H**] and [**G**] depend on the fundamental solutions, and the vectors {**U**} and {**T**} contain boundary displacements and tractions respectively. The system can be solved for the unknown displacements and tractions. The matrices of the system are full and nonsymmetric. For this reason the BEM in the original collocation version is inefficient in the analysis of structures with a large number of DOF.

To overcome the above difficulty the FMBEM can be applied. In this section a general idea of the fast multipole boundary element method will be introduced. For a detailed description of the method we refer the Reader to the literature (e.g. [16]).

The FMBEM uses *multipole expansions* of the integrals (potentials) at points located near to the integration points *x* (Figure 1a). The expansion terms are products of *multipole moments* and *functions*. The moments depend on the location of the expansion point and integration points, and densities of the potentials (the boundary displacements and tractions). The functions depend on the location of the expansion point and collocation point *x′*. Respective moments calculated for many boundary elements

are added together and thus influences of many integration points are reduced to the single point. The multipole functions are expanded further around point near to the collocation point (Figure 1a). The terms of the series are products of *local moments* and *local functions*. The local moments depend on the location of the multipole and local expansion points, and are calculated by the translation of the local moments (*multipole-to-local translation*, M2L). The local functions depend on the location of the local expansion points and the collocation points. Thus, the reduced influences are distributed to many points. The number of the potential term calculation operations is reduced significantly in comparison to the conventional BEM, where for each collocation point all the potentials coming from all the integration points have to be calculated.
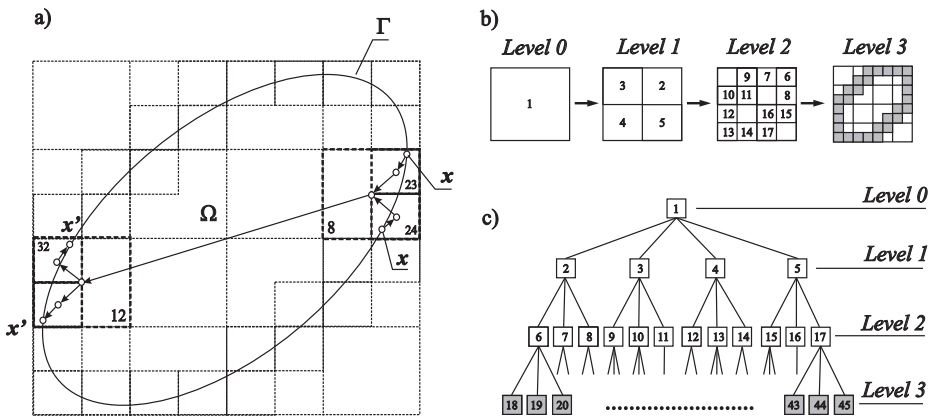

Fig. 1. a) The idea of FMBEM and the boundary element clustering,
b) The clustering stages, c) The hierarchical tree structure

The series of a finite number of terms are convergent when the integration points are far enough from the collocation points. For each collocation points *near* and *far fields* are determined. In the near field the series are not convergent and all the potentials are calculated directly. In the far field the expansions are used. The fields are determined by clustering of the boundary elements. The domain of the body Ω, with boundary Γ, is enclosed within a square which is divided recursively into smaller clusters, until they contain a fixed number of the boundary elements. The clusters form a hierarchical tree structure consisting of nodes, their children and ancestors, corresponding to the clusters. The clustering scheme and the tree structure are shown in Figures 1b, c.

Important steps of the algorithm are translations of the multipole and local moments. The first translation is shifting the multipole expansion points. The method is applied for the evaluation of the moments for larger clusters, without the necessity of integration along the same boundary elements. The operation is called *multipole-to-multipole translation* (M2M). Similarly the local moments are transformed by shifting

the local expansion point – *local-to-local translation* (L2L). Thus, new moments for smaller clusters are calculated which are applied to the evaluation of the far-field terms of the potentials. As the result of all the operations, products of the matrices and the boundary quantities vectors are obtained. Summarizing, the algorithm consists of the following steps:

- Clustering of the boundary elements.
- Calculation of the multipole moments of the smallest clusters.
- M2M translations.
- M2L translations.
- L2L translations.
- Evaluation of the potential terms by using the local series.

The sequence of the translations is shown in Figure 2. After all the operations the system of Equations (8) can be written in the following form:

$$[\mathbf{H}]^{near} \{\mathbf{U}\} + \{\mathbf{HU}\}^{far} = [\mathbf{G}]^{near} \{\mathbf{T}\} + \{\mathbf{GT}\}^{far}. \tag{9}$$
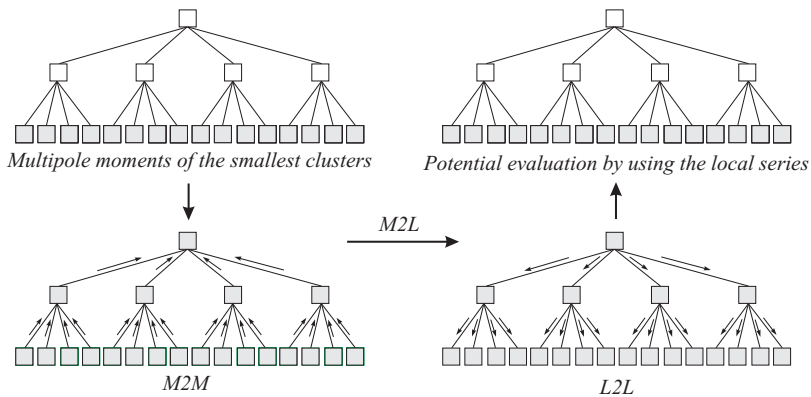

Fig. 2. The sequence of the moment translations

The "near" matrices include the near-field terms of the potentials calculated directly. The "far" vectors correspond to the far-field influence, and are computed by using the expansions. The system of equations can be solved only by using an iterative solver, as the matrices are not calculated explicitly. The complexity of a single iteration is $O(N)$. In this work the FMBEM code described in [14] was used.

4. Numerical examples

4.1. Porous material

The analysis of 2-D perforated plate suffices for the determination of effective Young's modulus of 3-D porous material, as it was shown in [17]. In the cited article a computer

code was used for the conversion of digitalized 2-D images of porous glass microstructure into finite element meshes, and the FEM analysis was performed for the determination of the effective Young's modulus. The results agreed with empirical formulas for the effective modulus, which is a function of the matrix modulus and the porosity.

The presented example shows analyses of 2-D models of sintered porous alumina specimens of different porosity. The models were constructed according to the data given in [18]. The RVEs were square plates under tension (the Reuss assumption), containing up to 200 randomly distributed circular holes of different radii, in plane stress (Figure 3). The porosity V ranged from 0.05 to 0.4. Young's modulus of the non-porous material was $E_0 = 400$ GPa and the Poisson ratio was $v = 0.23$. The length of the square side was equal to 2 μm. The tensile traction force was $t_1 = 100$ MPa. According to [17], the maximum pore (hole) size was increased with the increase of porosity, and ranged from about 0.05 μm to 0.075 μm, within the porosity range from about 0.075 to 0.4. Each hole was discretized by 16 boundary elements and each square side was discretized by 160 elements. The maximum number of DOF equalled 15 360. For a computer with 1 GB RAM such size of structure was beyond the scope of efficient analysis by the conventional BEM, and therefore the FMBEM was applied.
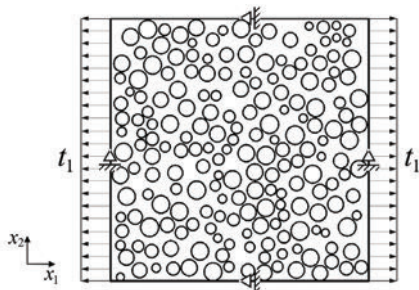

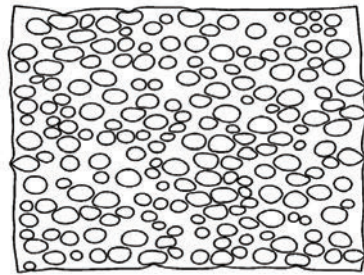Fig. 3. The RVE of porous material with porosity $V = 0.4$

Fig. 4. Deformed RVE of the porous material

The system of equations was solved by the preconditioned GMRES. The initial guess was the zero vector. The relative error for the iterative solver was set to 10^{-6}. The preconditioning sparsity pattern based on leaves of the tree was used [12]. The maximum number of elements in leaves was set to 20 and the number of expansion terms was set to 5. A deformed model is shown in Figure 4.

The formula given by the averaging theorem (2) can be transformed into the form containing only the integral along the external boundary of the plane RVE. Thus, the mean strain components can be calculated by the equation:

$$\left\langle \varepsilon_{ij} \right\rangle = \frac{1}{A} \int_{\Gamma_0} u_i n_j d\Gamma_0, \tag{10}$$

where A denotes the area of the plane RVE, and Γ_0 is the external boundary. For the case of the uniaxial tension the constitutive Equation (7) reduces to a simple form, by which the effective Young's modulus can be calculated:

$$E' = \frac{\langle \sigma_{11} \rangle}{\langle \varepsilon_{11} \rangle}, \tag{11}$$

where $\langle \sigma_{11} \rangle = t_1$.

The results were compared to analytical predictions obtained by using the Kachanov model for elastic medium with interacting (randomly distributed) holes [19]:

$$E' = E_0 \frac{1-V}{1+2V}, \tag{12}$$

where V denotes porosity.

The agreement of numerical results with empirical models was also examined. Two following empirical equations were taken under consideration [17–18]:

$$E' = E_0 (1-V)^{2.8}, \tag{13}$$

$$E' = E_0 \exp(-bV). \tag{14}$$

The parameter b depends on the pore shape and is close to 3 for the spherical pores. For example, for the porous glass it equals 3.19 [17] and for the porous alumina it equals 3.56 [18]. Figure 5 shows the comparison of the relative Young's modulus E'/E_0 obtained by using different methods. It can be seen, that the results of the FMBEM analysis are in better agreement with the empirical models, than the analytical ones.
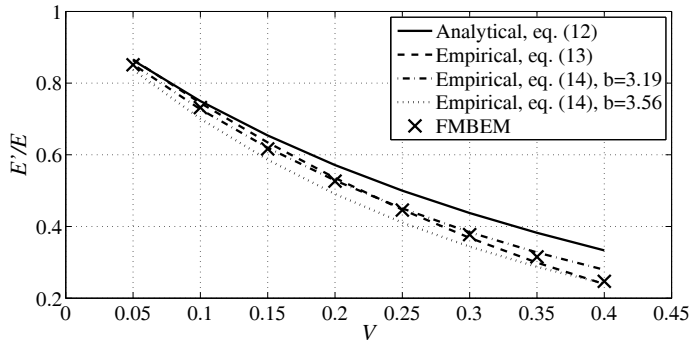

Fig. 5. The relative effective Young's modulus obtained by different methods

4.2. Composite material

In the second example a model of a fibre-reinforced composite material is under consideration. The material consisted of the epoxy resin matrix and aligned continuous glass fibres, of identical circular sections, which formed the hexagonal array. The cross section of such composite was analyzed.

Eight models with volume fraction of fibres V_f ranging from 0.05 to 0.4 were under consideration. A typical model is shown in Figure 6. Each model was a square plate with the side length equal to 0.5 mm and containing 105 identical inclusions, which were the fibre sections. The model was in plane strain. The tensile traction force was $t_2 = 50$ MPa. The radii of the inclusions were adjusted so as to obtain required volume fractions of fibres. The Young moduli and Poisson ratios of the matrix and the fibres were $E_m = 3.6$ GPa, $v_m = 0.35$, $E_f = 72$ GPa and $v_f = 0.2$ respectively. Each inclusion was discretized by 18 boundary elements and each square side was discretized by 160 elements. The number of DOF of each model equalled 10 120. Due to the computer memory limitation the analysis by using the conventional BEM would be ineffective.

The BEM formulation for many identical inclusions proposed in [5], with the perfect connection between fibres and matrix, was used. All the parameters of the FMBEM and the preconditioned iterative solver was set in the same way as in the previous example, except for the maximum number of elements in leaf, which here was set to 10. A deformed model is shown in Figure 7.
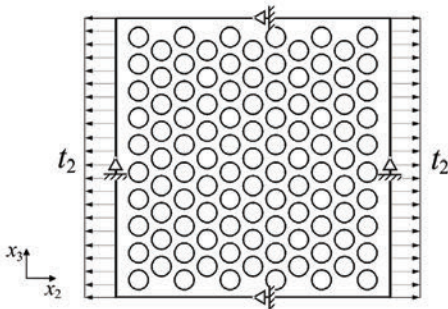

Fig. 6. The RVE of composite material with volume fraction of fibers $V_f = 0.4$

Fig. 7. Deformed RVE of the composite material
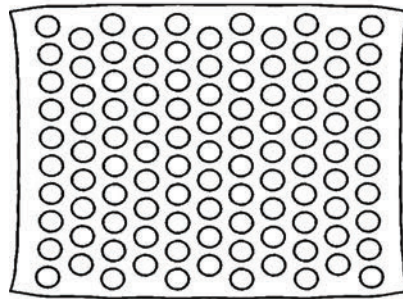
The transverse effective Young modulus E_2' was determined by the same method which was applied in the case of the porous material. The results were compared to two models. The first one was the simplest analytical model, the inverse rule of mixture, which determines the transverse effective modulus in the following way:

$$E_2' = \frac{E_f E_m}{V_f E_m + (1 - V_f) E_f}. \tag{15}$$

The second model was the Halpin–Tsai semi-empirical model [20]:

$$E_2' = E_m \frac{1 + \zeta \eta V_f}{1 - \eta V_f}, \tag{16}$$

with the parameters:

$$\zeta = 2 + 40 V_f^{10}, \eta = \frac{\dfrac{E_f}{E_m} - 1}{\dfrac{E_f}{E_m} + \zeta}. \tag{17}$$

The results were also compared to the values given by Eischen and Torquato [3], obtained by the analysis of unit cells using the conventional BEM. The comparison of the relative transverse Young's modulus is shown in Figure 8. One can see that the results of the present FMBEM analyses agree very well with the ones computed by Eischen and Torquato. Both the series of numerical experiments gave values of the transverse Young modulus lower than the ones determined by the Halpin–Tsai model. However, the computed values are higher than the ones obtained by using the inverse rule of mixture. The rule is known to state the lower bound for the effective moduli.
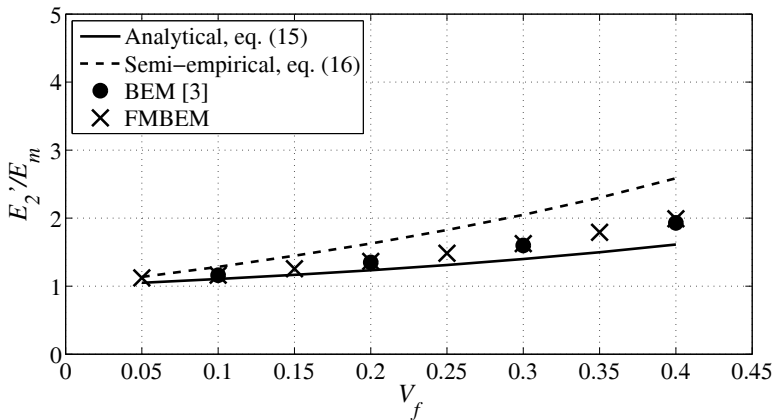

Fig. 8. The relative effective transverse Young's modulus obtained by different methods

5. Conclusions

The FMBEM using three-node boundary elements was applied to the analysis of micromechanical structures, such as porous and composite material. Effective Young's

moduli were determined and compared to values given by analytical, semi-empirical and empirical models, and to values resulted from numerical analysis performed by other authors. All the FMBEM results agreed with the above mentioned models. A comparison of computation time by using the conventional BEM and the FMBEM was shown in the article [14]. Analyses of the considered RVEs, which are relatively complex structures, by the conventional BEM would be inefficient due to the computation time and the computer memory limitation.

In order to fully prescribe the properties of the analyzed materials, the remaining elastic constants, as Kirchhoff's modulus or Poisson's ratio, should be also determined. This can be achieved by imposing another type of boundary conditions, e.g. such that cause shearing of the RVE. Such structures can be also modelled by using the presented FMBEM code.

Other types of boundary conditions satisfying the Hill-Mandel condition (e.g. the linear displacement or periodic boundary conditions) can be implemented. However, it was confirmed that for RVE with appropriate size the traction boundary condition was sufficient to provide homogenization results which are consistent with the empirical results.

In the numerical homogenization only knowledge of boundary quantities is required. For this reason the BEM (FMBEM) can be more efficient than domain methods, e.g. the FEM.

Acknowledgements

References

[1] Zohdi T.I., Wriggers P.: *An introduction to computational micromechanics*, Springer-Verlag, Berlin Heidelberg, 2008.
[2] Greengard L., Rokhlin V.: *A fast algorithm for particle simulations*, J. Comput. Phys., Vol. 73, No. 2, 1987, pp. 325−348.
[3] Eischen J.W., Torquato S.: *Determining elastic behaviour of composites by the boundary element method*, J. Appl. Phys., Vol. 74, No. 1, 1993, pp. 159−170.
[4] Hu N., Wang B., Tan G.W., Yao Z.H., Yuan W.F.: *Effective elastic properties of 2-D solids with circular holes: numerical simulations*, Comp. Sci. Techn., Vol. 60, 2000, pp. 1811−1823.
[5] Yao Z., Kong F., Zheng X.: *Simulation of 2D elastic bodies with randomly distributed circular inclusions using the BEM*, Electronic Journal of Boundary Element, Vol. 1, No. 2, 2003, pp. 270–282.
[6] Yang Q.S., Qin Q.H.: *Micro-mechanical analysis of composite materials by BEM*, Eng. Anal. Bound. Elem., Vol. 28, No. 8, 2004, pp. 919–926.
[7] Yamada Y., Hayami K.: *A multipole boundary element method for two dimensional elastostatics*, Tech. Report, METR 95-07, Math. Eng. Section, Dept. Math. Eng., Information Phys., Univ. Tokyo, 1995.

[8] Greengard L., Helsing J.: *On the numerical evaluation of elastostatic fields in locally isotropic two-dimensional composites*, J. Mech. Phys. Solids, Vol. 35, No. 7, 1998, pp. 1441–1462.

[9] Helsing J.: *Fast and accurate numerical solution to an elastostatic problem involving ten thousand randomly oriented cracks*, Int. J. Fracture, Vol. 100, 1999, pp. 321–327.

[10] Helsing J., Jonsson A.: *Complex variable boundary integral equations for perforated infinite plates*, Eng. Anal. Bound. Elem., Vol. 25, 2001, pp. 191–202.

[11] Yao Z., Kong F., Wang H., Wang P.: *2D Simulation of composite materials using BEM*, Eng. Anal. Bound. Elem., Vol. 28, 2004, pp. 927–935.

[12] Wang H., Yao Z., Wang P.: *On the preconditioners for fast multipole boundary element methods for 2D multi-domain elastostatics*, Eng. Anal. Boundary Elements, Vol. 29, 2005, pp. 673–688.

[13] Liu Y.J.: *A new fast multipole boundary element method for solving large-scale two-dimensional elastostatic problems*, Int. J. Numer. Meth. Engng, Vol. 65, 2006, pp. 863–881.

[14] Ptaszny J., Fedeliński P.: *Fast multipole boundary element method for the analysis of plates with many holes*, Arch. Mech., Vol. 59, No. 4–5, 2007, pp. 385–401.

[15] Brebbia C.A., Dominguez J.: *Boundary elements an introductory course*, McGraw-Hill, New York, 1992.

[16] Nishimura N.: *Fast multipole accelerated boundary integral equation methods*, Appl. Mech. Rev., Vol. 55, No. 4, 2002, pp. 299–324.

[17] Cannillo V., Leonelli C., Manfredini T., Montorsi M., Boccaccini A.R.: *Computational simulations for the assessment of the mechanical properties of glass with controlled porosity*, J. Porous Mat., Vol. 10, 2003, pp. 189–200.

[18] Deng Z.Y., Fukusawa T., Ando M., Zhang G.J., Ohji T.: *Microstructure and mechanical properties of porous alumina ceramics fabricated by the decomposition of aluminium hydroxide*, J. Am. Ceram. Soc., Vol. 84, No. 11, 2001, pp. 2638–2644.

[19] Kachanov M.: *On the effective moduli of solids with cavities and cracks*, Int. J. Fracture, No. 59, 1993, pp. 17–21.

[20] Halpin J.C., Kardos J.L.: *The Halpin–Tsai equations: A review*, Polym. Eng. Sci., Vol. 5, 1976, pp. 344–352.

Numeryczna homogenizacja szybką wielobiegunową metodą elementów brzegowych

Artykuł dotyczy numerycznej homogenizacji niejednorodnych materiałów liniowosprężystych za pomocą szybkiej wielobiegunowej metody elementów brzegowych (SWMEB). Zastosowanie SWMEB pozwala na analizę układów o większej liczbie stopni swobody w porównaniu z konwencjonalną kolokacyjną MEB, która charakteryzuje się złożonością kwadratową. SWMEB jest dogodna w numerycznej homogenizacji, gdzie należy modelować reprezentatywne elementy objętości o odpowiednio złożonej strukturze. Zaprezentowano dwa przykłady numerycznej homogenizacji. Pierwszy przykład dotyczy materiału porowatego, natomiast drugi – materiału kompozytowego. Wyniki analizy są zgodne z modelami analitycznymi, półempirycznym, empirycznymi, oraz z wynikami analizy numerycznej prezentowanej przez innych autorów.

Stability analysis of multilayered composite shells with cut-outs

A. SABIK, I. KREJA

Gdańsk University of Technology, G. Narutowicza 11/12, 80-233 Gdańsk, Poland.

A numerical stability analysis of an axially compressed multilayered composite shell is presented. The authors examine how the stability performance of a panel can be influenced by a centrally located square cut-out. The computations are performed within FEM computer program NX-Nastran (ver. 6.0). The stability is investigated by means of a *linearized buckling analysis* as well as of a *non-linear large deformations incremental analysis*. To get more insight into the performance of the layered structure, the failure index according to Tsai–Wu criterion is monitored in the study.

Keywords: *multilayered shells, stability, cut-out*

1. Introduction

Composite materials play very important role in modern building engineering. The most attractive advantage of these materials is above all a combination of a light weight with a high strength. Most common in use are multilayered composites made of fibre-reinforced layers with various orientations of fibres in a stacking sequence that determines the global anisotropy of a body. This permits a range of possibilities in design process. There is no exaggeration in opinion that composites are most suitable materials for modern light structures. The best support for this statement is the fact, that the development of composites is strongly connected with the progress of aerospace technology.

On the other side, shells, which we focus on, are in general light thin-walled structures or members of other constructions. From this point of view, they are usually subjected to instability. Of course, the stability depends on many aspects, i.e. slenderness, boundary conditions, imperfections. If the influence of these factors is strong enough, the loss of stability can occur before other limit effects like failure or delamination arise. This fact should be taken into account during design process and analysis of shells. It is however understandable that multilayered composite shells are typically slender constructions, so that, in the relation to previous considerations, the necessity of stability analysis is fairly evident in this case.

In the present paper, we examine how the stability of a multilayered panel can be influenced by centrally located square cut-outs. Such cut-outs appear quite often in practical applications, because holes can serve as doors, windows or input of pipelines. The presence of a hole can remarkably change the structural response. Due to

the reduction of a material volume significant changes of stiffness occur. A predictable decrease of the critical load in such a case is not a rule. Depending on the cutout size, both a decrease as well as an increase of the buckling resistance is possible [1]. It is also worth noticing, that due to the more complicated stress states in multi-layered composite structures than in isotropic media, some tendencies of the structure response caused by changes of the cut-out size that can be observed in the case of homogeneous isotropic shells are not directly applicable to multilayered structures [2].

2. Stability analysis

There are several ways to analyse the stability of a structure. In present study, two methods are used to estimate the critical load level, namely linearized buckling analysis and non-linear incremental large deformation analysis.

2.1. Linearized buckling analysis

The simplest way to get information about the critical load of a structure is to examine an appropriate linear eigenvalue problem. The system of equations, which has to be resolved, has a form:

$$\left[\mathbf{K}^{con} + \lambda \mathbf{K}^{\sigma} \right] \mathbf{v} = 0, \tag{1}$$

where:
  $\mathbf{K}^{con}$ is the constitutive stiffness matrix,
  $\mathbf{K}^{\sigma}$ represents the geometrical stiffness matrix,
  λ and $\mathbf{v}$ stand for an eigenvalue and the corresponding eigenvector, respectively. This approach can be very attractive due to its computational efficiency; however, as a linear formulation it is useless when the structure undergoes large deformations in the pre-buckling range.

2.2. Non-linear large deformations incremental analysis

Taking into consideration large deformations one has to carry out an incremental analysis, which states:

$$\left[\mathbf{K}_{T}(\mathbf{q}) \right] \Delta \mathbf{q} = \mathbf{R}(\mathbf{q}), \tag{2}$$

where:
  $\mathbf{K}_{T}(\mathbf{q})$ is the tangent stiffness matrix depending on actual displacements,
  $\Delta \mathbf{q}$ is the increment of displacement vector,

R(q) indicates the vector of residual forces. This approach is much more expensive from the computational point of view than solving the linear eigenvalue problem; additionally, some experience is usually required from the user for a proper handling. On the other hand, non-linear large deformations incremental analysis combined with the arc-length strategy enables the examination of structures undergoing large displacements including also the post-critical behaviour.

3. Composite shell modelling in NX-Nastran

The computations are performed within the commercial code NX-Nastran (ver. 6.0). The three-dimensional multilayered body is treated as a single layer with the equivalent stiffness of a multilayered cross-section. Such an approach is known as the Equivalent Single Layer (ESL) model [3]. As a consequence of this simplification, local effects like a delamination, matrix cracking or fibres breaking cannot be analysed.

The resulting two-dimensional model of a layered shell can be analysed adopting one of the theories established for homogeneous isotropic shells. In NX-Nastran, the so-called First Order Shear Deformation Theory (FOSD) is applied. It means that the straight line, normal to the reference surface, remains straight but not necessarily normal during the deformation. Such an approach can be also called Reissner-Mindlin type theory when comparing with the shell theories.

Another essential assumption with a reference to composites in NX-Nastran is the linear elastic material model. Nevertheless, according to previous considerations, the instability of slender structures can occur in elastic range; therefore, the NX-Nastran composite model seems to be sufficient for the present study.

In most common displacement formulations of finite elements, the assumption of a linear displacement profile through the shell thickness causes a necessity of a shear stiffness correction. This can be achieved by means of several ways. The simplest approach consists in using of pre-defined shear correction factors for each layer or for whole cross-section. It is however inconvenient to set the values of such pre-defined factors for laminated medium. More accurate for laminated bodies seem to be formulations in which shear factors for the whole cross-section or even the shear stiffness matrix are evaluated numerically. On the other hand, it is worth to mention, that such a method requires some essential presumptions. Very often, the basis for such an approach is an assumption of a cylindrical bending mode. This methodology is implemented also in NX-Nastran, and in the authors' opinion, this technique is very efficient due to its accuracy and simplicity [4].

For composite multilayered shells, only four-node flat elements are offered in NX-Nastran. The element possesses 6 degrees of freedom at each node. As a remedy for the locking phenomenon, the assumed strain field approach is applied. Stress recovery is possible only at the Gauss-point, which is located in the centre of element.

4. Tsai–Wu criterion

According to the previous sections, the load capacity of a structure can be very often strongly determined by other aspects than the strength of the material; hence, the stability study becomes the most important part of the analysis. Nevertheless, one should not forget of the stress state monitoring. In multilayered composites, due to the orthotropy of layers and various fibres orientations in the stacking sequence, a complicated stress state can appear; consequently, appropriate strength or failure [5] criteria are required.

Similarly, to homogeneous isotropic media, there exist several strength criteria for multilayered composites. The following theories are available in NX-Nastran: the maximum strain criterion, the Hill (or Tsai–Hill [5]) criterion, the Hoffmann criterion, and the Tsai–Wu criterion. The most general hypothesis has been proposed by Tsai and Wu [5]. This criterion enables the analysis of materials with different tensile and compressive strength. Moreover, the theoretical results obtained by using of the Tsai-Wu hypothesis usually match very well the experimental data.

The failure surface of the Tsai–Wu criterion is described by the following equation:

$$\left(\frac{1}{X_t}-\frac{1}{X_c}\right)\sigma_1+\left(\frac{1}{Y_t}-\frac{1}{Y_c}\right)\sigma_2+\frac{1}{X_tX_c}\sigma_1^2+\frac{1}{Y_tY_c}\sigma_2^2+2F_{12}\sigma_1\sigma_2+\frac{1}{S^2}\sigma_{12}^2=1, \qquad (3)$$

where:

X_t, X_c are the longitudinal tensile and compressive strength respectively,

Y_t, Y_c stand for the transverse tensile and compressive strength correspondingly,

S represents the shear strength of a layer, whereas σ_1, σ_2, σ_{12} symbolize stress components in the principal material coordinates.

F_{12} denotes the factor of an interaction between σ_1 and σ_2. Directly from (3) the formula for the failure index FI can be obtained as:

$$FI=\left(\frac{1}{X_t}-\frac{1}{X_c}\right)\sigma_1+\left(\frac{1}{Y_t}-\frac{1}{Y_c}\right)\sigma_2+\frac{1}{X_tX_c}\sigma_1^2+\frac{1}{Y_tY_c}\sigma_2^2+2F_{12}\sigma_1\sigma_2+\frac{1}{S^2}\sigma_{12}^2. \quad (4)$$

The failure occurs, when value of FI index is equal or greater than one.

The value of F_{12} should be determined experimentally in biaxial test. However, it is a little bit complicated [5]; therefore, very often F_{12} is set to zero or evaluated from the formula given by Tsai and Hahn [6]:

$$F_{12}=\frac{-1}{2\sqrt{X_tX_cY_tY_c}}. \qquad (5)$$

It will be shown later, that in spite of small value, F_{12} can significantly influence the shape of failure surface.

5. Numerical example and discussion

The analysed example was proposed by Chaplin and Palazotto in [7]. The axially compressed cylindrical panel is studied without and with centrally located square cut-outs, as shown in Figure 1.
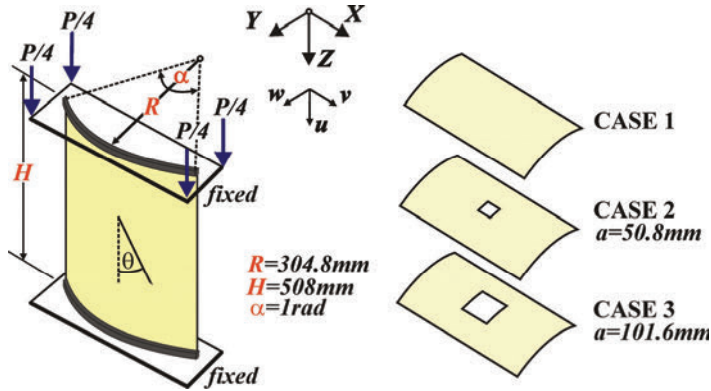

Fig. 1. Geometry of the shell and cut-outs (a – length of cut-out's edge)

Due to the specific loading conditions, a rigid movement of the loaded edge is enforced. The panel is fixed along the curved edges and the straight edges are free. The shell consists of 16 layers with a quasi-isotropic lamination scheme $[0/45/-45/90]_{2s}$. All layers have equal thickness $h = 0.127$ mm and they are made of the graphite-epoxy composite AS4/3501-6 with the following stiffness parameters: $E_1 = 135.8 \times 10^3$ MPa, $E_2 = 10.9 \times 10^3$ MPa, $G_{12} = G_{13} = 6.4 \times 10^3$ MPa, $G_{23} = 3.2 \times 10^3$ MPa, $v_{12} = 0.276$. The effective stiffness moduli for the 16-layers laminate were generated automatically within the NX-Nastran according to the ESL approach and the appropriate shear correction strategy (cf. [8]). In order to investigate the failure indices, also the strength parameters are required. Since they were not given in [7], the appropriate data were adopted after [9], where the same material (AS4/3501-6) was used: $X_t = 1950$ MPa, $X_c = 1480$ MPa, $Y_t = 48$ MPa, $Y_c = 200$ MPa, $S = 79$ MPa.

5.1. Linearized buckling analysis

Firstly, the linear eigenvalue problem has been analysed. Figures 2–4 illustrate five critical modes with the corresponding critical load for the three considered cases. It can be observed, that the critical load decreases when the cut-out occurs, moreover, an additional decrease of the critical load takes place for the increasing cut-out size. While comparing the obtained eigenmode shapes, one can observe, that they are the same for all three cases and that they occur in the same sequence in case 1 and 2; however, the presence of large cut-out (case 3) interchanges the order of mode 2 and 3.
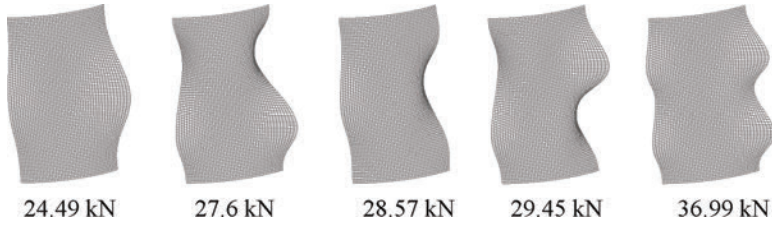
| 24.49 kN | 27.6 kN | 28.57 kN | 29.45 kN | 36.99 kN |

Fig. 2. Linear eigenvalue problem solution, case 1

| 21.95 kN | 26.10 kN | 26.51 kN | 27.70 kN | 34.55 kN |

Fig. 3. Linear eigenvalue problem solution, case 2

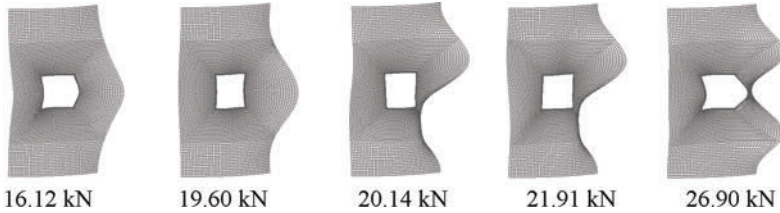| 16.12 kN | 19.60 kN | 20.14 kN | 21.91 kN | 26.90 kN |
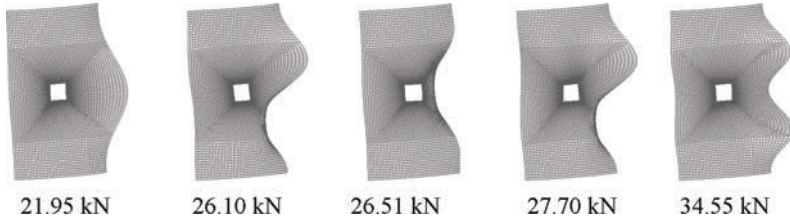
Fig. 4. Linear eigenvalue problem solution, case 3

5.2. Nonlinear solutions

The comparison of the results obtained by the use of linear eigenvalue problem and those of the nonlinear incremental analysis is presented in Figures 5–7. The critical load levels given by the linearized buckling analysis (as specified in Figures 2–4) are depicted in the graphs by the horizontal lines. In all three cases, the maximum load limit point lays above the level of the first critical load.

It is worth noticing, that in the case 1 the slope of the path arises in the vicinity of the first critical load level. This observation justifies the opinion, that there is a bifurcation point in the equilibrium path at the load level 24 kN; hence, the obtained path is not a fundamental one.

A more detailed study of this effect can be found in [3]. It has to be state, which the fundamental path cannot be obtained with the use NX-Nastran. The direct reason of this problem is the approximation of cylinder curvature with flat elements. It causes slight numerical imperfections, which the analysed panel, due to free straight edges, is

sensitive to. On the other hand, the secondary path obtained in the present study is much more important for practical purposes.
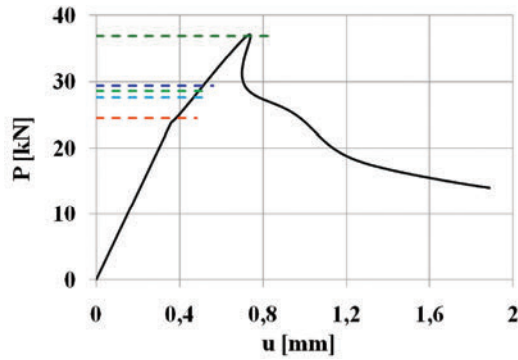

Fig. 5. Nonlinear incremental analysis; case 1 – comparison with linearized buckling analysis results
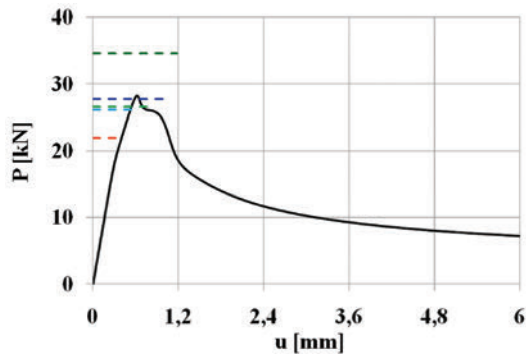

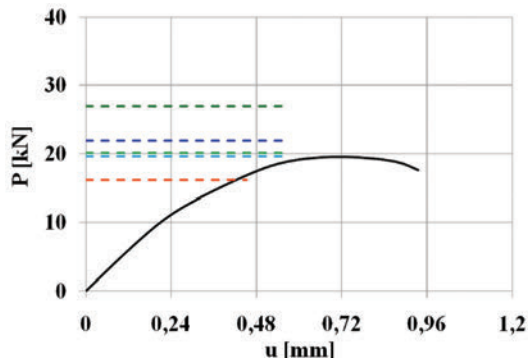Fig. 6. Nonlinear incremental analysis; case 2 – comparison with linearized buckling analysis results

Fig. 7. Nonlinear incremental analysis; case 3 – comparison with linearized buckling analysis results

One can observe in Figures 5–7, that with the occurring of the cut-out and with its growing size, the range of a linear shell response decreases. Only in the case 1 the structure behaves linearly up to the first critical force level. In other cases the nonlinear effects arise below the first critical force value, so the results computed in a linear eigenvalue problem are useless.
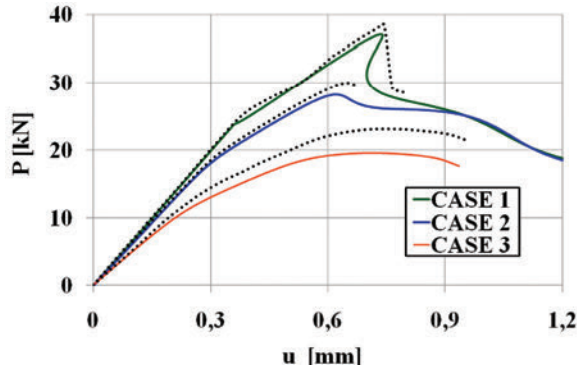

Fig. 8. Influence of cut-out, nonlinear solutions. Comparison with [7]

The cut-out influence on the limit load level is demonstrated in Figure 8. Likewise in the linear solution, the critical loads decrease with increase of the hole size. With dot-lines in Figure 8 the reference solution of Chaplin and Palazotto [7] is depicted. The observable quantitative discrepancies between the results of [7] and those of the present study can be explained by a too sparse FE discretization applied in [7].

5.3. Strength analysis

The range of the analysis can be further increased by taking into consideration the monitoring of the failure index *FI* for the three studied cases of the shell. The value of *FI* is calculated according to formula (4) resulted from the Tsai-Wu failure criterion.

Figure 9 shows the projection of failure surface on the $\sigma_1 - \sigma_2$ plane for two different values of interaction parameter F_{12}, namely $F_{12} = 0.0$ and $F_{12} = -3.004 \times 10^{-6}$ (the second value evaluated according to formula (5)). As one can observe in Figure 9, the value of F_{12} significantly influenced the shape of the failure surface.

The further results reported in the following were obtained for $F_{12} = -3.004 \times 10^{-6}$.

The distribution of the failure index *FI* at the limit load level for the three analysed cases are demonstrated in Figure 10. It is noteworthy that in the cases 1 and 2 the maximum values of *FI* occur in the first (bottom) layer, while in the case 3 the highest values are achieved in the ply 2.

In the case 1, the stress concentration takes place in the centre of the shell; however, the maximum value of *FI* is less than 0.5. As expected, the highest values of *FI* in the shells with cut-outs are achieved at the holes' corners. It should be stressed, that

FI values are slightly underestimated, as they are evaluated in Gauss points, not directly at the cut-outs' corners. One can observe a non-symmetrical distribution of *FI* with maximum values at the upper right and the bottom left corner in the case 2 (*FI* = 0.77) as well as in the case 3 (*FI* = 1.3). The non-symmetrical distribution of *FI* (and stresses) is caused mainly by non-symmetrical deformation patterns, see Figures 11–13.
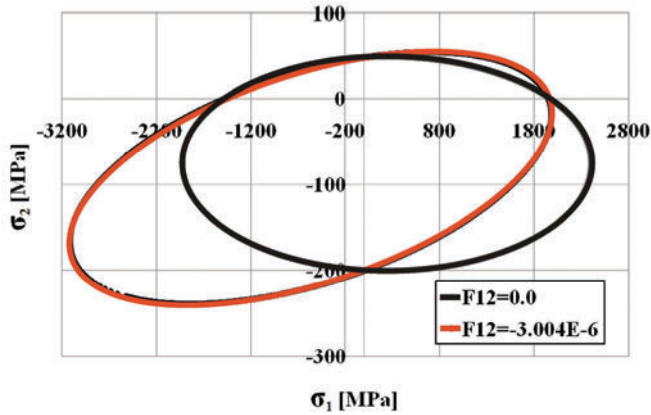
Fig. 9. Influence of Tsai-Wu interaction parameter F_{12} on Tsai-Wu failure surface
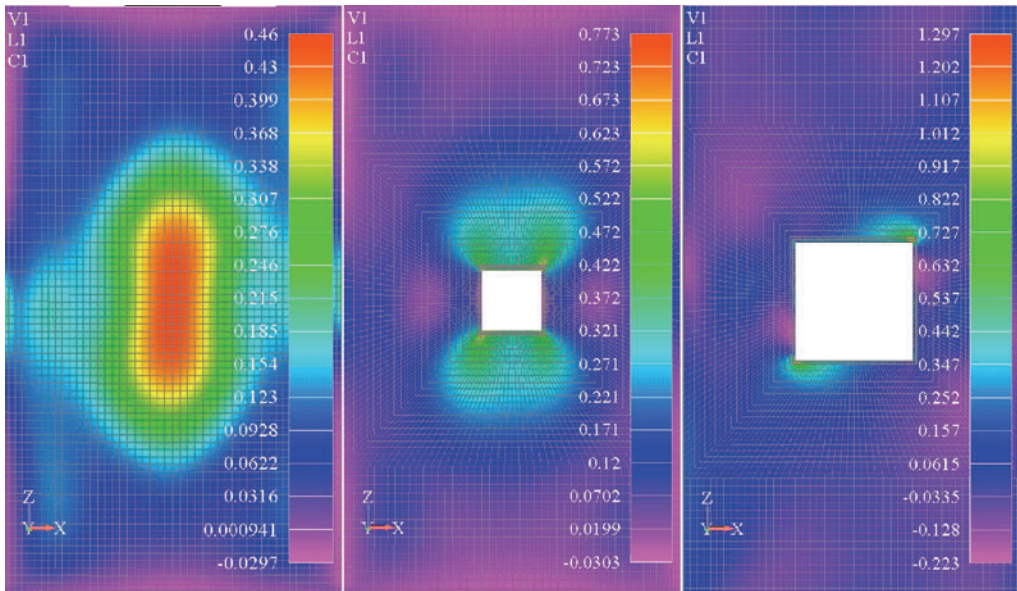
Fig. 10. Failure index *FI* distribution at limit load levels, 3 cases
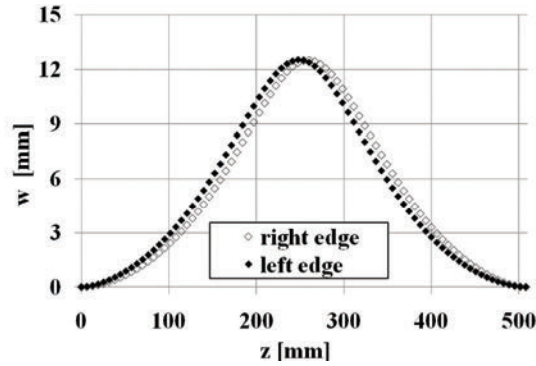
Fig. 11. Deformation of straight edges at limit load level, case 1

Fig. 12. Deformation of straight edges at limit load level, case 2
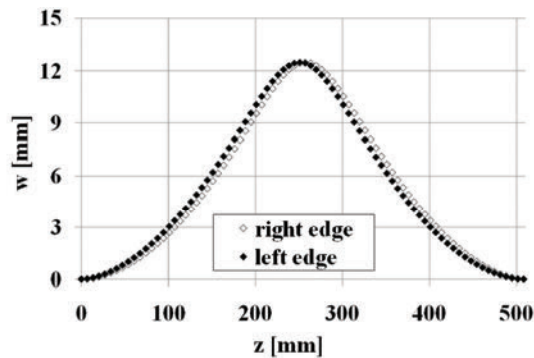
Fig. 13. Deformation of straight edges at limit load level, case 3

The increase of the cut-out's size causes a growth of the *FI* value. According to the obtained *FI results*, the failure at the limit point occurs only in the case 3.

It has to be mentioned, that NX-Nastran offers just a passive detection of a failure – the *FI* index value greater than 1 indicates the failure; however, the stiffness of the structure is not affected, what can be considered as a significant limitation of the program.

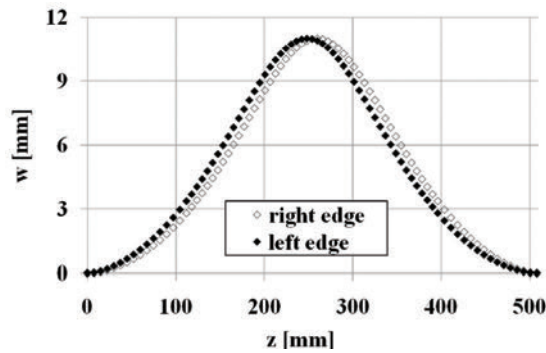Since the failure has been detected for the case 3, an additional study has been performed to examine, how the response of the structure would change when the corners of the largest cut-out were rounded. The equilibrium paths (axial displacement vs. load) obtained for the rounding $x = 0\%$, $x = 5\%$ and $x = 10\%$ are presented in Figure 14a. The interpretation of x parameter can be found in Figure 14a.
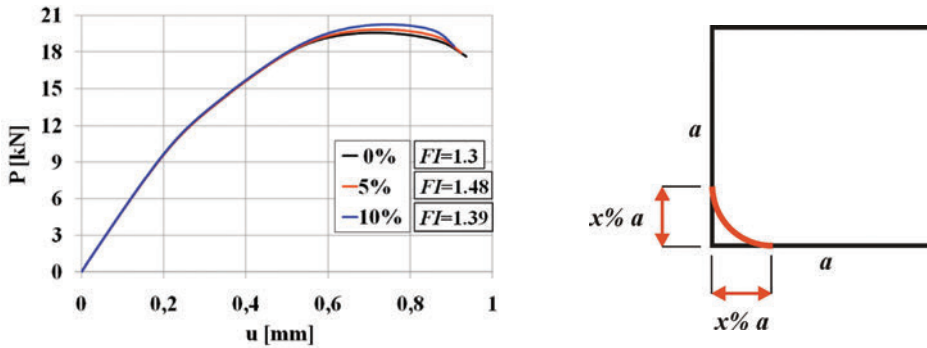
Fig. 14a. Case 3, influence of corner's rounding

One can observe that with the higher values of x the limit load increases; however, the *FI* values for the limit load are still above 1, as listed in Figure 14a. On the other hand, when the failure index is monitored for the constant load level (equal to the limit load for the structure without rounded cut-out's corners), by applying the rounding parameter $x = 10\%$ the value of *FI* can be cut down to 0.9 (Figure 14b).
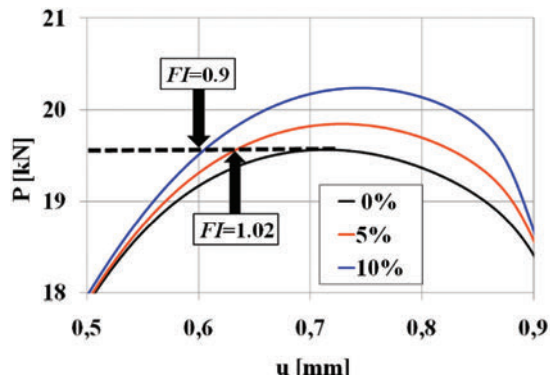
Fig. 14b. Case 3, influence of corner's rounding

6. Conclusions

A numerical stability study of an axially compressed multilayered composite shell has been presented. The authors have focused on the influence of a centrally located square cut-out on the structure instability. The analysis has been performed within NX-Nastran by using the four-node QUAD4 elements. The linearized buckling analysis as well as non-linear incremental analysis has been carried out to calculate critical load values. Additionally the material strength has been analysed by adopting the failure criterion of Tsai and Wu.

It has been shown, that cut-outs significantly change the structure behaviour. The increase of the cut-out's size reduces the critical load values and decreases the range of linear structure response. Furthermore, the presence of a cut-out causes considerably stress state changes when compared with a shell without any hole.

Future considerations can involve a more complex problem, where the shape and size of the cut-out would be established in the framework of the mass structure optimization with the constraint imposed on the critical load level.

It is also noteworthy, that the analysis of composite failure in NX-Nastran has only a passive character, since the stiffness of the structure is not modified according to the results of the failure analysis.

References

[1] Bailey R., Wood J.: *Stability characteristics of composite panels with various cutout geometries*, Composite Structures, Vol. 35, No. 1, 1996, pp. 21–31.

[2] Noor A.K., Burton W.S.: *Computational models for high-temperature multilayered composite plates and shells*, ASME, Appl. Mech. Rev., Vol. 45, No. 10, 1992, pp. 419–445.

[3] Kreja I.: *Geometrically non-linear analysis of layered composite plates and shells*, Monographs of Gdansk University of Technology, Gdańsk, Poland, Vol. 83, 2007, pp. 1–176.

[4] Sabik A., Kreja I.: *Analysis of multilayered plates with the use of equivalent single layer models* (in Polish), Acta Mechanica et Automatica, Vol. 2, No. 1, 2008, pp. 63–68.

[5] Jones R.M.: *Mechanics of composite materials*, Philadelphia, USA, 1999.

[6] Van Paepegem W., Degrieck J.: *Calculation of damage-dependent directional failure indices from the Tsai-Wu static failure criterion*, Composite Science and Technology, Vol. 63, No. 2, 2003, pp. 305–310.

[7] Chaplin C.P., Palazotto A.N.: *The collapse of composite cylindrical panels with various thickness using Finite Elements Analysis*, Computers and Structures, Vol. 60, No. 5, 1996, pp. 797–815.

[8] Sabik A., Kreja I.: *Imperfection sensitivity of multilayered composite shells*, Shell Structures: Theory and Applications, eds. W. Pietraszkiewicz & I. Kreja, CRC Press/Balkema, London, Vol. 2, 2010, pp. 137–140.

[9] Soden P.D., Hinton M.J., Kaddour A.S.: *Lamina properties, lay-up configurations and loading conditions for a range of fibre-reinforced composite laminates*, Composite Science and Technology, Vol. 58, No. 7, 1998, pp. 1011–1022.

Analiza stateczności kompozytowych powłok warstwowych z otworami

W pracy analizowana jest stateczność ściskanej osiowo kompozytowej powłoki warstwowej. Badany jest wpływ usytuowanego centralnie w powłoce otworu kwadratowego na stateczność konstrukcji. Obliczenia wykonano w programie NX-Nastran (wersja 6.0). Poziom obciążeń krytycznych wyznaczony został w rozwiązaniu liniowym (liniowy problem własny) oraz na drodze analizy przyrostowej z uwzględnieniem dużych przemieszczeń (statyka nieliniowa). Dodatkowo analizowano wytężenie konstrukcji wykorzystując kryterium Tsai–Wu.

Z analizy rezultatów wynika, że wraz z pojawieniem się otworu i wzrostem jego wymiarów obniża się poziom obciążeń krytycznych oraz maleje zakres liniowej odpowiedzi konstrukcji. Ponadto obserwowany jest znaczny wzrost wskaźników wytężenia w obszarach koncentracji naprężeń.

Application of microwaves for innovative hardening of environment-friendly water-glass moulding sands used in manufacture of cast-steel castings

M. STACHOWICZ, K. GRANAT, D. NOWAK

Wrocław University of Technology, Wybrzeże Wyspiańskiego 25, 50-370 Wrocław, Poland.

The paper presents examination results on possible implementing an innovative microwave technology for manufacture of high-quality, economic cores of water-glass moulding sands. A special attention was paid to improving technological properties of the examined moulding sands and in particular of their strength and knocking-out properties by selecting proper parameters of the hardening process. In addition, some benefits are indicated, resulting from applying such an innovative and environment-friendly solution effectively replacing traditional and energy-consuming processes of preparing moulding cores.

Keywords: *innovative foundry materials and technologies, microwaves, drying, moulding sand, water glass*

1. Introduction

Use of electromagnetic waves in manufacture of high-quality industrial products and foodstuffs heated-up with microwaves at 2.45 GHz finds wider and wider application [1–2]. As can be seen from the available literature data [3] and on the grounds of own results, dielectric drying with microwaves successfully replaces traditional, energy- and time-consuming solutions applied in manufacturing processes [4].

At present, thanks to significant progress in building heating devices employing microwaves with frequency 2.45 GHz combined with more and more comprehensive knowledge about influence of electromagnetic waves on structure of many materials and the occurring transformations, extending their effective application area can be continued [5–7]. The performed examinations were aimed at determining possibilities of implementing innovative solutions based on applying high-frequency microwaves in foundry processes. The presented scope of the examinations and their results are a part of a comprehensive range of problems included in the currently realised doctoral thesis of Mr. Mateusz Stachowicz and will significantly contribute to implementing the innovative and environment-friendly technology.

Because of still higher and higher environmental requirements posed to manufacturing processes in foundry industry, the highest attention is currently paid to the solutions requiring small financial expenditures and at the same time being simple and efficient. In the case of moulding and core sands where the used binder is hydrated sodium silicate commercially known as sodium water glass, an important advantage of

their common use is low harmfulness to the environment and low cost of the binding material. A well-known problem resulting from applying that ecological binder is high residual strength of the moulding sand, worsening its knocking-out properties. The relatively big amount of a binder used in traditional methods of preparing moulds and cores, like the CO_2 process, the Alkali, Floster S or Nishiyama processes [8], additionally hampers the moulding sands regeneration process. Solving the above-mentioned crucial problems related to usage of water-glass moulding sands can improve competitiveness of the produced sand castings as well as improve working conditions and reduce environmental nuisance.

2. Dielectric drying of moulding and core sands

Moulding or core sand consists basically of a sand matrix and a binder that binds the sand grains. In the announced composition of moulding sands, influence of gas (air) that fills pores present in the porous medium is often omitted. In the microwave heating processes, such mixtures should be considered in a ternary phase system. In examining the phenomenon of microwave heating of dielectric media (dielectric drying), the pores filled with air are of particular importance. Their influence is also decisive for effectiveness of bringing out the gases created during filling the moulds, i.e. for the moulding sand parameter called permeability. That parameter is important also during microwave hardening of a binder. Microwaves cause dielectric polarisation of molecules giving them the nature of dipoles, which results mainly in intensive, volumetric heating of the material [4]. It should be noted that nearly half of the binder components are water particles being a part of colloidal solution of sodium water glass. As the research revealed, permeability of the sandmix matrix is satisfactory and allows free bringing-out the releasing steam from inside of the moulding sand [9–10].
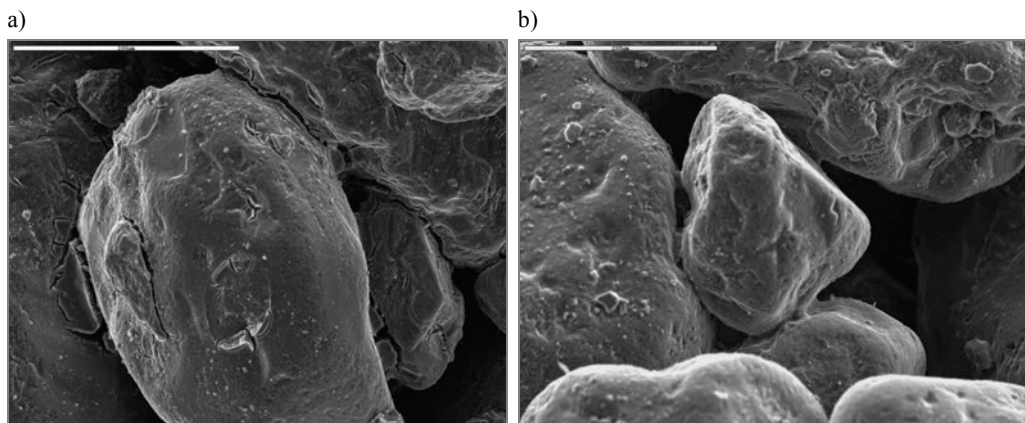
a)   b)

Fig. 1. Linking bridges made of a layer of dehydrated vitreous sodium silicate:
a) CO_2 hardening, b) traditional drying. SEM

In the case of water-glass dehydration in the process of traditional, convection heating of moulding sand in industrial or laboratory dryers, the reaction of hardening, i.e. of changing rheological properties of the binder during transition from viscoelastic to brittle condition, is described by the formula 1 [8]:

$$Na_2O \times nSiO_2 \times xH_2O + Q \rightarrow Na_2O \times nSiO_2,$$
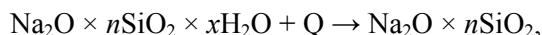
where n, x are stoichiometric coefficients.

As a final result of the dehydration reaction, a dehydrated layer of vitreous sodium silicate ($Na_2O \times nSiO_2$) is created, forming durable bridges linking the matrix grains.

It is supposed that the dielectric drying process, resulting also in hardening the binder, runs in a similar way to the convection drying process. The difference consists mostly in the process proceeding speed and in its final result, that is in quality of the created links between matrix grains, called linking bridges, see Figures 1a, 1b and 2a.

a)   b)
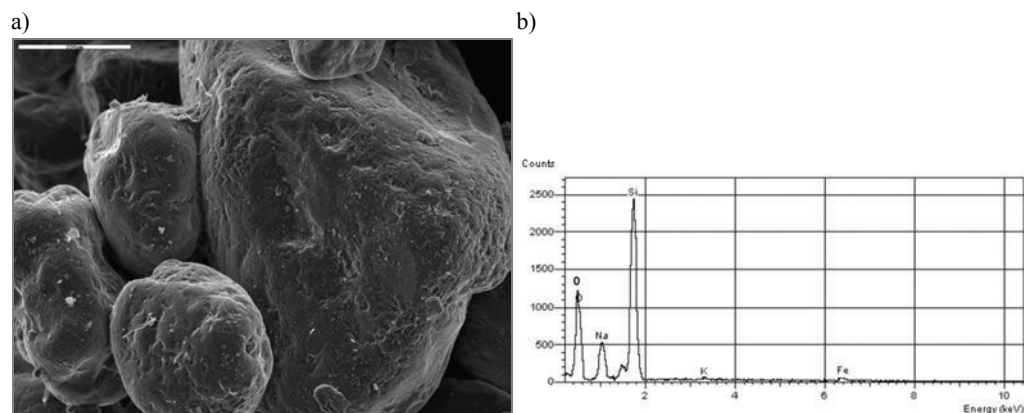
Fig. 2. Linking bridges made of a layer of dehydrated vitreous sodium silicate:
a) dielectric drying b) analysis of sodium silicate layer. SEM

Quality of the bridges formed of sodium silicate in the hardening process can be evaluated by the moulding sand strength measurements. The best results of tensile, bending and compression strength tests of moulding sands prepared with this binder were obtained after dielectric drying [9–11]. Figure 3 shows an exemplary comparison of bending strength values in hardened condition R_g^U determined for silica-based moulding sands containing 3.5% of the selected binder grade. The moulding sand was hardened in various ways, namely in the CO_2 process, with liquid esters (Flodur 1 and Mach 2) as well as by convection and microwave drying.
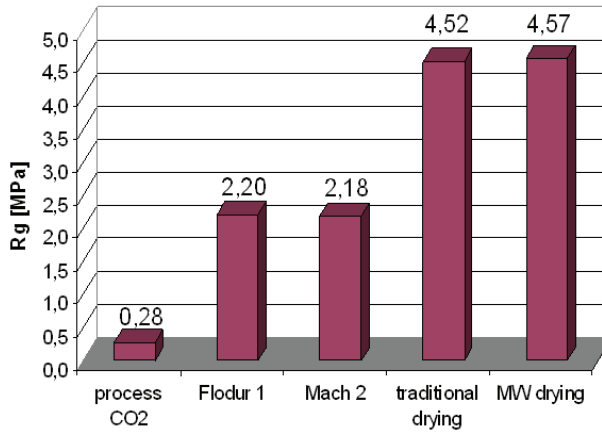
Fig. 3. Comparison of strength R_g^U of moulding sands hardened with various methods

Differences in strength of the examined moulding sands can be explained by analysing the hardening mechanism for individual applied processes shown schematically in Figure 4 and observing the created linking bridges, Figures 1–2. Chemical hardening (the first three methods in Figure 3) permits indeed obtaining satisfactory mechanical parameters (Flodur 1 and Mach 2), but the time required to remove water from the binder completely can reach even 24 hours, depending on conditions in the foundry.

Convection hardening (traditional, see Figure 3), connected with thermal conductivity of the mixture, is a process of gradually removing water as subsequent layers of moulding sand are heated, see Figures 1b, 4b. Due to energy losses during heating, related mainly to efficiency of the drying equipment and way of heat transmission, the convection drying is a time- and energy-consuming process.
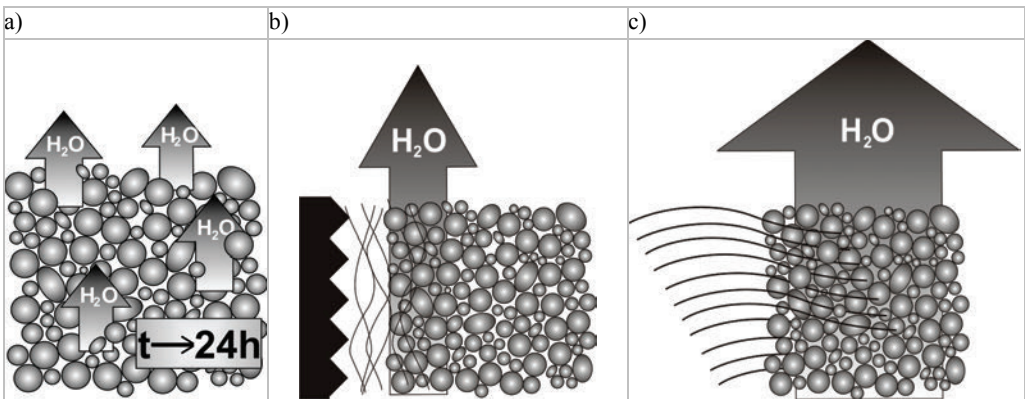
Fig. 4. Layouts of hardening processes of water-glass moulding sands: a) chemical methods, b) convection drying, c) microwave drying

In the microwave hardening process shown in Figure 4c, the binder containing water molecules of polar nature (dipoles) is first subject to heating. Electromagnetic wave, penetrating the moulding sand and increasing its temperature simultaneously in the entire volume, significantly reduces duration of the process. Due to high-frequency vibrations, energy of electromagnetic wave is transformed to thermal energy of the binder, intensifying the process of forming a dehydrated layer of vitreous sodium silicate, see Figure 2a.

3. Issue of microwave heating of moulding sands

The process of microwave hardening of moulding sands, combining benefits of some traditional ways of hardening water glass (velocity of the process, significant reduction of the binder content with maintained very good mechanical and technological parameters), can be implemented to industrial applications by means of special, properly selected devices and accessories. Their structure should guarantee safe work of the operating personnel and maintaining the set operating parameters. Besides a temperature control system inside the heating chamber, the microwave ovens should be also equipped with an efficient ventilation system. This is why a research of the binder hardening process in moulding sands can not be carried out using appliances equipped with typical control systems installed in common-use microwave ovens. A significant impediment is also caused by the limitations related to size of the heating chamber and to maintaining uniform operating parameters of a magnetron.

In the presented research, a microprocessor-controlled device was used, that permitted controlling power output of the magnetron and steplessly adjusting the microwave amplitude [3], as well as programming duration time and number of heating cycles matching the filling degree of the working chamber. The device was also provided with an additional ventilation system ensuring efficient removing moisture from inside of the oven chamber. Besides the properly selected operating parameters of the equipment, quality of the created links between matrix grains is also significantly influenced by composition of the suggested moulding and core sands.

Influence of a hardening method on final hardening result is demonstrated by comparing the bending strength values of the hardened moulding sand R_g^U for two physically similar drying processes, see Figure 5. In both cases, creation of the linking bridges was connected with dehydration of the binder: in the first case by traditional drying and in the second case by dielectric drying. As results from the performed examinations, the much faster method of intensive microwave hardening of moulding sands is also the more efficient method. The tests carried-out for contents of water glass in moulding sand ranging from 5% to 1.5% showed that influence of microwave hardening on bending strength R_g^U is more beneficial at lower binder content below 3.5%. In the case of traditional hardening methods, in contrast to innovative dielectric drying, at the binder content below 3.5% some problems happened with maintaining high and fully repeatable quality parameters of moulds and cores.
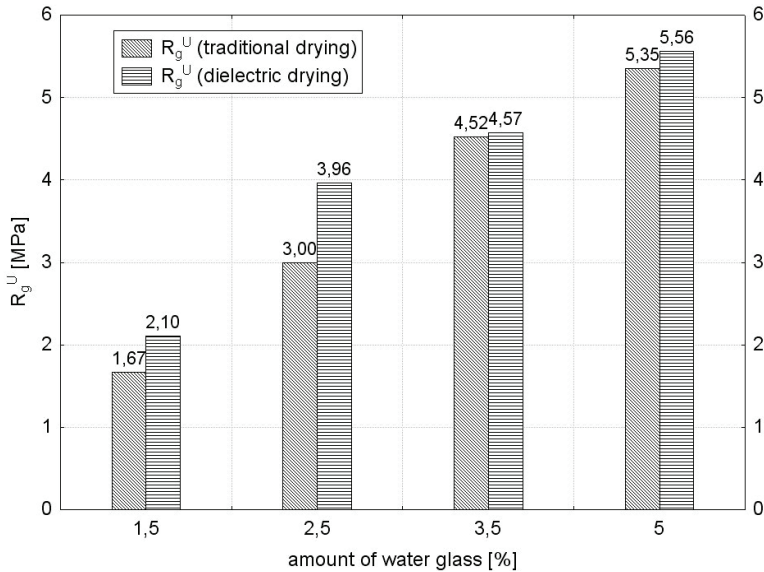
Fig. 5. Influence of hardening method and water glass 145 content on bending strength of moulding sand

Quality of water-glass moulding sands is also decided by contents of additives, like special carbon or carbon-free additives, natural binder, additives improving flexibility and knocking-out properties, and others. Before introducing the above-mentioned components, it is necessary to carry out additional tests to determine influence of microwaves on stability of moulding sands and on effectiveness of hardening. It is also essential to determine proper parameters of dielectric drying the sandmixes containing these additives.

Profits resulting from applying the innovative dielectric drying, found in laboratory tests and indicating clearly higher quality of so hardened moulding sands than of those chemically hardened, motivated undertaking industrial trials. It was assumed that higher strength of core sand after microwave hardening would permit reducing the so-far used wall thickness for certain shapes or reducing the volume of particular large-cores and thus obtaining real savings by smaller quantities of used material, as well as improving knocking-out properties of moulding sands. All the mentioned advantages should finally result in reduced costs of preparing cores with maintained high quality of the produced castings.

4. Manufacture of "economical" cores hardened with microwaves and trials of their industrial application

Trials of practical use of the innovative method of microwave hardening of moulding sands were undertaken in Foundry Department of Lower-Silesian Machinery Factory ZANAM-LEGMET in Legnica.

The moulding sands used in the industrial trials and in the preceding laboratory tests were prepared by mixing the reference high-silica sand from the mine Grudzeń Las with the main fraction 0.20/0.16/0.10 (fine) or from the mine Nowogród Bobrzański with the main fraction 0.32/0.20/0.16 (medium) with commercially available grades of water glass manufactured by Chemical Works "Rudniki" S.A., whose properties (acc. to the manufacturer's certificate) are given in Table 1 (grades commonly used in foundry practice [8] are marked by bold characters).

Moulding sands were prepared in a laboratory mixer to that a 4 kg batch of high-silica sand was dosed and the mixer started. Then, in the case of chemically hardened moulding sands, a liquid ester (Flodur 1 or Mach 2) was added. Next, water glass was dosed and the sandmix was stirred for 180 seconds. Total stirring time was 240 s to ensure uniform distribution of the binder on the sand grains.

In the case of moulding sands containing no liquid hardener, at the beginning of stirring 20 ml (0.5%) of water was dosed, which volume was determined on the grounds of literature data and analysis of the preliminary testing results. Initial wetting of sand is advantageous for repeatability of test results, guaranteed among others by uniformity of the moulding sand thanks to good distribution of the binder in the entire volume. Addition of water guarantees also reduced dust emission during mixing. After 60 s of stirring the silica matrix with water, water glass was added and stirring was continued for the next 180 s.

Table 1. Composition of selected core moulding sands designed for six industrial trials

No. of core	Matrix	Water glass grade/ modulus/quantity	Hardener grade/ quantity
1	High-silica sand; medium 1K	150/1.9–2.1/2.5%	–
2	High-silica sand; fine 1K	150/1.9–2.1/2.2%	–
3	High-silica sand; fine 1K	145/2.4–2.6/3.0%	–
4	High-silica sand; fine 1K	137/3.2–3.4/2.5%	–
5	High-silica sand; fine 1K	145/2.4–2.6/3.5%	Flodur 1/0.4%
6	High-silica sand; fine 1K	145/2.4–2.6/3.5%	Mach 2/0.4%

The moulds were prepared, according to the procedure accepted in the Factory, of traditional moulding sands designed for casting 70 kg cast steel hammers for an impact crusher. Next, the six cylindrical, thin-walled (average wall thickness ca. 21 mm) cores made of water-glass moulding sand (Table 1) hardened with microwaves were placed inside. Of numerous cores used in the Factory, the one of possibly simple structure was selected, because of high costs required for preparing a special core box.

In order to ensure identical conditions during pouring, each time the mould was provided with a core made acc. to the so-far used technology (wall thickness ca. 45 mm) and the one of the six "economical" cores made of the moulding sands numbered 1 to 6 in Table 1.

During the technological trials, a risk was also taken to make a casting with a thin-walled core of the moulding sand No. 2 in Table 1 with the smallest addition of the

binder grade 150 (the lowest modulus and the highest density) amounting to 2.2%. Surface of all the cores was covered with the alcohol-based protective coating used in the Factory.

The cores were made using the innovative microwave method in a deliberately designed core box (Figure 6) made of a heat-resisting material, transparent for the electromagnetic wave. Since the core-box material was impermeable for gases, it was necessary to design and make special channels to allow free taking away the intensely created steam.

a)   b)
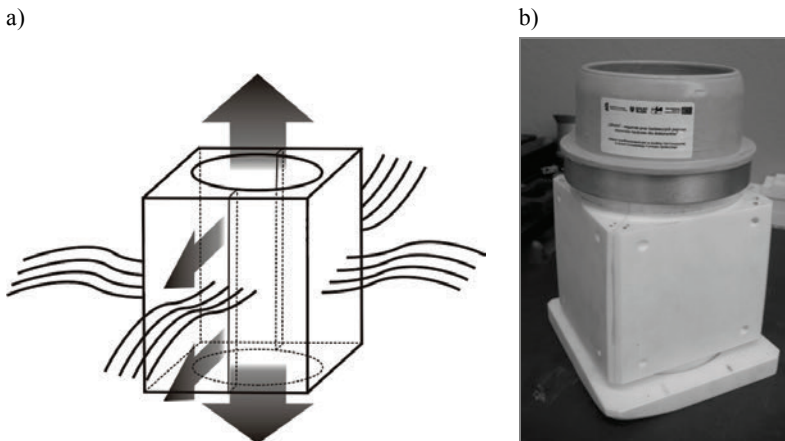
Fig. 6. Core box for preparing "economical" cores by microwave hardening:
a) idea of the microwave-heating process and places of removing steam from inside,
b) view of assembled core box

All the carried-out trials of casting the L120G13 cast steel to the moulds with installed innovative and traditional cores were successful. Despite significantly reduced wall thickness (down to ca. 21 mm) all the six cores were not destroyed either by the liquid metal stream or during solidification. The cast hammers for an impact crusher knocked-out from the mould prepared of the traditional moulding sand with the traditional and the "economical" core are shown in Figure 7.

By analysis of the trial results it was found that the reduced wall thickness of the six cores from 45 to 21 mm, possible thanks to using innovative microwave hardening, did not contribute to cracking caused by casting shrinkage. Except the core No. 3 with 3% of the binder grade 145, no other surface defects were found in the locations of cylindrical cores. After knocking-out the cores, it was found that some fragments of burnt moulding sand were left on the core No. 3 (Table 1) only, see Figure 8b. According to literature data, such a non-conformity are attributed to the kind of the applied matrix (high-silica in this case), compacting degree, covering the core surface with protective coatings, as well as to quantity and quality of the binder [8]. Unlike the

others (No. 1, 2 and 4), the core No. 3 was prepared for microwave hardening of the moulding sand with the highest binder content. Moreover, irregularities of the surface originated in the lower part of the core, exposed to the highest thermal loads by the liquid metal stream. In that case, the most probable causes of a burning can be such factors like restrictions of the binder content in the core sand or higher casting temperature of the alloy L120G13, although the latter was not verified. Therefore, it can be assumed that the applied innovative method of microwave hardening of core sand had no direct effect on the above-mentioned non-conformity.

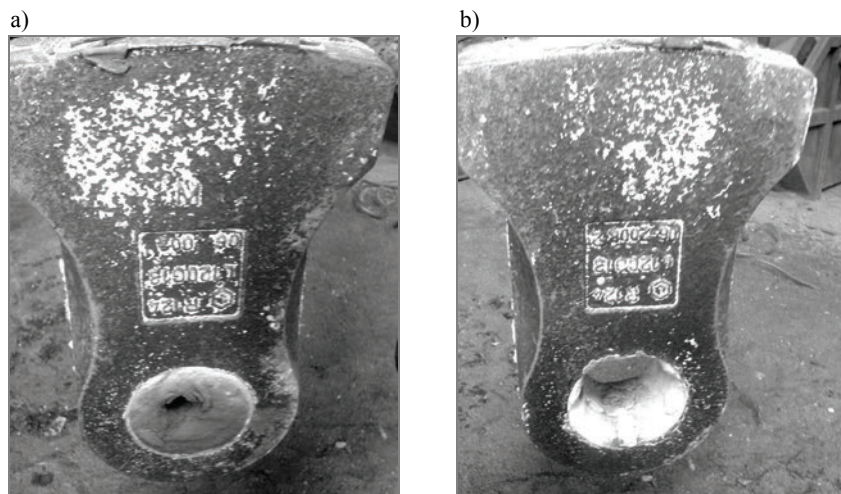a)   b)

Fig. 7. Castings knocked-out of moulds before the purification process: a) with traditional core, b) with an "economical" core, obtained by microwave hardening of moulding sand No. 3 (Table 1)
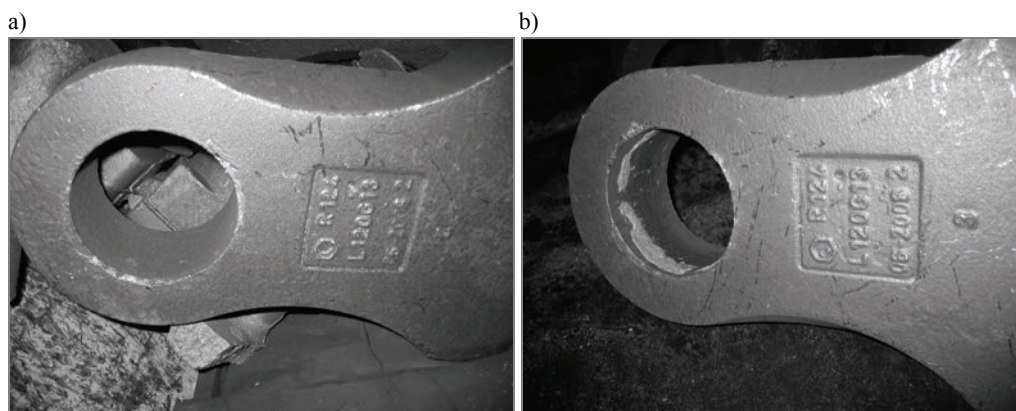
a)   b)

Fig. 8. Castings after knocking-out the "economical" cores: a) core No. 2, b) core No. 3, visible surface fragments with burnt core sand

5. Conclusions

Applying the innovative method of microwave heating in manufacture of "economical" cores allows producing L120G13 castings free of non-conformities, as confirmed by the quality control.

In the presented case, it was possible to reduce consumption of the binder by 30% and of silica matrix by ca. 60%, and the reduced wall thickness of the cores significantly improved the knocking-out properties of core sand. More intensive heating process and rapid evaporation of water during microwave hardening of the binder did not deteriorate mechanical parameters of the examined moulding sands.

Due to the reducing the quantity of binder in the microwave hardening process of water glass moulding sands, some positive effects can be expected in lower consumption of energy during the regeneration process.

Thin-walled cores made of environment-friendly water-glass moulding sands with very low quantity of binder hardened with microwaves may considerably improve the working conditions in foundries during casting process, effectively replacing traditional time- and energy-consuming processes of preparing moulding products.

In the case of applying liquid ester-based binders (cores No. 5 and 6), the innovative microwave heating of moulding sands is one of the most profitable – from economic point of view – ways of intensifying the hardening process. Possible is the proven in laboratory tests modification of the process, consisting in two-stage hardening that should ensure significant reduction of the time for preparing moulds and cores, as well as improve flexibility of manufacture.

Apart from reducing binder consumption, microwave hardening can also reduce quantity of the introduced hardener or even eliminate it completely) and guarantees smaller volume of disadvantageous water residue in the sand before pouring the moulds.

By proper selection of parameters (generator power, heating time, quantity and modulus of the binder), the microwave hardening permits forecasting the mechanical properties of moulds and cores, as well controlling these parameters, which can extend the application range of the moulding sands also for producing castings of other casting alloys. However, application of this innovative process requires using some special commercially available devices and materials to prepare the necessary instrumentation.

References

[1] Araszkiewicz M., Kozioł A., Skwarek A., Lupinski M.: *Microwave drying of porous materials*, Drying Technology, Vol. 22, No. 10, 2004.

[2] Maskan M.: *Microwave/air and microwave finish drying of banana*, Journal of Food Engineering, Vol. 44, 2000, pp. 71–78.

[3] Pigiel M., Granat K., Nowak D., Florczak W.: *Application of microwave energy in foundry processes* (in Polish), Archives of Foundry Engineering, Vol. 6, No. 21, 2006.

[4] Kowalski J.S., Rajewska K., Rybicki. A.: *Physical grounds of microwave drying* (in Polish), Editorial Office of Poznan University of Technology, Poznań, 2005.

[5] Stachowicz M., Nowak D., Kazimierz G., Haimann K.: *Influence of hardening method of water-glass moulding sands on structure of linking bridges* (in Polish), Monography edited by Jerzy Pacyna, XXXVII School of Material Engineering, Kraków, 2009.

[6] Grabowska B.: *Microwave crosslinking of polyacrylic compositions containing dextrin and their applications as molding sands binders*, Polimery, Vol. 54, No. 7–8, 2009, pp. 507–513.

[7] Grabowska B., Zapotoczny S., Holtzer M.: *Networking of polyacrylates by using microwave* (in Polish), The XLVII Convention PTChem and SITPChem, The Convention materials, Vol. III, Wrocław, 2004, pp. 955.

[8] Lewandowski J.L.: *Materials for casting moulds* (in Polish), Akapit, Kraków, 1997.

[9] Granat K., Nowak D., Pigiel M., Stachowicz M., Wikiera R.: *The influence of hardening method on basic properties of water glass molding sands*, Visnik Chmelnickogo Nacional'nogo Universitetu, Vol. 1, No. 4, 2007, pp. 98–104.

[10] Granat K., Nowak D., Pigiel M., Stachowicz M., Wikiera R.: *The influence of microwave heating and water glass kind on the properties of molding sands*, Archives of Foundry Engineering, Vol. 8, spec. iss. 1, 2008, pp. 119–122.

[11] Granat K., Nowak D., Pigiel M., Stachowicz M., Wikiera R.: *The influence of water glass on the properties of microwave cured molding sands*, Archives of Foundry Engineering, Vol. 8, spec. iss. 1, 2008, pp. 123–126.

Zastosowanie mikrofal do innowacyjnego utwardzania proekologicznych mas ze szkłem wodnym stosowanych w procesie wytwarzania odlewów staliwnych

W pracy przedstawiono wyniki badań nad możliwością wprowadzenia innowacyjnej technologii mikrofalowej do produkcji wysokiej jakości, oszczędnościowych rdzeni z mas sporządzonych ze szkłem wodnym – uwodnionym krzemianem sodu. W badaniach zwrócono szczególną uwagę na poprawę właściwości technologicznych badanych mas, a szczególnie ich wytrzymałości oraz wybijalności, poprzez dobór odpowiednich parametrów procesu utwardzania. Wskazano ponadto na korzyści wynikające z zastosowania takiego innowacyjnego i proekologicznego rozwiązania skutecznie zastępującego tradycyjne i energochłonne procesy wykonywania rdzeni odlewniczych.

Analysis of the earth-sheltered buildings' heating and cooling energy demand depending on type of soil

M. STANIEC, H. NOWAK

Wrocław University of Technology, Institute of Building Engineering, Wybrzeże Wyspiańskiego 27, 50-370 Wrocław, Poland.

The interest in the use of earth as an energy storage dates back to over 5000 years ago when in some cultures whole towns were built under the ground. Owing to its very high thermal capacity, the temperature of the ground is lower than that of the outdoor air in summer and higher in winter. Consequently, the heating and cooling energy of a building considerably sunk into ground is lower than that of a corresponding aboveground building. In aboveground buildings the type of soil on which they are founded may influence only slightly their annual energy balance since the floor is the only envelope being in direct contact with soil. In buildings partly sunk into ground (earth-sheltered buildings) not only the floor but also the walls and the flat roof are in contact with soil whereby the kind of soil may have a significant influence on the annual energy balance of the buildings.

Separate analyses of an aboveground building and an earth-sheltered building with its south elevation exposed and glazed in 80% and a one meter thick layer of soil on its flat roof were carried out. Calculation simulations were run for several thermal insulation (polystyrene foam) thicknesses, i.e. 5 cm, 10 cm and 20 cm, and for a case without thermal insulation.

Keywords: *earth-sheltered buildings, building's energy balance, heating, cooling, modelling*

1. Introduction

It is thought that the interest in earth as an element aiding the building's energy balance began to grow markedly with the imposition of the oil embargo in 1973, which caused a world energy crisis. As a result, the reduction of energy consumption in buildings became almost a national priority in the countries which suffered from the embargo. This applied mainly to the USA, most European countries and Japan [1].

The first mentions of the environmental impact of construction engineering appeared already a few years before the energy crisis of 1970. But the interest in the use of earth as an energy storage dates back to over 5 000 years ago when in some cultures whole towns were built under the ground. The examples are: the town of Matmata in Tunisia, the Goreme Valley in Turkey and the Henan Province in Shanxi [1]. All the ancient underground structures are located in hot countries, such as Turkey, Tunisia or northern China, which means that earth was originally used rather for cooling than heating. This is highly significant if one considers the fact that over one third of the continents (about 4.7 million km^2) is situated in hot-dry climate (i.e. between 15° and

35° respectively north and south of the equator) and only 12% of the continents are situated in the temperate climate (about 1.55 million km^2). Taking into account the other climatic conditions, one can say that half of the continents are situated in hot climate. Thus the use of earth as the building's cooling component is of major significance, particularly considering that 15% of the population inhabits desert areas.

In the present times, under the pressure of dwindling fossil energy sources, constantly rising fuel prices and the environmental movement associated with the greenhouse effect, energy-efficient construction became one of the major turn-of-the-century disciplines [5, 10, 11, 13]. Its philosophy is based on the three fundamental principles: energy saving, energy recovery and drawing energy from the environment, by exploiting, among other things, the building's thermal mass. The latter principle made researchers consider the effect of enclosing the building (not only covering its flat roof with soil) in earth on its annual energy balance. For many years now research into the heat demand of buildings partly sunk into ground, whose walls are banked with earth, has been conducted [1, 3, 10, 11, 15]. Such buildings are known as earth-sheltered buildings. Residential buildings of this kind usually have one elevation (the southern one) exposed (Figure 1.)
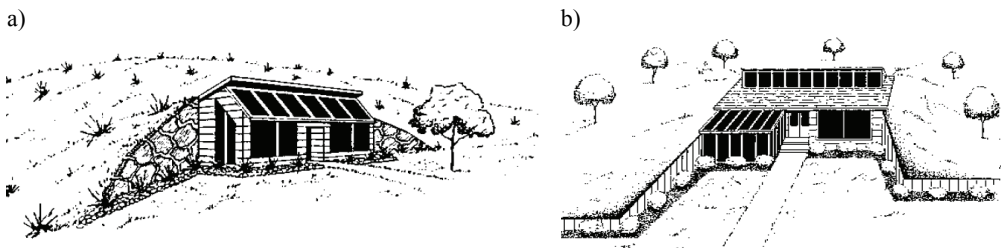
Fig. 1. Earth-sheltered buildings with one elevation exposed: a) one level, b) two levels

The use of earth as a large capacity heat storage makes it possible not only to reduce such buildings' demand for heating and cooling energy, but also helps to preserve the local microclimate. Therefore earth-sheltered buildings are characterized by lower heating and air-conditioning energy demand and little disturb the natural environment [3]. Earth-sheltered buildings offer also other benefits, such as:

• little disturbance of the surrounding environment and more effective land development,

• lower building maintenance costs (smaller surface area of exposed building envelopes),

• better noise and vibration damping (earth dampens well the amplitude of acoustic waves),

• by definition they are less exposed to weather conditions,

• and often are architectonically very interesting whereby they can become a city's pride or landmark, which is an important consideration for potential investors.

The most important elements in the design of such a building are: the shape of the building, the arrangement of the glazing, the thickness of the thermal insulation layer and the type of soil. So far the type of soil has not been taken into account in the building's annual energy balance. The analyses have been made for aboveground buildings in which the floor is usually the only envelope being in contact with soil and the percentage of the floor in the total area of the envelope surrounding the building's heated cubage is too small to be of significance. The situation is quite different in the case of earth-sheltered buildings. Here practically all the building partitions are in contact with soil. Thus the type of soil can have a significant impact on the annual energy balance of earth-sheltered buildings.

Considering the above, the present research was undertaken to determine the earth-sheltered building's heating and air-conditioning energy demand depending on the type of soil in which it is founded. For comparison, the corresponding results for the aboveground building are presented.

2. Calculation model

Computer programs FlexPDE and EnergyPlus, based on numerical solutions of the energy flow equations, were used in tandem for simulating respectively the thermal field of the building's envelope and the soil and the building's energy demand. The input for FlexPDE were one hour-step meteorological data, i.e. air temperature, air relative humidity, total solar radiation on a horizontal plane, total solar radiation on a vertical plane, wind velocity, sky cloud cover and snow cover thickness. The temperature soil surface determined this way became the boundary condition for the energy balance calculations in EnergyPlus. The step of one hour was adopted for all the simulations.

2.1. Numerical model of temperature distribution in soil

The distribution of temperature in the soil around underground and aboveground buildings is calculated using FlexPDE in which the solution is based on an equation of 3D unsteady heat conduction in an isotropic body, i.e. on the Fourier Equation [12]:

$$\alpha \left(\frac{\delta^2 T}{\delta x^2} + \frac{\delta^2 T}{\delta y^2} + \frac{\delta^2 T}{\delta z^2} \right) = \frac{\delta T}{\delta t}, \tag{1}$$

where:
   T – temperature [K],
   t – time [s],
   x, y, z – Cartesian coordinates [–],
   α – thermal diffusivity [m^2/s],
where:

$$\alpha = \frac{\lambda}{c_v} = \frac{\lambda}{c_p \rho}, \tag{2}$$

where:

λ – thermal conductivity [W/(mK)],

c_v – volumetric heat capacity [J/(m^{3}K)],

c_p – specific heat capacity [Ws/(kgK)],

ρ – volumetric density [kg/m^3].

The value of thermal conductivity coefficient λ was assumed to be time constant in the whole computation domain.

In order to solve the equation of heat conduction in the soil surrounding a heated building it is necessary to introduce conditions limiting the computation domain. The thermal balance of the ground's horizontal and vertical surfaces and the equation describing heat exchange through the building's internal surfaces are illustrated in Figure 2 (which is a graphic interpretation of formula (3)).
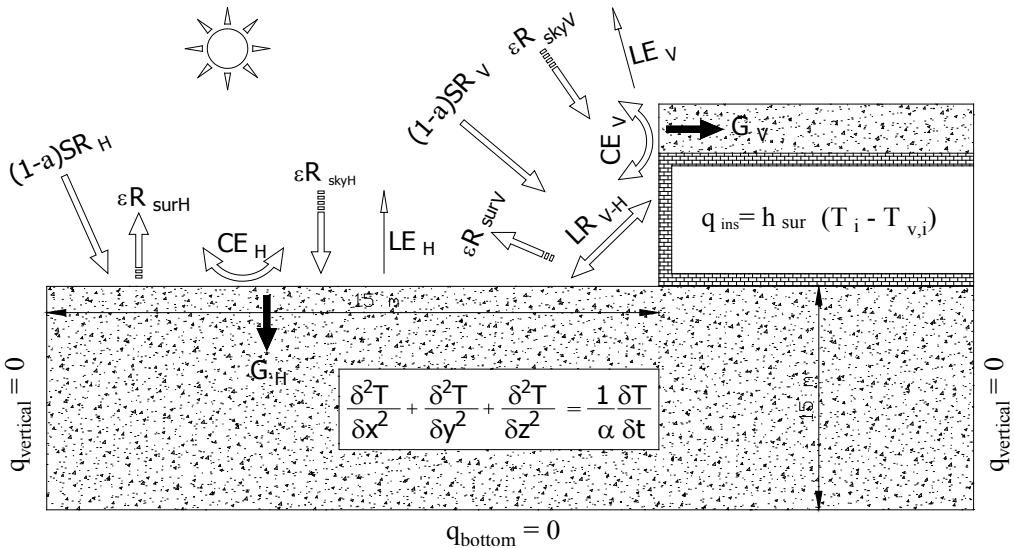

Fig. 2. Overall thermal balance on horizontal and vertical soil surfaces (not in scale)

The overall energy balance for the ground's surface is described by the equation used by Janssen [4] and other researchers [1, 6−7, 9, 14]:

$$G = R + CE - LE + HP, \tag{3}$$

where:

G – the energy flow at the soil surface [W/(m^{2}K)],
R – radiation energy [W/(m^{2}K)],
CE – convection energy [W/(m^{2}K)],
LE – latent evaporation energy [W/(m^{2}K)],
HP – sensible heat transfer by precipitation [W/(m^{2}K)].

Janssen [4] shows that transfer of sensible heat related to precipitation HP can be omitted, due to its insignificance influence on the energy flow at the soil surface. Thus no further elaboration on this issue will be made here.

The model boundary conditions are shown in Figure 2. The bottom and vertical boundary conditions are described as adiabatic [4, 15], i.e.:

$$q_{\text{bottom}} = q_{\text{vertical}} = 0. \tag{4}$$

The top boundary conditions describe heat exchange on the horizontal and vertical soil surfaces [1, 3]:

$$G_{H(V)} = SR_{H(V)} + R_{\text{sky}H(V)} - R_{\text{sur}H(V)} + CE_{H(V)} - LE_{H(V)}, \tag{5}$$

where:

$G_{H(V)}$ – the energy absorbed by the horizontal (vertical) soil surface [W/m^2],

$SR_{H(V)}$ – the shortwave sun radiation energy absorbed by the horizontal (vertical) soil surface [W/m^2],

$R_{\text{sky}H(V)}$ – the longwave sky radiation energy on the horizontal (vertical) soil surface [W/m^2],

$R_{\text{sur}H(V)}$ – longwave horizontal (vertical) soil surface radiation [W/m^2],

$CE_{H(V)}$ – the energy due to convection on the horizontal (vertical) surface [W/m^2],

$LE_{H(V)}$ – the energy due to the latent evaporation of the horizontal (vertical) surface [W/m^2].

In the thermal balance of the vertical surface one should also include the longwave radiation between horizontal and vertical surfaces LR_{V-H} [8]:

$$LR_{V-H} = 4\varepsilon\sigma\left(\frac{T_H + T_V}{2}\right)^3 (T_H - T_V), \tag{6}$$

where:

T_H – the temperature of the horizontal soil surface [K],

T_V – the temperature of the vertical soil surface [K].

The heat exchange through the building's internal surfaces is described by the equation [4–5]:

$$q_{\text{ins}} = h_{sur}(T_i - T_{V,i}), \tag{7}$$

where:

h_{sur} – a convective heat-transfer coefficient [W/(m^{2}K)],

T_i – inside air temperature [K],

T_{vi} – internal surface temperature [K].

The initial condition is defined with several steps. First, the soil temperature distribution is solved for 3D steady-state conditions, which assume bottom and top boundary conditions equal to the mean annual soil surface temperature, and the internal air temperature is set constant and equal to 20 °C. Second step is to simulate the analysed domain for unsteady-state with temperature distribution from the first step as an initial condition. The calculated temperature becomes initial condition for next steps. Calculations are repeated until the stable state is achieved, which means that the temperature difference between previous and calculated step is no larger than 0.5%.

3. Input data for simulations

An aboveground building and an earth-sheltered building with its southern elevation exposed and in 80% glazed and a one meter thick soil layer on its flat roof were analysed. Simulations were run for a few thermal insulation thicknesses, i.e. 5 cm, 10 cm and 20 cm and no thermal insulation.

Dimensions of 12 × 12 m in plan single-storey, single-family building with a floorage of 144 m^2 was adopted for the simulations. Since the room's height was assumed to be 2.8 m, the heated cubage was 403 m^3 at nearly 450 m^2 of envelopes. Because of the heavy loads, the building structure is made of reinforced concrete. The thickness of the bearing walls and that of the structural ceiling was assumed to be equal to 30 cm and the concrete ground slab was assumed to be 15 cm thick. All the building's envelopes (the structural ceiling, the external walls and the floor on ground) were lined with thermal insulation. Typical double-glazed windows filled with argon, with heat-transfer coefficient $U = 1.4$ W/(m^{2}K), were adopted.
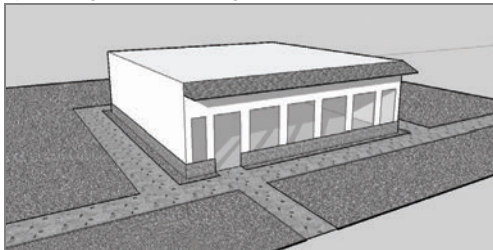
a) aboveground building   b) earth-sheltered building (one elevation exposed)
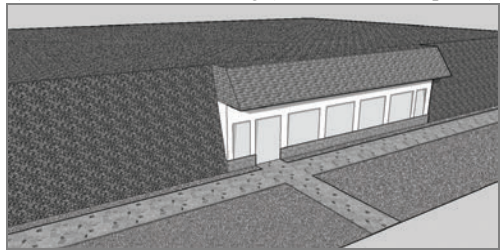

Fig. 3. Schemes of analysed buildings: a) aboveground, b) earth-sheltered (roof imitation)

Simulations of the building's heating and cooling energy demand were carried out for the climate of Poznań (the Wielkopolskie Province, Poland) because of the access to complete weather data for this area. The meteorological data (averages for the last thirty years) for the simulation of the building's demand were taken from the meteorological data files base of EnergyPlus (WEC).

Five types of soil, i.e. sand and clay according to PN-EN-ISO:13370 [8] and three types of medium sand according to Ickiewicz [2], differing in their moisture content (Table 1), were adopted for the analysis of the influence of the type of soil on the annual energy balance.

Table 1. Thermal-moisture properties of soils used in analysis

Symbol:	Standard sand	Standard clay	Medium sand $w = 12.5\%$	Medium sand $w = 4.3\%$	Medium sand $w = 0.27\%$
	Soil 1	Soil 2	Soil 3	Soil 4	Soil 5
Source:	PN-EN-ISO:13370 "*Thermal properties of buildings – Heat transfer via the ground – Calculation methods*" [8]		Ickiewicz I., "*Heat conduction in building soils*" [2]		
Moisture content, w, %	–	–	12.540	4.380	0.270
Thermal conductivity, λ, W/(mK)	2.000	1.500	1.150	0.770	0.320
Volumetric heat capacity, c_v, J/(m³K)	2.000×10^6	3.000×10^6	1.876×10^6	1.407×10^6	1.197×10^6
Thermal diffusivity, α, m²/s	1.000×10^{-6}	0.500×10^{-6}	0.613×10^{-6}	0.547×10^{-6}	0.267×10^{-6}

4. Influence of soil type on building's energy balance – simulation results and conclusions

In order to determine the soil factor having a bearing on the heating and cooling energy demand of the buildings, the dependence between building heating and cooling energy demand values and the coefficients expressing the thermal properties of the above soils was analysed. Simulation results for the earth-sheltered building without thermal insulation were chosen for the analysis in order to clearly demonstrate the dependence. Figure 4 shows a diagram of the annual heating energy demand for the five types of soil depending on their thermal conductivity, volumetric heat capacity and thermal diffusivity coefficients.

A comparison of the trend lines for the coefficients shows that the graph of the thermal diffusivity coefficient (i.e. the temperature equalization coefficient) reflects the building's heating energy demand. Therefore one can infer that the lower the thermal diffusivity of the soil, the lower the building's heating energy demand.
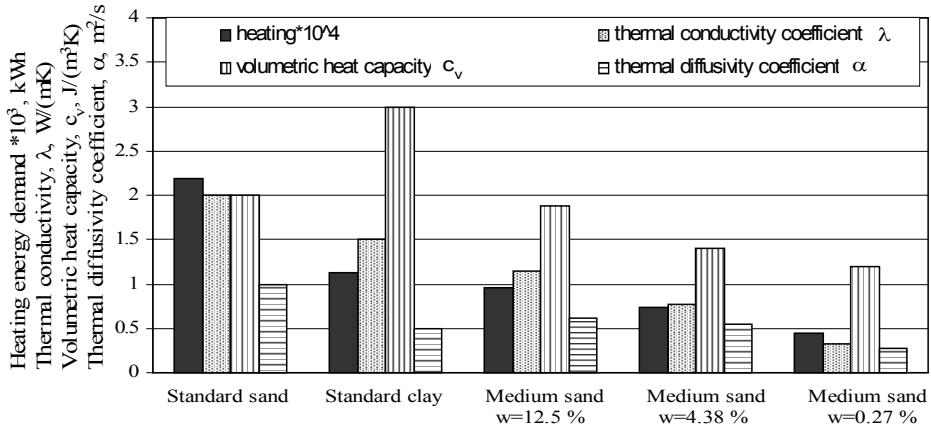
Fig. 4. Dependence of building's heating energy demand on thermal properties of analysed soils

A similar, but inverse, relationship is apparent for the building's cooling energy demand (Figure 5).
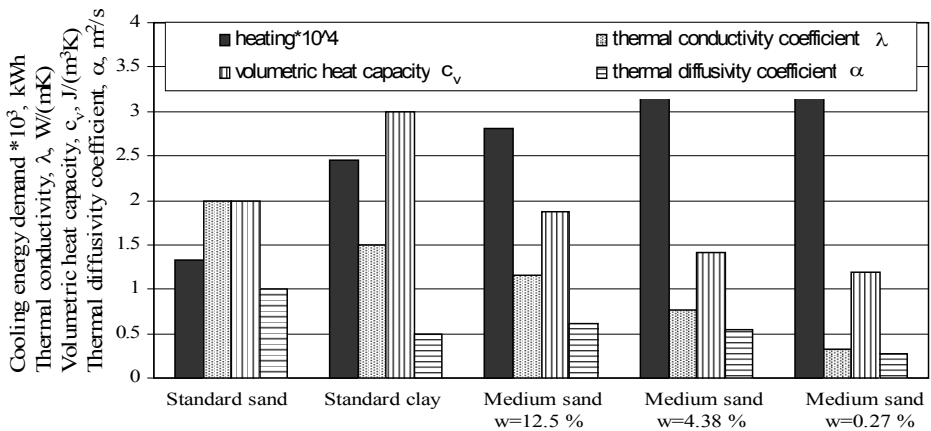
Fig. 5. Dependence of building's cooling energy demand on thermal properties of analysed soils

It is apparent that the lower the soil's thermal diffusivity coefficient (i.e. the lower the soil's density or moisture content), the higher the building's cooling energy demand. This means that it is the soil's thermal diffusivity, and not its thermal conductivity, which has a direct bearing on the building's energy balance. Therefore when analysing the type of soil surrounding the building one should take into account not only thermal conductivity coefficient λ, but also volumetric thermal capacity c_v. Those two determine the value of the soil's thermal diffusivity coefficient α. The latter, in turn, determines the rate of equalization of temperature in the soil and so the amount of energy stored in it, which directly affects the building's energy balance.

Figures 6 and 7 show the annual heating and cooling energy demand for the aboveground building and the earth-sheltered building as well as the difference between the highest and lowest energy demand and the percentage of this difference.

a) aboveground building

b) earth-sheltered building
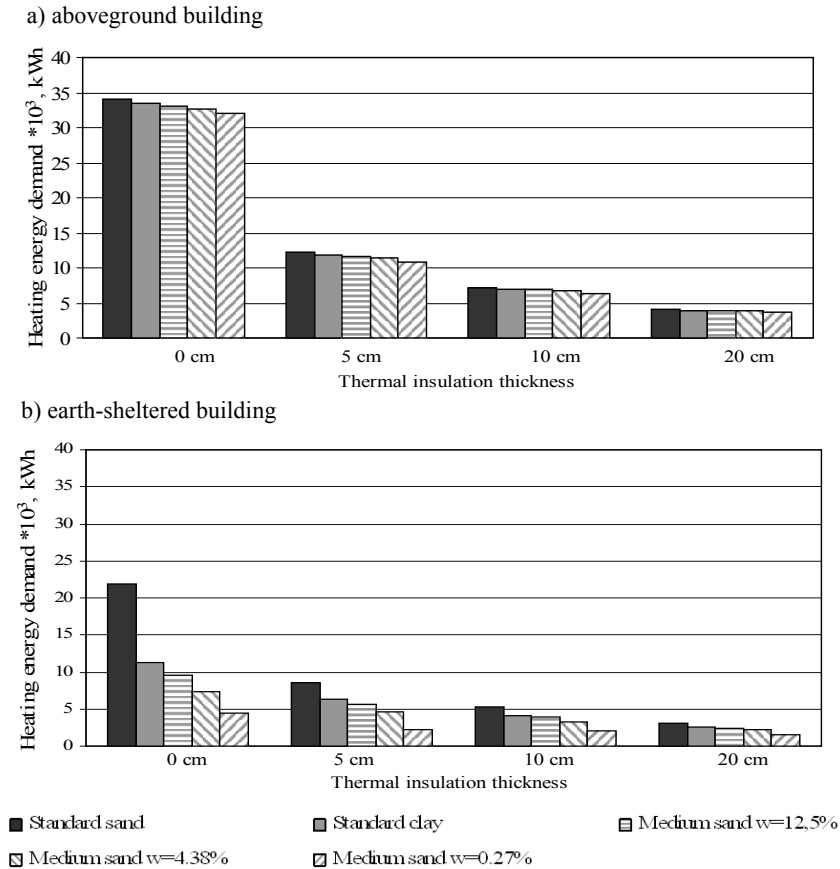
Fig. 6. Heating energy demand of aboveground building and earth-sheltered building depending on different types of soil and thermal insulation thickness

In the case of the aboveground building (Figure 6a), the type of soil has a negligible influence on both heating and air-conditioning energy demand. The aboveground building's annual heating energy demand decreases with the soil's thermal diffusivity. The heating energy demand of the building founded on soil 1 is ca 2 000 kWh lower, which for the total energy demand of the building founded on soil 1 (standard sand) amounting to about 34 000 kWh represents merely 6% lower heating energy demand than that of the aboveground building founded on soil 5 (Table 2). When 5 cm and 10 cm thick thermal insulation is applied, the heating energy demand of the building sunk into soil 5 is lower than for the building founded on soil 1 by respectively 1 300 and

800 kWh, which amounts to 11% of the heating energy demand of the building founded on soil 1. In the case of the buildings in which 20 cm thick thermal insulation was applied, this difference amounts to merely 400 kWh, which constitutes about 10% lower heating energy demand than that of the building founded on soil 1.

Table 2. Annual heating energy demand of aboveground building and earth-sheltered building depending on type of soil on which they are founded, kWh

Type of soil		Thermal insulation thickness, cm			
		0 cm	5 cm	10 cm	20 cm
Aboveground building					
Soil 1	Standard sand	34 132	12 175	7 236	4 011
Soil 2	Standard clay	33 463	11 823	7 037	3 922
Soil 3	Medium sand $w = 12.5\%$	33 141	11 630	6 925	3 871
Soil 4	Medium sand $w = 4.38\%$	32 702	11 338	6 744	3 778
Soil 5	Medium sand $w = 0.27\%$	32 118	10 872	6 427	3 591
Difference between soil 1 and 5, kWh		2 014	1 303	809	420
Percentage difference in w between pores and soil 1, %		6	11	11	10
Earth-sheltered building					
Soil 1	Standard sand	21 837	8 609	5 383	3 032
Soil 2	Standard clay	11 212	6 330	4 156	2 495
Soil 3	Medium sand $w = 12.5\%$	8 535	5 701	3 876	2 402
Soil 4	Medium sand $w = 4.38\%$	7 362	4 631	3 314	2 169
Soil 5	Medium sand $w = 0.27\%$	4 406	2 272	2 132	1 609
Difference between soil 1 and 5, kWh		17 431	6 337	3 251	1 423
Percentage difference in w between pores and soil 1, %		80	74	60	47

In the case of the earth-sheltered buildings shown in Figure 6b, the influence of the type of soil on the annual energy balance is much more notable. The heating energy demand of the building without thermal insulation, founded in soil 5 is by about 17 000 kWh lower than that of the building founded in soil 1. This constitutes ca 80% lower heating energy demand than that of the building founded in soil 5. For 5 cm thick thermal insulation this difference amounts to ca 6000 kWh and it decreases as thermal insulation thickness increases. For a 10 cm and 20 cm thick thermal insulation layer the difference in annual heating energy demand between soil 5 and soil 1 amounts to respectively ca. 3250 kWh and 1400 kWh, which represents ca. 74%, 60% and 47% lower heating energy demand than that of the building sunk into soil 1.

In conclusion, when the soil's thermal conductivity coefficient $\alpha = 1.000 \times 10^6$ m^2/s is reduced to $\alpha = 0.267 \times 10^{-6}$ m^2/s (this means a reduction in the soil's specific density by about 180 kg/m^3 or a reduction in its moisture content by about 12%), the building's heating energy demand decreases by ca 6–11% and 47–80% for respectively the aboveground buildings and the earth-sheltered buildings. Similarly as in the case of the annual heating energy demand of aboveground buildings, the type of soil has a negligible influence on their annual air-conditioning energy demand and the latter increases as the soil's thermal diffusivity decreases (Figure 7).

a) aboveground building

b) earth-sheltered building

- Standard sand
- Standard clay
- Medium sand w=12,5%
- Medium sand w=4.38%
- Medium sand w=0.27%
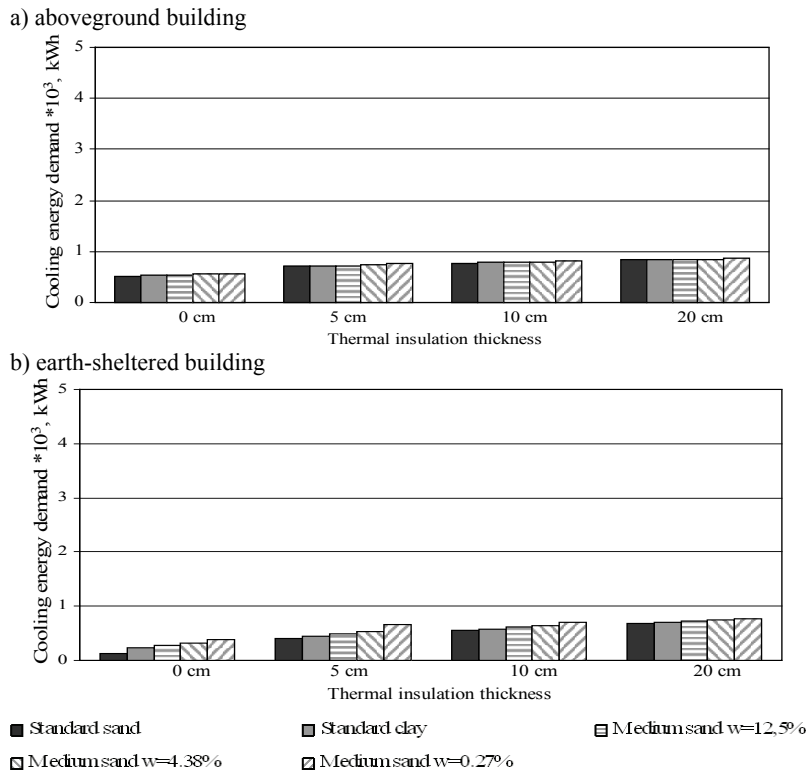
Fig. 7. Cooling energy demand of aboveground building and earth-sheltered building depending on different types of soil and thermal insulation thickness

The air-conditioning energy demand of the aboveground building without thermal insulation, founded on soil 5 is about 44 kWh (8%) higher than that of the building founded on soil 1. When 5 cm and 10 cm thick thermal insulation is applied, the air-conditioning energy demand of the building sunk into soil 5 is higher by respectively ca 50 and 40 kWh while for 20 cm thick thermal insulation it is higher by about 20 kWh, which represents respectively 7%, 5% and 3% lower air-conditioning energy demand than that of the building founded on soil 1.

Similarly as in the case of the heating energy demand of the buildings partly sunk into ground (Figure 7b), the type of soil has a marked influence on their air-conditioning energy demand. The air-conditioning energy demand of the uninsulated building sunk into soil 5 is by about 250 kWh (65%) higher than that of the building sunk into soil 1. For 5 cm thick thermal insulation the difference amounts to ca. 250 kWh (38%). It increases with thermal insulation thickness. For a 10 cm and 20 cm thick thermal insulation layer the difference in annual air-conditioning energy demand between the building sunk into soil 5 and into soil 1 amounts to respectively ca 160 kWh and 80 kWh, which constitutes about 23% and 11% higher air-conditioning energy demand of the buildings partly sunk into soil 5.

Table 3. Annual air-conditioning energy demand of above ground building
and earth-sheltered building depending on type of soil on which they are founded, [kWh]

Type of soil		Thermal insulation thickness [cm]			
		0 cm	5 cm	10 cm	20 cm
Aboveground building					
Soil 1	Standard sand	522	703	775	842
Soil 2	Standard clay	530	711	780	845
Soil 3	Medium sand $w = 12.5\%$	542	723	788	849
Soil 4	Medium sand $w = 4.38\%$	553	736	797	855
Soil 5	Medium sand $w = 0.27\%$	566	753	811	864
Difference between soil 1 and 5, kWh		44	50	37	22
Percentage difference in w between pores and soil 1, %		8	7	5	3
Earth-sheltered building					
Soil 1	Standard sand	133	405	548	694
Soil 2	Standard clay	244	459	583	710
Soil 3	Medium sand $w = 12.5\%$	281	497	611	723
Soil 4	Medium sand $w = 4.38\%$	320	543	646	741
Soil 5	Medium sand $w = 0.27\%$	377	654	713	778
Difference between soil 1 and 5, [kWh]		244	250	165	84
Percentage difference in w between pores and soil, %		65	38	23	11

In conclusion, when the soil's thermal diffusivity coefficient $\alpha = 1.000 \times 10^{-6}$ m^2/s is reduced to $\alpha = 0.267 \times 10^{-6}$ m^2/s, the annual air-conditioning energy demand increases by ca 3–8% and 11–65% for respectively the aboveground buildings and the buildings partly sunk into ground.

5. Conclusions

The very weak influence of the type of soil on the heating and air-conditioning energy demand of the aboveground buildings can be ascribed to two factors. Firstly, the temperature under the floor of the aboveground building (as well as the earth-sheltered building) is mainly determined by the thermal conditions inside the building. Owing to the relatively stable thermal-moisture conditions inside the building, the temperature under its floor is also stable and close to that of the outdoor air. Secondly, the floor in the aboveground building is the only envelope being in contact with soil. Consequently, the surface area through which heat exchange with the ground takes place constitutes merely ca 30% of the surface area of all the cooling envelopes (in the building analysed in this paper). Thus the heat exchange with the ground through the external envelope represents a relatively small percentage.

In the case of the earth-sheltered buildings, external factors (weather conditions), influencing the thermal balance on the ground's surface, have the greatest influence on the temperature field in the ground. Hence the kind of soil (more precisely, the rate of temperature equalization, determined by the soil's thermal diffusivity coefficient α) has a much stronger influence on the energy balance of the earth-sheltered buildings than thermal conductivity coefficient λ alone. However, the lower thermal conductivity coefficient of the soil, the lower heating and air-conditioning energy demand of the building. This becomes apparent when the energy consumption in the buildings founded in clay and medium sand with a moisture content of 4.38% are compared. Despite the fact that thermal diffusivity coefficients α are similar, i.e. amount to respectively 0.500 m^2/s and 0.547 m^2/s, the thermal energy consumption by the aboveground building on soil with a lower thermal diffusivity coefficient, i.e. $\alpha = 0.500$ m^2/s, is about 4% higher than for the building founded on soil 2. In the case of the buildings partly sunk into ground, the difference is even larger, amounting to ca. 14–27%. The air-conditioning energy consumption in the buildings founded on medium sand is by ca 4% and 8% lower for respectively the aboveground building and the earth-sheltered building, in comparison with the air-conditioning energy consumption in the buildings founded on clay (whose thermal diffusivity coefficient α is lower). This is due to the fact that, despite similar values of temperature equalization coefficient α of clay and medium sand with a moisture content of 4.38%, both thermal conductivity coefficient λ and volumetric heat capacity c_v for medium sand are twice lower than for clay. Thus the demand for heating energy and that for air-conditioning energy are lower.

Another factor determining the energy balance of the buildings is the surface area of the envelopes through which heat exchange with the ground takes place. The surface area of the envelopes being in contact with soil amounts to as much as ca. 90% and 80% of the total area of the cooling envelopes in earth-sheltered buildings with respectively one elevation (in the analysed buildings, the floor: 30%, the flat roof: 30%, three walls: 3 × 10%) and two elevations (in the analysed buildings, the floor:

30%, the flat roof: 30% and 2 walls: $2 \times 10\%$) exposed. Thus the percentage of soil type contribution to the energy balance of the buildings is also higher.

Considering the above, the type of soil under the aboveground building has a negligible influence (ca. 3–11%) on its annual energy balance. But the type of soil has a much greater influence (ca. 11–80%) on the energy balance of earth-sheltered buildings.

References

[1] Al-Temeemi A.A., Harris D.J: *A guideline for assessing the suitability of earth-sheltered mass-housing in hot-arid climates*, Energy and Buildings, Vol. 36, 2004, pp. 251–260.

[2] Ickiewicz I.: *Heat conduction in building soils* (in Polish), PhD Thesis, Białystok Polytechnic, Białystok, 1988.

[3] Jacovides C.P., Mihalakakou G., Santamouris M., Lewis J.O.: *On the ground temperature profile for passive cooling applications in buildings*, Solar Energy, Vol. 3, 1996, pp. 167–175.

[4] Janssen H.: *The influence of soil moisture transfer on building heat loss via the ground*, Ph.D. Thesis, Katholieke Universiteit Leuven, Belgium, 2002.

[5] Jędrzejuk H., Marks W.: *Optimization of shape and functional structure of buildings as well as heat source utilization. Partial problems solution*, Building and Environment, Vol. 37, 2002, pp. 1037–1043.

[6] Nowak H.: *External interaction of environmental thermal radiation on the building* (in Polish), Scientific Papers of the Institute of Building Engineering at Wrocław University of Technology, WUT Publishing House, Wrocław, 1999.

[7] Nowak H.: *Modelling of the longwave radiation incident upon a building*, Archives of Civil Engineering, XLVII, Vol. 2, 2001, pp. 243–267.

[8] PN-EN-ISO:13370, *Thermal performance of buildings – Heat transfer via ground – calculation methods* (in Polish).

[9] Sodha M.S.: *Short communication: Simulation of dynamic heat transfer between ground and underground structures*, International Journal of Energy Research, Vol. 25, 2001, pp. 1391–1394.

[10] Staniec M., Nowak H.: *Buildings partly or completely sunk in ground, as alternative to conventional aboveground buildings* (in Polish), X[th] Polish Scientific-Technical Conference on Physics of Buildings in Theory and Practice, Łódź, 2005, pp. 161–168.

[11] Staniec M., Włodarczyk D., Nowak Ł.: *Examples of earth-sheltered buildings in Great Britain* (in Polish), Renewable Energy. *Innovative ideas and technologies for construction*, Scientific Papers of Rzeszów Polytechnic, Rzeszów Polytechnic Publishing House, Solina, 2006, pp. 465–476.

[12] Staniszewski B.: *Heat exchange. Theoretical basis* (in Polish), 2nd Edition, Państwowe Wydawnictwo Naukowe, Warsaw, 1980.

[13] Thompson R.D.: *Man's Impact on Climate with particular reference to energy balance changes at the earth's surface*, Recourses and Planning, Pergamon Press, 1979.

[14] Xianting L., Zhen Y., Bin Z., Ying L.: *Numerical analysis of outdoor thermal environment around buildings*, Building and Environment, Vol. 40, 2005, pp. 853–866.

[15] Staniec M.: *Analysis of the influence of earth-sheltering on the building's energy balance* (in Polish), PhD Thesis, Series PRE No. 01/09, Wrocław University of Technology, 2009.

**Analiza zużycia energii grzewczej i klimatyzacyjnej w budynkach
częściowo zagłębionych w gruncie w zależności od rodzaju gruntu**

Pierwotnie zainteresowanie wykorzystaniem gruntu jako magazynu ciepła datuje się na ponad 5000 lat temu, kiedy w niektórych kulturach budowano pod ziemią całe miasta. Bardzo duża pojemność cieplna gruntu powoduje, że latem temperatura gruntu jest niższa niż powietrza zewnętrznego, a zimą wyższa. Właściwość ta powoduje, że budynek zagłębiony w gruncie charakteryzuje się mniejszym zapotrzebowaniem na energię do ogrzewania i chłodzenia niż odpowiadający mu budynek naziemny. W budynkach naziemnych rodzaj gruntu, na którym są one posadowione może mieć znikomy wpływ na roczny bilans energetyczny, ponieważ podłoga jest jedyną przegrodą, która styka się bezpośrednio z gruntem. W analizowanych w tej pracy budynkach częściowo zagłębionych w gruncie liczba przegród stykających się z gruntem nie ogranicza się tylko do podłogi na gruncie, ale dotyczy również ścian i stropodachu, stąd rodzaj gruntu może znacząco wpływać na roczny bilans energetyczny tych budynków.

W artykule przedstawiono wyniki analizy obliczeniowej, której poddano osobno budynek naziemny i podziemny z eksponowaną jedną elewacją, przy 80% stopniu przeszklenia elewacji południowej, z metrową warstwą gruntu, zalegającego na stropodachu budynku. Symulacje przeprowadzono dla kilku grubości termoizolacji, tj. 5 cm, 10 cm i 20 cm oraz przy jej braku.

Vibration insulation of hydraulic system control components

M. STOSIAK

Wrocław University of Technology, Wybrzeże Wyspiańskiego 25, 50-370 Wrocław, Poland.

This paper deals with the effects of external mechanical vibrations on hydraulic valves. A theoretical analysis of the contribution of selected vibration insulators to a reduction in hydraulic valve housing vibrations was carried out. The results of preliminary experimental tests of simple vibration insulators are reported.

1. Introduction

Major features of hydraulic systems are periodic changes of pressure around an average value, commonly referred to as pressure fluctuations. Their consequences are definitely negative. The cyclic operation of the pump's displacement components [1] or the self-excitation of the control components in hydraulic valves [2] due to the action of the flowing liquid [4] or to external mechanical vibrations [3, 5, 6] are among the causes of pressure fluctuations. Pressure fluctuations cause the individual system components to vibrate. This has an adverse effect, particularly on the precision of positioning of, for example, the cutting tool in a machine tool. This also applies (although to a smaller degree) to mobile machines which are the source of vibrations affecting the rigidly fixed hydraulic valves. Generally, the complex problem of the transmission of vibrations by a machine or a piece of equipment can be divided into three interconnected categories:

- vibration sources,
- vibration transmission paths,
- effects.

The most frequent cause of vibrations are disturbances connected with the motion or operation of the machine, for example when a mobile machine moves on an uneven surface or when the rotating parts are unbalanced during material machining. Another major vibration source are drive units, for example a combustion engine performing a periodic variable-characteristic work cycle [7, 8]. An operating hydraulic system is also a source of mechanical vibrations caused mainly by pressure surges and the periodic operation of the displacement pump. Since the generated vibrations have different frequencies the paths of their transmission are also different. The irregularities of the surface on which a mobile machine moves cause excitations in a frequency range of 0.5–250 Hz [9–11]. The latter includes excitations generated by the driving (combustion) engine and the displacement pump kinematics, manifesting themselves in pres-

sure fluctuations in the machine's hydraulic system. The vibrations due to the resistance of flowing air are in a frequency range of 250–16 000 Hz and they are caused by airflow separation from the machine's components. Also the flow of the working medium in the hydraulic system causes vibration and noise. Sometimes cavitation occurs, generating high-frequency noise. The vibrations generated and transmitted by a machine produce various effects. Mechanical vibrations affect the machine operator. The components of the systems with which the machine is equipped, particularly hydraulic components and systems are also subject to mechanical vibrations. Such components are required to have good dynamic properties and to be characterized by stability, positioning precision, operating reliability and certainty and little noisiness. Modern proportional hydraulic valves or hydraulic microvalves are particularly exposed to external mechanical vibrations since the disturbing forces in them can amount to the controlling forces, which may lead to many adverse effects, such as stability loss, positioning inaccuracy, damage to seals and increased noisiness [12].

2. Flexible fixing of hydraulic valve

As mentioned above, in order to minimize the vibration of the hydraulic valve's control element it seems sensible to isolate the valve housing from the external mechanical vibrations of the base (for example the vibrating frame of a mobile machine or a machine tool). For the analysis of the effect of the flexible fixing of a hydraulic valve on the vibration of its housing a special clamping holder for the hydraulic distributor was designed. The latter is on its two sides supported by a system of springs with a known linear characteristic and a known pre-deflection (Figure 1).

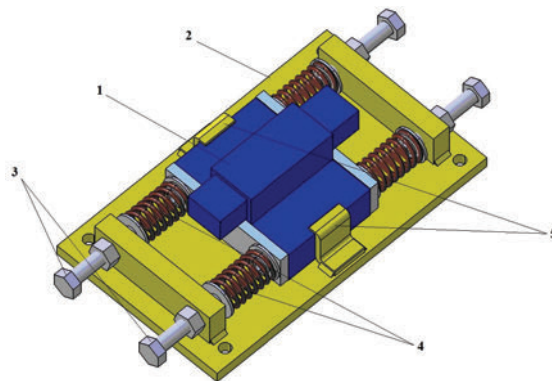Fig. 1. Valve holder: 1 – hydraulic valve (distributor), 2 – holder base,
3 – spring pre-deflection bolts, 4 – springs, 5 – securing catches

The design of the holder is such that the valve mounted in it is constrained by springs (with an equivalent stiffness) and it moves on the holder base (2 in Figure 1) rubbing against it in accordance with the dry friction model. On its two sides the valve

is supported by springs. A scheme of the hydraulic system in which the proportional distributor type 4WRE 6 E08-12/24Z4/M operates is shown in Figure 2.
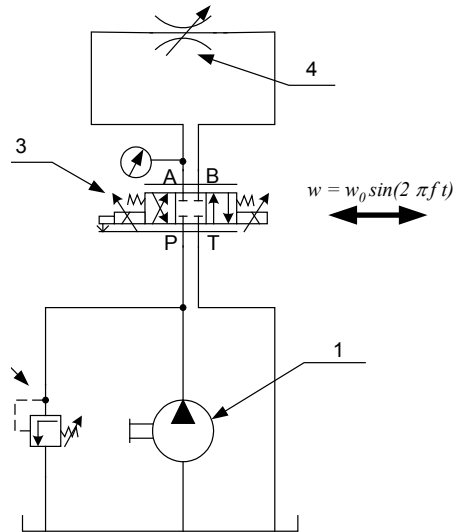

Fig. 2. Scheme of hydraulic system incorporating investigated component: 1 – feed pump,
2 – relief valve, 3 – investigated component, 4 – adjustable throttle valve

For a two-mass system the model of the proportional distributor operating in the hydraulic system shown in Figure 2 can be represented by the following system of four equations:

$$
\begin{cases}
m_1 \cdot \ddot{X}_1 + \pi \cdot d_t \cdot \dfrac{l}{h} \cdot \mu \cdot \left(\dot{X}_1 - \dot{X}_2\right) + 0.72 \cdot \dfrac{1}{\sqrt{\xi}} \cdot 2 \cdot s_s \cdot \dfrac{\left(X_1 - x_p\right)^2}{x_m} \cdot \left(p_1 - p_2\right) + \\[2mm]
\quad + c_1 \cdot \left(X_1 - X_2\right) = F_M, \\[2mm]
Q_p - 1.5 \cdot s_s \cdot \dfrac{\left(X_1 - x_p\right)^2}{x_m} \cdot \sqrt{\dfrac{2}{\rho} \cdot \left(p_1 - p_2\right)} - a_{p1} \cdot p_1 - c_{k1} \cdot \dot{p}_1 = 0, \\[2mm]
Q_p - a_{p1} \cdot p_1 - c_{k1} \cdot \dot{p}_1 - c_{k2} \cdot \dot{p}_2 - C_{q1} \cdot A_a \cdot \sqrt{\dfrac{2 \cdot p_2}{\rho}} = 0, \\[2mm]
m_2 \cdot \ddot{X}_2 + c_1 \cdot \left(X_2 - X_1\right) + k_1 \cdot \left(\dot{X}_2 - \dot{X}_1\right) + c_z \cdot \left(X_2 - w\right) + \\[2mm]
\quad + m_2 \cdot \mu_2 \cdot g \cdot \left(1 - H\left(l_0 - |X_2 - w|\right)\right) \cdot sing\left(\dot{X}_2 - \dot{w}\right) + \\[2mm]
\quad + sing\left(\dot{X}_2 - \dot{w}\right) \cdot m_2 \cdot \mu i \cdot g = 0.
\end{cases}
\tag{1}
$$

The fourth equation describes the forces acting on the valve housing in the considered case. Further on this equation will be modified to describe the characteristics of the proposed vibration insulation elements. Some simplifying assumptions to Equations (1):

- working liquid does not change its properties,
- Coulomb friction is neglected in pair: spool-muff inside directional control valve,
- Coulomb friction represents cooperation between valve body and valve holder,
- after play (between valve body and securing catches) is cancelled Coulomb friction represents cooperation between valve body and securing catches,
- springs characteristics are linear and described by stiffness coefficient c,
- description of hydraulic system is based on concentrated parameter model,
- the model does not represent influence pipes on valve body vibrations.

List of major symbols:

Symbol	Parameter	Dimension in SI
a_{p1}	leakage coefficient	[m^{4}s/kg]
A_a	throttle valve gap area	[m^2]
c_1	equivalent stiffness of valve centring springs	[N/m]
c_z	equivalent stiffness of springs fixing valve in holder	[N/m]
C_{q1}	throttle valve flow ratio	[–]
d_t	piston diameter	[m]
f	frequency	[Hz]
g	Earth's acceleration	[m/s^2]
h	valve-sleeve pair gap thickness	[m]
H	Heaviside step function	[–]
k_1, k_2	damping in respectively valve-sleeve pair and housing-holder pair	[Ns/m]
l	piston length	[m]
l_0	gap of valve body and securing catches	[m]
m_1	mass of piston valve and 1/3 of spring mass	[kg]
m_2	mass of distributor housing	[kg]
p_1	pressure before distributor	[Pa]
p_2	pressure after distributor	[Pa]
p_z	sink line pressure	[Pa]
Δp_2	throttle valve pressure drop	[Pa]
s_s	maximum gap width	[m]
t	time	[s]
w	excitation vibration amplitude	[m]
Q_p	theoretical pump delivery	[m^3/s]
x_m	gap length	[m]
x_p	mutual shift of valve and housing edges	[m]
X_1	displacement of piston valve	[m]
X_2	displacement of distributor housing	[m]
$\mu2$	coefficient of friction of valve housing against securing catches	[–]
μi	coefficient of friction of valve housing against holder base	[–]
ρ	working liquid density	[kg/m^3]
ω	angular frequency	[rad/s]

Model (1) also takes into account the interaction between the valve housing and securing catches 5 (Figure 1). A numerical solution in the form of a "transmission function", understood as a ratio of valve housing vibration acceleration amplitude a_2 to excitation vibration acceleration amplitude a_0, is shown in Figure 3.
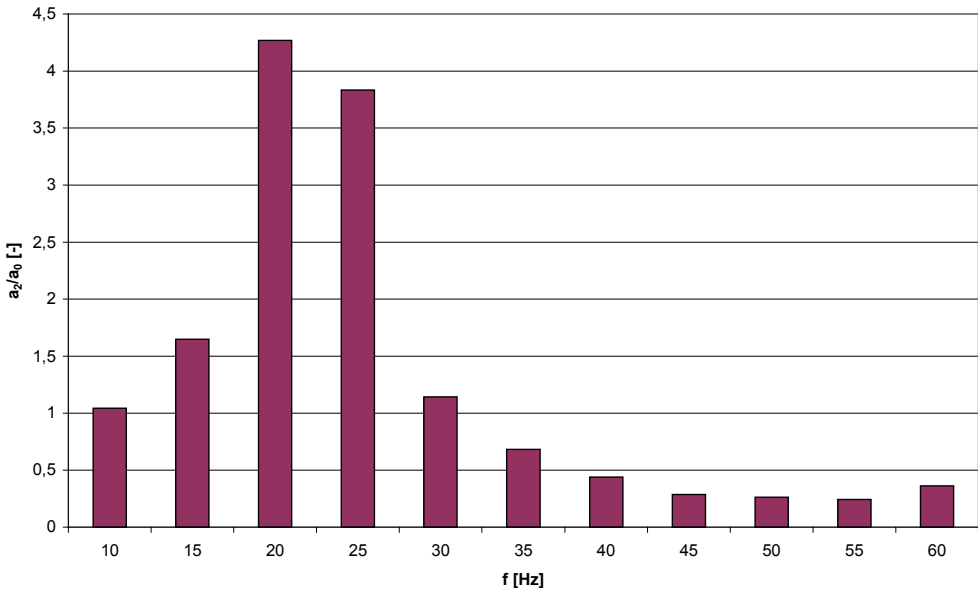

Fig. 3. Proportional distributor housing vibration acceleration amplitude a_2 relative
to excitation vibration acceleration amplitude a_0 for $f = 10–60$ Hz

An analysis of the simulation results shows a considerable gain in housing vibration amplitude at a frequency of about 20 Hz. This is due to resonance since the mass of the vibrating valve amounts to about 4.5 kg and the equivalent stiffness of the holder springs is 86 000 N/m. Hence a gain in distributor housing vibration amplitude is observed in the range of 10–30 Hz (ineffective vibration insulation).

This means that valve insulation which will widen the insulation zone and reduce the resonance zone should be proposed. The black-box approach (Figure 4) was adopted to solve the problem.

Different forms of the insulating element can be assumed. The introduction of a vibration insulator with quasi-zero stiffness significantly contributes to the minimization of valve housing vibrations. The ideal characteristic of the vibration insulator with quasi-zero stiffness is described by the following Equation [13]:

$$F(x) = P_{1H} + c_{1w}l_H \sin \alpha_H + (c_{1w} + 2c_{2w})x - 2(P_{2H} + c_{2w}l_H)\frac{x}{\sqrt{x^2 + l_H^2 \cos^2 \alpha_H}}, \qquad (2)$$

where:

c_{1w}, c_{2w} – stiffness of respectively the main spring and the compensation spring,

α_H – angle of initial, original inclination of the side arm to axis y,

P_{1H}, P_{2H} – initial spring tensions in position α_H [N],

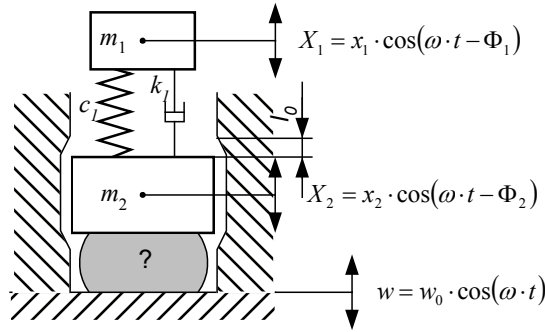l_H – length of the side arm in position α_H.

Fig. 4. Black-box approach to valve vibration insulation

The total stiffness of such a vibration insulator in the excitation direction (the direction of the external mechanical vibration) is:

$$c(x) = c_{1w} + 2c_{2w} - \frac{2(P_{2H} + c_{2w}l_H)}{\sqrt{x^2 + l_H^2 \cos^2 \alpha_H}} \left(\frac{l_H^2 \cos^2 \alpha_H}{x^2 + l_H^2 \cos^2 \alpha_H} \right). \tag{3}$$

Thus the fourth equation of model (1) can be written as:

$$m_2 \cdot \ddot{X}_2 + c_1 \cdot (X_2 - X_1) + k_1 \cdot (\dot{X}_2 - \dot{X}_1) +$$
$$+ \left(c_{1w} + 2c_{2w} - \frac{2(P_{2H} + c_{2w}l_H)}{\sqrt{X_2^2 + l_H^2 \cos^2 \alpha_H}} \left(\frac{l_H^2 \cos^2 \alpha_H}{X_2^2 + l_H^2 \cos^2 \alpha_H} \right) \right) \cdot (X_2 - w) = 0. \tag{4}$$

Exemplary solutions of model (1) supplemented with Equation (4) are shown in the figures below for excitation frequency $f = 10–60$ Hz.

An analysis of the simulation results shows that thanks to the use of the vibration insulator with quasi-zero stiffness the vibration of the valve housing can be considerably reduced. However, because of its dimensions such an insulator cannot be used in small spaces. Therefore materials with good vibration insulation properties and suitable for the use in small spaces should be sought. It seems that special pads (mats) for mounting hydraulic valves on them could meet the requirements. Such materials should also be resistant to hydraulic fluids and extreme ambient temperatures. Using the

black-box approach one can select an insulator material characteristic ensuring effective vibration insulation in a wide excitation range.
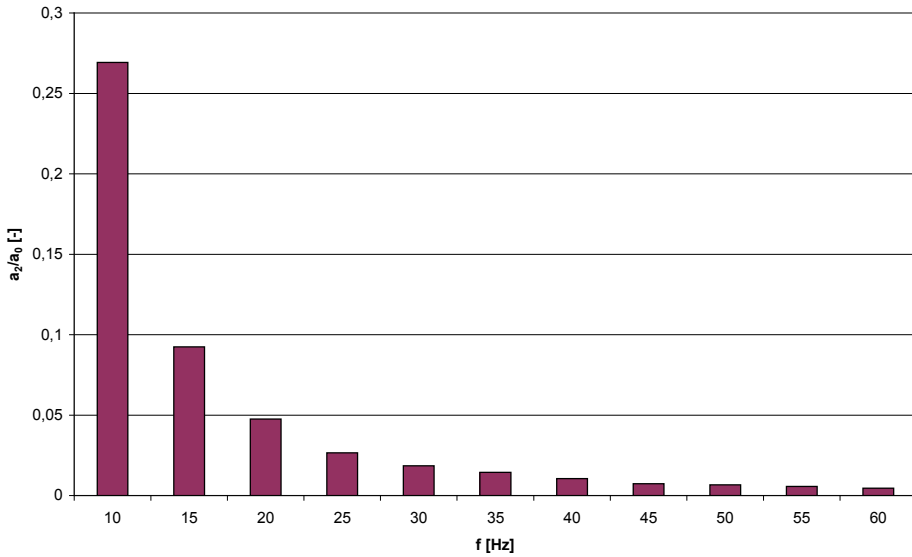

Fig. 5. Proportional distributor housing vibration acceleration amplitude a_2 relative to excitation vibration acceleration amplitude a_0 for $f = 10–60$ Hz
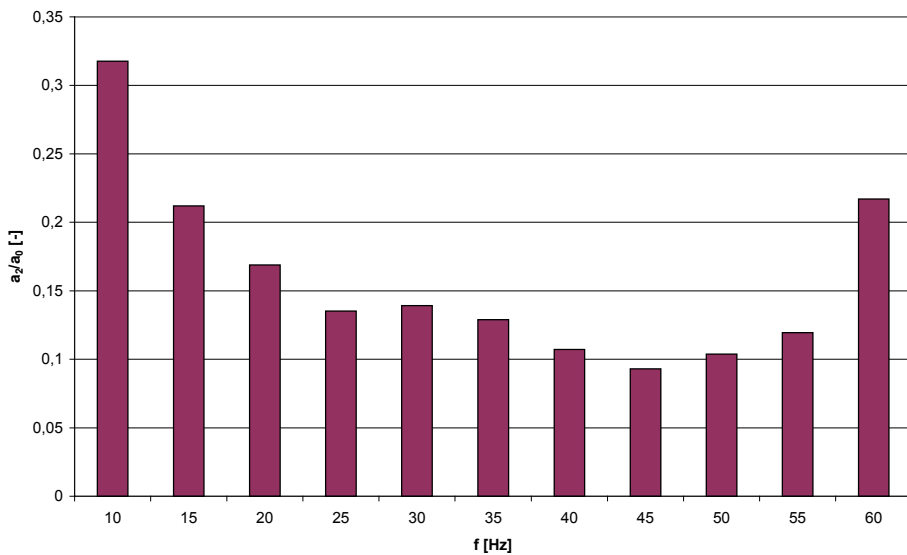

Fig. 6. Proportional distributor housing vibration acceleration amplitude a_2 relative to excitation vibration acceleration amplitude a_0 for $f = 10–60$ Hz

The results of the application of a vibration insulator with characteristic $c_2 \cdot x^2 + k_2 \cdot \dot{x}$ and $c_2 = 20\ 000$ N/m and $k_2 = 50$ Ns/m are shown in Figure 6. In this case, the fourth equation of model (1) should be supplemented with a nonlinear vibration insulator characteristic.

When a vibration insulator with a nonlinear damping characteristic ($k_2 = 250$ Ns/m) and linear stiffness ($c_2 = 20\ 000$ N/m) $c_2 \cdot x + k_2 \cdot \dot{x}^2$ is used to insulate base vibrations the valve housing vibrations are as shown in Figure 7.
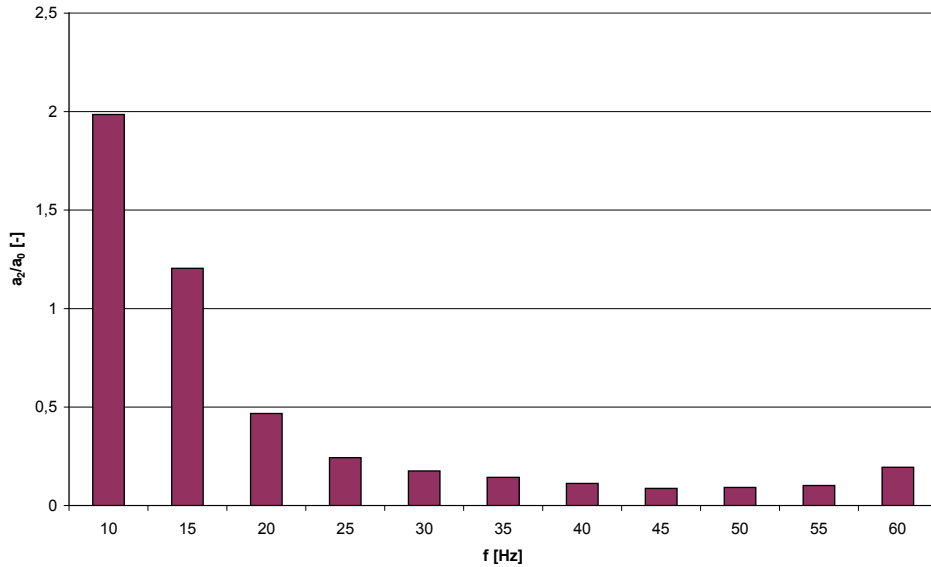

Fig. 7. Proportional distributor housing vibration acceleration amplitude a_2 relative to excitation vibration acceleration amplitude a_0 for $f = 10$–60 Hz

Figures 5 and 6 show that such a nonlinear vibration insulator characteristic can be selected that the insulation will be effective in the whole considered excitation frequency range.

The problem of influence of mechanical vibrations on valve was considered in theoretical and experimental way. Theoretical considerations were based on numerical calculations according to mathematical model. For some theoretical considerations experimental tests were done using test stand (hydraulic simulator, valve holder, spring set).

3. Experimental tests

A test rig enabling the generation of mechanical vibrations characterized by a prescribed frequency was built to experimentally verify the theoretical results and conclu-

sions. The investigated valve – Mannesmann-Rexroth proportional distributor type 4WRE 6 E08-12/24Z4/M – fixed in the holder was mounted on the test rig and subjected to external mechanical vibrations (photo 1). Tests were done without pipes connected to valve.

A linear hydrostatic drive simulator Hydropax ZY25 made by Mannesmann-Rexroth, capable of generating vibrations up to 100 Hz, was the source of external mechanical vibrations. Main component of simulator of linear hydrostatic drive is servo valve which controls hydraulic cylinder. The simulator consists three main parts: hydraulic part, control part and control software. Displacement of simulator table is controlled by displacement transducer and its acceleration is controlled by accelerometer. On simulator table the tested valve was mounted. Electrical control signal for simulator was supported by external harmonic signal generator. The simulator is described in more detail in [4]. The proportional distributor was placed in the special holder and bilaterally supported with springs (there were two springs connected in parallel on each of the sides). Preliminary tests were carried out for springs with an equivalent stiffness of 86 000 N/m and a pre-deflection of 2 mm. The external excitation parameters are shown in Table 2.

Photo 1. Proportional distributor placed in special holder and bilaterally
supported with springs, during testing

Table 2. Amplitude of vibrations acting on tested hydraulic distributor

f [Hz]	w_0 [m]
30	0.000483
35	0.000406
40	0.000366
45	0.000269
50	0.000214
55	0.000145
60	0.0000522

Figure 8 shows an overall valve vibration diagram for the external excitation, i.e. a ratio of proportional distributor housing acceleration amplitude a_2 to excitation vibration amplitude a_0 versus a frequency of 25–60 Hz.

It appears from the diagram shown in Figure 8 that for a system of springs with equivalent stiffness $c_z = 86\,000$ N/m and a proportional distributor with a mass of 4.5 kg the vibration insulation is effective (transmission function $a_2/a_0 < 1$) in the given external vibration frequency range. As a result of the insulation, the distributor housing vibration amplitude and the distributor slide-valve vibration amplitude decrease [5]. Consequently, the amplitude of the pressure fluctuations due to the excitation of distributor slide-valve vibrations also decreases. However, in the case of so simple vibration insulation, resonance may be generated at external vibration frequencies other than the ones used in the test. Therefore, as Figures 5 and 6 indicate, a vibration insulation element with other properties and characteristics, e.g. with nonlinear stiffness and with damping, should be used.
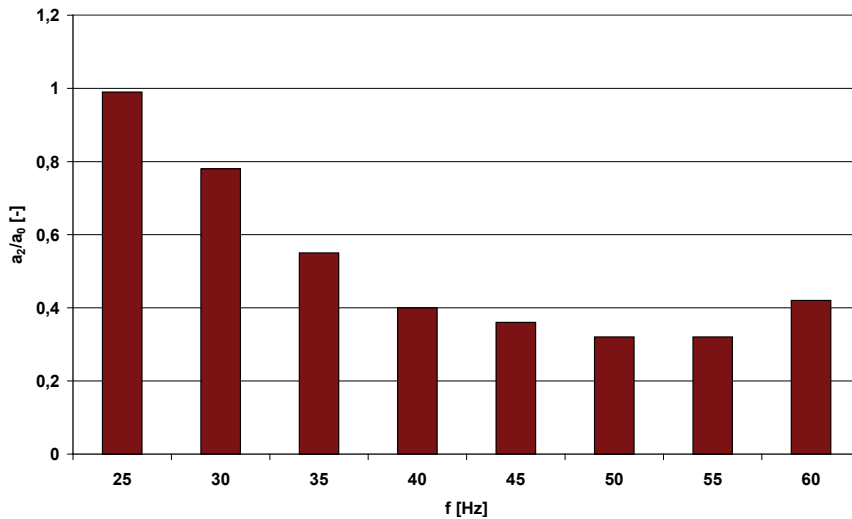

Fig. 8. Proportional distributor housing vibration acceleration amplitude a_2 relative to excitation vibration acceleration amplitude a_0 for $f = 25-60$ Hz

4. Conclusion

It has been shown that there is a need to reduce the vibration of the hydraulic valves with which machine tools and mobile machines are commonly equipped. The use of vibration insulators in the form of springs whose characteristics are linear results in a reduction in valve housing vibration acceleration amplitude at certain external vibration frequencies, but it may be conducive to resonance at other frequencies. Comparison of results presented on Figure 3 and Figure 8 shows, that differences between model and test are not great for frequency range 35–60 Hz. The biggest differences are observed in resonant area (25 Hz). It follows from the presented cases of vibration insulation (Figures 5–8) that materials with linear charac-

teristics should be used in order to extend the range of effective vibration insulation. Thanks to the use of a vibration insulator with a nonlinear characteristic the valve housing vibration acceleration amplitude was reduced by a few tens of percent: by over 90% for the vibration insulator with quasi-zero stiffness and by about 80% for the vibration insulator whose stiffness or damping was proportional to displacement or velocity to the second power. A reduction in valve housing vibration will lead to a reduction in slide-valve vibration, particularly in the resonant vibration range. As a result, the pressure fluctuations and the emitted noise (particularly in a low frequency range) will decrease and the precision of the motions of the hydraulic receivers will increase. Vibration insulators in such applications should also satisfy other criteria, such as: resistance to changes in ambient temperature, resistance to hydraulic fluids, and small geometric dimensions. Therefore, besides having proper physicochemical properties, a vibration insulator should have a standardized design suitable for typical connection plates for hydraulic valves.

References

[1] Lisowski E., Szewczyk K.: *Theoretical determination of multi-piston axial-flow pump delivery fluctuations* (in Polish), Sterowanie i Napęd Hydrauliczny, No. 1, 1984, pp. 3–6.

[2] Kudźma Z.: *Frequency of the free vibration of a relief valve and a hydraulic system* (in Polish), Sterowanie i Napęd Hydrauliczny, No. 3, 1990, pp. 27–30.

[3] Amini A., Owen I.: *A practical solution to the problem of noise and vibration in a pressure-reducing valve*, Experimental Thermal and Fluid Science, No. 10, 1995, pp. 136–141.

[4] Misra A., Behdinan K., Cleghorn W.L.: *Self-excited vibration of a control valve due to fluid-structure interaction*, Journal of Fluids and Structures, Vol. 16, No. 5, 2002, pp. 649–665.

[5] Stosiak M.: *The effect of the low-frequency mechanical vibrations of the base on the control component of the hydraulic valve* (in Polish), [in:] *Rozwój maszyn i urządzeń hydraulicznych*, Edit. Wacław Kollek, Wrocław, Wydaw. Wroc. Rady FSNT NOT, Vol. 11, No. 2–3, 2006, pp. 83–94.

[6] Stosiak M.: *An influence of mechanical vibrations of ground for pressure pulsation in hydraulic system* (in Polish), Hydraulika i Pneumatyka, No. 3, 2006, pp. 5–8.

[7] Engel Z.: *Protection of the environment against vibrations and noise* (in Polish), Wydawnictwo Naukowe PWN, Warsaw, 2001.

[8] Leea E.C., Nianb C.Y., Tarng Y.S.: *Design of a dynamic vibration absorber against vibrations in turning operations*, Journal of Materials Processing Technology, Vol. 108, 2001, pp. 278–285.

[9] Grajnert J.: *Vibration insulation in machines and vehicles* (in Polish), Oficyna Wydawnicza Politechniki Wrocławskiej, Wrocław, 1997.

[10] Pytlik A.: *Vibrations in hydraulic systems of mechanized casing section* (in Polish), Napędy i Sterowanie, Vol. 10, No. 4, 2008, pp. 121–130.

[11] Krylov V., Pickup S., McNuff J.: *Calculation of ground vibration spectra from heavy military vehicles*, Journal of Sound and Vibration, Vol. 329, No. 115, 2010, pp. 3020–3029.

[12] Kollek W., Kudźma Z., Maga K., Stosiak M.: *Disturbances in the operation of proportionally controlled hydrostatic systems* (in Polish), Napędy i Sterowanie, Vol. 6, No. 5, 2004, pp. 53–57.

[13] Joint publication edited by Świder J., Kazimierczak J.: *Computer-aided design of machine vibration and noise reducing systems* (in Polish), WNT, Warsaw, 2001.

Wibroizolacja elementów sterujących układów hydraulicznych

W artykule skupiono się na problemie oddziaływania zewnętrznych drgań mechanicznych na zawory hydrauliczne. Omówiono skutki tych oddziaływań. Przeprowadzono analizę teoretyczną wpływu charakterystyki wybranych izolatorów na redukcję drgań korpusu zaworu hydraulicznego. Przedstawiono wstępne badania eksperymentalne dla prostych przykładów izolatorów.

The effectiveness of CFRP materials strengthening
of eccentrically compressed reinforced concrete columns

T. TRAPKO, M. MUSIAŁ

Wrocław University of Technology, Wybrzeże Wyspiańskiego 25, 50-370 Wrocław, Poland.

In the paper the investigations of load-bearing capacity of eccentrically compressed reinforced concrete columns strengthened with CFRP strips and sheets are presented. The aim of the conducted researches was to estimate the influence of changeable longitudinal CFRP reinforcement intensity on load-bearing capacity of columns. In the experimental investigations three longitudinal CFRP strengthening intensities were applied – 2.10%, 1.68% and 1.26%. The experimental tests were performed on columns models with cross-section of 200×200 mm and height of 1 500 mm. The investigative members were loaded axially or eccentrically. The eccentric force was exerted in the area of cross-section core (h/12 and h/6 from neutral axis).

In the paper the results of experimental studies on load-bearing capacity depending on longitudinal strengthening intensity were presented and discussed. The failure mechanisms were described. The values of failure force and maximum longitudinal strain were given.

The application of longitudinal CFRP strips (as external composite strengthening) causes the increase of column rigidity. Additional transverse strengthening implies delay in debonding the strips from concrete. The interaction of both CFRP materials entails the reduction of strains increase velocity which transfers to the increase of load-bearing capacity.

Keywords: *CFRP, columns, eccentric compression, strain, strengthening*

1. Introduction

The method of strengthening of reinforced concrete structures with FRP composite materials is more and more popular in engineering practice. Benefits of the applying additional FRP composite reinforcement are generally known. This strengthening technology is being used for bending, shearing and compressed members.

The confining of columns with external FRP composite jacket is the equivalent for applying steel spiral rebars as internal transverse reinforcement. The confining causes three-axial state of stress in cross-section of compressed members and reduces the increase of transverse strains as well. Fundamental difference between members confined with internal steel spiral and external FRP jacket is that in case of composite reinforcement the whole cross-section is strengthened and composite material works elastically till failure, whereas in case of the steel spiral reinforcement the confinement concerns only the core of cross-section. Moreover, when stress in steel reaches a yield strength strains increase under constant level of load.

In recent decades it was proved that crucial factors in identifying the level of strengthening of compressed members are: the number of FRP reinforcement layers, the shape of cross-section and the type of composite sheet [1−5, 13, 15]. The most beneficial results of strengthening were observed in case of cylindrical specimens confined with CFRP sheet for several times. Less spectacular effects were received for quadrangular cross-sections − square and rectangular. In both cases the level of strengthening depends on the radius of corner rounding. However, in practice it is difficult to round corners with high radius in strengthening column with quadrangular cross-section. Very often it is possible only to chamfer concrete cover in the corner (with dimension of 10−20 mm).

In case of quadrangular members the investigations of strengthening technologies with longitudinal CFRP reinforcement has been started. On the basis of the own researches results [6−12, 16−18] it was proved that strengthening with longitudinal CFRP strip segments causes the increase of column rigidity. It is revealed with the limitation of longitudinal strains in strengthened elements in relation to control elements (without strengthening). The velocity of strains increase depends on the longitudinal strengthening intensity, whereas it does not depend on the way of constructing of transverse strengthening. The influence of transverse strengthening in the form of CFRP bands (arranged similar as steel stirrups) and in the form of continuous confinement with CFRP sheet was analyzed in own studies. It was found that strengthening only with CFRP strips is disadvantageous. The fibres of strip are directed parallel to the axis of the column. It causes debonding of composite and concrete. The longitudinal external strengthening should be supported with transverse reinforcement to prevent from delamination of composite.

2. Experimental studies

2.1. Purpose and programme of study

The objective of the preformed investigations was to estimate the influence of three longitudinal strengthening intensities ρL on load-bearing capacity and strains of eccentrically compressed members strengthened with CFRP strips and sheets. The longitudinal strengthening intensity ρL was described as the ratio of the area of CFRP strip A_L to the area of concrete A_c.

In the experiment three intensities of strengthening ρ_L were applied: 2.10%, 1.68% and 1.26%. As the transverse strengthening a single continuous confinement executed with CFRP sheet was taken.

The investigation was conducted with eccentricity of load in the core of cross-section: h/12 and h/6. The axially compressed columns were tested for comparison.

To reach stated purposes nine strengthened elements were executed and tested. Additionally, three control (unstrengthened) specimens were investigated. The investigative programme was listed in the Table 1.

Table 1. Investigative programme

Strengthening type	Eccentricity of force		
Unstrengthened	0	h/6	h/12
Strengthening intensity ρ_L = 1.26% Transverse strengthening – single continuous CFRP jacket	0	h/6	h/12
Strengthening intensity ρ_L = 1.68% Transverse strengthening – single continuous CFRP jacket	0	h/6	h/12
Strengthening intensity ρ_L = 2.10% Transverse strengthening – single continuous CFRP jacket	0	h/6	h/12

2.1. Investigative elements

The investigations were conducted on the models of columns. The dimensions of cross-section were 200×200 mm and height was of 1 500 mm (Figure 1). The longitudinal steel reinforcement was four bars ∅12, a steel grade was A-IIIN (B500SP) [14], the transverse steel reinforcement was stirrups ∅6, a steel grade A-I (St0S) [14].
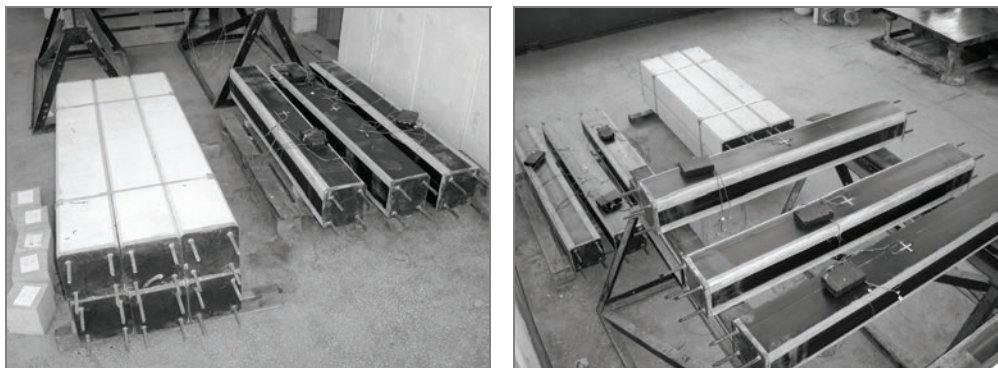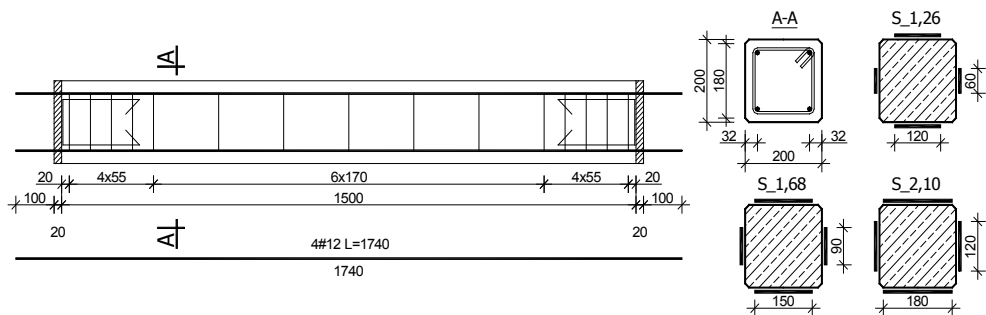

Fig. 1. Performed specimens

The distance between the stirrups was reduced to 1/3 of the main distance at the ends of the elements (Figure 1). The parts of the columns with the reduced stirrups base were the length of 250 mm. The stirrups were provided with semicircular hooks

as bonds and tied on the longitudinal bars. Each stirrup was rotated in relation to the previous one with angle of 90°. The edges of the specimens were chamfered with dimensions 10×10 mm.

The columns were provided with steel frontal plates to guarantee the surfaces of load being parallel. The longitudinal internal reinforcement was passed through the plates. It was welded to the plates and cut off before the investigations. The way of construction of the ends of the columns assured equal load of concrete and steel reinforcement. Moreover, it prevented the longitudinal steel bars from pushing into the concrete. In the investigations the anchorages of the transverse sheets was executed as 70 mm overlap. Each overlap of the sheet (300 mm width) was rotated in relation to the previous one with angle of 90°.

2.2. Properties of materials

Ten concrete cubes with dimensions of 150×150×150 mm were performed from the same batch of concrete mixture as main investigative elements. Described specimens and columns were consolidated with internal vibrator in the same way. After two days they were pulled out from forms and kept in the same constant environmental conditions as the investigative elements. The day before the beginning of experimental studies the mean compressive strength was estimated $f_{cm,\text{cube}} = 31.9$ MPa.

The longitudinal steel reinforcement was made of steel with yield strength of $f_y = 608$ MPa, tensile strength of $f_t = 704$ MPa and modulus of elasticity of $E_s = 224$ MPa.

The strengthening of the investigative elements was performed with CFRP strip and sheet. The CFRP strips were arranged as in the scheme shown in Figure 1 (along the columns' axes).

Table 2. Strength properties of CFRP materials

Property	Own investigations	Given by producers
	CFRP sheet	
Tensile strength [MPa]	2 937	3 500
Modulus of elasticity [MPa]	237 000	230 000
Ultimate tensile strain [%]	1.11	1.50
	CFRP strip	
Tensile strength [MPa]	3 468	> 2 400
Modulus of elasticity in tension test [MPa]	228 227	> 210 000
Modulus of elasticity in compression test [MPa]	230 410	–
Ultimate tensile strain [%]	1.37	> 1.2

Strength parameters were taken from the own investigations described in the paper [8, 18]. The investigative procedures determining tensile strength and modulus of elasticity of CFRP strip and sheets were described there as well. Table 2 shows the comparison of data resulted from the own investigations and given by producers.
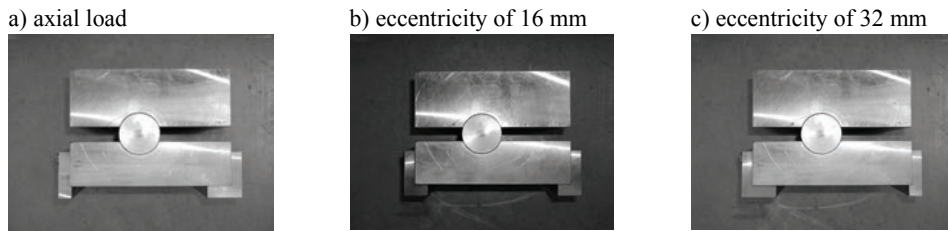
a) axial load

b) eccentricity of 16 mm

c) eccentricity of 32 mm

Fig. 2. Cylindrical bearing used in the experiment

2.3. Investigations methodology

A cylindrical bearing was designed and performed to apply load. Different eccentricities were applied with the bearing: axial load (Figure 2a), eccentricity of $h/12 = 16$ mm (Figure 2b) and eccentricity of $h/6 = 32$ mm – force on the boundary of the core (Figure 2c). In each load step following values were measured:

1) longitudinal strains ε_{cv} and transverse strains ε_{ch} of concrete with electrical resistance strain gauge rosettes attached at mid-height on two sides of column,

2) longitudinal strains ε_{Lv} and transverse strains ε_{Lh} of CFRP strips with electrical resistance strain gauge rosettes attached at mid-height on the surfaces of the strips on two sides of column,

3) longitudinal strains ε_{wv} and transverse strains ε_{wh} of CFRP sheets with electrical resistance strain gauge rosettes attached at the middle part of column.

The results were registered with PC and measuring system UPM 100 made by Hottinger Baldwin Messtechnik. Loads were applied with a pneumatic press with range of 0−6000 kN (Figure 3). Experimental investigations were carried out in Building Engineering Institute Laboratory of Wroclaw University of Technology.

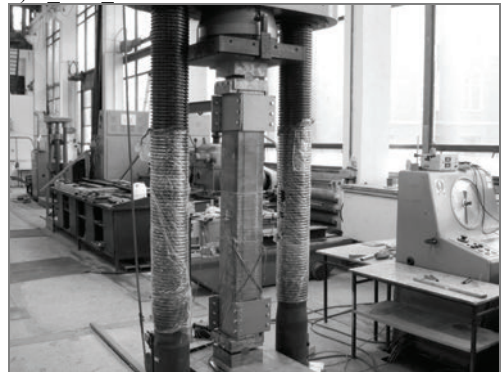a) S_1.68_16
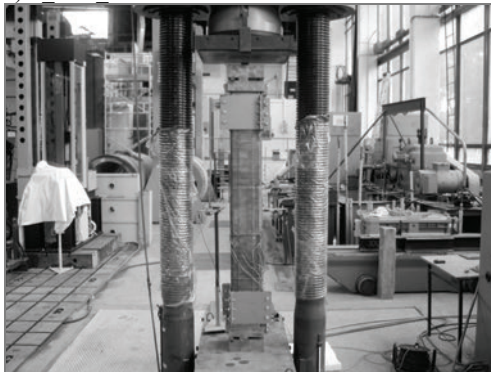
b) S_1.68_32

Fig. 3. Columns in experimental set-up

The support zones, where load application causes significant stress concentration, external reinforcement – screwed steel bands, 200 mm high (Figures 3 and 4) was added. They eliminated the risk of failure caused with local pressure.

3. Tests results and discussion

3.1. Observed behaviour and failure mechanisms

The aim of destructive testing was to determine following values:

1) load-bearing capacity of columns N_u, (destructive force registered during the compression test),

2) ultimate longitudinal strains $\varepsilon_{v2,\lim}$ and $\varepsilon_{v1,\lim}$, at the more compressed and less compressed (tensioned) side of the cross-section,

Furthermore, the failure mechanisms were described.

Table 3. Tests results

	Column symbol	N_u [kN]	$\varepsilon_{v2,\lim}$ [‰]	$\varepsilon_{v1,\lim}$ [‰]	Failure mechanism
1	S_0_0	1548	−2.152	−1.760	Crush of concrete in the upper part and yielding of longitudinal steel reinforcement
2	S_0_16	1386	−3.108	−0.988	Crush of concrete in the upper part at the more compressed side and yielding of longitudinal steel reinforcement (Figure 5a)
3	S_0_32	1098	−2.953	0.688	Crush of concrete in the middle part at the more compressed side and yielding of longitudinal steel reinforcement
4	S_1.26_0	1943	−1.663	−1.940	Rupture of CFRP sheet jacket at the edges of column and crush of concrete in the lower part, crush and debonding of concrete cover and CFRP strip in the area of failure, yielding of longitudinal steel reinforcement
5	S_1.26_16	1814	− 2.180	−1.098	Rupture of CFRP sheet jacket at the edges of column and crush of concrete in the lower part at the more compressed side, crush and debonding of concrete cover and CFRP strip in the area of failure
6	S_1.26_32	1578	−2.772	0.248	Rupture of CFRP sheet jacket at the edges of column and crush of concrete in the upper part at the more compressed side, crush and debonding of concrete cover and CFRP strip in the area of failure, yielding of longitudinal steel reinforcement (Figure 4a)
7	S_1.68_0	2051	−1.582	−1.574	Rupture of CFRP sheet jacket at the edges of column and crush of concrete in the upper part, crush and debonding of concrete cover and CFRP strip in the area of failure, yielding of longitudinal steel reinforcement

8	S_1.68_16 S_1.68_16 (Fig. 3a)	1895	−1.776	−0.836	Rupture of CFRP sheet jacket at the edges of column and crush of concrete in the lower part at the more compressed side, crush and debonding of concrete cover and CFRP strip in the area of failure, yielding of longitudinal steel reinforcement (Figure 5b)
9	S_1.68_32 (Fig. 3b)	1648	−2.451	0.074	Rupture of CFRP sheet jacket at the edges of column and crush of concrete in the upper part at the more compressed side, crush and debonding of concrete cover and CFRP strip in the area of failure, yielding of longitudinal steel reinforcement
10	S_2.10_0	2246	−1.643	−1.850	Rupture of CFRP sheet jacket at the edges of column and crush of concrete in the upper part, crush and debonding of concrete cover and CFRP strip in the area of failure, yielding of longitudinal steel reinforcement
11	S_2.10_16	2047	−1.954	−1.123	Rupture of CFRP sheet jacket at the edges of column and crush of concrete in the upper part at the more compressed side, crush and debonding of concrete cover and CFRP strip in the area of failure, yielding of longitudinal steel reinforcement
12	S_2.10_32	1760	−1.984	−0.045	Rupture of CFRP sheet jacket at the edges of column and crush of concrete in the upper part at the more compressed side, crush and debonding of concrete cover and CFRP strip in the area of failure, yielding of longitudinal steel reinforcement (Figure 4b)
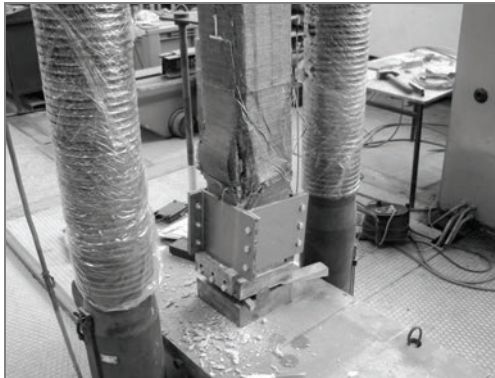
a) S_1.68_16   b) S_2.10_32

Fig. 4. Failure of column S_1.68_16 and S_2.10_32

All of the strengthened columns underwent damage in the same way, by the rupture of CFRP sheet at the edge of column. The rupture of CFRP sheet was preceded by sound of carbon fibres fracture.

In the area of failure concrete underwent crush and fragmentation. The CFRP strips were rumpled there (Figure 4). In each column, except for S_1.26_16, the yielding of longitudinal steel reinforcement was observed (Figure 4b).

In case of column S_1.68_32 the rupture of some fibres of CFRP sheet was noticed by the load near the capacity N_u. The rupture had occurred at the less compressed side of the column. For the column S_1.68_32 the stress redistribution in cross-section was registered (Figure 5).

The differences between the values of limit longitudinal strains $\varepsilon_{v2,\lim}$ i $\varepsilon_{v1,\lim}$ in axially compressed columns should be attributed to accidental (unintended) eccentricities. The specimens were executed in horizontal position, which caused concrete non-homogeneity in process of vertical loading. Moreover, the accidental eccentricities could be introduced by faults in load application and arrangement of steel reinforcement despite of providing with the steel frontal plates.
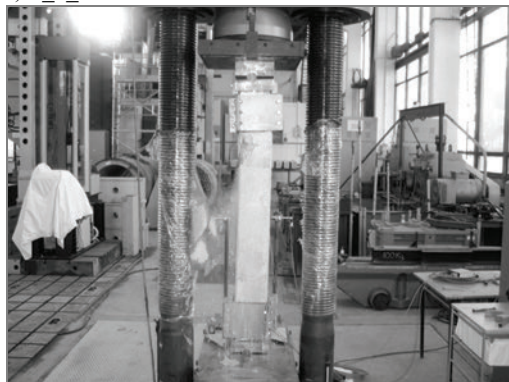
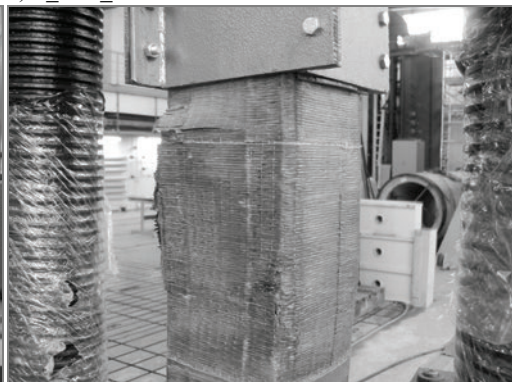a) S_0_16   b) S_1.68_32

Fig. 5. Failure of column S_0_16 i S_1.68_32

The differences between the values of limit longitudinal strains $\varepsilon_{v2,\lim}$ i $\varepsilon_{v1,\lim}$ in axially compressed columns should be attributed to accidental (unintended) eccentricities. The specimens were executed in horizontal position, which caused concrete non-homogeneity in process of vertical loading. Moreover, the accidental eccentricities could be introduced by faults in load application and arrangement of steel reinforcement despite of providing with the steel frontal plates.

The load-bearing capacity of strengthened columns N_u in function of the eccentricity of longitudinal force shows the diagram below (Figure 6). It can be seen in the diagram that applied longitudinal CFRP strips implied constant and regular increase of load-bearing capacity N_u, irrespective of eccentricity of longitudinal load in relation to control columns (without strengthening).

In Figure 7 and in the Table 4 the relative increase ($\Delta N_u/N_{u,S0i}$) of load-bearing capacity of strengthened column $\Delta N_u = N_{u,S\rho Li} - N_{u,S\_0\_i}$ in relation to capacity of respec-

tive control column $N_{u,S0i}$ depending on eccentricity of load ("*i*" – index corresponds to following eccentricity).
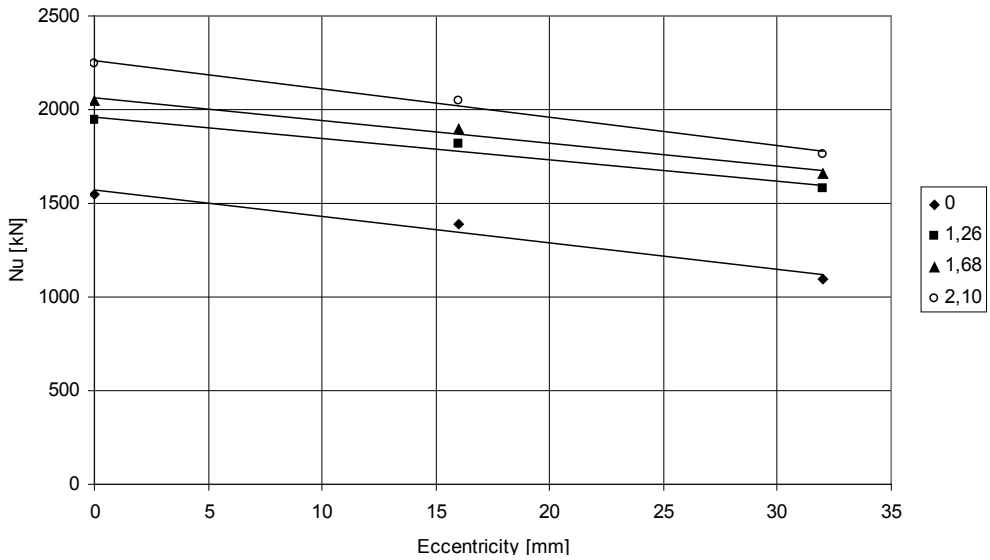

Fig. 6. Load-bearing capacity of the strengthened columns versus eccentricity
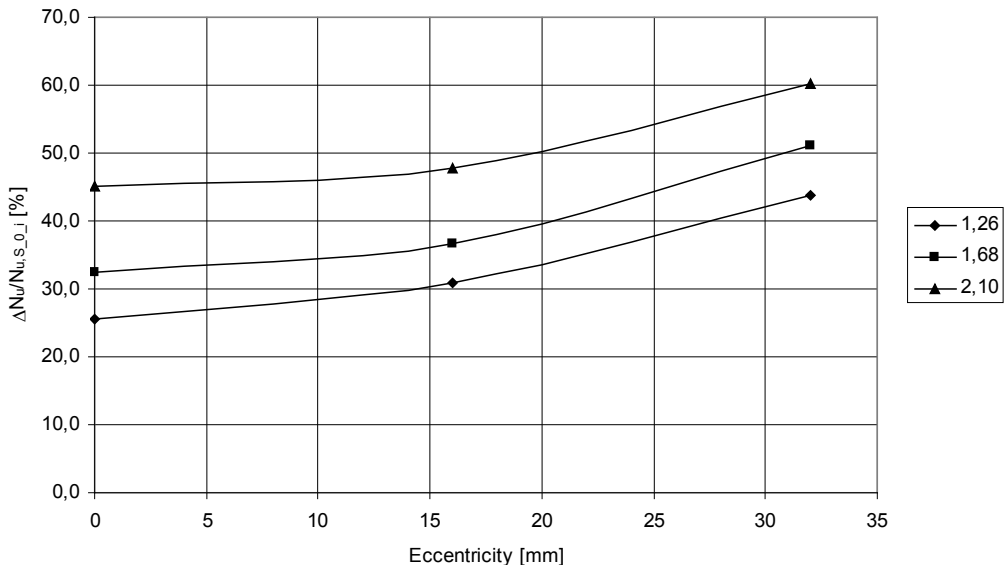

Fig. 7. Relative increase of load-bearing capacity of strengthened columns
in relation to control columns versus eccentricity

Table 4. Relative increase of load-bearing capacity [%]

Eccentricity [mm]	$\rho_L = 1.26\%$	$\rho_L = 1.68\%$	$\rho_L = 2.10\%$
0	25.52	32.49	45.09
16	30.88	36.72	47.69
32	43.72	51.00	60.29

According to the Figure 7 and Table 4 it was claimed that the increase of the eccentricity of load is associated with the increase of the load-bearing capacity $N_{u,S\rho Li}$ in relation to the capacity of analogous members without strengthening $N_{u,S0i}$. The level of utilization of the longitudinal CFRP strengthening is increasing with the increase of the eccentricity of load. The relative difference between the capacity of the columns loaded with eccentricity of 16 mm and the capacity of columns loaded axially is ~3−5%. Whereas the capacity of the columns loaded with eccentricity of 32 mm was ~12−14% higher than the capacity of the columns loaded with eccentricity of 16 mm. Significantly, the most advantageous results of the capacity increase were observed in case of the columns compressed with the eccentricity of load at the boundary of the core (h/6 = 32 mm).
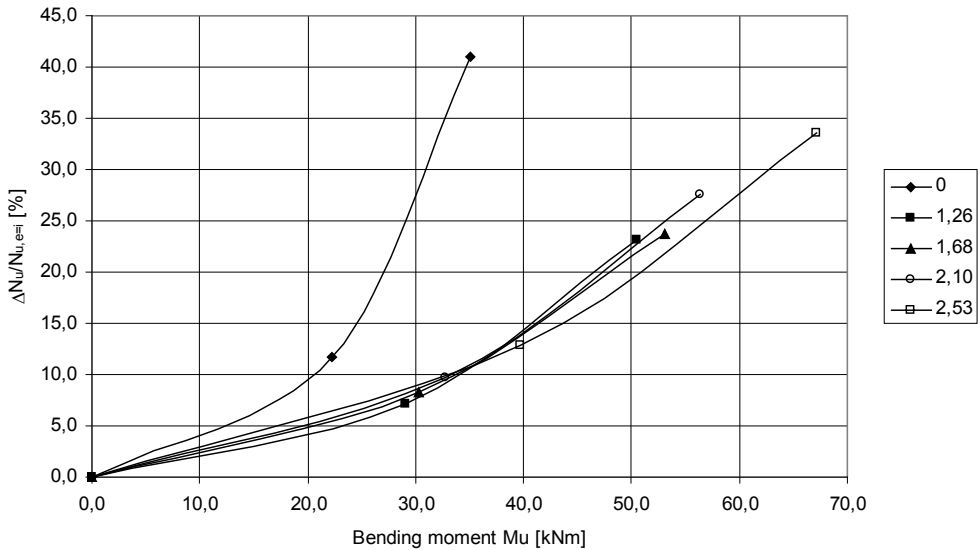

Fig. 8. Relative decrease of the load-bearing capacity versus bending moment

The relative decrease of the load-bearing capacity ($\Delta N_u / N_{u,e=i}$) of the reinforced concrete and strengthened columns $\Delta N_u = N_{u,e=0} - N_{u,e=i}$ in relation to the load-bearing capacity of respective columns loaded eccentrically $N_{u,e=i}$, depending on the value of bending moment ("i" − index corresponds to the eccentricities of 16 and 32 mm) is

presented in Figure 8. The curve for the strengthening intensity $\rho_L = 2.53\%$ is taken from the own investigations [7, 18].

It is seen in Figure 8 that the decrease of the load-bearing capacity of strengthened columns does not depend on the longitudinal strengthening intensity ρ_L. Whereas it depends on the presence of longitudinal reinforcement (in comparison with the columns without strengthening). In case of the bending moment of about 35 kNm the load-bearing capacity of each strengthened specimen drops by ~12%. The capacity decrease of the column without strengthening for the same load level is four times higher and drops by ~41%.

On the basis of measured longitudinal strains secondary eccentricities (e_2) were calculated and listed in the Table 5:

$$e_2 = \frac{l_0{}^2}{10} \cdot \frac{\varepsilon_{v2,\lim} - \varepsilon_{v1,\lim}}{h}, \tag{1}$$

where:

$\varepsilon_{v2,\lim}$ and $\varepsilon_{v1,\lim}$ – ultimate strains at the more and less compressed side,
l_0 – distance between the axes of cylindrical bearings ($l_0 = 1\ 690$ mm),
h – cross-section height.

The secondary effects analysis shows that the application of the longitudinal CFRP reinforcement improves plastic properties of the columns in comparison to the columns without strengthening. The significant decrease of analyzing values is clearly seen near the destructive load within one strengthening intensity. With the increase of the longitudinal rigidity (vertical direction in the Table 5) the redistribution of internal forces is not as significant as within the single strengthening intensity ρL for following eccentricities (horizontal direction in the Table 5).

Table 5. Secondary eccentricities

	Strengthening intensity ρ_L [%]	Eccentricity e_2 [mm]		
		$e_1 = 0$	$e_1 = 16$ mm	$e_1 = 32$ mm
1	0	0.6	3.03	5.20
2	1.26	0.37	1.54	4.31
3	1.68	−*	1.34	3.61
4	2.10	0.30	1.19	2.77

* − lack of the experimental data caused with strain gauge failure

4. Conclusions

The effectiveness of CFRP materials strengthening of eccentrically compressed reinforced concrete columns has been described. Performed studies lead to the following conclusions:

1) the damage of eccentrically compressed quadrangular reinforced concrete columns strengthened with CFRP strip and sheets occurs as a result of the sheet rupture at

the edges of columns. The crush of concrete and CFRP strip in the area of the jacket rupture follows the rupture immediately,

2) the longitudinal CFRP strengthening increases the column rigidity on condition that the longitudinal reinforcement is accompanied with transverse CFRP sheet reinforcement,

3) in the case being analyzed (quadrangular columns without significant rounding of corners) the increase of the load-bearing capacity is associated mainly with the presence of longitudinal CFRP strengthening (not with one layer of transverse CFRP strengthening); strains of concrete and longitudinal composite strengthening may reach a higher values in case of more intensive transverse reinforcement, it transfers directly into load-bearing capacity increase [2],

4) the usage of the longitudinal CFRP strengthening increases with the value of eccentricity. It manifests itself in the decrease of the secondary eccentricities with the increase of the longitudinal strengthening intensity ρ_L.

On the basis of the performed experiments it seems to be justified to enlarge the range of investigations with the analysis of the influence of columns slenderness (for $l_0/h > 10$) and transverse strengthening intensity (the number of layers of CFRP sheet). The analyzed columns should be classified as thickset ($l_0/h = 8.45$).

Acknowledgements

References

[1] Demers M., Neale K.W.: *Strengthening of existing concrete columns with unidirectional composite sheets*, Proceedings 4th International Conference on Short and Medium Span Bridges, Montreal, Canada, 1994, pp. 895–905.

[2] Ignatowski P., Kamińska M.E.: *On behaviour of compressed concrete confined with CFRP composites* (in Polish), Inżynieria i Budownictwo, 2004, No. 4, pp. 204–208.

[3] Ignatowski P., Kamińska M.E.: *On the effect of confinement of slender reinforcement concrete columns with CFRP composites*, International Journal for Restoration, Vol. 10, No. 1, 2004, pp. 73–98.

[4] Li J., Hadi M.N.S.: *Behaviour of externally confined high-strength concrete columns under eccentric loading*, Composite Structures, No. 62, 2003, pp. 145–153.

[5] Mirmiran A., Shahawy M.: *Behaviour of concrete columns confined by fibre composites*, Journal of Structural Engineering, Vol. 123, No. 5, May 1997, pp. 583–590.

[6] Kamiński M., Trapko T.: *Experimental behaviour of reinforced concrete column models strengthened by CFRP materials*, Journal of Civil Engineering and Management, Vol. 12, No. 2, 2006, pp. 109–115.

[7] Kamiński M., Trapko T.: *On effective use of CFRP as strengthening reinforcement of eccentric compressed RC column* (in Polish), Inżynieria i Budownictwo, 2006, No. 1, pp. 39–43.

[8] Kamiński M., Trapko T.: *Research methodic on compression of reinforced concrete elements strengthened with CFRP strips and wraps* (in Polish), Research on building materials and engineering structures, Wrocław University of Technology, Wrocław, Poland, 2006, pp. 185–192.

[9] Kamiński M., Trapko T., Musiał M., Bywalski Cz.: *Rheological strains of the compressed concrete elements strengthened with CFRP sheets subjected to cyclically changeable temperature*, Proceedings of the 8th international conference on creep, shrinkage and durability mechanics of concrete and concrete structures, Ise-Shima, Japan, Vol. 1, 2008, pp. 775–780.

[10] Kamiński M., Trapko T., Musiał M., Bywalski Cz.: *The influence of longitudinal CFRP strips on the load-bearing capacity of RC columns*, Proceedings of the 4th International Conference on FRP Composites in Civil Engineering CICE 2008, Zurich, Switzerland, 2008, on CD, Paper No. 3.A.2.

[11] Kamiński M., Trapko T., Musiał M., Bywalski Cz.: *Calculation of load-bearing capacity of RC columns strengthened with CFRP materials*, Proceedings of the 4th International Conference on FRP Composites in Civil Engineering CICE 2008 Zurich, Switzerland, 2008, on CD, Paper No. 2.A.1.

[12] Kamiński M., Trapko T., Musiał M.: *Rheological strains of the compressed concrete elements strengthened by CFRP materials*, Proceedings of the 8th International Symposium on Fiber-Reinforced Polymer Reinforcement for Concrete Structures, Patras, Greece, 2007, on CD, Paper No. 6–28.

[13] Łagoda M.: *Externally bonded reinforcement in bridge strengthening* (in Polish), Cracow University of Technology, Cracow, Poland, 2005.

[14] Polish Standard PN-B-03264:2002. *Plain, reinforced and prestressed concrete structures. Analysis and structural design* (in Polish).

[15] Rochette P., Labossière P.: *Axial testing of rectangular column models confined with composites*, Journal of Composites for Construction, Vol. 4, No. 3, 2000, pp. 129–136.

[16] Trapko T., Musiał M., Trapko W.: *The influence of transverse CFRP strengthening on rheological strains of compressed concrete elements*, Proceedings of the Second Asia-Pacific Conference on FRP in Structures APFIS 2009, Seoul, Korea, 2009, pp. 487–492.

[17] Trapko T., Musiał M., Kamiński M.: *Strains of eccentrically compressed RC columns strengthened with CFRP materials*, Proceedings of the Second Asia-Pacific Conference on FRP in Structures APFIS 2009, Seoul, Korea, 2009, pp. 279–284.

[18] Trapko T.: *Load capacity of RC columns strengthening with CFRP strips and wraps* (in Polish), PhD. dissertation, Wrocław University of Technology, Wrocław, Poland, 2004.

Wpływ intensywności wzmocnienia podłużnego na nośność elementów żelbetowych mimośrodowo ściskanych wzmacnianych materiałami CFRP

W pracy opisano badania nośności mimośrodowo ściskanych słupów żelbetowych wzmacnianych taśmami i matami CFRP. Celem przeprowadzonych badań była ocena wpływu zmiennej intensywności wzmocnienia podłużnego CFRP na nośność słupów. W badaniach zastosowano trzy intensywności wzmocnienia podłużnego CFRP – 2,10%, 1,68% i 1,26%. W pracy przedstawiono i omówiono wyniki badań nośności granicznej słupów w zależności od intensywności wzmocnienia podłużnego. Opisano mechanizmy zniszczenia oraz podano wartości sił niszczących i maksymalnych odkształceń podłużnych elementów.

Zastosowanie podłużnych taśm CFRP, jako zewnętrznego wzmocnienia, powoduje wzrost sztywności słupów. Dodatkowe wzmocnienie poprzeczne powoduje opóźnienie w procesie odspojenia się taśm od betonu. Współpraca obydwu materiałów CFRP powoduje zmniejszenie szybkości przyrostu odkształceń podłużnych, co przekłada się na wzrost nośności słupów.